Modelling wall interactions of a high-pressure, hollow cone spray

Vom Fachbereich Maschinenbau
an der Technischen Universität Darmstadt
zur
Erlangung des Grades eines Doktors der
Naturwissenschaften (Dr. rer. nat.)
genehmigte

Dissertation

vorgelegt von

Dipl.-Phys. Monika Mühlbauer

aus Amberg

Berichterstatter:	Prof. Dr.-Ing. Dr.-Ing. habil. C. Tropea
Mitberichterstatter:	Prof. Dr.-Ing. habil. M. Sommerfeld
	Priv.-Doz. Dr.-Ing. habil. I. Roisman
Tag der Einreichung:	29.06.2009
Tag der mündlichen Prüfung:	04.09.2009

Darmstadt 2009
D17

Abstract

Spray/wall interactions significantly influence air/fuel mixing and emissions in modern spark-ignited, direct injection engines. Yet, the complex phenomena are hardly understood - especially not with respect to the large number of parameters and the associated wide ranges occuring in an engine. Modelling spray/wall interactions thus presents a major drawback in numerical simulations done in engine development.

This thesis focuses on the impact of dense, high-pressure hollow cone sprays for which existing wall interaction models are evaluated in detail and shown to fail. To the best of the author's knowledge no model adapted to the considered spray type was available which was furthermore accompanied by a severe lack of quantitative experimental data. Therefore, Phase Doppler Anemometry (PDA) is used to gather data on the normal impact of an isooctane spray with 50 bar injection pressure on a hemispherical copper target. The latter can be heated and wall temperatures up to 200°C are studied. Moreover, an additional oil film can be applied on the surface to simulate the oil film on a cylinder liner lubricating the piston motion. Variations in the particle Reynolds number between 2000 and 3000 on impact are achieved in changing the distance between injector and target.

As the question how PDA data concerning spray/wall interaction have to be evaluated has not been studied thoroughly yet, a fundamental analysis was carried out and is presented in this thesis. The results are not limited to dense and high-pressure, hollow cone sprays but may serve as general guidelines for future data evaluation.

Based on the measurements, the impact mechanisms of dense, high-pressure sprays are discussed where film fluctuations leading to ligament breakup are found to be decisive. For the considered high Reynolds numbers, inertial forces dominate all other forces which results in negligible parameter influence of the mean Reynolds number and the wall temperature. The oil film is observed to be quickly removed by the impacting spray which points out that spray/wall interactions on a cylinder liner may seriously endanger the operability of an engine.

Finally, empirical correlations describing the secondary spray on wall interaction are developed from the gathered data and an extrapolation to oblique impact is proposed. This first empirical model adapted to dense, high-pressure hollow cone sprays is implemented in numerical code in a Lagrangian approach. Details of the implementation are given. The model is validated in several cases for impact angles between 30° and 90° measured relative to the wall and for injection pressures of 50 bar and 200 bar with very good results.

Kurzzusammenfassung

Gemischbildung und Emissionen moderner direkt einspritzender Ottomotoren werden entscheidend durch Spray/Wand-Wechselwirkungen beeinflusst. Die damit verbundenen, komplexen Phänomene sind bisher jedoch kaum verstanden - insbesondere nicht im Hinblick auf die beträchtliche Anzahl an Parametern, die mit jeweils großem Wertebereich im Motorbetrieb vorkommen. Die Modellierung von Spray/Wand-Wechselwirkungen stellt deshalb einen Schwachpunkt in der zu einem Großteil mittels numerischer Simulationen durchgeführten Motorenentwicklung dar.

Die vorliegende Arbeit konzentriert sich auf den Aufprall dichter Hohlkegelsprays für den die Unzulänglichkeit existierender Modelle detailliert aufgezeigt wird. Nach bestem Wissen der Autorin gab es bisher kein für diesen Spraytyp geeignetes Wandwechselwirkungs-Modell, was zudem mit einem völligen Mangel an quantitativen experimentellen Daten verbunden ist.

Deshalb werden zunächst mittels Phasen Doppler Anemometrie (PDA) Daten zum normalen Aufprall eines Isooktansprays mit 50 bar Einspritzdruck auf ein halbkugelförmiges Kupfertarget gewonnen. Letzteres ist beheizbar, wobei Wandtemperaturen bis 200°C betrachtet werden. Zudem kann ein Ölfilm auf die Oberfläche aufgebracht werden, um den für die Kolbenbewegung entscheidenden Schmierfilm auf einer Zylinderbuchse nachzustellen. Durch unterschiedliche Abstände zwischen Target und Injektor wird beim Aufprall eine Variation der Reynoldszahl im Bereich von 2000 bis 3000 erreicht.

Da die Fragestellung, wie PDA Daten bezüglich Spray/Wand-Wechselwirkungen auszuwerten sind, bisher nicht ausreichend untersucht wurde, werden fundamentale Aspekte zur Datenauswertung analysiert und in der Arbeit dargestellt. Die Ergebnisse sind dabei nicht auf dichte Hohlkegelsprays beschränkt, sondern können als allgemeine Anleitung für zukünftige Datenauswertungen dienen.

Im Rahmen der Messauswertung wird der Aufprallmechanismus bei dichten Hohlkegelsprays diskutiert, wobei Filmfluktuationen, die zum Aufbruch von Ligamenten führen, identifiziert werden. Bei den betrachteten hohen Reynoldszahlen dominieren Trägheitskräfte alle anderen Kräfte, was zu einem vernachlässigbaren Parametereinfluss der Reynoldszahl und der Wandtemperatur führt. Ein Ölfilm wird durch das aufprallende Spray sehr schnell verdrängt. Dies verdeutlicht, wie Spray/Wand-Wechselwirkungen auf der Zylinderbuchse die Funktionsfähigkeit des Motors gefährden können.

Schließlich werden auf Basis der experimentellen Daten empirische Korrelationen zur Beschreibung des Sekundärsprays aufgestellt und eine einfache Extrapolation auf schiefe Aufprälle vorgeschlagen. Details der Implementierung dieses ersten empirischen Modells zur Wandwechselwirkung dichter Hohlkegelsprays in einem Lagrange-Ansatz werden erläutert. Anhand mehrerer Fälle wird das Modell für einen Aufprallwinkelbereich von etwa 30°-90° relativ zur Wand und für Einspritzdrücke von 50 bar und 200 bar mit sehr guten Ergebnissen validiert.

Acknowledgement

At this point I would like to express my sincerest thanks to Prof. Dr.-Ing. Dr.-Ing. habil. Cameron Tropea for supervising this work and offering incessant assistance and fruitful discussions. Similarly, I am very much indepted to Priv.-Doz. Dr.-Ing. habil. Ilia Roisman for many ideas and constant support. Dr.-Ing. Feras Batarseh helped me immensely in realising the experiment and Silke Wallner with all formalities concerning the thesis.

I would also like to thank Prof. Dr.-Ing. habil. Martin Sommerfeld most sincerely for kindly accepting to be second referee.

Moreover, I am deeply grateful to Dr.-Ing. Bodo Durst from BMW for giving me the opportunity to do this work in his team for CAE combustion, for allowing me great latitude in the realisation and for supporting me in all respects. My special thanks extend to my supervisors Dr.-Ing. Björn Hußmann and Dr.-Ing. Markus Selder from BMW for constantly listening to problems, providing helpful comments and spending much time in reading the drafts of this work.

Both at the Chair of Fluid Mechanics and Aerodynamics of the TU Darmstadt and at BMW I found a very welcoming atmosphere, great assistance and good friends who turned the past three years into happy ones.

I would also like to thank Dr.-Ing. Thomas Esch and Dr.-Ing. Wolfgang Bauer from ANSYS CFX for very good cooperation and quick, direct communication.

Last but not least, my sincerest thanks go to my parents Sieglinde and Georg Mühlbauer, my brother Wolfgang and my partner Jakob Mayer for enduring my varying moods and providing endless encouragement.

Contents

List of Symbols

Abbreviations

cdf	cumulative distribution function	
pdf	probability density function	
BMW	Bayerische MotorenWerke	
CFD	Computational Fluid Dynamics	
COSY	COordinate SYstem	
DDM	Discrete Droplet Model	
DI	Direct Injection	
DNS	Direct Numerical Simulation	
LES	Large-Eddy Simulation	
PDA	Phase Doppler Anemometry	
RANS	Reynolds-Averaged Navier-Stokes equations	
RMS	Root Mean Square	
rpm	revolutions per minute	1/min
SEM	Scanning Electron Microscope	
SMD	Sauter Mean Diameter, D_{32}	m
SST	Shear-Stress-Transport turbulence model	

Dimensionless characteristic numbers

Ca	Capillary number, $\mathrm{Ca} = \frac{\mu_p \cdot v_p}{\sigma}$
CFL	Courant-Friedrichs-Lewy number
La	Laplace number, $\mathrm{La} = \frac{\rho_p \cdot \sigma \cdot D_p}{\mu_p^2}$
Nu	Nusselt number, $\mathrm{Nu} = \frac{h_c \cdot D_p}{\lambda_f}$

Oh	Ohnesorge number, $\mathrm{Oh} = \frac{\mu_p}{\sqrt{\rho_p \cdot \sigma \cdot D_p}}$
Pr	Prandtl number, $\mathrm{Pr} = \frac{\mu_p \cdot c_P}{\lambda_p}$
Re	Reynolds number, $\mathrm{Re} = \frac{\rho_p \cdot v_p \cdot D_p}{\mu_p}$
Re*	another definition of the Reynolds number, $\mathrm{Re}^* = \frac{\rho_f \cdot v_s \cdot D_p}{\mu_f}$
Sc	Schmidt number, $\mathrm{Sc} = \frac{\mu_p}{\rho_p \cdot \mathcal{D}}$
Sh	Sherwood number, $\mathrm{Sh} = \frac{\beta_c \cdot D_p}{\mathcal{D}}$
We	Weber number, $\mathrm{We} = \frac{\rho_p \cdot v_p^2 \cdot D_p}{\sigma}$

Greek symbols

α, β	impact and reflection angle (between primary/secondary velocity vector and surface)	rad
α_ω, $\beta_{k/\omega}$, $\sigma_{k/\omega}$	constants in the k-ω model	-
α_p	angle between the particle velocity vector and the normal to the mean direction of both laser beams	rad
α_T	thermal expansion coefficient	1/K
$\bar{\Phi}$, Φ'	ensemble or time average and turbulent fluctuation of a scalar quantity Φ	
β_c	mass transfer coefficient	m/s
$\Delta\phi_{1-2}$	phase difference measured by two PDA detectors	rad
$\Delta\Theta$, $\delta\Theta$	width of Θ-classes oriented on target apex and on the mean impact area respectively	deg
$\Delta\Theta_{\mathrm{con},i}$	uncertainty of $\Theta_{\mathrm{con},i}$	deg
$\Delta\Theta_{\mathrm{prim}}$	angle range of the main impact area	deg
$\Delta\tilde{\Phi}_{\mathrm{vel}}$	spray diversification angle, used for primary data filtering	deg
δt	timestep of the Lagrangian phase	s
Δt_i	injection duration	s
Δt_{si}	time between two injections (from start to start)	s
δ	non-dimensional wall film thickness, $\delta = h_{\mathrm{film}}/D_{\mathrm{prim}}$	-
δ_{ij}	Kronecker symbol	-
ϵ_S, $\epsilon_{S,\mathrm{val}}$	relative signal presence of all detected and all validated signals respectively	-

$\epsilon_{\mathrm{compression}}$	compression ratio	-
ϵ_{rel}	relative error of the mean of a scalar quantity X, $\epsilon = \sigma_{X_{10}}/X_{10}$	-
$\epsilon_{A,p}$, $\epsilon_{E,p}$	absorptivity and emissivity of a particle	-
$\eta_{\mathrm{val},i}$	correction factor of drop i accounting for multiple and non-validated drops in the detection volume	-
$\Gamma^{*}_{X,k,\mathrm{class}\,n}$	flux density (summed over all directions) of a scalar quantity X of the drops k in Θ-class n relative to that of all drops k	-
Γ_{Φ}	diffusion coefficient of a scalar quantity Φ	
γ_a, γ_z	non-dimensional, mean and peak-to-peak wall roughness, $\gamma_a = R_a/D_p$ and $\gamma_z = R_z/D_p$ respectively	-
$\Gamma_{X,k,\gamma}$	flux density of a scalar quantity X in direction $\vec{e}_{\gamma}$ of all drops k relative to that of all primary drops $(k = 1)$	-
$\Gamma_{X,k,\mathrm{class}\,n}$	flux density (summed over all directions) of a scalar quantity X of the drops k in Θ-class n relative to that of all primary drops $(k = 1)$	-
$\Gamma_{X,k}$	flux density (summed over all directions) of a scalar quantity X of all drops k relative to that of all primary drops $(k = 1)$	-
κ	von Kármán constant	-
λ	thermal conductivity	W/(m·K)
Λ, τ, Υ	length, time and velocity scale of film fluctuations	m, s, m/s
λ_A	probability of drop appearance in the detection volume	-
λ_b, $\lambda_{\mathrm{green/blue}}$	wavelength of a general or green/blue laser beam	m
λ_{air}	available air mass/air mass of a stoichiometric mass ratio	-
μ	dynamic viscosity	kg/(m·s)
μ_l	half axis ratio of the illuminated ellipsoid	-
μ_t	turbulent viscosity	kg/(m·s)
ν_{oil}	kinematic viscosity of oil	m^2/s
ω	tilt between COSYs for dry and wetted target surface	deg
ω	turbulent frequency	1/s
Φ	unspecified scalar quantitiy	
Φ_{op}	off-axis angle in a PDA setup (detection angle)	deg

Φ_{vel}	angle between velocity vector and wall	deg
Ψ	deviation angle (between impact and reflection plane)	rad, deg
Ψ_{op}	elevation angle in a PDA setup	deg
ρ	density	kg/m^3
σ	surface tension	N/m
σ, μ	fit parameters	-
σ_S	Stefan-Boltzmann constant	W/(m^2·K^4)
σ_X	standard deviation of a quantity X	
$\sigma_{k/\varepsilon}$, $C_{\mu/\varepsilon 1/\varepsilon 2}$	constants in the k-ε model	-
$\sigma_{X_{10}}$	mean error of the mean X_{10}	
τ	non-dimensional time describing crown propagation	-
τ_e	time scale of a virtual eddy	s
τ_i	signal duration	s
τ_w	wall shear stress	N/m^2
τ_{ij}	component ij of the stress tensor	N/m^2
Θ	azimuthal angle on the hemispherical target	deg
Θ_0	azimuthal angle of the main impact area on the target	deg
Θ_1, Θ_2	smallest and largest value of Θ in $\Delta\Theta_{\mathrm{con},i}$	deg
Θ_i	azimuthal angle of MP$_i$ on the target	deg
$\Theta_{\mathrm{class,min/max}}$	smallest and largest value of Θ in a considered Θ-class	deg
$\Theta_{\mathrm{con,min/max}}$	minimal and maximal angle Θ where impacts can occur on the target	deg
$\Theta_{\mathrm{con},i}$	azimuthal angle on the target where drop i impinges	deg
Θ_{op}	angle enclosed by two laser beams in a PDA setup	deg
$\tilde{\Phi}_{\mathrm{vel,10}}$	mean angle between $U1$ and $V1$ for all drops impacting in the central Θ-class, equal to $\tilde{\Phi}_{\mathrm{vel,10,central\ class}}$	deg
ε	turbulent dissipation rate	J/(kg·s)

Latin symbols

Δh_{vap}	latent heat per mass unit	J/kg

$\dot{m}_{\text{inj}}$	injected mass flow rate	kg/s
$\dot{m}_{\text{stat}}$	injected mass flow rate for stationary needle lift	kg/s
$\dot{Q}$, $\dot{Q}_1$, $\dot{Q}_2$	volume flux of film fluid	m^3/s
$\dot{Q}_C$, $\dot{Q}_m$, $\dot{Q}_R$	convective heat transfer, transfer of latent heat and radiative heat transfer	J/s
$\dot{q}_i$	component i of a heat flux	$\text{J}/(\text{s}\cdot\text{m}^2)$
$\mathbf{A}$, $\vec{b}$	solution matrix and vector of a linearised problem	
$\mathcal{D}$	mass diffusity of the gaseous mixture	m^2/s
$\mathcal{R}$	fluid specific gas constant	J/(kg·K)
$\vec{e}$	unit vector	-
$\vec{e}_b$, $\vec{e}_1$, $\vec{e}_2$	unit vectors in beam direction	-
$\vec{e}_i$	unit vector parallel to the velocity vector of drop i	-
$\vec{e}_{pr}$	unit vector pointing from particle to receiver	-
$\vec{q}_X$	flux density vector of a scalar quantity X	
A	area	m^2
A, B, C	material-dependent constants in the Antoine equation	-
a, b, k	fit parameters	-
a, b, n, r, s	integers	-
a_0, b_0, c_0	lengths of the half axes of the illuminated ellipsoid	m
A_{impact}	impact area	m^2
A_{inj}	injection area	m^2
$A_{\text{val},i}$	validation area of drop i	m^2
$A_{\text{wall cell}}$	characteristic size of a wall cell	m^2
AT	arrival time of a particle in the measurement volume	s
AT_{rel}	relative arrival time of a particle in the measurement volume counted from the arrival of the first particle of an injection	s
C	constant in the logarithmic wall law depending on surface roughness	-
c	speed of light in the respective medium	m/s
C_D	drag coefficient	-
c_P	specific heat capacity at constant pressure	J/(kg·K)

C_S, R_S	terms in the definition of a general particle source term	
c_{N}	wall-normal restitution coefficient, $c_{\mathrm{N}} = v_{\mathrm{N,sec}}/v_{\mathrm{N,prim}}$	-
c_{T}	wall-tangential restitution coefficient, $c_{\mathrm{T}} = v_{\mathrm{T,sec}}/v_{\mathrm{T,prim}}$	-
D	drop diameter	m
d, d'	average blob diameter along a ligament and subblob size	m
d_i	distance between MP$_i$ and target surface	m
$d_{\mathrm{inj.point}}$	distance between virtual injection point and target	m
$D_{B,0}$, $D_{B,1/2}$	average and arbitrary diameters resulting from a ligament	m
D_L, $D_{L,0}$	diameter of a ligament and its initial value	m
$d_{t,i}$, $d_{w,i}$	diameter of the detection volume for drop i and its projection onto the surface	m
DT	timestep of the Eulerian phase	s
e	internal energy per mass unit	J/kg
F	function dividing the secondary mass between child parcels	-
f_1, f_2, f_D	detected frequencies and difference frequency	Hz
f_b	frequency of a laser beam	Hz
f_{dev}	±1, describes forward/backward scattering	-
f_{shift}	frequency shift in a Bragg cell	Hz
$F_{B,i}$	component i of the basset-history force	N
$F_{D,i}$	component i of the viscous drag force	N
$F_{EXT,i}$	component i of external forces	N
$F_{M,i}$	component i of the Magnus force	N
$f_{N/T,\mathrm{backward}}$	function relating the average normal/tangential momentum of secondary drops in backward direction to the average absolute primary momentum	-
$f_{N/T,\mathrm{forward}}$	function relating the average normal/tangential momentum of secondary drops in forward direction to the average absolute primary momentum	-
$F_{P,i}$	component i of the pressure gradient force	N
$F_{S,i}$	component i of the Saffman force	N
$f_{V,i}$	component i of a volume force	N/m^3
$F_{VM,i}$	component i of the virtual mass force	N

fd_{calc}	coefficient describing $h_{\text{film}} \cdot (\sin\Theta)^{2/3}$, calculated for a given volume flux and determined from image evaluation respectively	m
G_k	production term of turbulent kinetic energy in the k-ε and k-ω model	J/(m^3·s)
h	enthalpy per mass unit	J/kg
h_c	heat transfer coefficient	W/(m^2·K)
h_l	thickness of the viscous boundary layer	m
h_{film}	wall film thickness	m
i, j, k	integers	-
I_d	minimal detectable intensity	m
$j_{n,i}$	component i of a diffusive flux of species n	kg/(m^2·s)
k	integer separating primary/secondary drops (primary drops $k = 1$, secondary drops assigned to the outside/ inside of the hollow cone $k = 2/3$),	-
k	turbulent kinetic energy per mass unit	J/kg
k_T	parameter used to define $f_{T,\text{forward}}$	-
L, L_0	target length at arbitrary and reference temperature	m
l_e	length scale of a virtual eddy	m
L_i, $\bar{L}_k$	Doppler burst length of drop i and mean of size class k	m
l_s	effective slit length	m
m	mass	kg
m_{inj}	injected mass	kg
N	number, e.g. the number of secondary child parcels per impact or the sample number	-
n	particle number rate (scaled with DT in CFX)	- (1/s)
N_P	number of parcels	-
n_{refr}	refractive index	-
$N_{\text{size classes}}$	number of size classes	-
N_D	number of drops passing through the detection volume	-
N_S, $N_{S,\text{val}}$	number of detected and validated signals respectively	-
p	pressure	Pa

p_{ambient}	ambient pressure	Pa
p_{inj}	injection pressure	Pa
p_{rand}	random number	-
p_{ref}	reference pressure	Pa
p_{vap}	vapour pressure	Pa
$q_{\mathrm{E_{kin}},\gamma}$	kinetic energy flux density in direction $\vec{e}_\gamma$	$\mathrm{J/(m^2 \cdot s)}$
$q_{\mathrm{E_{tot}},\gamma}$	total mechanical energy flux density in direction $\vec{e}_\gamma$	$\mathrm{J/(m^2 \cdot s)}$
$q_{\mathrm{Nr},\gamma}$	number flux density in direction $\vec{e}_\gamma$	$\mathrm{1/(m^2 \cdot s)}$
$q_{j\text{-mom},\gamma}$	j-momentum flux density in direction $\vec{e}_\gamma$	
$q_{m,\gamma}$	mass flux density in direction $\vec{e}_\gamma$	$\mathrm{kg/(m^2 \cdot s)}$
$q_{V,\gamma}$	volume flux density in direction $\vec{e}_\gamma$	m/s
$q_{X,\gamma}$	flux density of a scalar quantity X in direction $\vec{e}_\gamma$	
$q_{X,k}$	flux density of a scalar quantity X for all drops k summed over all directions	
R_0	target radius	m
R_a, R_z	average and peak-to-peak surface roughness respectively	m
r_w	half the beam diameter at beam waist	m
R_{crown}	crown radius	m
S_Φ	source term of a scalar quantity Φ	
S_h	enthalpy source term	$\mathrm{J/(m^3 \cdot s)}$
S_m	mass source term	$\mathrm{kg/(m^3 \cdot s)}$
S_n	mass source term for species n	$\mathrm{kg/(m^3 \cdot s)}$
S_p	particle source term	N/kg
$S_{p,i}$	component i of a momentum source term	N/kg
T	temperature	K
t	time	s
t^*	large time span compared to turbulent fluctuations	s
T_{ambient}	ambient temperature	K
t_{meas}	total measurement time	s
T_{sat}	saturation temperature	K

T_{wall}	wall temperature	K
$T_{L/N}$	Leidenfrost and Nukiyama temperature respectively	K
TT	transit time of a particle through the measurement volume	s
$U1$, $V1$	velocity components measured with PDA	m/s
$U1_{1-2}$, $V1_{1-2}$	measured phase difference for the respective detector pair	rad
$U2$, $V2$	velocity components after transformation	m/s
V	volume	m^3
v^+	non-dimensional velocity tangential to the wall given by the logarithmic wall law	-
v_i	component i of the velocity vector	m/s
V_L	volume of a ligament	m^3
v_s, $v_{s,i}$	vector amount and component i of the slip velocity between fluid and particle	m/s
v_τ	friction velocity	m/s
v_{inj}	injection velocity	m/s
$v_{\text{nozzle exit}}$	liquid velocity at nozzle exit	m/s
$w_{n,i}$	weight of drop i in Θ-class n	m
X	unspecified scalar quantity	
x, y, z	cartesian coordinates	m
x_i	component i of the coordinate vector	m
y^+	non-dimensional distance to the wall used in the logarithmic wall law	-
C_xH_y	unspecified hydrocarbon	
MP_i	measurement point i	

Subscripts

10	arithmetic mean
20	surface mean
30	volumetric mean
32	Sauter mean
a, b	after impact, before impact

B	blob
b	beam
f	fluid
L	ligament
p	particle
r	receiver
abs	absolute velocity
central	central Θ-class where most primary drops impact
central area	central Θ-class plus both neighbouring ones
class n	Θ-class n
deg	angle to be applied exceptionally in degrees
fit	denotes fitted quantities
flux	mean value calculated from flux density values
gev	generalised extreme value distribution
impro	characterises an improved mean value which includes correction and weighting factors
inj	injection
liquid	liquid
max, min	maximal, minimal value
meas	measured
N, T	normal and tangential to the considered surface
op	optics
prim	primary
sec	secondary
sec backward	secondary drops scattered in backward direction
sec forward	secondary drops scattered in forward direction
stat	stationary
total	total (secondary drops in all directions)
Weibull	Weibull distribution

Superscripts

$'$	characterises the turbulent fluctuation of a quantity
$-$	characterises the ensemble or time average of a quantity
$\rightarrow$	characterises a vector

Extra symbols for Elsässer’s model

α_r	virtual impact angle	rad
$\alpha_{\min}$	virtual profile angle	deg
β_r	virtual reflection angle	rad
$D_{\min}$	diameter limit	-
F_δ	polynomial in δ	-
$f_{n,\mathrm{sec}j,b}$	secondary to primary number rate ratio for child parcel j in boiling (HW)	-
$f_{n,brk}$	total secondary to primary number rate ratio for breakup (HNW)	-
$f_{n,sp}$	secondary to primary number rate ratio for splashing (CW/HW)	-
$h_{\mathrm{film,r}}$	wall film thickness in the virtual roughness profile	m
K	characteristic number, $K = \mathrm{We} \cdot \mathrm{Oh}^{-0.4}$	-
K_{dry}, K_S	parameters used to define the splashing criterion	-
s_{KD}	final splashing criterion	-
T^*_{CW}	non-dimensional wall temperature in CW	-
T^*_{HNW}	non-dimensional wall temperature in HNW	-
T^*_{HW}	non-dimensional wall temperature in HW	-
$T_{L/N,\mathrm{contact}}$	modified Leidenfrost and Nukiyama temperature respectively	K
$x_{\mathrm{D,sec}j,brk}$	secondary to primary diameter ratio for child parcel j for breakup (HNW)	-
$x_{\mathrm{D,sec}j,b}$	secondary to primary diameter ratio for child parcel j in boiling (HW)	-
$x_{\mathrm{m},b}$	secondary to primary mass ratio for boiling (HW)	-
$x_{\mathrm{m},sp}$	secondary to primary mass ratio for splashing (CW/HW)	-
$x_{c,sp}$	secondary to primary velocity ratio for splashing (CW/HW)	-

$x_{D,sp}$	secondary to primary diameter ratio for splashing (CW/HW)	-
CW	Cold wetting regime	
HNW	Hot non wetting regime	
HW	Hot wetting regime	
$\mathrm{We}_{\mathrm{crit}}$	critical Weber number separating different impact phenomena	-
$\mathrm{We}_{t,\mathrm{increase}}$	Weber number defined in HNW	-

Extra symbols for Kuhnke's model

α	impact angle relative to wall in deg	deg
α_r	impact angle relative to wall in rad	rad
$\bar{r}$	standard deviation from mean impingement point	m
η_{ha}	half axis ratio in the system of ellipses	-
κ	drop spacing	-
κ_j	spacing parameter in the elliptic ring j	-
λ_{MD}	blending factor between single and multiple drop correlations	-
ν_{32}	$D_{32,\mathrm{sec}}/D_{10,\mathrm{sec}}$	-
ν_{wf}	wall film mass in a computational cell scaled with impinging mass	-
ω	parameter used to define the deviation angle	-
A_j	area of elliptic ring j	m^2
B	function using a random number in the determination of the secondary to primary mass ratio	-
c_α	polynomial in α_r	-
c_{MD}	constant used in λ_{MD} for a wetted wall	-
D_L^*	non-dimensional, maximal spread of a lamella on drop impact	-
K	kinematic parameter, $K = \mathrm{We}_{\mathrm{N}}^{5/8} \cdot \mathrm{La}^{1/8}$	-
K_{crit}	critical value of K, separating splash	-
MD	multiple drop correlations	
r_j	length used to define the system of ellipses	m
SD	single drop correlations	

T^*	non-dimensional wall temperature	-
T^*_{crit}	critical, non-dimensional wall temperature separating adhesion and rebound for small values of K	-
t^*_{exp}	scaled expansion time of a drop lamella till maximal spread	-
t_{exp}	expansion time of a drop lamella till maximal spread	s

Extra symbols for Roisman's/Horvat's model

$\Gamma_{\mathrm{E_{tot}}}$	secondary to primary flux of total mechanical energy	-
Γ_V	secondary to primary volume flux and mass ratio	-
h_L	thickness of a lamella	m
K	kinematic parameter, $K = \mathrm{We}_{\mathrm{N}}^{0.8} \cdot \mathrm{Re}_{\mathrm{N}}^{0.4}$	-
K_{crit}	critical value of K separating splashing and deposition for not too small Weber numbers	-

Chapter 1

Introduction

1.1 Motivation and outline

In a spark-ignited, direct injection (DI) engine, spray/wall interactions strongly influence air/fuel mixing and emissions where both, the secondary (post-impingement) spray and the forming wall film, play an important role. However, the associated complex phenomena have been hardly understood yet. This is connected to a general lack of quantitative experimental data for the extremely wide parameter ranges in a running engine. The conditions comprise high surface temperatures (up to 600 K) and ambient pressures of several bars.

The scarcity of physical understanding and experimental data is reflected in rather insufficient modelling of spray/wall interactions. These are usually still described as superpositions of single drop impacts although this is known to be incorrect, cf. [58] for instance. Poor modelling presents a major drawback in engine development where the design of the combustion chamber and the associated spray targeting are determined to a large extent by numerical simulations due to the high costs of experimental test rigs.

The focus of this thesis lies on the modelling of wall interactions of high-pressure and dense hollow cone sprays. The latter are characterised, amongst others, by a good spray stability and reproducability which predestines them to fulfill the high demands on injections in modern DI engines. Drop sizes are mostly smaller than $100\,\mu$m while their velocities can achieve up to around 200 m/s.

It is shown that existing spray/wall interaction models fail to describe the impingement of the considered spray type even in the rather simple case of a cold, horizontal plate as target surface. The thesis therefore aims at the development of a new spray impact model suitable to the conditions in a running engine and at its implementation in numerical code.

To achieve this, quantitative data are gathered in the experimental part of the study. The secondary spray generated by spray impact onto a heated surface is measured using Phase Doppler Anemometry (PDA). This measurement technique is appropriate to obtain quantitative information on both, drop sizes and velocities, and is very common to characterise free sprays nowadays. Yet, it has hardly been used to study spray/wall interactions and the associated procedure of data evaluation has not been developed thoroughly so far. Hence, this work treats some very fundamental questions on data evaluation giving guidelines for future work.

On the basis of the evaluated data the influence of important parameters such as wall temperature and kinematic drop parameters on spray/wall interactions is considered and the impact mechanism for the dense spray is discussed. The effect of a thin oil layer on the surface which is applied, for instance, on the cylinder liner to lubricate the piston motion in an engine, is also studied.
The analysis of the experimental data allows to develop an empirical model for the typical quantities of the secondary spray (average drop diameters, velocities and masses) as functions of the parameters of the impinging spray. To the best of the author's knowledge, it is the first model adapted to the wall interaction of a high-pressure and dense hollow cone spray. A number of validation cases are finally presented which prove the model to be a major improvement compared to existing modelling.

The work is carried out for BMW, where ANSYS CFX, a commercial CFD (Computational Fluid Dynamics) code, is employed. All numerical simulations of spray propagation and wall impact are performed with this software. As it showed very limited possibilities concerning the implementation of interaction models, the code has been significantly modified in cooperation with ANSYS in the framework of this thesis, e.g. parcel breakup on impact and a wall film module have been introduced.

The outline of this dissertation is as follows:

- The introductory chapter continues with a description of the conditions under which spray/wall interactions occur in a spark-ignited direct injection engine. A short survey of CFD fundamentals is then presented. The status of numerical modelling of spray/wall interactions is discussed and three existing models are considered in more detail. It becomes clear why the possibilities offered by the commercial code CFX to implement a spray/wall interaction model have been insufficient at the beginning of this work. Section 1.5 summarises the main subjects of the latter.

- Chapter 2 considers the impact of a hollow cone spray on a cold, horizontal plate. Simulations done with CFX are compared to transmitted-light images. The existing models described in Chapter 1 do not lead to satisfactory results. The improvements in CFX which only allow for the implementation of the models are discussed.

- To improve modelling, experiments with a hollow cone spray have been performed using isooctane as spray liquid. Chapter 3 describes the setup and experimental methods. The wall temperature and the droplet kinematics, as well as an oil film on the surface have been varied in the experiments.

- Chapter 4 proceeds with a detailed look on data evaluation. Fundamental issues concerning the treatment of PDA data describing spray/wall interaction are studied.

- The results of the experiments are presented in Chapter 5. The parameters influencing the post-impingement spray as well as the impact mechanism are discussed. A new empirical model is developed.

- For verification of the model, the experiment is simulated using CFX and Chapter 6 presents the outcome. The numerically predicted spray parameters of the new model are compared with those of the existing models and with the experimental data. The proposed new spray impact model improves significantly the predictive capabilities of the code which is shown in two further validation cases.

1.2 Combustion and spray/wall interaction in a spark-ignited, direct-injection engine

The current development concerning spark-ignited engines (Otto engines) is challenged by the demand for high performance yet, at the same time, low emissions and low fuel consumption. To fulfil this task, the concept of direct gasoline injection into the combustion chamber has been developed, see e.g. [29], [84], [53].

1.2.1 Combustion principles and sprays

1.2.1.1 Main concepts of engine combustion

With respect to the formation of the air/fuel mixture in DI engines two main concepts are distinguished:

- The homogeneous concept aims at a uniform mixture distribution throughout the cylinder. For complete combustion, air and fuel have to be available in a stoichiometric mass ratio which equals 15.1:1 for isooctane, for instance. This case is commonly expressed by a value $\lambda_{\text{air}} = 1$, where λ_{air} describes the ratio between the available air mass and the air mass needed for a stoichiometric mass ratio.
  The major advantage of direct spray injection is the cooling of the gaseous mixture due to the evaporation of the liquid spray drops in the combustion chamber. This reduces the risk of uncontrolled ignitions at full load, i.e. of knocking, and thus enables an increase of the compression ratio. The latter is defined as

  $$\epsilon_{\text{compression}} = \frac{V_{\text{cylinder,max}}}{V_{\text{compression}}}\,, \tag{1.1}$$

  where $V_{\text{compression}}$ is the compression volume. It equals the minimal cylinder volume with the piston situated at the top dead center. For the piston at the bottom dead center, the cylinder volume attains its maximum $V_{\text{cylinder,max}}$. Larger $\epsilon_{\text{compression}}$ means an increase in efficiency, i.e. lower fuel consumption (until an optimum where the growing thermal losses change the trend again). This is especially relevant for turbocharged engines, where the cylinder fill and hence the power are increased by drawing in compressed air. The larger risk of knocking even requires a decrease in $\epsilon_{\text{compression}}$. Due to the cooling effect, the lowering of the compression ratio is reduced in DI engines.

- In a stratified concept, applicable at part load, a flammable air/fuel mixture is established only in a locally restricted area around the spark plug. The rest of the cylinder is filled with a lean air/fuel mixture, $\lambda_{\text{air}} > 1$. It isolates the walls from the combustion which leads to reduced heat losses. Moreover, the stratified concept is mainly advantageous in fuel consumption due to reduced throttle losses.

The major challenge, however, is a more expensive exhaust-gas aftertreatment as a common three-way catalytic converter is only suitable for an overall value of $\lambda_{\text{air}} = 1$ to successfully convert hydrocarbons C_xH_y, carbon monoxide CO and nitrogen oxides NO_x.

1.2.1.2 Demands on spray quality and injector types

Direct injection imposes high demands on fuel injectors because the available time for air/fuel mixing is very short compared to an injection in the intake manifold: for homogeneous operation, where the injection may start during the intake stroke, the injection and subsequent mixing may take at most as long as half a crankshaft revolution in a four-stroke engine. For 6000 rpm an injection time of $\Delta t_i \approx 5\,\text{ms}$ results. At engine idling speed with lower fuel demand or in stratified operation with a later start of injection the available time may reduce to only $\Delta t_i \approx 0.4\,\text{ms}$.
This leads to the requirements of fast opening and closing mechanisms of the injector nozzle and a high quality of spray atomisation which is achieved by injection pressures of up to 200 bar. Small drops are very important as drop evaporation and especially the heating of the drop liquid can be the slowest component in the whole combustion process and can thus determine the overall burning rate, see [72].

Depending on the combustion principle, further demands on spray design arise and determine the choice of the respective injector (for an overview see [37], [53]):

- In the homogeneous concept already the liquid spray has to be distributed in the combustion chamber as best as possible to achieve a spatially even vapour distribution in time. A very common injector type is a high-pressure multihole nozzle controlled by a magnetic system. The number and direction of the jets is adapted to the cylinder geometry.
- In the stratified concept and its established spray-guided realisation no walls or air flows are used to place the air/fuel cloud around the spark plug. This has to be provided by a good and stable spray design. An excellent shot-to-shot reproducability with respect to cyclic fluctuations and varied ambient conditions is indispensible. Therefore, piezo-electric, outward-opening injectors which produce a dense hollow cone spray, see Figure 1.1, are more suitable as they do not suffer from magnetic remanence. They show shorter opening/closing times and a smaller minimal value of injected liquid due to a shorter minimal signal time. Their tendency to coke is also reduced. Yet, these advantages face increased costs (which is the reason why multihole injectors are often preferred in engines which operate only in the homogeneous mode).

In this work, the hollow cone spray of piezo-driven, outward-opening nozzles is considered.

1.2.2 Spray/wall interaction

1.2.2.1 Occurence

In the homogeneous concept, direct spray/wall interaction may occur on various surface parts, e.g. the piston, the cylinder liner, the intake valves or the spark plug, see Fig-

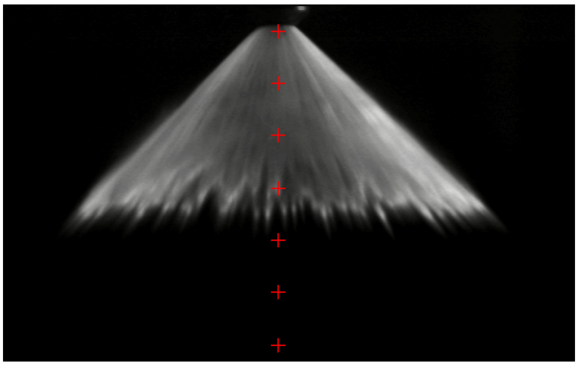

Figure 1.1: Exemplary image of the considered spray at normal ambient conditions and for an injection pressure of 150 bar, 0.32 ms after start of injection.

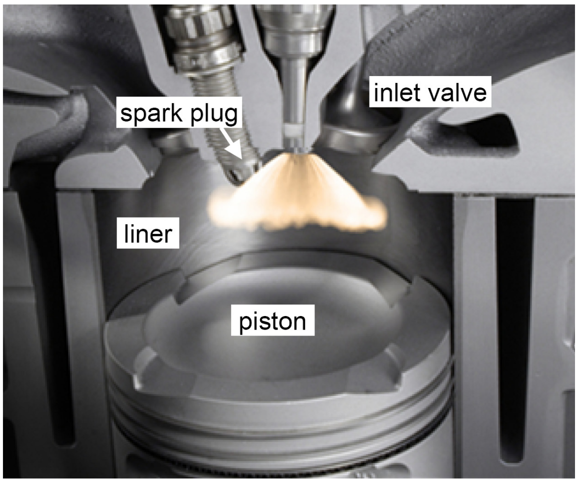

Figure 1.2: Combustion chamber.

ure 1.2. It influences thoroughly air/fuel mixing and hence the combustion process by reducing drop sizes and changing directions and velocities before complete evaporation. These effects may be quite desirable, yet spray/wall interaction shows predominantly very negative consequences:

- They cause large thermal stresses and can thus reduce the lifetime e.g. of the spark plug by damaging its ceramics.
- Parts of the impacting mass may remain on the surface and lead to the formation of a wall film. If the wall temperature is below the saturation temperature at the considered ambient conditions, the wall film may evaporate only during the exhaust stroke, i.e. the associated fuel mass lacks in the combustion and is emitted unburnt. Or the wall film may burn by a diffusion flame causing high soot and hydrocarbon emissions due to incomplete combustion.
- On the surface of the cylinder liner an oil film provides adequate lubrication of the piston motion. If spray fluid is added to and dilutes this film, serious engine damage may result.

In contrast to the stratified concept it is hardly possible to completely avoid spray/wall interaction in a homogeneous concept. Yet, due to the associated problems the understanding has to be improved. This is not an easy task because of the large number of influencing parameters and the difficulties in accurately characterising the dense fuel spray under real conditions.
Note that the impacts of scattered single drops which are carried by the charge motion are of minor importance in this work.

1.2.2.2 Influencing parameters

Besides the ambient temperature and pressure, T_{ambient} and p_{ambient}, the properties of the target and spray parameters play a role in spray/wall interactions. The most important surface properties are:

- wall temperature T_{wall},

- material properties, e.g. thermal conductivity λ, specific heat capacity c_P, density ρ, wettability, thermal effusivity etc. .
  Common materials for the liner are aluminium or grey cast iron, which is an iron alloy with fractions of carbon ($> 2\%$) in form of graphit, silicium ($> 1.5\%$), nickel, chromium and manganese. The piston is customarily made of an aluminium alloy (mainly Al-Si) and the inlet valves of various steels.
- Surface coverage which may vary widely. In addition to dry metallic surfaces treated differently and hence showing different roughness values in the order of micrometers, the piston or the intake valves can be coked, i.e. covered by a rough and porous or lacquer-like structure. On the cylinder liner, an oil film exists to lubricate the piston motion.
- Surface curvature, where especially the piston displays large varieties.

Depending on the load, the surface temperatures, T_{wall}, and the ambient conditions change significantly and over a wide range, see Figure 1.3: at rated power, for instance, the intake valves can exhibit temperatures of up to 600 K with cylinder pressures in an approximate range of $p_{\text{ambient}} = 0.8$-2.5 bar. At part load, impacts at $p_{\text{ambient}} = 0.3$-1.2 bar may occur on the piston with a temperature up to 400 K.

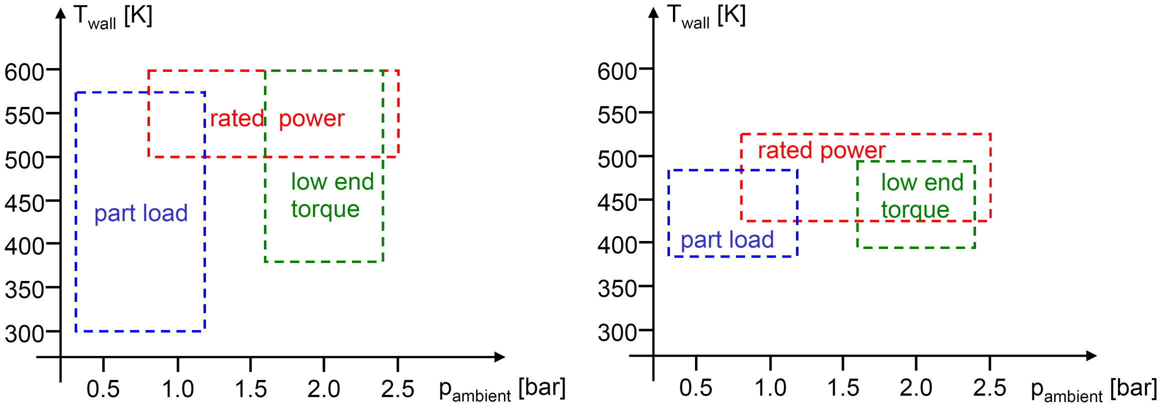

(a) Inlet valves.

(b) Cylinder liner.

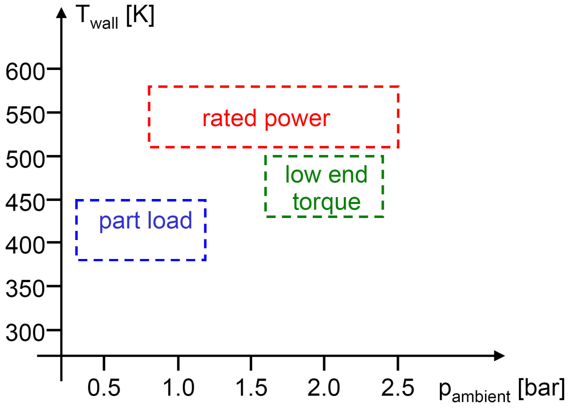

(c) Piston.

Figure 1.3: Wall temperatures and ambient pressures for different operating points.

The properties of the impacting spray which influence the outcome of spray impact are:

- drop size distributions,
- distributions of velocity components and impact angles,
- material properties, such as density ρ, surface tension σ, dynamic viscosity μ etc.. Fuel is a multi-component mixture of hydrocarbons C_xH_y in a boiling range of ca. 30-215°C. Various additives provide for the purity of the fuel and injection system or prevent deposits in the cylinder, for instance.
- Spray density and drop/drop interactions.

No experiment is able to cover the range of all parameters affecting the complex phenomena of wall interaction and some parameter variations are very demanding to realise. Consequently, the quantitative data base of spray/wall interaction under engine conditions is still poor. And physical understanding of the underlying phenomena and numerical modelling lag even further behind.

1.3 Fundamentals of Computational Fluid Dynamics

All numerical simulations in this work are done with the commercial CFD software ANSYS CFX, which is used at BMW for in-cylinder calculations. These comprise the simulation of entire engine cycles with spray injection and combustion in the combustion chamber. An Euler-Lagrangian approach is chosen to describe the two-phase flow of spray liquid in a gaseous ambience.

1.3.1 Continuous gas phase

Any numerical simulation has to start with a suitable, mathematical description of the problem in adapted coordinates. In a next step, the problem is discretised: the considered spatial domain is divided in a finite number of small volumes and the continuous equations are replaced by algebraic ones. The system of the latter is then solved by an efficient solver algorithm. Finally, the vast amount of resulting information has to be filtered and studied by the user with the help of a post-processor, which is not addressed further.

1.3.1.1 Mathematical description

Together with suitable initial and boundary conditions, conservation equations from continuum mechanics for mass, momentum and energy describe the gaseous flow mathematically. In the following, they are given in differential form and cartesian coordinates, see [19], [76]. The index summation according to Einstein is used[1]. ρ signifies the density, μ the dynamic viscosity and λ the thermal conductivity of the fluid. The velocity component in direction i is denoted as v_i.

---

[1] If an index i occurs twice in any term, the term is summed with the index i taking values from 1 to 3.

- **Mass conservation (continuity equation):**

$$\frac{\partial \rho}{\partial t} + \frac{\partial \left(\rho \cdot v_i\right)}{\partial x_i} = S_m \, . \tag{1.2}$$

  The term S_m represents mass source terms which occur in two-phase flows, e.g. due to evaporation of liquid spray drops.

- **Momentum conservation (Navier-Stokes equations):**

$$\frac{\partial \left(\rho \cdot v_i\right)}{\partial t} + \frac{\partial \left(\rho \cdot v_i \cdot v_j\right)}{\partial x_j} = \frac{\partial \tau_{ij}}{\partial x_j} - \frac{\partial p}{\partial x_i} + \rho \cdot f_{V,i} + S_{p,i} \quad (i = 1, 2, 3) \, , \tag{1.3}$$

  where the components τ_{ij} of the stress tensor matrix for a Newtonian fluid are defined as

$$\tau_{ij} = \mu \cdot \left(\frac{\partial v_i}{\partial x_j} + \frac{\partial v_j}{\partial x_i} - \frac{2}{3} \cdot \frac{\partial v_k}{\partial x_k} \cdot \delta_{ij} \right) \, . \tag{1.4}$$

  The term $f_{V,i}$ stands for all volume forces, e.g. gravity, centrifugal, Coriolis or buoyancy forces, arising in the chosen reference system. The source term $S_{p,i}$ refers mainly to the drag force in coupled two-phase flows. δ_{ij} denotes the Kronecker symbol.

- **Energy conservation:**

$$\frac{\partial \left(\rho \cdot h\right)}{\partial t} + \frac{\partial \left(\rho \cdot v_i \cdot h\right)}{\partial x_i} = \tau_{ij} \cdot \frac{\partial v_i}{\partial x_j} + \frac{\partial p}{\partial t} + v_i \cdot \frac{\partial p}{\partial x_i} - \frac{\partial \dot{q}_i}{\partial x_i} + S_h \, , \tag{1.5}$$

  where $h = e + p/\rho$ specifies the enthalpy with e the internal energy, both defined per mass unit. $\dot{q}_i = -\lambda \cdot \frac{\partial T}{\partial x_i}$ (Fourier's law) describes the heat flux in direction i due to a temperature gradient.
  Additional energy fluxes e.g. due to a concentration gradient as well as thermal radiation are omitted in the equation, cf. [7] for further details.
  The source term S_h is coupled to the vapour mass sources due to liquid drop evaporation.

Besides the velocity components v_i and the enthalpy h, the five Equations 1.2-1.5 contain the unknown density, pressure and temperature fields: $\rho = \rho(x_1, x_2, x_3, t)$, $p = p(x_1, x_2, x_3, t)$ and $T = T(x_1, x_2, x_3, t)$. The system of equations must therefore be completed by state equations

$$p = p(\rho, T) \qquad \text{and} \qquad h = h(\rho, T) \, , \tag{1.6}$$

which describe the thermodynamic properties of the fluid. For an ideal gas, they are given as $p = \rho \cdot \mathcal{R} \cdot T$ and $h = c_P \cdot T$ with $\mathcal{R}$ the fluid-specific gas constant and c_P the specific heat capacity per mass unit for constant pressure.

So far, the equations have been presented for a single, pure fluid. In case of a multi-component gaseous phase with varying composition, e.g. due to evaporation or chemical reactions (the latter being not considered in this work), a continuity equation has to be solved for every species $n = 1 \ldots N$:

$$\frac{\partial \rho_n}{\partial t} + \frac{\partial \left(\rho_n \cdot v_{n,i}\right)}{\partial x_i} = -\frac{\partial j_{n,i}}{\partial x_i} + S_n \quad . \tag{1.7}$$

S_n describes the production of the species. In comparison to Equation 1.2 which is still applicable for the overall mixture and can be used instead of one of the n equations for the individual species, diffusive fluxes $j_{n,i}$ appear in these equations. They describe the motion of a species relative to the mean fluid motion and comprise mass diffusion due to mechanical driving forces (Fick's law), i.e. due to a concentration gradient, a pressure gradient or possibly due to an external force acting unequally on the various species (e.g. an electromagnetic force), as well as mass diffusion due to a temperature gradient (Soret effect). The contributions due to a concentration and a temperature gradient are often the most important ones.

Momentum and energy equation, cf. Equations 1.3 and 1.5, can be employed further in case of a multi-component fluid, if values, like the velocity, are considered as averages over all species. However, analogous to the diffusive mass fluxes in Equation 1.7, additional energy fluxes besides the Fourier term appear from the interdiffusion between the different species due to different mechanical driving forces (Dufour effect), cf. [7] for further details.

1.3.1.2 Reynolds averaging for turbulent flows

The flows addressed in this work and in most industrial applications show a very complex and irregular behaviour in space and time: they are turbulent. To resolve the associated high-frequency fluctuations, which can consist of many scales, in simulations, the spatial and temporal resolution have to capture the smallest vortex and fluctuation as well as the largest. Such a direct numerical simulation (DNS) is much too expensive in most engineering applications, see [25] and references therein.

In large-eddy simulations (LES), only the large scale eddies are resolved. These transport conserved quantities very effectively and comprise most of the turbulent energy. The latter is passed through all length scales in a cascade of decaying eddies and finally dissipates into heat at the smallest scale. Small eddies are not resolved but modelled. Yet, LES is still very demanding with respect to computational time and capacity.

Therefore, a statistical model is usually chosen with all turbulent fluctuations being modelled. In many applications and in the approach considered in this work, the resulting average quantities describe the respective flows sufficiently.

According to Reynolds, the instantaneous value of a quantity $\Phi(x_1, x_2, x_3, t)$ (e.g. velocity components, pressure, temperature, density etc.) is divided in an averaged and a stochastic fluctuation term. The latter is high-frequent in comparison to the stationary or slowly changing averaged term:

$$\Phi(x_1, x_2, x_3, t) = \bar{\Phi}(x_1, x_2, x_3, t) + \Phi'(x_1, x_2, x_3, t)\,, \tag{1.8}$$

where the ensemble average[2] is defined as

$$\bar{\Phi}(x_1, x_2, x_3, t) = \lim_{n\to\infty} \frac{1}{n} \sum_{k=1}^{n} \Phi^{(k)}(x_1, x_2, x_3, t)\,. \tag{1.9}$$

For statistically stationary flows this averaging can be replaced by a simpler time-averaging:

$$\bar{\Phi}(x_1, x_2, x_3, t) = \bar{\Phi}(x_1, x_2, x_3) = \lim_{t^*\to\infty} \frac{1}{t^*} \int_{t-t^*/2}^{t+t^*/2} \Phi(x_1, x_2, x_3, t')\, dt'\,, \tag{1.10}$$

---

[2] The flow is realised n times and every time, the value of Φ is noted at the same time and position.

where t^* is a large time span compared to the turbulent fluctuations.

Inserting decompositions according to Equation 1.8 for the velocity components v_i, the pressure field p etc. into Equations 1.2-1.5, the Reynolds-averaged equations result after an averaging as described in Equation 1.10. Restricted to a statistically stationary and incompressible flow, the momentum equations become:

$$\frac{\partial\left(\rho\cdot\bar{v}_i\right)}{\partial t}+\frac{\partial\left(\rho\cdot\bar{v}_i\cdot\bar{v}_j\right)}{\partial x_j}=\frac{\partial\bar{\tau}_{ij}}{\partial x_j}+\rho\cdot f_{V,i}+S_{p,i}-\frac{\partial\left(\rho\cdot\overline{v_i'\cdot v_j'}\right)}{\partial x_j}\quad(i=1,2,3)\,. \tag{1.11}$$

An incompressible flow is volume-conserving, i.e. $\frac{\partial\rho}{\partial t}+v_i\cdot\frac{\partial\rho}{\partial x_i}=0$. In combination with the continuity Equation 1.2 this equals the condition $\frac{\partial v_i}{\partial x_i}=0$.
To solve for the statistical means, the new unknowns $\rho\cdot\overline{v_i'\cdot v_j'}$, which are called Reynolds stresses and which arise due to the non-linearity of the Navier-Stokes equations, have to be approximated. For the transport equation of any other scalar quantity, e.g. the energy, additional turbulent scalar fluxes, like $\rho\cdot\overline{v_i'\cdot e}$, appear and have to be treated, too.
This so-called turbulence modelling can be done with zero-equation models, where the stresses are modelled by algebraic equations. This is not very accurate and one- or two-equation models are preferable. These solve one or two additional differential equations for the turbulent kinetic energy k and possibly the dissipation rate ε. Another possibility are Reynolds stress models, where transport equations are solved for all stresses and the dissipation rate. These models promise better accuracy but are also more expensive and in general less robust.

Throughout this work, the standard two-equation models k-ε, see [36], and Shear-Stress-Transport (SST), cf. [3], [41], are considered. Both belong to the so-called eddy viscosity turbulence models: the effects of turbulent fluctuations in the flow are described by the introduction of a turbulent viscosity μ_t. This is done in analogy to laminar flows, where energy dissipation is mainly due to viscous forces. Yet, μ_t is not a fluid property like μ but dependent on the flow.

k-ε-model. Using the Boussinesq approximation, see [8], the Reynolds stresses are modelled in a form analogous to the components of the friction part of the stress tensor matrix for Newtonian fluids:

$$\rho\cdot\overline{v_i'\cdot v_j'}=-\mu_t\cdot\left(\frac{\partial\bar{v}_i}{\partial\bar{x}_j}+\frac{\partial\bar{v}_j}{\partial\bar{x}_i}\right)+\frac{2}{3}\cdot\rho\cdot\delta_{ij}\cdot k\,. \tag{1.12}$$

$k=0.5\cdot\overline{v_i'\cdot v_i'}$ defines the turbulent kinetic energy.
The problem is not closed yet as μ_t and k are unknown. The ansatz

$$\mu_t=C_\mu\cdot\rho\cdot\frac{k^2}{\varepsilon} \tag{1.13}$$

and the definition of the dissipation rate

$$\varepsilon=\frac{\mu}{\rho}\cdot\overline{\frac{\partial v_i'}{\partial x_j}\cdot\frac{\partial v_i'}{\partial x_j}} \tag{1.14}$$

lead to the transport equations for k and ε, which are used for closure:

$$\begin{aligned} \frac{\partial(\rho\cdot k)}{\partial t}+\frac{\partial}{\partial x_i}(\rho\cdot\bar{v}_i\cdot k) &= \frac{\partial}{\partial x_i}\left(\mu+\frac{\mu_t}{\sigma_k}\right)\cdot\frac{\partial k}{\partial x_i}+G_k-\rho\cdot\varepsilon\,, \qquad (1.15)\\ \frac{\partial(\rho\cdot\varepsilon)}{\partial t}+\frac{\partial}{\partial x_i}(\rho\cdot\bar{v}_i\cdot\varepsilon) &= \left(\mu+\frac{\mu_t}{\sigma_\varepsilon}\right)\cdot\frac{\partial\varepsilon}{\partial x_i}+\frac{\varepsilon}{k}\cdot(C_{\varepsilon 1}\cdot G_k-C_{\varepsilon 2}\cdot\rho\cdot\varepsilon)\,. \end{aligned}$$

The values of the empirical constants are commonly set to $C_\mu = 0.09$, $\sigma_k = 1.0$, $\sigma_\varepsilon = 1.33$, $C_{\varepsilon 1} = 1.44$ and $C_{\varepsilon 2} = 1.92$. G_k is the production term of turbulent kinetic energy and given as

$$G_k = -\rho\cdot\overline{v_i'\cdot v_j'}\cdot\frac{\partial\bar{v}_i}{\partial\bar{x}_j}\approx\mu_t\cdot\left(\frac{\partial\bar{v}_i}{\partial x_j}+\frac{\partial\bar{v}_j}{\partial x_i}\right)\cdot\frac{\partial\bar{v}_i}{\partial\bar{x}_j}\,. \qquad (1.16)$$

Source terms due to two-phase interactions do not occur, cf. Section 1.3.2.2.

The k-ε-model has proved to be very robust and efficient in many applications. The underlying assumptions are valid in highly turbulent flows with isotropic turbulence (due to k and ε being scalars). The latter is no longer fulfilled in the proximity of walls, i.e. in the viscous sublayer. The turbulent transport equations lose their validity there and the near-wall turbulence has to be modelled separately.

If the computational grid, see the following subsection, is fine enough to resolve the laminar sublayer, so-called "low Reynolds" models are to be used. Yet, the thickness of the viscous boundary layer scales with the Reynolds number, $h_l \sim \mathrm{Re}^{-0.5}$. For large values of Re, the first grid point often lies already in the fully developed, turbulent sublayer. There, the well-known logarithmic wall law can be used to describe the velocity profile:

$$v^+ = \frac{v_T}{v_\tau} = \frac{1}{\kappa}\cdot\ln(y^+)+C\,. \qquad (1.17)$$

v_T is the known velocity component tangential to the wall in a distance Δy from the wall, which is presumed in the already fully turbulent boundary layer. $v_\tau = (\tau_w/\rho)^{0.5}$ signifies the friction velocity with τ_w the wall shear stress. $\kappa \approx 0.41$ denotes the empirical von Kármán constant. y^+ is the non-dimensional distance from the wall defined as $y^+ = \rho\cdot v_\tau\cdot\Delta y/\mu$. C is a constant depending on the wall roughness.

For further details on the implementation of near-wall treatment, especially in CFX, cf. [3].

SST-model. Another two-equation turbulence model is the k-ω-model, see [91]. It is very similar to the k-ε-model but uses the turbulent frequency ω instead of the eddy dissipation rate ε. The turbulent viscosity μ_t is linked to k and ω via:

$$\mu_t = \rho\cdot\frac{k}{\omega}\,. \qquad (1.18)$$

The transport equations to close the problem become:

$$\begin{aligned} \frac{\partial(\rho\cdot k)}{\partial t}+\frac{\partial}{\partial x_i}(\rho\cdot\bar{v}_i\cdot k) &= \frac{\partial}{\partial x_i}\left(\mu+\frac{\mu_t}{\sigma_k}\right)\cdot\frac{\partial k}{\partial x_i}+G_k-\beta_k\cdot\rho\cdot k\cdot\omega\,, \qquad (1.19)\\ \frac{\partial(\rho\cdot\omega)}{\partial t}+\frac{\partial}{\partial x_i}(\rho\cdot\bar{v}_i\cdot\omega) &= \left(\mu+\frac{\mu_t}{\sigma_\omega}\right)\cdot\frac{\partial\omega}{\partial x_i}+\alpha_\omega\cdot\frac{\omega}{k}\cdot G_k-\beta_\omega\cdot\rho\cdot\omega^2\,. \end{aligned}$$

The empirical constants are usually given as $\beta_k = 0.09$, $\sigma_k = 2.0$, $\sigma_\omega = 2.0$, $\alpha_\omega = 5/9$ and $\beta_\omega = 0.075$. The turbulent production term G_k is identical to that in the k-ε-model.

The k-ω-model usually allows a more robust treatment of the near-wall region than the k-ε model but is very sensitive to free shear flows.
To combine the advantages of both models, the SST-model applies the k-ω-model near a rigid surface and the k-ε in the outer regions. A blending function is used in-between which depends on the distance to the wall and on flow variables, see [3] for further information.

1.3.1.3 Discretisation

In the previous two subsections, the coupled basic equations which describe the gaseous phase have been presented shortly. Analytical solutions for these equations in combination with appropriate initial and boundary conditions are only available for very simple flows under ideal conditions. Usually a numerical solution has to be found which requires a discretisation of the problem in space and time.

First, the considered domain has to be split in a finite number of small control volumes, see Figure 1.4. ANSYS Icem CFD is used for mesh generation in this work. Structured, regular grids are very efficient in numerical algorithms yet they should be oriented to the flow to prevent systematic errors, see [22]. For complex geometries such as a combustion chamber and for automatic grid generation unstructured grids are more flexible, cf. [56]. Therefore these are used for in-cylinder calculations at BMW and the meshes in this thesis are set up accordingly with tetrahedron cells. The solution variables and fluid properties are stored at the element nodes. To account for a better resolution of near-wall flow, flat prism layers are created on the surfaces.
Per default the maximal edge length of the tetrahedra and the total height of the prism layers is chosen as 1 mm in the simulations carried out.

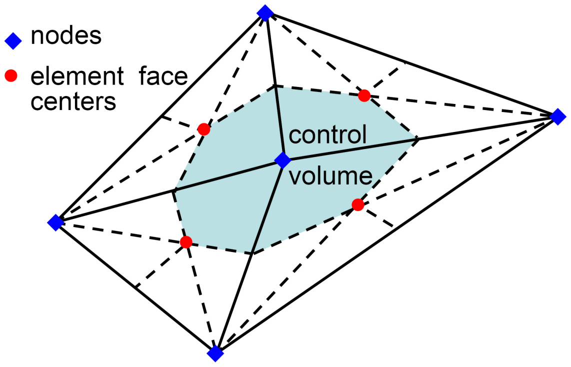

Figure 1.4: Definition of an exemplary two-dimensional control volume in CFX.

Second, the partial differential equations as well as the boundary conditions have to be discretised into a manageable, algebraic system. For that purpose, different mathematical descriptions are well-known: the finite-volume, the finite-element, the finite-difference as well as the spectral method, see [25], [67], [85].
In CFX, the finite-volume method is implemented, which has the advantage to be conservative in mass, momentum and energy in a global as well as in a discrete sense,

i.e. for every control volume. Its main idea can be summarised in looking at the general form of a transport equation:

$$\underbrace{\frac{\partial\left(\rho\cdot\Phi\right)}{\partial t}}_{\text{local change in time}}+\underbrace{\frac{\partial\left(\rho\cdot v_i\cdot\Phi\right)}{\partial x_i}}_{\text{convection}}=\underbrace{\frac{\partial\left(\Gamma_\Phi\cdot\frac{\partial\Phi}{\partial x_i}\right)}{\partial x_i}}_{\text{diffusion}}+\underbrace{S_\Phi}_{\text{sources, sinks}}\ . \tag{1.20}$$

All governing Equations 1.2-1.5 and 1.15 can be written in this form. The change of the respective transport quantity Φ in time is given by the convective and diffuse transport and its sources and sinks. The diffusion coefficient Γ_ϕ and the source terms S_Φ can be easily determined by comparing Equation 1.20 with the respective governing equation. In the finite-volume method, the transport equation is considered in integral form for every control volume. Applying Gauss' divergence theorem, it becomes:

$$\int_A\underbrace{\left(\rho\cdot v_i\cdot\Phi-\Gamma_\Phi\cdot\frac{\partial\Phi}{\partial x_i}\right)}_{\text{convective and diffusive flux}}d\overrightarrow{A}=\int_V\left(-\frac{\partial\left(\rho\cdot\Phi\right)}{\partial t}+S_\Phi\right)dV\,. \tag{1.21}$$

The terms of this equation are then discretised, i.e. approximated by discrete values: for the convective flows, the values of Φ at the surface border of a control volume have to be approximated. The upwind differencing scheme is a very common, first-order scheme, where the values are simply approximated by the values of Φ at the node in upstream direction. In contrast to higher order schemes it is bounded and does not yield oscillatory solutions in case of large gradients of the transport quantity. Yet, it is numerically diffusive, i.e. the leading error resembles a diffusive flux. More accurate but less robust is the second-order central differencing scheme which uses an interpolation between neighboured nodes to get the value of Φ at the border of a control volume. In this work, the "high-resolution" scheme in CFX is chosen. It is a flux-blending technique, where a blending factor is calculated based on the gradients in the flow. This factor is used to interpolate between the mentioned first-order and second-order schemes in such a way that the discretisation is as close to second order as possible without local oscillations.

The diffusive fluxes are less problematic and always discretised second-order using the central differencing scheme.

For the volume integrals on the right-hand side of Equation 1.21, the midpoint rule is applied. The time derivate is finally approximated by an implicit second-order backward Euler approach.

1.3.1.4 Solving the system of equations

From discretisation an algebraic nonlinear system results. It has to be solved numerically at the representative positions of every control volume and for a finite number of time values. To do so, it is linearised and assembled into a solution matrix:

$$\mathbf{A}\,\overrightarrow{\Phi}=\overrightarrow{b}\ . \tag{1.22}$$

CFX uses a multigrid accelerated solver with an Incomplete Lower Upper factorization technique for the solution matrix, see [3], [67]. The velocity components v_i $(i=1,2,3)$ and the density ρ are treated as a single algebraic system first. After this hydrodynamic system, volume fractions, additional variables, energy, turbulence and finally the liquid phase in form of Lagrangian parcels, cf. the next subsection, are solved in subsequent iterations. The residual vector

$$\overrightarrow{r}^{(n)} = \overrightarrow{b} - \mathbf{A}\overrightarrow{\Phi}^{(n)} \tag{1.23}$$

of the n^{th}-iteration is subject to a normalization procedure. If the resulting values for all quantities lie below a user-defined convergence criterion, called the residual target, or if a user-defined maximal number of iterations is reached, the solution procedure is stopped. A target for the global balances, called conservation target, can additionally be set. In a transient calculation the solver then proceeds to the next timestep.

1.3.2 Discrete liquid phase

The motion of a dispersed solid particle, bubble or drop in a continuous flow can be described by a force balance. Thereby, the coupling between liquid and gas phase through e.g. drag or evaporation has to be accounted for. As the calculation of all particles is too costly in most applications, only a reduced number of representative Lagrangian parcels is tracked through the flow.

1.3.2.1 Motion of a single particle

The general equation of motion for a particle, marked by the index p in this subsection, in a surrounding fluid flow, marked by the subscript f, is given as, cf. [26], [42]:

$$m_p \cdot \frac{dv_{p,i}}{dt} = F_{D,i} + F_{P,i} + F_{MV,i} + F_{B,i} + F_{S,i} + F_{M,i} + F_{EXT,i} \quad (i = 1, 2, 3)\,. \tag{1.24}$$

The particle is treated as a point mass, i.e. its size is not accounted for in the calculation of the Eulerian phase. The inertial force on the left-hand side, where $v_{p,i}$ is the particle velocity, equals the sum of

- the viscous drag force,

  $$F_{D,i} = \frac{\pi}{8} \cdot C_D \cdot \rho_f \cdot D_p^2 \cdot v_s \cdot v_{s,i}\,, \tag{1.25}$$

  where C_D is the drag coefficient and $v_{s,i} = v_{f,i} - v_{p,i}$ the component i of the slip velocity (relative velocity) between surrounding fluid and particle. $v_s = \sqrt{v_{s,i} \cdot v_{s,i}}$ denotes the vector amount. D_p is the particle diameter.
  Per default the Schiller-Naumann specification of the drag coefficient C_D is chosen in this work:

  $$C_D = \max[0.44, \frac{24}{\mathrm{Re}^*} \cdot \left(1 + 0.15 \cdot (\mathrm{Re}^*)^{0.678}\right)]\,. \tag{1.26}$$

  Here, the Reynolds number Re^* is defined differently to Equation 1.42, which is normally used in this thesis. The density and dynamic viscosity of the continuous phase and the relative slip velocity are applied:

  $$\mathrm{Re}^* = \frac{\rho_f \cdot v_s \cdot D_p}{\mu_f}\,.$$

- The force $F_{P,i}$ due to a pressure gradient in the surrounding fluid.

- The virtual or added mass force $F_{VM,i}$ due to the no-slip condition for the surrounding fluid on the particle surface: the particle has to move and accelerate not only its own mass but also the fluid mass. This leads to an additional flow resistance, i.e. drag. $F_{VM,i}$ is significant especially for bubbles.

- The time-dependent Basset-history term $F_{B,i}$ which accounts for the past particle motion and flow patterns. It is also particularly important for bubbles.

- The Saffman force $F_{S,i}$ for a particle in a shear flow. The non-uniform pressure distribution across the particle surface leads to a lateral force in the reverse direction of the pressure gradient. It is important particularly near walls or in flows with high velocity gradients.

- The Magnus force $F_{M,i}$ for rotating particles in a parallel flow. The pressure difference between the particle side which moves in the same direction as the flow due to its rotation and the opposite side provokes a force perpendicular to the flow direction.

- External forces $F_{EXT,i}$, such as gravity, buoyancy or electromagnetic forces. In a rotating frame of reference, centripetal and Coriolis forces also occur.

In the considered two-phase flows with small liquid drops the drag force is usually dominant. Besides gravity it is the only force taken into account in this work.
The influence of particle deformations on the different force terms is hardly known and the particles are hence assumed spherical. They are considered non-rotating and drop/drop interactions, i.e. collisions, are not accounted for, see Section 1.3.2.4. Drop breakup is not modelled either.

In the discretised problem of numerical simulations the particle displacement is calculated by simple forward Euler integration of the particle velocity components in CFX:

$$x_{p,i}(t + \delta t) = x_{p,i}(t) + v_{p,i}(t) \cdot \delta t \,. \tag{1.27}$$

δt denotes the particle timestep which is defined locally: a characteristic length scale of the element where the particle momentarily resides is divided by the particle velocity and a user-defined factor, the so-called "number of integration time steps per element", which is set to 10 by default. When the particle crosses an element border or if an Eulerian timestep ends, the value of δt is shortened to synchronise both phases and a new value is calculated.
To determine the new particle velocity $v_{p,i}$ at time $t + \delta t$, the equation of motion 1.24 is numerically integrated. All fluid properties, like velocity or density, are taken from the start of the Eulerian timestep. In space, they are interpolated from the vertices to the particle position. To perform the integration, CFX simplifies the appearing force terms in linearising them with respect to the particle velocity components $v_{p,i}$.

1.3.2.2 Influence of turbulence

Solving the equation of motion for the dispersed particle phase it would be rather restricted to consider only averaged properties of the continuous phase, e.g. $\bar{v}_{f,i}$ $(i = 1, 2, 3)$. Yet, using Reynolds averaging, the equations of the Eulerian phase are only solved for these averaged quantities while the turbulent fluctuations $v'_{f,i}$ are not known.

To account for the influence of the turbulence all the same, the turbulent part $v'_{f,i}$ is modelled and the resulting velocity components $v_{f,i} = \bar{v}_{f,i} + v'_{f,i}$ are used in the equations of the previous subsection:
At any time a particle is assumed to reside in one discrete virtual eddy. The characteristics of the latter are calculated based on known local turbulent flow properties:

$$l_e = \frac{C_\mu^{3/4} \cdot k^{3/2}}{\varepsilon}, \tag{1.28}$$

$$\tau_e = l_e \cdot \left(\frac{2 \cdot k}{3}\right)^{-1/2}. \tag{1.29}$$

l_e denotes the eddy length and τ_e the eddy lifetime. During the particle/eddy interaction, the turbulent fluctuations are determined as

$$v'_{f,i} = p_{\text{rand},i} \cdot \left(\frac{2 \cdot k}{3}\right)^{1/2} \quad (i = 1, 2, 3) \tag{1.30}$$

in CFX. Due to the introduced random numbers $p_{\text{rand},i}$, which are normally distributed, particle trajectories are not deterministic. If the particle/eddy interaction time reaches τ_e or if the displacement of the particle relative to the eddy gets as large as l_e, the particle leaves the considered virtual eddy and enters a new one with other characteristics and a new value of $v'_{f,i}$ is calculated.

In reality, particles may also dampen or excite the turbulence field of the continuous phase. Yet, there are no appropriate models describing these effects so far and therefore these are usually neglected. No source terms due to phase coupling appear in the turbulent transport equations 1.15 and 1.19 respectively. Particles affect the turbulence field of the Eulerian phase only indirectly by influencing the velocity field.

1.3.2.3 Coupling of the continuous and the dispersed phase

Besides the turbulent dispersion, i.e. the virtual eddies, which are related to the turbulence of the continuous gas phase and which affect the discrete liquid phase, the following interactions between Eulerian and Lagrangian phase occur:

- momentum transfer due to viscous drag.
- Heat transfer which comprises three terms:
  - The convective heat transfer (forced convection, unit [J/s]) due to a temperature difference is given as

$$\dot{Q}_C = h_c \cdot \pi \cdot D_p^2 \cdot (T_f - T_p), \tag{1.31}$$

where the sign has to be chosen such that the heat flow is directed from the warmer to the colder phase. h_c denotes the heat transfer coefficient and can be expressed by the Nusselt number

$$\text{Nu} = \frac{h_c \cdot D_p}{\lambda_f} \tag{1.32}$$

which defines the ratio between convective and conductive heat transfer. λ_f is the thermal conductivity of the gas phase.
Assuming homogeneous, steady gas conditions around a spherical drop and a spatially constant temperature inside the drop, the Nusselt number is often expressed as

$$\mathrm{Nu} = 2 + 0.6 \cdot \mathrm{Re}^{0.5} \cdot \mathrm{Pr}^{0.33}\,, \tag{1.33}$$

where the influence of the drop motion is modelled empirically, see [54], [42]. The Prandtl number is given as $\mathrm{Pr} = \frac{\mu_p \cdot c_P}{\lambda_p}$ calculated with drop properties.

- Latent heat transfer due to evaporation of a drop is expressed by the heat flow

$$\dot{Q}_m = \frac{dm_p}{dt} \cdot \Delta h_{\mathrm{vap}}\,. \tag{1.34}$$

The value of the latent heat per mass unit, Δh_{vap}, depends on the ambient temperature. It is withdrawn from the gas phase in case of evaporation and inserted in case of condensation assuming a drop of homogeneous temperature, i.e. omitting cooling/heating of the drop liquid.

- Radiative heat transfer can be described as

$$\dot{Q}_R = (\epsilon_{A,p} \cdot T_f^4 - \epsilon_{E,p} \cdot T_p^4) \cdot \sigma_S \cdot \pi \cdot D_p^2\,, \tag{1.35}$$

where $\sigma_S = 5.67 \cdot 10^{-8}\,\mathrm{W/(m^2 \cdot K^4)}$ is the Stefan-Boltzmann constant. $\epsilon_{E,p}$ denotes the emissivity of the liquid (which equals 1 for a black body and is smaller else) and $\epsilon_{A,p}$ its absorptivity. Radiation is neglected in this work.

The sum of all contributions constitutes the collective heat transfer rate for the liquid $m_p \cdot c_P \cdot \frac{dT_p}{dt}$ which is equal to the enthalpy change of the drop.
Further terms, e.g. due to a time-variable or inhomogeneous temperature field or due to drop acceleration (i.e. rotation) are neglected, see [42].

- Mass transfer, where the vapour pressure is calculated using the empirical Antoine equation:

$$p_{\mathrm{vap}} = p_{\mathrm{ref}} \cdot \exp\left(A - \frac{B}{T_p + C}\right)\,. \tag{1.36}$$

A, B and C are material dependent constants. If p_{vap} is larger than the surrounding gaseous pressure, the particle boils and the mass transfer rate is determined by the convective heat transfer

$$\frac{dm_p}{dt} = \frac{1}{\Delta h_{\mathrm{vap}}} \cdot \dot{Q}_C\,. \tag{1.37}$$

Else it can be described analogous to the heat transfer rate in Equation 1.31 as

$$\frac{dm_p}{dt} = \beta_c \cdot \pi \cdot D_p^2 \cdot (\rho_f - \rho_p)\,, \tag{1.38}$$

where β_c is the mass transfer coefficient. It can be replaced by the Sherwood number

$$\mathrm{Sh} = \frac{\beta_c \cdot D_p}{\mathcal{D}}\,, \tag{1.39}$$

where $\mathcal{D}$ is the mass diffusity of the gas mixture. The Sherwood number describes the ratio between convective and diffusive mass transport and is often approximated similar to the Nusselt number for heat transfer as

$$\mathrm{Sh} = 2 + 0.6 \cdot \mathrm{Re}^{0.5}\mathrm{Sc}^{0.33}\,. \tag{1.40}$$

The Schmidt number is given as $\mathrm{Sc} = \frac{\mu_p}{\rho_p \cdot \mathcal{D}}$.

The equations in this subsection have been presented for one liquid material component only, because CFX is currently not able to describe multi-component evaporation which is generally difficult, cf. [72].

Apart from turbulence, two-way coupling is always considered throughout this work: besides the influence of the continuous fluid on particles, these in turn affect the Eulerian phase. Therefore, the discussed source terms already appeared in the equations of the continuous phase, see above. They are non-zero for any control volume where a particle is located during the timestep. The general definition of a particle source term S_p is given as

$$\frac{dS_p}{dt} = C_S \cdot \Phi_p + R_S\,. \tag{1.41}$$

$C_S \cdot \Phi_p$ marks all contributions linear in the solution variable Φ_p and the term R_S summarises the rest. The frequency with which particle source terms are introduced to the continuous phase can be controlled by the user and for large source terms only every second iteration might be advisable. Moreover, underrelaxation factors can be used to gradually increase the introduced source terms with the number of iterations per Eulerian timestep from a reduced to their full value. It is also possible to smear them over several volume elements, which might help to avoid divergence in case of strong source accumulations, e.g. on wall impact. Yet, it strongly reduces the accuracy and is generally not applied in this work.

1.3.2.4 Discrete Droplet Model

The calculation of all single spray drops is usually much too costly with respect to computational time and storage. Therefore, the ensemble is represented by a comparatively small number of Lagrangian parcels. In this Discrete Droplet Model (DDM), see [18] and [3], every parcel stands for a number n of real drops with identical properties. In CFX, n is called “number rate”, because the quantity is scaled with the timestep value of the continuous phase.

The considerations of the previous subsection remain valid with parcels considered instead of individual drops.

A significant simplification in the considered Lagrangian approach is the neglect of the liquid volume fractions in the calculation of the Eulerian phase. It is only valid in dilute flows where the liquid volume fractions are small. This restriction imposes in principle also a limit to grid refinement in an area of liquid accumulations, e.g. near injection regions.

Additionally, inter-particle collisions, e.g. statistical models of [51] or [74], become important in dense flows. They are usually computationally expensive and not addressed in this work.

1.4 Modelling and implementation of spray/wall interaction

In the considered simulations, physical phenomena of spray/wall interactions are resolved neither in time nor in space, i.e. deformations of an impinging drop and the breakup process are not calculated in detail, for instance. To treat spray/wall interactions, models have to provide secondary (= post-impingement) diameters, velocity components and masses in dependence on the properties of the primary (=impinging) drops and the ambient conditions on impact.

1.4.1 State-of-the-art in modelling

1.4.1.1 Single drop models

Most existing models still treat the impact of a spray as a simple superposition of single drop events, e.g. [47], [77] and [78], [71] and [70], [4] and [5], [52], [27], [44], [64], [23]. The majority of these examples has been conceived for engine applications, where the number of influencing parameters is large. The associated wide parameter ranges are usually subdivided into several regimes based on similar post-impingement characteristics. A model then has to describe the transition criteria between regimes as well as the properties of the secondary droplets and the influences on the wall film in every regime. Commonly, the following impact outcomes are classified:

- deposition, where the liquid drop stays on the wall. It occurs mainly for drops with relatively small impact velocities. If the drop spreads, cf. Figure 1.5(a), and adheres as a liquid lamella on the surface (a film of lenticular shape), the regime is often called spread. If the drop keeps its original form without large deformation in case of non-wettable surfaces, it is sometimes specified as stick.

- Full or partial rebound, where the impinging drop is reflected with a possible energy loss. In case of partial rebound, parts of the drop mass form a film on the wall. Full rebound is favoured in case of hot walls above the Leidenfrost temperature, where a vapour cushion between drop and surface exists due to liquid evaporation.

- Secondary atomisation, where kinematic breakup, often called splash, and thermal breakup, often called boiling, are distinguished.
  For splash mainly three types are described, see e.g. [45], [44], [57], [50]:

  - In corona splash, see Figure 1.5(b), a liquid sheet with an unstable rim arises from the wall in an almost wall-normal direction. Secondary drops are ejected from so-called fingers which form at the rim. A reduction in the surface tension increases the tendency towards this type of splash. On a wetted surface corona splash is usually dominant where the film thickness is decisive: The number of secondary drops decreases with an increasing thickness of a liquid layer, whereas the drop diameter is found to increase due to a thicker crown-sheet, see [79], [12].
    For very thin films, [89] observe that the crown sheet no longer moves in a

wall-normal direction but also expands tangentially, which results in a bowl-like shape. Shortly after impact, the crown breaks up in many tiny droplets.

- In jet splash, cf. Figure 1.5(c), a liquid jet is formed from a receding lamella or inside a corona for not too large wall roughness values. It may break up into relatively large secondary droplets.
- In prompt splash, see Figure 1.5(d), droplets are generated at a very early stage of impact in contrast to corona and jet splash. They are ejected directly from the region between the surface and the spreading lamella in a radial direction. Large drop velocities and rough surfaces yield this type of atomisation.

Thermal breakup for hot walls is mainly distinguished in nucleate/bubble and film boiling, cf. e.g. [9], [17], [65], [24]:

- In case of surface temperatures above the liquid saturation temperature, bubbles start to form in the drop liquid and may rupture generating secondary droplets. Secondary atomisation starts a few milliseconds after impact and the secondary droplets are ejected in a rather wall-normal direction. Nucleate boiling becomes stronger and more chaotic for increasing surface temperature due to enforced bubble formation. This reduces increasingly direct wall contact of the drop and a transition to film boiling occurs.
- Above the Leidenfrost temperature, the impacting drop levitates and hovers above the surface on a vapour cushion which prevents direct contact to the surface. Secondary atomisation starts immediately after impact in a mainly radial direction. The number of secondary drops is found to be about one tenth compared to the number observed for bubble boiling under the same conditions. A central jet is sometimes found in case of a rather smooth wall and a relatively large drop may be ejected in a wall-normal direction. Due to the breakup of the film layer, some relatively large drops are also observed.

Regime descriptions and distinctions vary in literature because numerous parameters interact and show considerable influence on secondary diameters, velocities and directions: kinematic parameters (such as the drop size, the impact angle and the impact velocity, which generally enhances all breakup mechanisms), liquid material properties (such as the surface tension and the liquid viscosity, which supports deposition) and surface properties (like roughness, wettability and a possible film thickness, see [79], [12] and [90]).
It is neither the aim nor in the scope of this work to give a summary of parameter influences with respect to single drop impact but it is only to be pointed out that multi-dimensional parameter ranges have to be distinguished for single drop impacts and that the individual setting strongly influences the impact mechanisms and consequently the post-impingement characteristics. Reviews on single drop impact can be found, for instance, in [55], [11] and [94].

1.4.1.2 Characteristic numbers

Usually, the results of one experiment are too restricted to allow for the development of a complete wall interaction model, especially if the latter is intended for an application

(a) Spreading drop forming a lamella. In case of deposition the drop liquid stays on the wall. If the lammela recedes again, rebound or jet splash may occur.

(b) Corona splash.

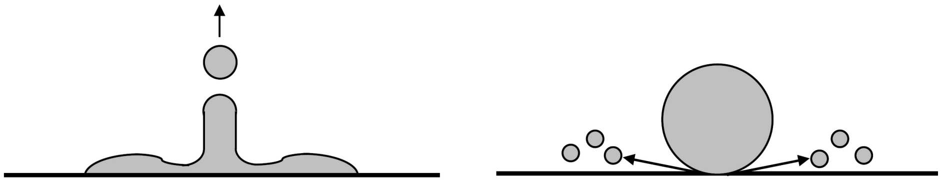

(c) Jet splash.

(d) Prompt splash.

Figure 1.5: Single drop impacts.

in engine calculations with the associated large parameter ranges. Therefore, it is necessary to assemble various studies which are often taken under different experimental conditions. These commonly do not correspond to those in an engine, e.g. water drops with millimetric diameters are considered. Quantitative measurements under conditions occurring in a DI engine with impacting diameters $< 100\,\mu$m and velocities $> 10\,$m/s are still very rare as they are difficult to access.

To transfer available experimental results to conditions outside those of the actual measurements scaling is applied, i.e. it is assumed that the same forces and physical phenomena still underlie. Non-dimensional, characteristic numbers are used for comparison, such as

- the Reynolds number which is defined as the inertial relative to the viscous forces:

  $$\mathrm{Re} = \frac{\rho_p \cdot v_p \cdot D_p}{\mu_p}\,. \tag{1.42}$$

  ρ_p and μ_p are the density and dynamic viscosity of the drop which moves with velocity v_p and has a diameter D_p. The latter is chosen as length scale in all listed characteristic numbers in this work.

- The Weber number which relates the deforming aerodynamic drag and the stabilising surface tension force:

  $$\mathrm{We} = \frac{\rho_p \cdot v_p^2 \cdot D_p}{\sigma}\,. \tag{1.43}$$

  σ denotes the surface tension.

- The Ohnesorge number which characterises the viscous influence relative to the square root of inertial and surface tension forces:

  $$\mathrm{Oh} = \frac{\mu_p}{\sqrt{\rho_p \cdot \sigma \cdot D_p}} = \mathrm{Re} \cdot \sqrt{\mathrm{We}}\,. \tag{1.44}$$

- The Laplace number which compares the inertial times the surface tension forces with the viscous drag squared:

  $$\mathrm{La} = \frac{\rho_p \cdot \sigma \cdot D_p}{\mu_p^2} = \frac{1}{\mathrm{Oh}^2}\,. \tag{1.45}$$

  Like the Ohnesorge number it is independent from the drop velocity and often used as a measure for the drop size.

- The Capillary number which relates the viscous drag and the surface tension forces:

  $$\mathrm{Ca} = \frac{\mu_p \cdot v_p}{\sigma}\,. \tag{1.46}$$

With respect to experiments on the impact of water drops with diameters in the order of 1 mm and 1 μm respectively, [66] finds that the drops of both size classes show the same behaviour depending on their Weber number. Hence, scaling is confirmed. However, [93] state a different behaviour of drops with sub-millimetric and millimetric size: In their experiments at wall temperatures above Leidenfrost the smaller drops appeared to bounce on the surface and showed a growth in the evaporation time with rising T_{wall}. By contrast, the larger drops levitated and evaporated increasingly slowly. In summary, the applicability of scaling still has to be tested thoroughly.

Even if scaling is applicable, most models should be analysed with care because the correlations may be extended far beyond the validity range of the underlying data. Moreover, only some influencing parameters are usually considered and others disregarded in the correlations.

1.4.1.3 Spray models

Besides the assembly of a rather broad data base concerning single drop impacts, also the theoretical understanding has improved a lot in recent years, e.g. of corona formation: [95] describe the uprising crown as kinematic discontinuity. [83] extended the description by the inclusion of viscosity and [62] generalised it to describe also inclined impacts and the interaction of two drops.
In comparison to single drop impacts, the physical understanding of spray impact is still at the outset and a general lack of quantitative spray impact data for the various parameter settings and nozzle types persists. Therefore, single drop models may still be used for some time although it is by now clear that the associated correlations do not meet spray impact very well:

- Existing single drop models are demonstrated to fail in the description of secondary spray data in [58]. Moreover, the superposition of two nozzles proved not to result in the same spray distributions as obtained from both nozzles injecting at the same time.

- Lamella interactions are shown to be decisive for the outcome of impinging droplet chains, see [95], [24] and references therein, and of spatial droplet arrays, e.g. [13], [14], [15], [65], [24].

- For relatively sparse sprays the importance of interactions between drops before impact and between neighbouring crowns during impact is shown in [82]. Different crown formation due to changed film flow by adjacent impingements is also stated in [73] and [32].

- For dense sprays it is shown in [63] that secondary drops mainly result from pressure fluctuations in the film induced by spray impact. The impingement is then no longer characterised by crown formation and the subsequent breakup which are typical for single drop impact, but by uprising finger-like jets which emerge directly from the film.
  A theoretical description of the film fluctuations and different film modes due to spray impact is not yet available. A first attempt in this direction is given in [63] with a characterisation of the associated scales. A length scale Λ, a time scale τ and a velocity scale Υ are proposed:

  $$\Lambda = \left(\frac{q_{\mathrm{mom}}}{q_{\mathrm{Nr}}^2 \cdot \pi^2 \cdot \rho_p} \right)^{1/6} , \quad \tau = \left(\frac{\rho_p}{q_{\mathrm{mom}} \cdot q_{\mathrm{Nr}} \cdot \pi} \right)^{1/3} , \quad \Upsilon = \frac{\Lambda}{\tau} . \tag{1.47}$$

  q_{mom} denotes the impinging normal momentum flux and q_{Nr} the number flux. For the considered impact of a Diesel spray, secondary diameters and velocities are confirmed to be of the same order as Λ and Υ.

1.4.2 Description of three existing models

Instead of giving a further extended, general literature review of drop/wall and spray/wall interaction models, this subsection describes exemplarily three existing models of spray impact. Their applicability to dense hollow cone sprays will be considered in the following chapters of this thesis.
Elsässer's model is chosen as an example for treating spray/wall interaction as a superposition of single drop impacts. Kuhnke's model already acknowledges the importance of drop/drop interactions and combines a single with a multiple drop impact model depending on the spray density. Finally, Roisman's/Horvat's model is presented which is one of the rare models actually based on spray impact data.
The original notation is adapted in large part to the naming conventions used in this work.

1.4.2.1 Elsässer's model

Elsässer's model, see [23], is intended for use in in-cylinder simulations and applied at BMW. It meets the whole range of relevant ambient pressures and surface temperatures by assembling results from a multitude of single drop studies (without own data). A wall film of a different liquid than the spray itself is not considered in the model.

Distinction of regimes. The hydrodynamic impingement regimes are classified on the basis of heat transfer regimes which refer to the evaporation behaviour of a drop set on a dry wall of initial temperature T_{wall}, see Figure 1.6: at the Nukiyama temperature T_N, a minimum of the drop lifetime occurs corresponding to maximal heat flux between drop and wall. At the Leidenfrost temperature T_L, the heat flux gets minimal and the

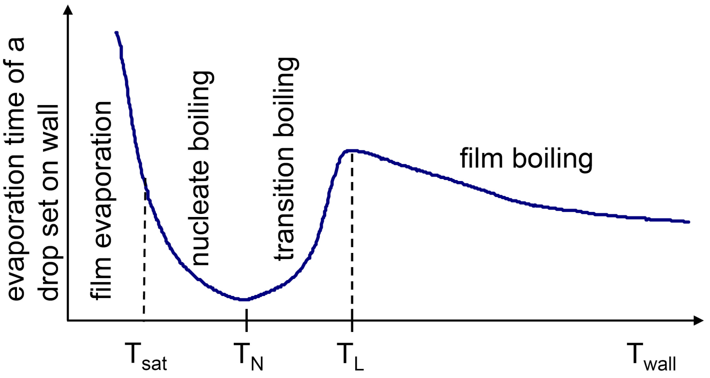

Figure 1.6: Drop lifetime as a function of the initial wall temperature.

lifetime maximal due to the vapour cushion preventing direct drop/wall contact, see [92].

Separated by the two characteristic temperatures T_N and T_L, and by the liquid boiling temperature T_{sat}, four different heat transfer regimes are usually distinguished (e.g. [92], [46], [33]): convection regime/film evaporation ($T_{\text{wall}} < T_{\text{sat}}$), nucleate/bubble boiling ($T_{\text{sat}} < T_{\text{wall}} < T_N$), transition ($T_N < T_{\text{wall}} < T_L$) and film boiling ($T_L < T_{\text{wall}}$).
Elsässer defined fits for T_N and T_L at $p_{\text{ambient}} = 1\,\text{bar}$ from various collected literature values ([81], [33], [30], [6], [9] and [48]). These functions consider dependencies on the material properties of surface and drop but neglect drop dynamics and surface roughness, for instance. An extension to different ambient pressures is introduced using results from [81]. Moreover, the transient temperature decrease due to heat transfer during wall contact is considered by inferring from T_N and T_L to mean surface temperatures during impact according to [92] and [6].
The resulting values[3], $T_{N,\text{contact}}$ and $T_{L,\text{contact}}$, are finally used to distinguish three hydrodynamic regimes, see Table 1.1. All three are important under engine conditions, which is revealed by comparing Figure 1.7 to Figure 1.3.

Regime	Wall temperature range	Non-dimensional wall temperature
Cold wetting (CW)	$T_{\text{wall}} \leq T_{N,\text{contact}}$	$T^*_{CW} = \frac{T_{\text{wall}}-T_f}{T_{N,\text{contact}}-T_f} + 1$
Hot wetting (HW)	$T_{N,\text{contact}} < T_{\text{wall}} \leq T_{L,\text{contact}}$	$T^*_{HW} = \frac{T_{\text{wall}}-T_{N,\text{contact}}}{T_{L,\text{contact}}-T_{N,\text{contact}}} + 1$
Hot non wetting (HNW)	$T_{\text{wall}} > T_{L,\text{contact}}$	$T^*_{HNW} = \frac{T_{\text{wall}}}{T_{L,\text{contact}}}\,.$

Table 1.1: Regime classification in Elsässer's model. T_f is the temperature of the ambient fluid. The third column gives the definitions of characteristic, non-dimensional wall temperatures used in the model.

Implementation of wall roughness. Under engine conditions, peak-to-peak roughness values can be of the same order as impinging drop sizes, i.e. $\gamma_z \sim 1$ with

$$\gamma_z := R_z/D_{\text{prim}}\,. \tag{1.48}$$

---

[3] $T_{N,\text{contact}}$ and $T_{L,\text{contact}}$ are called T_{pA} and T_{pR} in [23] referring to "pure adhesion" and "pure rebound" as in [4], [77]. These names are misleading and therefore changed here.

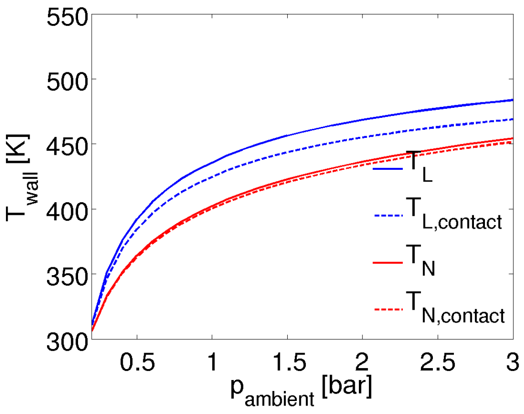

Figure 1.7: Dependence of the regime temperatures in Elsässer's model on the ambient pressure for an n-heptane drop on an aluminium surface.

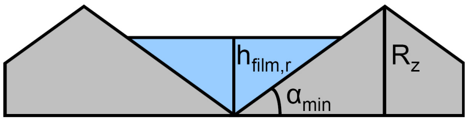

Figure 1.8: Effective wall film thickness $h_{\text{film},r}$ in case of a rough surface.

As the computational mesh is created for an ideally smooth geometry, Elsässer includes the roughness by an illustrative approach. The two-dimensional roughness profile (in the plane of incidence) is presented as neighbouring isosceles triangles with angle α_{min} and height R_z, see Figure 1.8. Using the value of the film thickness h_{film} in the considered computational wall cell where the impact occurs, a preliminary, effective film thickness $h_{\text{film},r} = \sqrt{2 \cdot R_z \cdot h_{\text{film}}}$ is calculated between the virtual roughness edges. It is used to determine the virtual profile angle, α_{min}:

$$\alpha_{\text{min}} = \begin{cases} 0^\circ & \text{if } \gamma_z \leq 0.25 \lor h_{\text{film},r} > R_z \,, \\ (-60 \cdot \gamma_z^2 + 135 \cdot \gamma_z - 30)^\circ & \text{if } 0.25 < \gamma_z \leq 1 \land h_{\text{film},r} \leq R_z \,, \\ 45^\circ & \text{if } \gamma_z > 1 \land h_{\text{film},r} \leq R_z \,. \end{cases} \tag{1.49}$$

With respect to the idealised profile, the impact angle α is then transferred to a virtual impact angle $\alpha_r \in [0, \frac{\pi}{2}]$ using simple geometric considerations in combination with a random number. The velocity components normal and tangential to the wall are calculated with respect to α_r. Depending on the impact location on the profile, an individual value of the non-dimensional film thickness δ (scaled by the primary drop diameter) is also determined for a considered drop.
After calculating the properties of the secondary drops, the virtual reflection angles β_r are finally retransferred from the idealised profile to the smooth surface giving β.

Cold wetting regime (CW). In this wall temperature regime, three impingement outcomes are modelled: complete rebound, drop deposition (called spread), and secondary atomisation (called splash), see Figure 1.9.

Rebound is addressed on wetted surfaces for small Weber numbers, $\text{We}_{\text{prim}} < \text{We}_{\text{crit}}$, where We_{crit} is determined according to [68], [69] and [55]:

$$\text{We}_{\text{crit}} = \left(\frac{26.6}{\alpha_{r,\text{deg}} + \text{La}_{\text{prim}}^{0.13}} \right)^4 - 0.0023 \cdot \text{La}_{\text{prim}} + 34.5 \,. \tag{1.50}$$

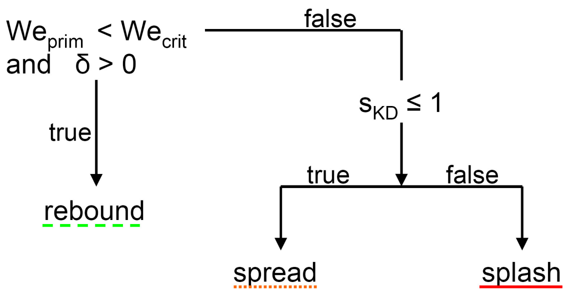

Figure 1.9: Possible outcomes in the cold wetting regime.

Drop diameter and absolute velocity are conserved, only the direction is changed:

$$\beta = (1 - \frac{\alpha_{\min}}{\pi}) \cdot \alpha_r + \frac{\alpha_{\min}}{2} \,. \tag{1.51}$$

The distinction between spread and splash is drawn by gathering the results of several references:

- For a wetted wall, Elsässer refers to [64], who studies a shear stress driven, wavy film with secondary drops torn off. A critical Reynolds number is developed as a function of the Laplace number and the non-dimensional film thickness. It is converted to the non-dimensional criterion $s_{KD} > 1$ in case of splash.

- For a dry wall, Elsässer uses the splashing limit of [12], $K_{\mathrm{dry}} = 649 + \frac{3.76}{\gamma_z^{0.63}}$ with $K := \mathrm{We} \cdot \mathrm{Oh}^{-0.4}$, and converts it also to the form of s_{KD}.

In both cases, no matter what value δ takes, a temperature dependence is additionally impressed which is based on the temperature dependence of the maximal lamella diameter forming on drop impact. It is deduced from data of [9] and [33].
Including finally a smooth transition from dry to wetted walls, Elsässer gets as spread/ splash boundary:

$$s_{KD} = \begin{cases} \sqrt{\frac{\mathrm{We}_{\mathrm{N,prim}}}{K_S}} \cdot \mathrm{La}_{\mathrm{prim}}^{0.0811} \cdot (T^*_{CW})^{0.1395} & \text{for a dry wall}\,, \\ \sqrt{\frac{\mathrm{We}_{\mathrm{N,prim}}}{K_S}} \cdot \mathrm{La}_{\mathrm{prim}}^{0.0811} \cdot (T^*_{CW})^{0.1395} \cdot \frac{1}{\sin \alpha_r^{0.37}} & \text{else}\,, \end{cases} \tag{1.52}$$

$$\text{with} \quad K_S = \begin{cases} K_{\mathrm{dry}} \cdot \left[\left(\frac{1451.61 \cdot F_\delta^2}{K_{\mathrm{dry}}} - 1 \right) \cdot \frac{\delta}{\gamma_z} + 1 \right] & \text{for } \delta \le \gamma_z\,, \\ 1451.61 \cdot F_\delta^2 & \text{else}\,. \end{cases} \tag{1.53}$$

F_δ is a polynomial of second order in δ which has been defined in [64].

For spread, i.e. if $s_{KD} \le 1.0$, the impinging mass is assigned to the wall film. Else, i.e. if $s_{KD} > 1.0$, the correlations from [64] are used to define the properties of the secondary droplets. These are represented by one computational parcel per impact with total secondary to primary mass ratio $x_{m,sp} = m_{\mathrm{sec}}/m_{\mathrm{prim}}$, diameter ratio $x_{D,sp} =$

$D_{\mathrm{sec}}/D_{\mathrm{prim}}$, number rate ratio $f_{n,sp} = n_{\mathrm{sec}}/n_{\mathrm{prim}}$, reflection angle $\beta_{r,\mathrm{deg}}$ and velocity ratio $x_{c,sp} = \mathrm{v}_{\mathrm{abs,sec}}/\mathrm{v}_{\mathrm{abs,prim}}$:

$$x_{m,sp} = \begin{cases} \min[1.5\,;\, x^*_{m,sp}] & \text{for}\, \delta > 2.0\,, \\ \min[1.0\,;\, x^*_{m,sp}] & \text{else}\,, \end{cases} \tag{1.54}$$

$$\text{with } x^*_{m,sp} = 0.0866 \cdot (s_{KD} - 1.0)^{0.3189} \cdot \alpha_{r,\mathrm{deg}}^{0.1223} \cdot \delta^{-0.9585}\,,$$

$$x_{D,sp} = \max[x_{D,\min}\,,\, 1.0 - (0.03454 \cdot s_{KD}^{0.175} \cdot \alpha_{r,\mathrm{deg}}^{0.1239} \cdot \mathrm{La}_{\mathrm{prim}}^{0.265})]\,, \tag{1.55}$$

$$f_{n,sp} = \frac{x_{m,sp}}{x^3_{D,sp}}\,, \tag{1.56}$$

$$\beta_{r,\mathrm{deg}} = 2.154 \cdot s_{KD}^{1.0946} \cdot \alpha_{r,\mathrm{deg}}^{0.3389} \cdot \delta^{-0.1589}\,, \tag{1.57}$$

$$x_{c,sp} = \frac{0.08214}{s_{KD}^{0.3384}} \cdot \alpha_{r,\mathrm{deg}}^{0.2938} \cdot \delta^{-0.03113} \cdot \mathrm{La}_{\mathrm{prim}}^{0.1157}\,. \tag{1.58}$$

For a deep wall film, parts of the film mass may be torn off and the splashing mass may exceed the impinging mass. Note that it must be artificially ensured that $\beta_{r,\mathrm{deg}} \in [0°, 90°]$.

In the original implementation of the model in AVL Fire version 7, some limits are added: The diameter ratio is restricted by a user-defined value $x_{D,\min}$ and the number rate ratio is limited to values larger than 0.5 with the diameter ratio adapted to $x_{D,sp} = (2.0 \cdot x_{m,sp})^{1/3}$ in that case.

Hot wetting regime (HW). The outcomes of spread, rebound and splash are continued from cold wetting to this temperature regime with hardly any changes - only T^*_{CW} is substituted by $(T^*_{HW} + 1)$. A fourth outcome, named boiling, is added in case of a dry surface to account for bubble boiling, see Figure 1.10. It is mainly defined according to [46] and [1]. In contrast to splashing, secondary atomisation is no longer due to droplet kinematics but generated by the explosion of vapour bubbles at the liquid interface of the spreading lamella, cf. [24]. It can therefore also occur for $\mathrm{We}_{\mathrm{N,prim}} \to 0$. A large number of small secondary droplets is observed as well as often a single large drop per impact, which is ejected almost normal to the surface due to Rayleigh jet breakup, see also [24] and [65].

The total boiling mass ratio, $x_{m,b} = m_{\mathrm{sec},b}/m_{\mathrm{prim}}$, is fitted as:

$$x_{m,b} = \min[1.0\,,\, 0.7315 \cdot (T^*_{HW} - 1)^{0.25} \cdot \mathrm{La}_{\mathrm{prim}}^{-0.0677} + 0.01165 \cdot \mathrm{We}_{\mathrm{N,prim}}^{0.458}]\,. \tag{1.59}$$

It is ensured that splashing and boiling reflect at most the impinging mass with $x_{m,b}$ reduced adequately. Otherwise, splashing and boiling are modelled independently from each other. Both can occur for one and the same impact event. Such a simultaneous occurance of splashing and boiling is a pure assumption of Elsässer and not confirmed by any of his references.

Two secondary parcels are provided in boiling: one containing the large drops representing jet breakup (child 1) and the other standing for the large number of small secondary drops (child 2) ejected normally. Child parcels $j = 1, 2$ are characterised by the drop

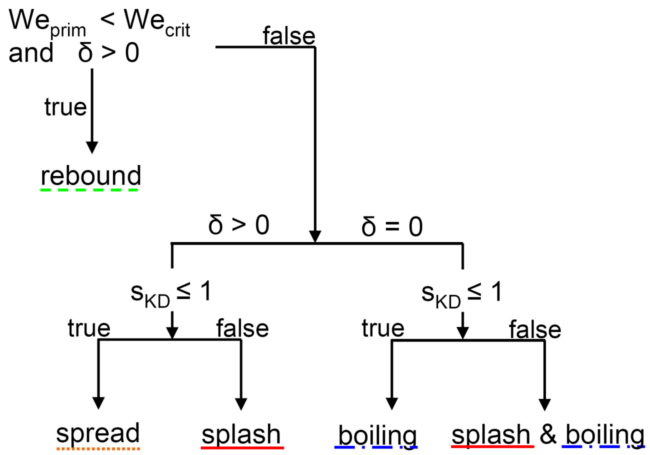

Figure 1.10: Possible outcomes in the hot wetting regime. Up to three child parcels may result per impinging parcel: one for splashing and two for boiling.

diameter ratios $x_{D,\text{sec}j,b} = D_{\text{sec}j,b}/D_{\text{prim}}$, the number rate ratios $f_{n,\text{sec}j,b} = n_{\text{sec}j,b}/n_{\text{prim}}$, the absolute velocities $\text{v}_{\text{abs,sec}j,b}$ and the ejection angles $\beta_{j,b}$:

$$x_{D,\text{sec1},b} = (0.8388 - 0.4724 \cdot 10^{-9} \cdot \text{La}_{\text{prim}}^{1.643}) \cdot (T_{HW}^{*})^{0.0975} \cdot x_{D,\text{sec1,max}}\,, \tag{1.60}$$

$$f_{n,\text{sec1},b} = \max\Bigg[0.5\,, \left(\frac{\text{We}_{\text{N,prim}}}{96.877}\right)^2 + \left(\frac{\text{La}_{\text{prim}}}{18399.15}\right)^2 + \left(\frac{T_{HW}^{*}}{0.5928}\right)^2 - 4.385\Bigg]\,, \tag{1.61}$$

$$\text{v}_{\text{abs,sec1}} = \left(\frac{\text{We}_{\text{N,prim}}}{0.4781 \cdot \text{La}_{\text{prim}}}\right)^2 + \left(\frac{T_{HW}^{*}}{0.7835}\right)^2 - 1.129\,, \tag{1.62}$$

$$\beta_{1,b} = 0.5 \cdot (\alpha + 0.5 \cdot \pi)\,, \tag{1.63}$$

$$x_{D,\text{sec2},b} = \max\Bigg[(0.3353 - 0.4724 \cdot 10^{-9} \cdot \text{La}_{\text{prim}}^{1.643}) \cdot (T_{HW}^{*})^{0.0975} \cdot x_{D,\text{sec1,max}}\,, \frac{D_{\text{sec2,min}}}{D_{\text{prim}}}\Bigg]\,, \tag{1.64}$$

$$f_{n,\text{sec2},b} = \frac{x_{m,b} - f_{n,\text{sec1},b} \cdot x_{D,\text{sec1},b}^3}{x_{D,\text{sec2},b}^3}\,, \tag{1.65}$$

$$\text{v}_{\text{abs,sec2}} = \left(\frac{\text{We}_{\text{N,prim}}}{0.4126 \cdot \text{La}_{\text{prim}}}\right)^2 + \left(\frac{T_{HW}^{*}}{0.7991}\right)^2 - 0.066\,, \tag{1.66}$$

$$\beta_{2,b} = \frac{\pi}{2}\,. \tag{1.67}$$

where $x_{D,\text{sec1,max}} = \left(\frac{x_{m,b}}{f_{n,\text{sec1},b}}\right)^{1/3}$ and where $D_{\text{sec2,min}}$ is user-defined.

If the drops in the first boiling parcel are calculated to be very small, the second parcel is discarded and the whole mass and number rate ratios are assigned to the first. If $f_{n,\text{sec1},b} < 0.5$, boiling is prevented completely.

Hot non wetting regime (HNW). The film boiling regime bases mainly on the same references, [1] and [46], as the hot wetting regime. A variation in T_wall does not lead to significant changes within this regime.

Rebound and rebound with breakup are distinguished, see Figure 1.11, where the boundary between these two outcomes is given by a correlation for the total number rate ratio:

$$f_{n,brk} = \frac{n_\text{sec}}{n_\text{prim}} = \left(\frac{\text{We}_\text{N,prim} + 3.46 \cdot (T^*_{HNW})^{-0.59} \cdot \ln(\text{La}_\text{prim})}{83.43 \cdot (T^*_{HNW})^{-1.53}}\right)^{1/0.35} . \tag{1.68}$$

For a more familiar presentation, $f_{n,brk}$ can be transformed to a critical Weber number:

$$\text{We}_\text{crit} = 83.43 \cdot (T^*_{HNW})^{-1.53} - 3.46 \cdot (T^*_{HNW})^{-0.59} \cdot \ln(\text{La}_\text{prim}) . \tag{1.69}$$

For the deduction of Equation 1.68, Elsässer cites [46], [1], [88] and [33]. The temperature dependence is inferred e.g. from [9]. However, the correlations do not hold a test on the reference data very well.

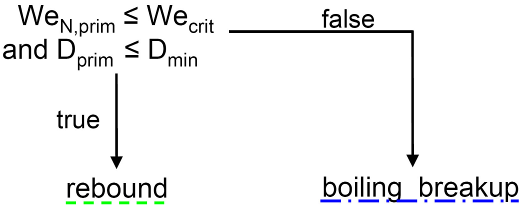

Figure 1.11: Possible outcomes in the hot non wetting regime.

Rebound is modelled if $f_{n,brk} \leq 1$. A fit of [38] based on the data of [88] is used to determine the normal velocity component of secondary drops:

$$\text{We}_\text{N,sec} = 0.14 \cdot \text{La}_\text{prim}^{0.11} \cdot \text{We}_\text{N,prim} \cdot \exp(-0.044 \cdot \text{We}_\text{N,prim}) . \tag{1.70}$$

Tangential velocity component and diameter are conserved.

Elsässer replaced the original coefficient of 0.678 in [38] by $0.14 \cdot \text{La}_\text{prim}^{0.11}$ to introduce an additional dependence on the Laplace number which is in turn deduced from data of [46]. This procedure is often applied in the model formulation, yet it is very critical because it assumes parameter independence.

In case of very small primary drops, which are supposed to follow the air flow with practically no energy loss, rebound is also applied but normal velocity is conserved in this case.

Rebound with breakup is modelled similarly to boiling in the hot wetting regime. For n_prim drops in the impacting parcel, a first reflected parcel with the same number rate represents large drops formed by jet breakup. A second child parcel stands for a high number of small secondary drops and gets the number rate $(f_{n,brk} - 1) \cdot n_\text{prim}$ according to mass conservation. The total impinging mass is reflected in the secondary parcels and no wall film forms in contrast to the cold and hot wetting regime where parts of the mass remain on the surface.

The correlation for the mean diameter ratio of the small secondary drops is deduced from [46] and [80]:

$$x_{D,\text{sec2},brk} = \begin{cases} 0.26 \cdot \text{La}_\text{prim}^{0.04} & \text{if } \text{We}_\text{N,prim} \leq 80\,; \\ 0.26 \cdot \text{La}_\text{prim}^{0.04} \cdot (\text{We}_\text{N,prim}/80)^{-1/2} & \text{else }. \end{cases} \tag{1.71}$$

The condition $\mathrm{We}_{\mathrm{N,prim}} \leq 80$ arises from [88]. Further limits are added to prevent too small secondary drops.
The diameter ratio of the other child parcel is found via mass conservation:

$$x_{D,\mathrm{sec1},brk} = \left[1 - (f_{n,brk} - 1) \cdot x^3_{D,\mathrm{sec2},brk}\right]^{1/3} . \tag{1.72}$$

If $x_{D,\mathrm{sec1},brk} \leq x_{D,\mathrm{sec2},brk}$, which contradicts the notion of child parcel 1 containing the large drops and child parcel 2 the numerous small ones, Elsässer switches to the reflection of only one parcel. Its diameter ratio is then set to

$$x_{D,\mathrm{sec1},brk} = \left(\frac{1}{f_{n,brk}}\right)^{1/3} \tag{1.73}$$

and the normal velocity component is calculated as for rebound, see Equation 1.70 with $\min[120, \mathrm{We}_{\mathrm{N,prim}}]$ instead of $\mathrm{We}_{\mathrm{N,prim}}$. This limit is reasoned by reference [88].
The tangential velocity component is assumed to increase and the increase is described as

$$\mathrm{We}_{t,\mathrm{increase}} = 94.94 \cdot \mathrm{La}_{\mathrm{prim}}^{-0.64} \cdot (\mathrm{We}_{\mathrm{N,prim}} - \mathrm{We}_{\mathrm{crit}})^{0.13} \cdot \sin \alpha_r . \tag{1.74}$$

$\mathrm{We}_{\mathrm{crit}}$ is used from Equation 1.69.

In case of two reflected child parcels, i.e. if $x_{D,\mathrm{sec1},brk} > x_{D,\mathrm{sec2},brk}$, Elsässer develops a model based on energy and momentum consideration where a questionable separation of control volumes is done. It leads to quite lengthy correlations for the parcel properties besides the already discussed diameter ratios.

Concluding remarks on Elsässer's model. The references on which the model correlations are based have been revised thoroughly in this work and in some cases they seem to hardly agree with Elsässer's final correlations, especially in the hot wetting and hot non wetting regime. The origins of some equations could not be retraced at all. This is due to the fact that various models from literature (concerning very different conditions with respect to wall and drop material, drop sizes and velocities) are mixed: Some constant coefficients are, for instance, substituted by functions of other parameters (without further motivation rational functions are assumed) to gain an additional dependence on those, see e.g. Equation 1.70. This procedure must be carefully examined, because it assumes independence of the parameters without further proof.
Another obvious drawback of the model concerns the deviation angle. Only backward or forward scattering is allowed for - but, for example in case of normal impingement of a single drop, a uniform distribution of the deviation angle in $[0, 2\pi[$ is to be expected.
In summary, Elsässer's model is rather doubtful in some aspects. Yet, due to the lack of a better model which covers the whole parameter ranges occuring in an engine, it has been used for in-cylinder calculations at BMW with the CFD software AVL Fire version 7 so far.

1.4.2.2 Kuhnke's model

This model, cf. [34], developed in the framework of the European project [24], already accounts for the fact that drop/drop interactions are important and that multiple drop impacts cannot be described by a simple superposition of single drop impingements like

done in Elsässer's model.
To include single as well as multiple drop impacts (denoted by the subscripts SD and MD), models for both situations are combined by the introduction of a blending factor λ_{MD}, which refers to spray density. An arbitrary quantity X is then calculated as

$$X = X_{SD} + \lambda_{MD} \cdot (X_{MD} - X_{SD})\,. \tag{1.75}$$

A wall film of different material properties than the spray liquid is not considered.

Blending function. For a smooth transition between single and multiple droplet correlations, λ_{MD} is proposed as a linear blending factor depending on the drop spacing κ:

$$\lambda_{MD} = \begin{cases} 1 & \kappa < 1\,, \\ \max\left[\frac{D_L^* - \kappa}{D_L^* - 1}; 0\right] & \kappa \geq 1, \text{ dry wall}\,, \\ \exp(\frac{1-\kappa}{c_{MD}}) & \kappa \geq 1, \text{ wetted wall}\,. \end{cases} \tag{1.76}$$

κ is defined as the drop centre to drop centre distance divided by the drop diameter. For $\kappa = 1$, neighbouring drop lamellae just touch. If the drop spacing is even smaller, the pure multiple droplet correlations are used, i.e. $\lambda_{MD} = 1$.
If the wall is dry, the largest distance to which interactions take place is set to the maximal spread D_L^* of the lamella (scaled by the drop diameter) that forms on single drop impact. An energy consideration yields $D_L^* = (0.28 \cdot \mathrm{We}_{\mathrm{N,prim}} + 1)^{0.39}$. For even larger distances, pure single drop correlations are assumed, $\lambda_{MD} = 0$.
If the wall is wetted, the spatial range of drop interactions may be enlarged by the film and it is adjusted by a model parameter c_{MD}: the larger the value, the larger the range.

The special feature of Kuhnke's model is the determination of the drop spacing parameter κ. In numerical simulations its value or equivalently the local, impinging spray density, is usually not known. It depends on injection parameters and ambient conditions and varies in space and time. To define useful values, a system of ellipses is set up on the impinged surface:

- During a timestep DT, the number of impinging drops is counted. At the end of the timestep the mean impingement point and the standard deviation $\bar{r}$ from this center are calculated.
- A system of ellipses with half axis ratio $\eta_{ha} \geq 1$ is defined around the impingement center. The area, A_j $(j \geq 1)$ of an arbitrary elliptic ring j is given as $A_j = \pi \cdot (r_j^2 - r_{j-1}^2)/\eta_{ha}$ with $r_j = \bar{r}\exp(j-2)$, $j \geq 1$, $r_0 = 0$.
- The spacing parameter κ_j for the elliptic ring j is then defined as:

  $$\kappa_j = \left(\frac{A_j}{\sum_i n_{\mathrm{prim},i} \cdot D^2_{\mathrm{prim},i} \cdot t^*_{\mathrm{exp},i}}\right)^{1/2}\,. \tag{1.77}$$

  $t^*_{\mathrm{exp}} := t_{\mathrm{exp},i}/DT = \left(\frac{\pi}{2} - \arcsin\frac{1}{D^*_{L,i}}\right)$ denotes the scaled expansion time of a drop lamella till maximal spread. It is estimated by an energy consideration. The sum over i comprises all parcels impinging in the area A_j during the considered timestep DT.

The evaluated system of ellipses is used in the subsequent timestep: every impinging parcel gets the value κ_j of the ellipse where its impact occurs. For normal impact, the system of ellipses simplifies to a system of concentric rings.
The system of ellipses is always one timestep old - to get an up-to-date system the run could be done twice. From the first run, the system of ellipses could be evaluated for each timestep and the information given to the second run. Yet, this procedure is rather costly and error-prone.

The determination of the drop spacing, which is considered as one of the first attempts to include spray density in modelling, is far from universal. It restricts the application of the model to plane surface geometries and axisymmetric sprays. Moreover, the values of κ_i are dependent on the timestep size DT and the number of introduced Lagrangian parcels. In case of parallel computing, it is furthermore required that the spray/wall interactions occuring on all partitions be evaluated simultaneously to define the system of ellipses. Many CFD codes, e.g. CFX, are not designed for such a user-defined communication between the slave and the master processes and expensive workarounds have to be conceived.

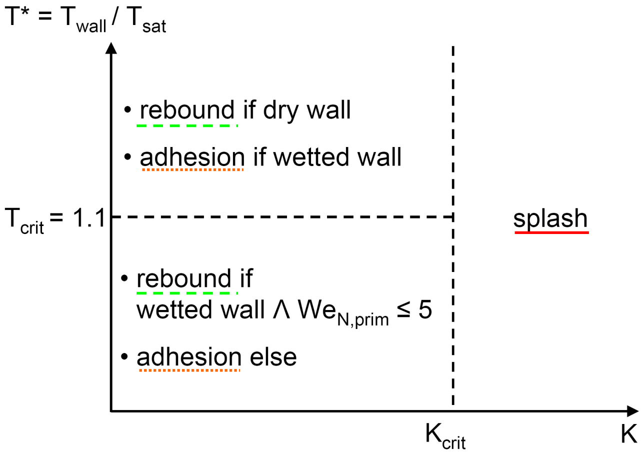

Figure 1.12: Schematic regime classification of Kuhnke's model.

Regime classification. Three impact outcomes are distinguished in Kuhnke's model, see Figure 1.12: deposition, rebound and splash. The regime boundaries are characterised by the non-dimensional wall temperature $T^* := T_{\mathrm{wall}}/T_{\mathrm{sat}}$ and the kinematic parameter $K := \mathrm{We}_{\mathrm{N,prim}}^{5/8} \cdot \mathrm{La}_{\mathrm{prim}}^{1/8}$.

Due to a lack of impact data for multiple drops, the transition temperature, which separates adhesion and rebound for small values of K, is deduced solely from single drop experiments of [24] and set to $T^*_{\mathrm{crit}} = 1.1$.
For adhesion the impinging mass is put into the wall film. Rebound is defined according to data of [88], which has been evaluated in [71]. Drop size and tangential velocity are conserved and the normal velocity can be deduced from:

$$\mathrm{We}_{\mathrm{N,sec}} = 0.678 \cdot \mathrm{We}_{\mathrm{N,prim}} \cdot \exp(-4.415 \cdot 10^{-2} \cdot \mathrm{We}_{\mathrm{N,prim}})\,. \tag{1.78}$$

Splash occurs if $K > K_{\mathrm{crit}}$ no matter what value T^* takes. Thermal atomisation for hot walls is modelled in the same way as kinematic splashing for cold walls.

For single drop events, the critical kinematic parameter $K_{\text{crit,SD}}$ is determined rather costly and wetted and dry walls are considered separately. In case of a dry surface, cold and hot walls are further distinguished.
For multiple drop impact, a value of $K_{\text{crit,MD}} = 25$, which is slightly smaller than in single drop impacts, is assumed. Using the linear blending factor λ_{MD}, the regime boundary to splash is finally obtained as $K_{\text{crit}} = K_{SD} + \lambda_{MD} \cdot (K_{MD} - K_{SD})$.

In the following, the correlations for splash are addressed further.

Secondary to primary mass ratio. The correlations for the mass ratio are based on existing single drop models, e.g. [4] for cold walls and [24] for higher wall temperatures:

$$\frac{m_{\text{sec}}}{m_{\text{prim}}} = \begin{cases} \min\left[1, \frac{T^*-0.8}{1.1-0.8}(1-B)+B\right] & , B = 0.2 + 0.6 \cdot p_{\text{rand}}, \text{ dry wall}, \\ \min\left[1+\nu_{wf}, \frac{T^*-0.8}{1.1-0.8}(1-B)+B\right] & , B = 0.2 + 0.9 \cdot p_{\text{rand}}, \text{ wetted wall}. \end{cases} \tag{1.79}$$

In case of wetted walls, secondary drops are supposed to entrain parts of the wall film mass which is reflected in the term $1 + \nu_{wf}$, where $\nu_{wf} = m_{wf}/m_{\text{prim}}$ denotes the liquid mass fraction in the computational wall film cell scaled by the impinging mass.

Size of secondary drops. For single drop impact the mean drop size ratio is mainly defined according to [71], [77] and [49]:

$$\left(\frac{D_{10,\text{sec}}}{D_{10,\text{prim}}}\right)_{SD} = \begin{cases} 3.3 \cdot \exp(3.6 \left(\frac{\alpha_r}{\pi}\right)^2) \cdot \text{We}_{\text{N,prim}}^{-0.65} & \text{dry wall}, \\ 2.2 \cdot \exp(3.6 \left(\frac{\alpha_r}{\pi}\right)^2) \cdot \text{We}_{\text{N,prim}}^{-0.36} & \text{wetted wall}, \end{cases} \tag{1.80}$$

with α_r the impingement angle measured relative to the wall (in radiants). Minimal limits for the ratio are additionally defined and based on an energy consideration. Their presentation is omitted at this point.
For multiple drop impact, the size is assumed to be generally larger than for single drop impacts, see [49]. On dry walls the lamellae interaction creates larger drops since breakup occurs earlier and thus at an expansion stage where the sheet is still thicker. On wetted walls, the early collision of arising crowns also prevents the typical formation of thin crowns with breaking rim and leads to the creation of finger-like jets which break up in larger secondary drops. However, quantitative data lacks and Kuhnke simply assumes

$$\left(\frac{D_{10,\text{sec}}}{D_{10,\text{prim}}}\right)_{MD} = \begin{cases} 0.5 & , \text{dry wall}, \\ 1.0 & , \text{wetted wall}. \end{cases} \tag{1.81}$$

Using the linear blending function of Equation 1.75, the mean ratio of secondary to primary diameters results.
The associated distribution functions are suggested to be of Weibull type, where the same variability is chosen for single and multiple drop impact:

$$pdf_{\text{Weibull}}(D_{\text{sec}}) = \frac{1.35}{D_{10,\text{sec}}} \cdot \left(\frac{D_{\text{sec}}}{D_{10,\text{sec}}}\right)^{0.35} \cdot \exp\left(-\left(\frac{D_{\text{sec}}}{D_{10,\text{sec}}}\right)^{1.35}\right). \tag{1.82}$$

Number of secondary parcels and number rates. Implementing the model in a Lagrangian approach, $N_{\text{sec},i}$ secondary parcels are defined per impinging parcel i. In this work, $N_{\text{sec},i} = 3$ is set as in [77], which seems an adequate compromise between resolution and computational cost.

The secondary diameters of all child parcels, $j = 1, 2, 3$, are chosen as random numbers which are distributed according to the *pdf* of Equation 1.82. (The procedure to get such values is described in more detail in Section 5.4.)

The number rate for each child parcel per impact is deduced accounting for mass balance and the deposited mass:

$$n_{\text{sec},j} = \frac{m_{\text{sec}}}{m_{\text{prim}}} \cdot D^3_{\text{prim},i} \cdot n_{\text{prim},i} \cdot \frac{pdf_{\text{Weibull}}(D_{\text{sec},j})}{\sum_{k=1,2,3} D^3_{\text{sec},k} \cdot pdf_{\text{Weibull}}(D_{\text{sec},k})} . \tag{1.83}$$

This definition will be further discussed in Section 5.4.

Secondary droplet velocities. The mean absolute velocity of child parcels is calculated from:

$$\mathrm{We}_{\text{sec}} = \begin{cases} \frac{D_{10,\text{sec}}}{D_{10,\text{prim}}} \cdot (\mathrm{We}_{\text{prim}} \cdot (1 - 0.85(\sin\alpha_r)^2) + 12) - \frac{12}{\nu_{32}} , \\ \quad \text{dry wall} , \\ \max\left[51 - 7.1 \exp(3.4\alpha_r/\pi); c_\alpha \mathrm{We}_{\text{prim}}\right] , \\ \quad \text{wetted wall} , \end{cases} \tag{1.84}$$

$$v_{\text{abs},10,\text{sec}} = \sqrt{\frac{\sigma \cdot \mathrm{We}_{\text{sec}}}{\rho \cdot D_{10,\text{sec}}}} , \tag{1.85}$$

where $c_\alpha = -0.378 \left(\frac{\alpha_r}{\pi}\right)^2 - 0.123\frac{\alpha_r}{\pi} + 0.156$. $\nu_{32} = D_{32,\text{sec}}/D_{10,\text{sec}}$ can be calculated using Equation 1.82:

$$\nu_{32} = \frac{\int D^3_{\text{sec},i} \cdot pdf_{\text{Weibull}}(D_{\text{sec},i})\, dD_{\text{sec},i} \cdot \int pdf_{\text{Weibull}}(D_{\text{sec},j})\, dD_{\text{sec},j}}{\int D^2_{\text{sec},r} \cdot pdf_{\text{Weibull}}(D_{\text{sec},r})\, dD_{\text{sec},r} \cdot \int D_{\text{sec},s} \cdot pdf_{\text{Weibull}}(D_{\text{sec},s})\, dD_{\text{sec},s}} . \tag{1.86}$$

The values for multiple drop impact are supposed to differ from those describing single drop impact only in a negligible way.

The distribution of the velocity values around the mean is assumed to be of Weibull type and the procedure to determine $\mathrm{v}_{\text{abs},\text{sec},j}$ for each child parcel j is the same as for their size.

The mean ejection angle is developed as

$$\beta_{10,SD} = \begin{cases} 0.225 \cdot \alpha \cdot \exp(0.017\alpha - 0.937)^2 & \text{wetted wall} , \\ 9.3 + \ln\gamma_z \cdot (2.7 - 0.03 \cdot \alpha) + 0.22 \cdot \alpha & \text{cold, dry wall} , \\ \alpha \cdot 0.96 \cdot \exp(-0.0045 \cdot \mathrm{We}_{\text{N,prim}}) & \text{hot, dry wall} , \end{cases} \tag{1.87}$$

$$\beta_{10,MD} = 1.5 \cdot \beta_{10,SD} . \tag{1.88}$$

with all angles in degree and α being the impact angle. γ_z denotes the non-dimensional peak-to-peak roughness value, $\gamma_z = R_z/D_{\text{prim}}$. In [24], the ejection angle is observed to increase with multiple drop impact. The factor of 1.5 is only an estimate, however.

For the ejection angle, a logistic distribution is found to be most adequate, where the width is also assumed larger for multiple than for single drop impact:

$$pdf_{\text{logistic}}(\beta_{\text{sec},SD}) = \frac{\exp(-x_{SD})}{4\cdot(1+\exp(-x_{SD}))^2} \quad \text{with}\, x_{SD} = \frac{\beta_{\text{sec},SD}-\beta_{10,SD}}{4}\,, \tag{1.89}$$

$$pdf_{\text{logistic}}(\beta_{\text{sec},MD}) = \frac{\exp(-x_{MD})}{6\cdot(1+\exp(-x_{MD}))^2} \quad \text{with}\, x_{MD} = \frac{\beta_{\text{sec},MD}-\beta_{10,MD}}{6}\,. \tag{1.90}$$

As for the size and the absolute velocity, values $\beta_{\text{sec},SD}$ and $\beta_{\text{sec},MD}$ are calculated for each child parcel and the usual blending between single and multiple drop correlations, cf. Equation 1.75, is applied.

The deviation angle Ψ, see Figure 1.14(b), is taken from [47], where an early spray/wall interaction model for cold walls based on single drop impacts is introduced. The study of a liquid jet which impinges on an inclined wall and transforms into a liquid sheet on the surface leads to the description

$$\Psi = -\frac{\pi}{\omega}\cdot\ln[1-p_{\text{rand}}\cdot(1-\exp(-\omega))]\,, \tag{1.91}$$

where p_{rand} is a uniform random number in $[0,1]$. The parameter ω is approximated by an explicit function in [34]:

$$\omega = \begin{cases} \sqrt{\frac{1+8.872\cdot\cos(1.152\alpha)}{1-\cos\alpha}} & \alpha \le 80^\circ\,, \\ \frac{\pi^2}{2}\cdot\cos\alpha & 80^\circ < \alpha\,. \end{cases} \tag{1.92}$$

Concluding remarks on Kuhnke's model. The model is one of the first to distinguish single and multiple drop impacts. The single drop correlations are developed using correlations from literature, e.g. [71], [4], [47], [77] and [49]. These are mingled which bears mainly the same problems occuring in Elsässer's model. The multiple droplet model relies on drop chain data of [24] (not on actual spray data), which are furthermore rather scarce and hardly sufficient to formulate a comprehensive model. Therefore, a lot of assumptions have to be used.
The calculation of the spray density restricts the application of the model to plane surfaces and axisymmetric sprays. Moreover, some doubts arise in the definition of the child number rate. These will be explained in Section 5.4.

1.4.2.3 Roisman's/Horvat's model

Compared to the two models discussed so far, this model, described in [28] and [59], is actually developed from spray data. These concern the normal impact of a continuous, relatively sparse full cone spray of water on a cold wall. Splash is defined semi-empirically, i.e. in addition to the usual fitting of empirical data, physical relations of the underlying phenomena have been used to define the correlations.
A wall film of different material properties than the spray is not considered.

Impact regimes. The model description in [28] distinguishes three impact regimes[4], namely deposition, rebound and splash depending on the normal Weber number of the

---

[4] Reference [59] describes only splash.

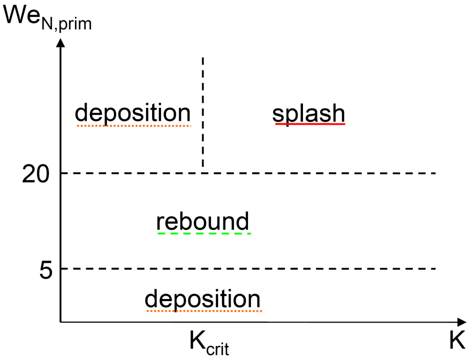

Figure 1.13: Schematic regime classification of Roiman's/Horvat's model.

impacting drop, see Figure 1.13.
The regime boundary of deposition, $\mathrm{We}_{\mathrm{N,prim}} < 5$, is chosen as in [4]. If $5 \leq \mathrm{We}_{\mathrm{N,prim}} < 20$, rebound occurs which is defined exactly as in Kuhnke's model. If $20 \leq \mathrm{We}_{\mathrm{N,prim}}$, splash or deposition take place depending on the kinematic parameter $K := \mathrm{We}_{\mathrm{N,prim}}^{0.8} \cdot \mathrm{Re}_{\mathrm{N,prim}}^{0.4}$. The critical value is determined based on empirical correlations from literature, e.g. [45] and [12]:

$$\text{dry wall: } K_{\mathrm{crit}} = 657\,, \tag{1.93}$$

$$\text{wetted wall: } K_{\mathrm{crit}} = \begin{cases} 2000 \cdot \left(1 + \frac{3}{40} \cdot \frac{h_{\mathrm{film}} \cdot \mathrm{Re}_{\mathrm{N,prim}}^{0.5}}{D_{\mathrm{prim}}}\right) & \text{if } \frac{h_{\mathrm{film}} \cdot \mathrm{Re}_{\mathrm{N,prim}}^{0.5}}{D_{\mathrm{prim}}} < 40\,, \\ 8000 & \text{else}\,. \end{cases} \tag{1.94}$$

If $K < K_{\mathrm{crit}}$, deposition is set, else splash. The latter is studied in more detail in the following. The two model versions in [28] and [59] differ slightly in some coefficients where the version of [59] is favoured here.

Diameters of secondary drops. The main breakup mechanism is considered to be corona splash, see Section 1.4.1: A single drop impacting on a stationary film creates a crown-like upraising sheet. At the unstable rim at the free edge of the liquid sheet, cusps develop. Finger-like jets emerge and break up into secondary droplets. A scaling of the secondary drop diameters is developed by Roisman:

- The thickness of a lamella, h_L, which is produced by the normal impact of a single drop, is studied in [60]. It is found to scale with $h_L \propto D_{\mathrm{prim}} \cdot \mathrm{Re}_{\mathrm{prim}}^{-1/3}$ for small Reynolds numbers, $\mathrm{Re}_{\mathrm{prim}} < 1000$. At higher values, $\mathrm{Re}_{\mathrm{prim}} > 2000$, it scales to the thickness of the viscous boundary layer,

  $$h_L \propto D_{\mathrm{prim}} \cdot \mathrm{Re}_{\mathrm{prim}}^{-1/2}\,. \tag{1.95}$$

  As high Reynolds numbers leading to splash are of interest for spray impact, the second correlation is used.

- In [82], correlation 1.95 is successfully used to scale the thickness of the uprising crown in the same way.

- The rim instabilities of the liquid crown-sheet are studied in [59] and the characteristic finger radius is found to be proportional to the thickness of the stretching liquid sheet. The secondary drop diameters are in turn supposed to scale with the finger radius and finally one gets:

$$D_{\text{sec}} \propto D_{\text{prim}} \cdot \mathrm{Re}_{\text{prim}}^{-1/2} \,. \tag{1.96}$$

This scaling is found to fit very well the mean values of the considered spray data. The semi-empirical definition of the volumetric mean secondary diameter $D_{30,\text{sec}}$ results:

$$D_{30,\text{sec}} = \begin{cases} D_{30,\text{prim}} \cdot \left(0.65 + 0.017 \cdot \exp\left(\frac{\mathrm{Re}_{\text{N,prim}} - 252}{73.5}\right)\right) & \text{if } \mathrm{Re}_{\text{N,prim}} < 500\,, \\ 24 \cdot D_{30,\text{prim}} \cdot (\mathrm{Re}_{\text{N,prim}})^{-0.5} & \text{else}\,. \end{cases} \tag{1.97}$$

The correlations presumably only hold for sparse sprays. Otherwise, film fluctuations and collisions between neighbouring crowns may lead to totally different breakup phenomena, e.g. finger-like jets emerging directly from the wall film.

The distribution function of the secondary droplet diameters is deduced from measured data:

$$\mathit{pdf}(x) = 2.38 \cdot x^{0.94} \cdot \exp(-1.23 \cdot x^{1.94})\,, \tag{1.98}$$

where $x = D_{\text{sec}}/D_{30,\text{sec}}$. Individual values for every child parcel are determined as random values distributed according to the *pdf*.

Secondary to primary mass ratio. An empirical correlation for the relative volume fluxes is used to describe the mass ratio, assuming equal density of primary and secondary drop liquid:

$$\Gamma_V = \frac{q_{V,\text{sec}}}{q_{V,\text{prim}}} = \frac{m_{\text{sec}}}{m_{\text{prim}}} = 0.005 \cdot \mathrm{K}_{\text{prim}}^{2.25} \cdot \mathrm{Re}_{\text{N,prim}}^{-0.5} \cdot (0.0011 - \frac{q_{V,\text{prim}}}{v_{10,\text{prim}}})\,. \tag{1.99}$$

$q_{V,\text{prim/sec}}$ denotes the impinging/reflected volume flux and $v_{10,\text{prim}}$ the mean impinging velocity. The correlation is only applicable for sparse sprays, see Chapter 2, and a validity range of $4.6 \cdot 10^{-5} < q_{V,\text{prim}}/v_{10,\text{prim}} < 5.3 \cdot 10^{-4}$ is given. Beyond this range, i.e. for large values of $q_{V,\text{prim}}$ or very small values of $v_{10,\text{prim}}$, Γ_V may get negative.
A drawback consists in the fact that the volume flux $q_{V,\text{prim}}$, which impinges on the target, is usually not well known in numerical calculations. (This is the reason for the system of ellipses in Kuhnke's model.)

Number and number rates of secondary parcels. In the implementation of the model into numerical code, three child parcels, $j = 1, 2, 3$, are declared as for Kuhnke's model. Their number rates are set to:

$$\begin{aligned} n_{\text{sec},1} &= \frac{6 \cdot m_{\text{sec}}}{\rho \cdot \pi \cdot \left(D_{\text{sec},1}^3 + \sum_{j=2,3} \frac{\mathit{pdf}(D_{\text{sec},j}/D_{30,\text{sec}})}{\mathit{pdf}(D_{\text{sec},1}/D_{30,\text{sec}})} \cdot D_{\text{sec},j}^3\right)}\,, \\ n_{\text{sec},2/3} &= \frac{\mathit{pdf}(D_{\text{sec},2/3}/D_{30,\text{sec}})}{\mathit{pdf}(D_{\text{sec},1}/D_{30,\text{sec}})} \cdot n_{\text{sec},1}\,. \end{aligned} \tag{1.100}$$

This definition will be further discussed in Section 5.4.

Velocities of secondary drops. Instead of using mean values evaluated directly from the measured spray data, the ratio of the total mechanical energy fluxes (kinetic plus surface energy fluxes) is approximated with the volume ratio:

$$\Gamma_{\mathrm{E_{tot}}} = \frac{q_{\mathrm{E_{tot},sec}}}{q_{\mathrm{E_{tot},prim}}} \approx 0.36 \cdot \Gamma_V^{1.1} \,. \tag{1.101}$$

The kinetic energy flux and hence the surface mean value of the absolute velocity of secondary drops are then deduced as:

$$q_{\mathrm{E_{kin},sec}} = q_{\mathrm{E_{tot},sec}} - 0.82 \cdot \pi \cdot D_{30,\mathrm{sec}}^2 \cdot \sigma \cdot q_{\mathrm{Nr,sec}} \,, \tag{1.102}$$

$$v_{20,\mathrm{abs,sec}} = \left(\frac{2 \cdot q_{\mathrm{E_{kin},sec}}}{\rho \cdot q_{V,\mathrm{sec}}} \right)^{1/2} , \tag{1.103}$$

where $q_{\mathrm{Nr,sec}}$ is the secondary number flux.
The distribution function for the absolute velocity is fitted from measured data:

$$pdf\left(\frac{v_{\mathrm{abs,sec}}}{v_{20,\mathrm{abs,sec}}} \right) = 21.267 \cdot \left(\frac{v_{\mathrm{abs,sec}}}{v_{20,\mathrm{abs,sec}}} \right)^2 \cdot \exp\left(-3.723 \cdot \frac{v_{\mathrm{abs,sec}}}{v_{20,\mathrm{abs,sec}}} \right) \,. \tag{1.104}$$

The value $v_{\mathrm{abs,sec},j}$ for child parcel j is determined analogously to its size as a random number distributed according to this *pdf*.

The ejection angle β is also randomly chosen from

$$pdf(\beta) = 0.0169 \cdot \exp\left[-\exp\left(1.74 - 0.075 \cdot \beta\right) \right] \,, \tag{1.105}$$

where β is given in degrees and $\beta = 0°$ refers to a normal ejection.

The deviation angle, i.e. the rotation between the incident and outgoing plane, see Figure 1.14(b), is set randomly in $[0, 360°[$, because normal impact is considered.

Extrapolation to oblique impacts. Although it is mentioned in [59] that the correlations seem to fit inclined impact data also rather well, the extrapolation is not worked out thoroughly, see [28]. For very oblique impacts, the velocity of the wall film presumably has a very strong influence and should be considered.

Concluding remarks on Roisman's/Horvat's model. The model, which is restricted to normal impingements of relatively sparse sprays (see Equation 1.99) on cold walls, is one of the first to be based on spray impact data. Corona splash is identified as main impact phenomenon and a semi-empirical correlation for the volumetric mean diameters of secondary drops is deduced.
The introduction of deposition and rebound for small Weber numbers has to be questioned, although [28] states an improvement if these are included in model validations. The distinction of these regimes for small Weber numbers is not motivated by the underlying, experimental spray impact data. The latter only define the so-called splash regime. Deposition and rebound as well as the thresholds to distinguish the regimes base only on single drop studies. It is arguable that these can be directly transferred to spray impact since they do not account for wall film fluctuations or drop interactions. This is noted in [59], where only splash is considered, but [28] does the distinction regardless of this fact.
Some additional remarks on possible inconsistencies concerning the definition of the child number rates are given in Section 5.4.

1.4.3 Implementation in CFX

The next step after the description of a model is its implementation in numerical code. In CFX version 10 (the latest version available at the beginning of this work) the possibilities are rather limited. An impinging parcel can either die, i.e. it is no longer tracked after the timestep, or it can rebound. In case of rebound, one child parcel is reflected:

- Using standard options the drop diameter, number rate and therefore also mass of the child parcel cannot be changed compared to the impinging parcel. Only the restitution coefficients for wall-normal and wall-tangential velocity components, $c_\mathrm{N} := v_\mathrm{N,sec}/v_\mathrm{N,prim}$ and $c_\mathrm{T} := v_\mathrm{T,sec}/v_\mathrm{T,prim}$, can be set by the user to a value $\in [0, 1]$, see Figure 1.14(a). For ideal reflexion c_N and c_T equal 1. Backscatter is possible by negative values of c_T.
- The user can define his/her own rebound model as Fortran code. Besides the restitution coefficients, diameters and number rates of secondary parcels can then be calculated according to user-defined correlations. Variables like the wall temperature can be read in as arguments to the routines.

Considering the descriptions of Elsässer's, Kuhnke's or Horvat's model in the previous subsection it is revealed that the possibilities in CFX are too limited to implement any of these models. Severe drawbacks are:

- Not more than one secondary parcel can be defined per impact. The breakup of impinging drops can hardly be illustrated in that way and the implementation of any slightly more elaborate model including e.g. splash in Kuhnke's or Roisman's/Horvat's model is not feasible.
- Any kind of wall film implementation lacks in CFX. Not reflected mass and momentum are simply lost.
- The scattering plane must equal the incident plane and an arbitrary deviation angle cannot be declared, see Figure 1.14(b).
- An impacting parcel ignores the presence of other parcels during wall interaction. It is not possible to get any of their properties because no access to the data base is provided.

Essential improvements in CFX have been achieved in the course of this thesis to overcome the limitations presented. They will be shown in Section 2.3.

Besides the problems specific to CFX, the definition of spray/wall interaction is confronted with a general problem inherent to the Lagrangian description: The interaction is defined for one parcel at a time, i.e. in principle as a single drop impact independent of all other parcels. Yet, in case of spray impact, not single drop properties but the overall ensemble of polydispersed secondary drops has to be represented correctly. The implementation of a model has to provide this and random numbers distributed according to the model-defined *pdf*s are therefore commonly chosen to determine the properties of secondary parcels, cf. Kuhnke's or Roisman's/Horvat's model.
If the correlations to describe the secondary spray distributions require mean impact

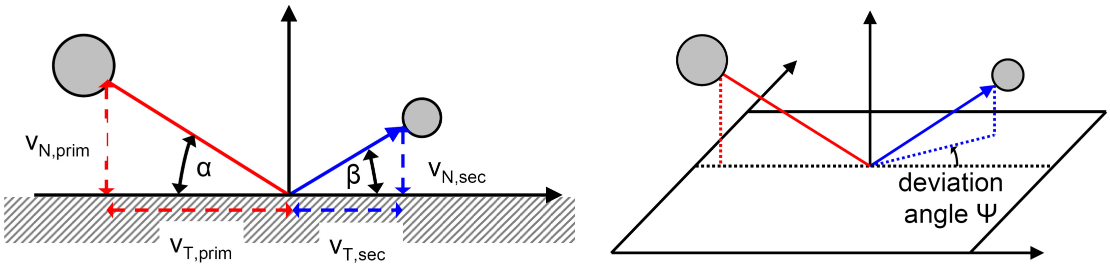

(a) Concerning the definitions of the restitution coefficients.

(b) Deviation angle.

Figure 1.14: Angle definitions with respect to spray/wall interactions.

properties, see e.g. Equation 1.97 or 1.80, the implementation gets rather complex. Usually, the mean impact properties are not known before the simulation. They can hence either be determined in doing the simulation twice using the evaluated means from the first in the second run which is rather costly and error-prone. Or they could be deduced from the previous timestep. This procedure is preferable and is carried out in this work, yet it demands rather complex workarounds as CFX does not allow for simple sharing of particle data between partitions during the run. Special attention has to be paid in case of oblique or curved surfaces where the mean values have to be determined depending on the location. If the surface structure is very irregular, the properties of each individual impacting parcel i may be introduced into the correlations instead of the mean values. Yet, it has to be kept in mind that the model outcome may then differ significantly from the intended one, because the widths of the primary distributions are wrongly superimposed on the secondary ones.

1.5 Main subjects of this work

Summarising the preceding sections it shows that spray/wall interactions represent an important yet weak point in in-cylinder calculations carried out in engine development. This is due to several reasons:

- The status of modelling spray/wall interaction is not satisfactory. Underlying physics of the complex phenomena are not yet well understood and spray impact is often still modelled as a superposition of single drop impacts although this is known to fail. Models from several references are usually assembled in a questionable procedure to cover large parameter ranges.

- A general lack of quantitative spray impact data persists. A dense and high-pressure hollow cone spray, which is often used in a DI engine has not been considered at all. Moreover, the impact on a wall film of different material properties than the spray liquid (e.g. the impact of a fuel spray on the lubricating oil film on the cylinder liner in an engine) has not been studied in a quantitative way.

- The implementation of a model in numerical code and especially in CFX is associated with severe drawbacks. At the beginning of this work, in CFX version 10, only one child parcel can be defined per impact and no wall film model exists. Besides parcel death and rebound, it is not possible to describe any

slightly more elaborate impact outcome. Neither Elsässer's nor Kuhnke's or Roisman's/Horvat's model can be implemented.
Compared to AVL Fire version 7, which has been used at BMW before a software change and where Elässer's model has been originally implemented, modelling spray/wall interactions is rather limited in CFX simulations.

This thesis covers the following improvements:

- The status of spray/wall interaction in CFX is enhanced to the one in AVL Fire previously used for in-cylinder calculations at BMW. This requires an extended data structure in CFX, which has been funded by BMW in the course of this work and which enables the breakup of Lagrangian parcels on impact and a basic wall film model. Elsässer's model can then be implemented in user Fortran routines within this work.

- A reference case is set up to validate the applicability of Elsässer's as well as Kuhnke's and Roisman's/Horvat's model for a dense, high-pressure, hollow cone spray with available transmitted-light images.

- Experimental data concerning the impact of the same spray type are gathered using a dual PDA setup. The influence of the wall temperature is studied over a large range. Kinematics and an oil film on the target surface are also addressed.

- A thorough study on the evaluation of PDA data concerning spray/wall interaction lacks so far because these have been mostly used to characterise free sprays. This is carried out and some fundamental questions are treated giving guidelines for data evaluation in future work.

- An empirical model describing the impact of the considered high-pressure, hollow cone spray is developed and implemented in CFX. A number of simulations, comprising a reproduction of the experiment, are performed for verfication.

Chapter 2

Reference case: spray impact on a horizontal plane

As discussed in Section 1.4, CFX version 10, available at the beginning of this work, is too limited concerning the possibilities to implement spray/wall interaction models. However, essential improvements have been provided in the course of this thesis which allowed for the definition of Elsässer's model within this work. The status of CFX with respect to spray/wall interaction can thus be enhanced to that of AVL Fire, previously used in simulations at BMW. This has been a first aim of this thesis.
To present the improvements in the code and to validate the outcome of Elsässer's model with respect to the impact of a dense hollow cone spray, a reference case is studied in this chapter. A rather simple and rotationally symmetric case is chosen which is separated from complex engine geometries with the associated curved surfaces. The application of Kuhnke's and Roisman's/Horvat's model is addressed as well.

2.1 Description of the reference case

The case considers the impact of a dense and high-pressure hollow cone spray, cf. Section 1.2, on an unheated aluminium plate in a horizontal position. The distance between nozzle exit and the plate is $\approx 20\,\mathrm{mm}$. Due to a cone angle of $\approx 90°$ the spray liquid of the hollow cone impacts with an angle of $\approx 45°$. The ambient conditions and the injection settings are summarised in Table 2.1. Figure 2.1 illustrates the situation.
Transmitted-light images are available every $0.05\,\mathrm{ms}$ from $t = 0\,\mathrm{ms}$ until $t = 0.8\,\mathrm{ms}$. The injection starts at $t \approx 0.05\,\mathrm{ms}$. Note that each image is taken in a different injection. The images of the spray shape are compared to the results of numerical simulations in the following.

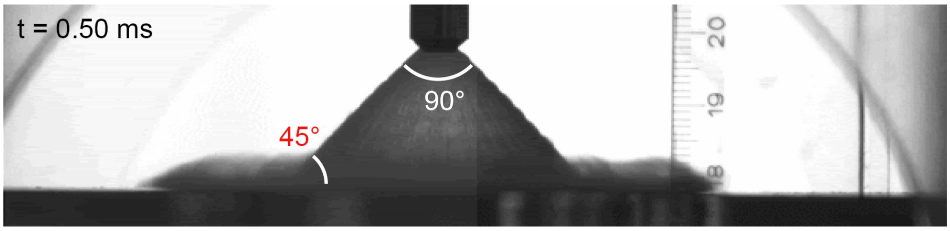

Figure 2.1: Reference case at $t = 0.5\,\mathrm{ms}$ ($\approx 0.45\,\mathrm{ms}$ after start of injection).

Wall material	aluminium
Wall temperature T_{wall}	20°C
Wall roughness (average)	$R_a \approx 17\,\mu\mathrm{m}$
Gas fluid	air, initially quiescent
Ambient pressure p_{ambient}	1 bar
Ambient temperature T_{ambient}	20°C
Spray liquid	C_7H_{16} (n-heptane)
Full spray cone angle	90°
Injection pressure p_{inj}	200 bar
Injection duration Δt_i	0.4 ms
Injected mass m_{inj}	26.6 mg
Liquid temperature $T_{\mathrm{C_7H_{16}}}$	20°C

Table 2.1: Ambient and injection settings of the reference case.

2.2 Setup of the simulation

To treat spray/wall interaction correctly in a numerical simulation, it is first necessary to describe the free spray properly. This comprises in principle the characterisation of the flow inside the specific nozzle, of the subsequent liquid atomisation (primary and secondary breakup) and of the spray propagation. The individual steps are very complex and not fully understood yet. Moreover, it is much too costly to consider all of them in detail for every specific case.

Therefore, spray initialisation at the nozzle exit, which concerns the setting of drop diameters and velocities, for instance, is mainly deduced from available experimental spray data and estimates. This is not an easy task because experimental data are usually scarce and restricted to special conditions. Spray propagation is described by adapted models, e.g. for the drag. Numerical parameters, like the mesh resolution, may exert a strong influence, cf. Appendix A.1 for more details.

The settings applied in the simulations considered are discussed in the following with focus on the initialisation of the hollow cone spray. As this subject concerns only a side aspect of this work, the presentation is rather short.

2.2.1 Geometry, mesh and further parameter settings

A cylindrical box is set as computational domain, cf. Figure 2.2 where the boundary types are also specified. Through the opening boundary the fluid may flow in an arbitrary direction. Due to the rotational symmetry most calculations are performed calculating only half the box, i.e. 180° instead of 360°, leading to an additional symmetry boundary on the middle plane.

The computational mesh, see Section 1.3, is defined similar to those used in in-cylinder calculations at BMW[1] and bases on an unstructured topology of tetrahedra. On rigid surfaces (plate and nozzle), five prism layers with a thickness growth ratio of 1.4 are created. The edge lengths of the tetrahedron cells as well as the total height of the prism layers are set to a maximal value of 1 mm. This results in a mesh with approximately

---

[1] A local mesh refinement around the injector, which is sometimes used to better resolve the high gradients, is rejected throughout this work to ensure the same conditions for primary and secondary spray.

$4.3 \cdot 10^5$ nodes and $2.4 \cdot 10^6$ elements (half-cylindrical box). Figure 2.3 presents an arbitrary cut through the mesh.

The convergence criteria for the presented calculations are set to $5.0 \cdot 10^{-5}$ for the RMS residual target and to 1% for the conservation target, cf. Section 1.3. Further simulation and modelling parameters are summarised in Table 2.2.

Eulerian timestep DT	$5.0 \cdot 10^{-6}\,\mathrm{s}$
Discretisation of convective terms	high resolution
Turbulence model	SST
Number of parcel integration time steps per element	10
Drag model	Schiller-Naumann
Breakup model	none

Table 2.2: Parameter settings and convergence criteria.

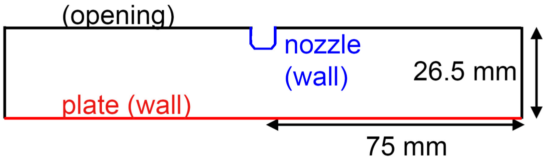

Figure 2.2: Section plane through the middle of the cylindrical geometry used in simulations.

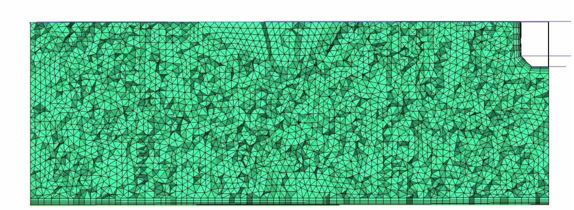

Figure 2.3: Arbitrary cut through the mesh with edge length $\leq 1\,\mathrm{mm}$ of the tetrahedra.

2.2.2 Spray initialisation

To define the primary spray the following quantities have to be set:

- the injection area and positions where Lagrangian parcels are initiated.
  The actual opening area of the injector is not resolved in the computational mesh and a simplified injection region in form of a small ring is addressed. It is situated near the nozzle exit in the first cell layers to avoid incorrect backward flow along the nozzle wall. The ring width is assumed constant, i.e. opening and closing phase are neglected. The starting positions of the parcels are distributed randomly on the injection ring with a virtual width of 0.03 mm.

- The mass flow rate of the injected liquid.
  Mass conservation gives

$$\dot{m}_{\text{inj}} = \int \rho \cdot v_{\text{nozzle exit}}\, dA_{\text{inj}} \,. \tag{2.1}$$

  As mentioned the opening area A_{inj} at the injector tip is not resolved. Furthermore, the spatial profile of the velocity across this area is unknown. Therefore, a simplified mass flow rate is used based on the needle lift function. A measurement of that is provided for an injection pulse width of $\Delta t_i = 1.0\,\mathrm{ms}$, see Figure 2.4(a).

Transferring the approximated (needle oscillations are ignored) and scaled function to a pulse width of $\Delta t_i = 0.4\,\mathrm{ms}$ by shortening the stationary part and taking into account the total injected mass of $m_{\mathrm{inj}} \approx 26.6\,\mathrm{mg}$, the mass flow rate shown in Figure 2.4(b) results. The stationary value amounts to $\dot{m}_{\mathrm{stat}} \approx 66.4\,\mathrm{g/s}$. The opening and closing ramps of length 0.14 ms are maintained and agree with the transmitted-light images.

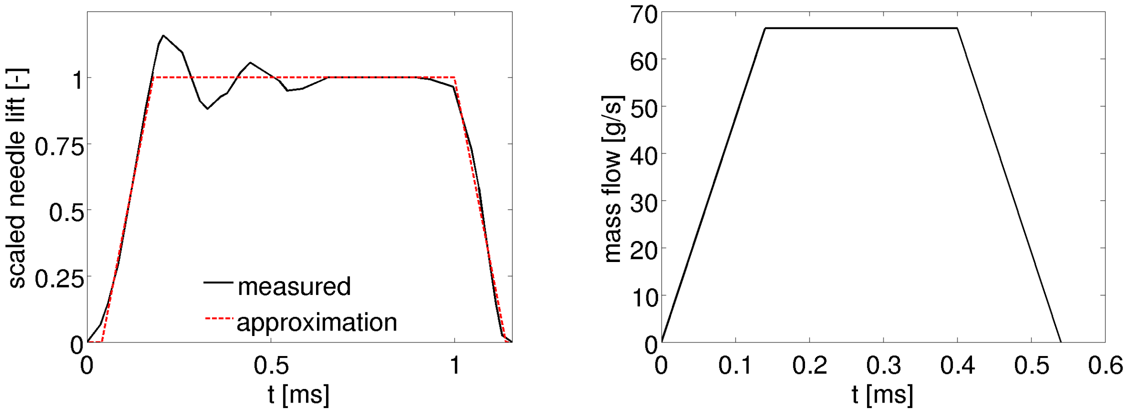

(a) Measured and scaled needle lift function for $\Delta t_i = 1\,\mathrm{ms}$.

(b) Setting in the simulation.

Figure 2.4: Injected mass flow rate.

- The number of Lagrangian parcels.
  A number of 40 000 parcels is chosen to represent the total injected mass of $m_{\mathrm{inj}} \approx 26.6\,\mathrm{mg}$. The number injected per timestep is directly related to the mass flow rate with fewer parcels injected during the opening and closing phase of the injector.
- The injection velocity vector, which is determined by its amount v_{inj} and the known cone angle of 90°.
  v_{inj} is time-dependent and shows a spatial profile across the injector opening area. Yet, measurements near the nozzle exit are very difficult due to the high spray density and v_{inj} is not known for the considered injector and injection conditions. The final function, see Figure 2.5(a), neglects the spatial profile and is deduced as follows:
  - A nozzle flow calculation (courtesy Dr. Wolfgang Kern of BMW) is used to define the ramping functions during the opening and closing phase, see Figure 2.5(b). The progression of the maximal velocity values is considered here because these (and not the means) determine the penetration of the spray front.
  - The results of the nozzle flow calculation refer to a slightly different nozzle and a pulse width of $\Delta t_i = 1.0\,\mathrm{ms}$. Cavitation is not included in the calculation and only the lower part of the injector is considered where the pressure drop occuring in the upper part is not accounted for. Hence, the calculated stationary value of $v_{\mathrm{stat}} \approx 232\,\mathrm{m/s}$ is rather uncertain.
    A simple Bernoulli approximation,

$$0.5 \cdot v_{\mathrm{stat}}^2 + \frac{1\,\mathrm{bar}}{\rho} = \frac{200\,\mathrm{bar}}{\rho}\,, \tag{2.2}$$

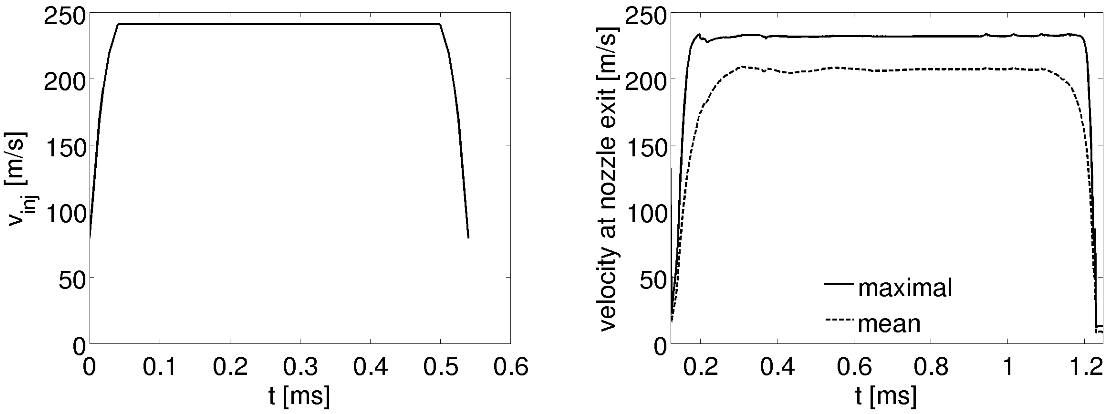

(a) Setting in the simulation.

(b) Results from a nozzle flow calculation. The progression of the maximal velocity values is approximated to define the ramping functions during the opening and closing phase of the injector.

Figure 2.5: Injection velocity.

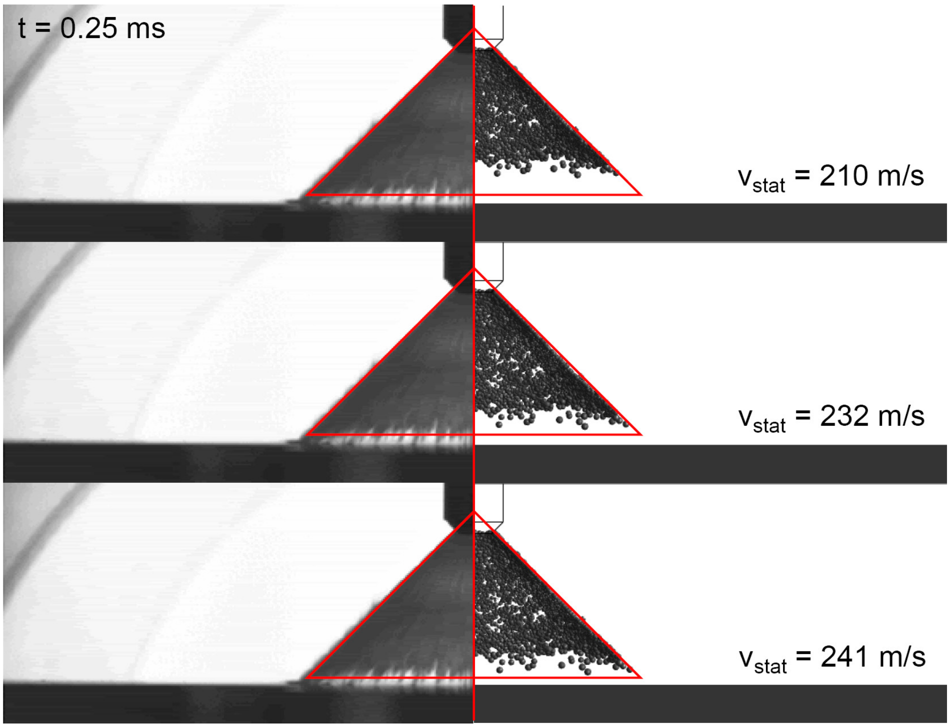

Figure 2.6: Comparison of different stationary velocities v_{stat} at $t = 0.25\,\text{ms}$ for the measured drop size distribution with $D_{32} = 18\,\mu\text{m}$. $v_{\text{stat}} = 210\,\text{m/s}$ refers to the progression of the mean velocity in Figure 2.5(b), $v_{\text{stat}} = 232\,\text{m/s}$ to that of the maximal velocity and $v_{\text{stat}} = 241\,\text{m/s}$ is the value deduced from the Bernoulli equation and finally used in the setup.

gives $v_{\text{stat}} \approx 241\,\text{m/s}$ with $\rho_{C7H16,20°C} = 685\,\text{kg/m}^3$. This value is finally chosen in the setup because the simulation results then agree with the spray penetration observed in the transmitted-light images, which offer the only possibility to test the setup.

For smaller values of v_{stat} the calculated penetration shows to be too slow, see Figure 2.6. The value of 241 m/s is considered as a maximal limit, though, because it already neglects a pressure loss in the nozzle. The associated overestimate of the velocity at nozzle exit is motivated by the fact that drag is also overestimated there: it has been observed that the ejected liquid sheet only breaks up in distinct drops in a distance of several millimeters after the nozzle exit due to turbulent and aerodynamic forces, see Figure 2.7. In an Euler-Lagrangian approach this cannot be modelled and the initialised individual drops experience larger drag.

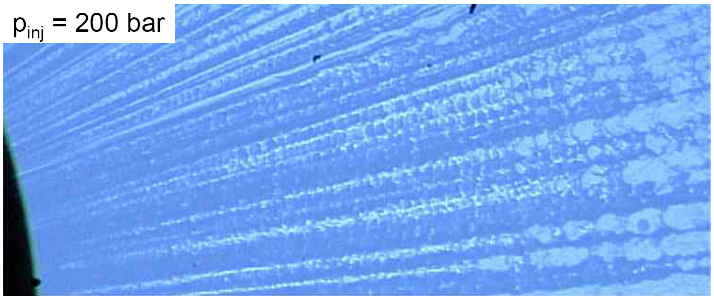

Figure 2.7: Breakup of the injected liquid sheet several millimeters after the nozzle exit.

- The drop size distribution.
  Its initialisation presents a well-known problem in spray simulations. Primary breakup cannot be modelled in a satisfactory way yet. For the considered injector and injection conditions, measurements of the drop sizes are only available in a distance of 40 mm to the nozzle exit: At the outer border of the spray cone, a distribution with a Sauter mean diameter of $D_{32} \approx 15\,\mu\text{m}$ is obtained, see Figure 2.8. Measuring even closer to the spray cone, the diameter increases and the distribution functions show a value of $D_{32} \approx 18\,\mu\text{m}$. They seem to stabilise there, yet, measurements have not been performed crossing the spray cone completely and drop sizes might still be larger in the core.
  Using the measured distributions directly for spray initialisation at the nozzle exit without any further breakup model applied, it is not possible to reproduce the spray penetration of the transmitted-light images with the measured diameter distribution of $D_{32} \approx 18\,\mu\text{m}$ for the chosen velocity value $v_{\text{stat}} \approx 241\,\text{m/s}$. Therefore, the distribution is scaled with a factor of 1.2 resulting in $D_{32} \approx 21\,\mu\text{m}$. Even larger drops, which also lead to good results just before wall interaction, see Figure 2.9(b), are not justified because the penetration of the main mass flow is then too fast in the beginning, cf. Figure 2.9(a).

In Figure 2.10 the numerical predictions of spray propagation resulting with the finally chosen setup are compared with the transmitted-light images. The overall agreement is rather good - the more so as an impartial evaluation of the transmitted-light images is also difficult.

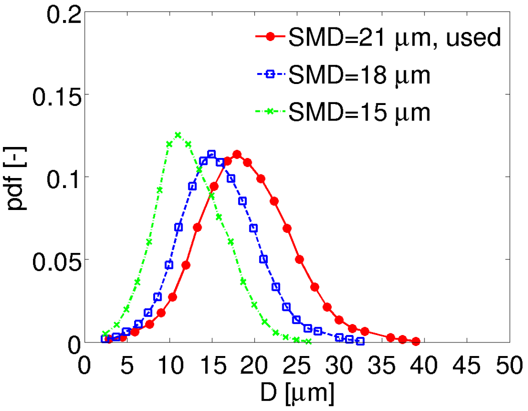

Figure 2.8: Drop distributions considered for initialisation.

2.3 Spray/wall interaction

In the course of this work the software CFX has been significantly modified and improved with respect to wall impingement. Only thus, the implementation of Elsässer's, Kuhnke's and Roisman's /Horvat's models, see Section 1.4, became possible.
To test the applicability of these models to the impact of a high-pressure, hollow cone spray, the associated simulation results are compared to the transmitted-light images available for the reference case.

2.3.1 Modifications of CFX

This thesis started with CFX version 10, where the definition of parcel/wall interaction is very limited, see Section 1.4.3: A primary parcel can only be redefined to a single secondary parcel. The fraction of the primary mass, which is not reflected, is lost as no wall film module exists. These aspects prevent a satisfying implementation of any more elaborate impact outcome than full rebound.
Therefore, BMW funded developments in CFX, which are available from the official release of CFX version 12 onwards:

- In the so-called "real droplet breakup" several children can be created upon the wall contact of a dying parent parcel. The maximal number of children as well as the maximal number of generations are set by the user. A parcel of the last generation impinges without further breakup according to user-defined restitution coefficients - set to ideal reflection per default.

- A wall film in form of Lagrangian wall parcels has been implemented. Deposited mass can be assigned to wall parcels. In this first approach, the latter can evaporate but are geometrically stationary. On moving geometries they remain on their physical position, i.e. they move with the geometry.

Some limitations still persist and must be addressed in future work:

- The wall film development is still in the early stages and gives rise to some problems:

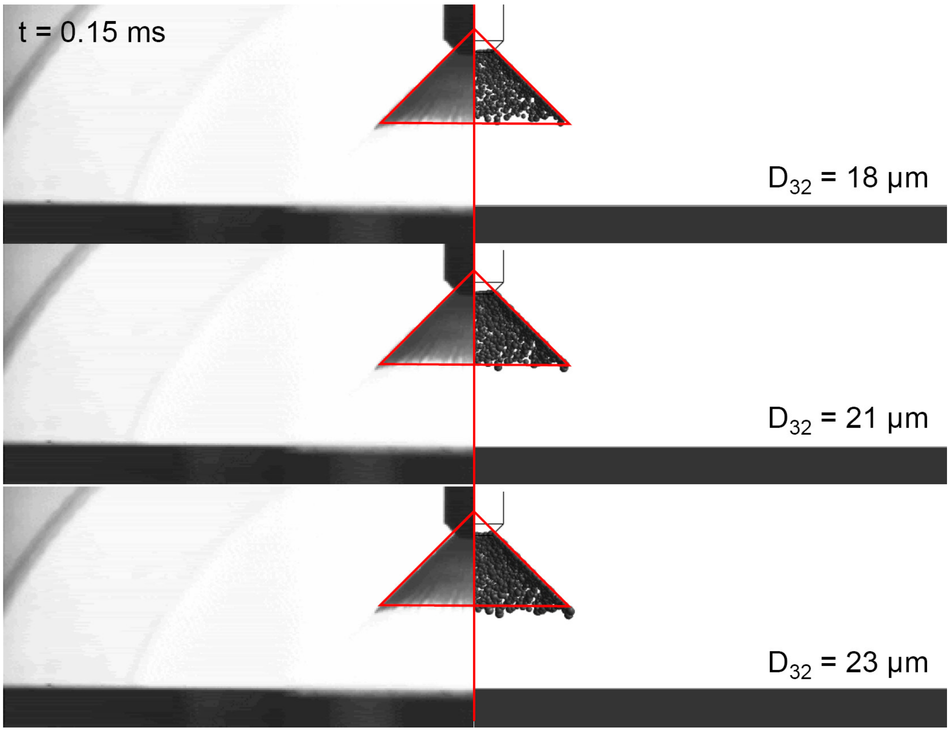

(a) $t = 0.15\,\mathrm{ms}$

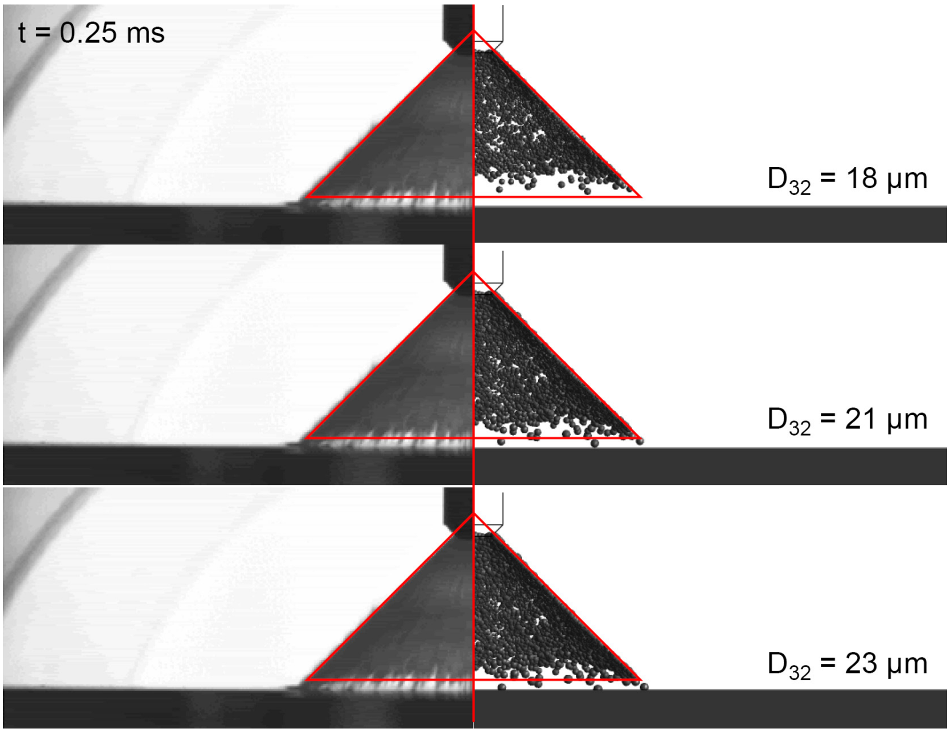

(b) $t = 0.25\,\mathrm{ms}$

Figure 2.9: Comparison of different drop size distributions for $v_{\mathrm{stat}} = 241\,\mathrm{m/s}$.

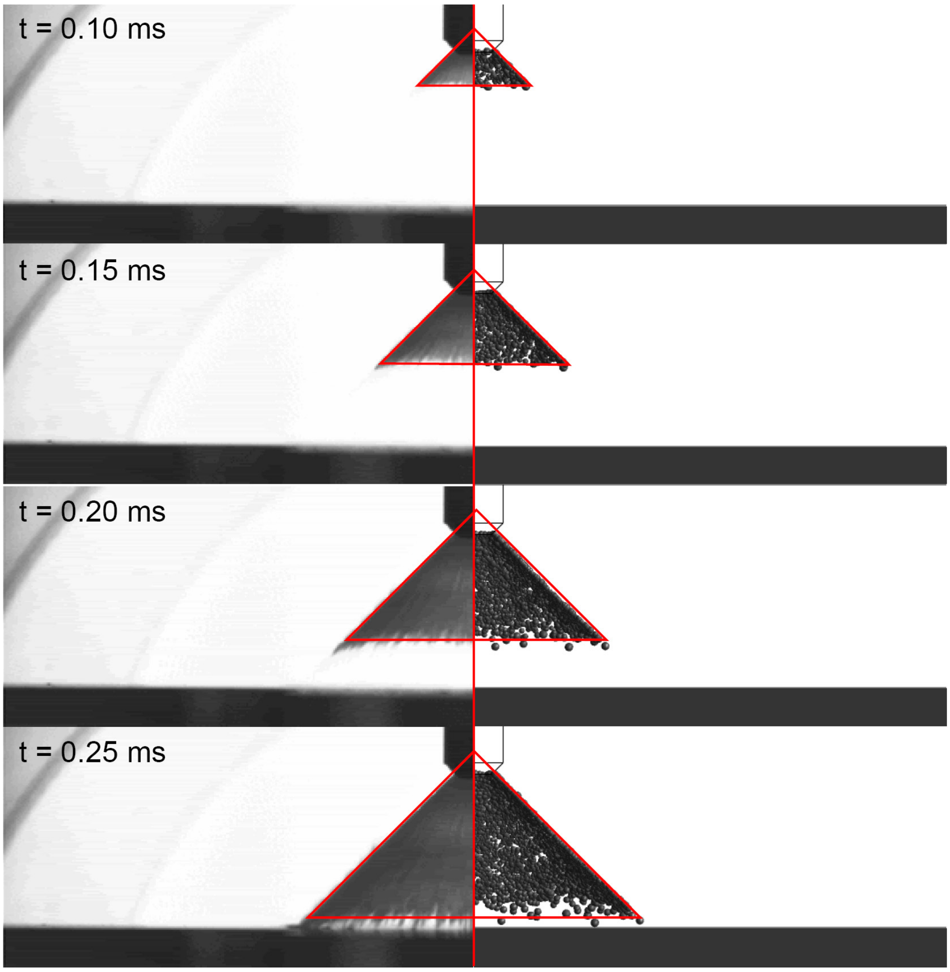

Figure 2.10: Spray propagation till wall impact. $v_{\mathrm{stat}} = 241\,\mathrm{m/s}$, $D_{32} = 21\,\mu\mathrm{m}$.

- The Lagrangian description by means of wall particles may be unfavourable compared to an Euler description for an additional implementation of wall film motion.
- Due to the stationary character of the wall parcels, liquid mass may add up in main impact regions and lead to unphysical values of the wall film thickness, defined simply as

  $$h_{\mathrm{film}} = \frac{m_{\mathrm{liquid}}}{A_{\mathrm{wall\ cell}} \cdot \rho_{\mathrm{liquid}}}\,, \tag{2.3}$$

  which furthermore depends on the mesh size. Liquid volume fractions in wall cells possibly exceed unity and large source terms, e.g. in case of evaporation, can arise.

  Liquid mass may also pile up in case of moving geometries: Assume a wall parcel on the liner in an engine geometry. If the piston moves upwards and crosses the parcel position, the latter is relocated on the nearest surface. Eventually, large amounts of liquid mass may be shifted to the top position of the liner or the edges of the piston and remain there without further distribution.
- As the film does not stop to accumulate and is not distributed, no steady state of spray impact can develop in simulations in contrast to reality. Any

simulation where parts of the impacting mass are put to wall particles has to be transient.

  - Apart from evaporation it is not possible to retrieve mass from wall particles.
  - No momentum can be transferred to or from wall parcels. However, modelling such a momentum transfer is not yet well understood in general.

- No information about other parcels is available in the wall interaction routines when they are called for an individual parcel. This would be very important to account for spray density and drop/drop interactions, for instance.
- An arbitrary deviation angle, i.e. $\Psi \in [0°, 360°[$, is not possible and the scattering plane must still equal the incident plane.

In spite of all these restrictions, the implementation of Elsässer's model - a declared goal of this thesis - has been made possible with the achievements performed. Several tests between results obtained in AVL Fire, where Elsässer's model had been originally implemented and used so far at BMW, and the results obtained in CFX have been carried out. For every regime and every possible outcome, single parcel properties have been quantitatively compared for verification.
Kuhnke's and Roisman's/Horvat's model have also been implemented.

2.3.2 Model comparison

To evaluate the capabilities of the three models with respect to the impact of a dense hollow cone spray, the respective numerical results are compared to transmitted-light images of the reference case. Figures are exemplarily presented at $t = 0.60\,\mathrm{ms}$ ($\approx 0.55\,\mathrm{ms}$ after start of injection) with the parcels shown as small spheres scaled with the mean drop diameter.
Since no measured data of drop size or velocity distributions are available, a quantitative comparison of the models is not considered for this reference case but postponed to Chapter 6.

Ideal reflection. Figure 2.11 demonstrates that the assumption of ideal reflection leads to completely wrong results, as expected. The normal velocity of secondary spray propagation is significantly overestimated.

Elsässer's model. As no wall film motion is implemented in CFX so far, the calculated wall film thickness h_{film}, see Equation 2.3, does not agree with the real value. Therefore, the simulation is carried out twice:

- once assuming a dry plate, i.e. with the film thickness set to zero in the calculation of the model outcome, $h_{\mathrm{film}} = 0$ and $\delta = h_{\mathrm{film}}/D_{\mathrm{prim}} = 0$ respectively.
- Secondly, using the transient value h_{film} calculated in CFX.

As shown in Figure 2.11, Elsässer's model provides better results than ideal reflection. The regime of cold wetting is addressed with the dominant outcome of splash and rarely spread. Rebound does not occur.

Secondary drops show considerably reduced diameters compared to the primary spray. They follow the air flow and curl with the vortex. The latter forms at the outside of the primary spray and moves along with the secondary spray in a rather tangential direction on the surface. In both cases the tangential spread of the secondary spray is predicted too slow in comparison to experimental data, which is not due to the mesh resolution as might be assumed, cf. the results for a finer mesh in Appendix A.1.
Table 2.3 gives a notion of the magnitude of the secondary drop properties compared to ideal reflection. The differences between a dry or wetted wall seem minor in contrast to the significant changes in Figure 2.11. Yet, the film thickness, if considered, is a transient value there and not a fixed one as in the table.

Model	h_{film} [μm]	D_{sec} [μm]	$v_{\text{abs,sec}}$ [m/s]	β [°]	Deposited mass [mg] at $t = 0.60\,\text{ms}$
Ideal reflection	–	21	115	45	0
Elsässer	0	8.2	44	–	3.8
Elsässer	30	11	48	–	15.4

Table 2.3: Results of Elsässer's model considering an impinging drop with $D_{\text{prim}} = 21\,\mu\text{m}$, $v_{\text{abs,prim}} = 115\,\text{m/s}$ and $\alpha = 45°$. The reflection angle is not presented for Elsässer's model because it depends on a random number. Note that the values for the deposited mass are the results of complete simulations of the reference case. In case of wetted wall the simulation is done with the transient value of h_{film} not with $h_{\text{film}} = 30\,\mu\text{m}$ fixed.

Kuhnke's model. This model interpolates between single and multiple drop correlations depending on the spray density on impact. The latter is characterised by the parameter κ and determined from a system of ellipses which is set up around the impingement center during the simulation run. The application is restricted to plane geometries. In the considered reference case, where the spray axis is perpendicular to the plate, the system of ellipses reduces to a system of concentric rings.
In Figure 2.12 the simulation results are compared to those where either pure single or pure multiple drop correlations are applied. It shows that the dense spray actually impacts in a single ring where the value of κ is smaller than unity thus leading to the usage of pure multiple droplet correlations.

The results presented in Figure 2.12 are obtained with h_{film} set to zero in the calculations due to the same reasons as in the application of Elsässer's model. A comparison to the outcome with the transient values of h_{film} is given in Figure 2.13.
Note that the actual value of h_{film} is only used to calculate regime distinctions for the single drop model in case of wetted wall, i.e. $K_{\text{crit},SD}$, as well as to determine the secondary to primary mass ratio in the splashing regime. Else Kuhnke's model only distinguishes the general state of dry and wetted. Therefore, the transient character of h_{film} is not as important as in Elsässer's model.
It can be stated that:

- $K > K_{\text{crit}}$ is fulfilled for almost all drops using either the single or the multiple drop model. Consequently, splash is the dominant outcome. Only very small and slow primary drops lead to adhesion or, in case of wetted wall, rarely to rebound ($T^* \approx 0.8 < T_{\text{crit}}$).

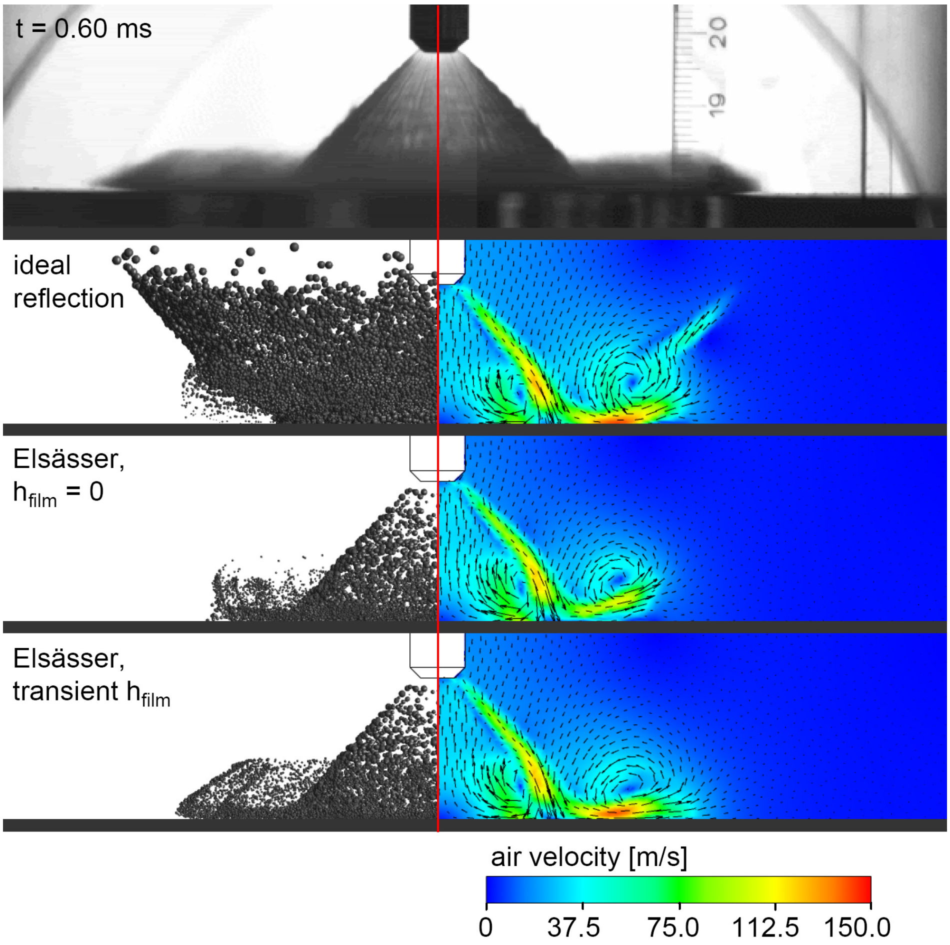

Figure 2.11: Comparison of the transmitted-light image at $t = 0.60$ ms with simulation results using ideal reflection and Elsässer's model.

- Considering an average impinging drop with $D_{\mathrm{prim}} = 21\,\mu\mathrm{m}$, $v_{\mathrm{abs,prim}} = 115\,\mathrm{m/s}$ and impact angle $\alpha = 45°$, Equations 1.80 and 1.81 result in the following secondary/primary ratios of the average diameters:

	$\left(\frac{D_{10,\mathrm{sec}}}{D_{10,\mathrm{prim}}}\right)_{SD}$	$\left(\frac{D_{10,\mathrm{sec}}}{D_{10,\mathrm{prim}}}\right)_{MD}$
dry wall, $\delta = 0$	0.017	0.5
wetted wall, δ as argument	0.13	1.0

  In combination with equal distribution widths the differences in these values are clearly reflected in Figure 2.13. Using the single drop model, secondary drop sizes become tiny, especially for a dry wall. In this case the sizes are in the range of the minimal limit in Kuhnke's model which is based on an energy consideration. In case of multiple drop correlations the mean size ratio is generally larger with a factor of two between the cases of dry and wetted wall, respectively.
  Table 2.4 gives a notion of the absolute magnitudes for the secondary drop sizes. The deposited mass is remarkably larger in case of single drop compared to multiple drop correlations and also to Elsässer's model, cf. Table 2.3.

- The dimension of the mean ejection angles according to Equations 1.87 and 1.88 is also listed in Table 2.4. For the multiple drop model the mean ejection angle

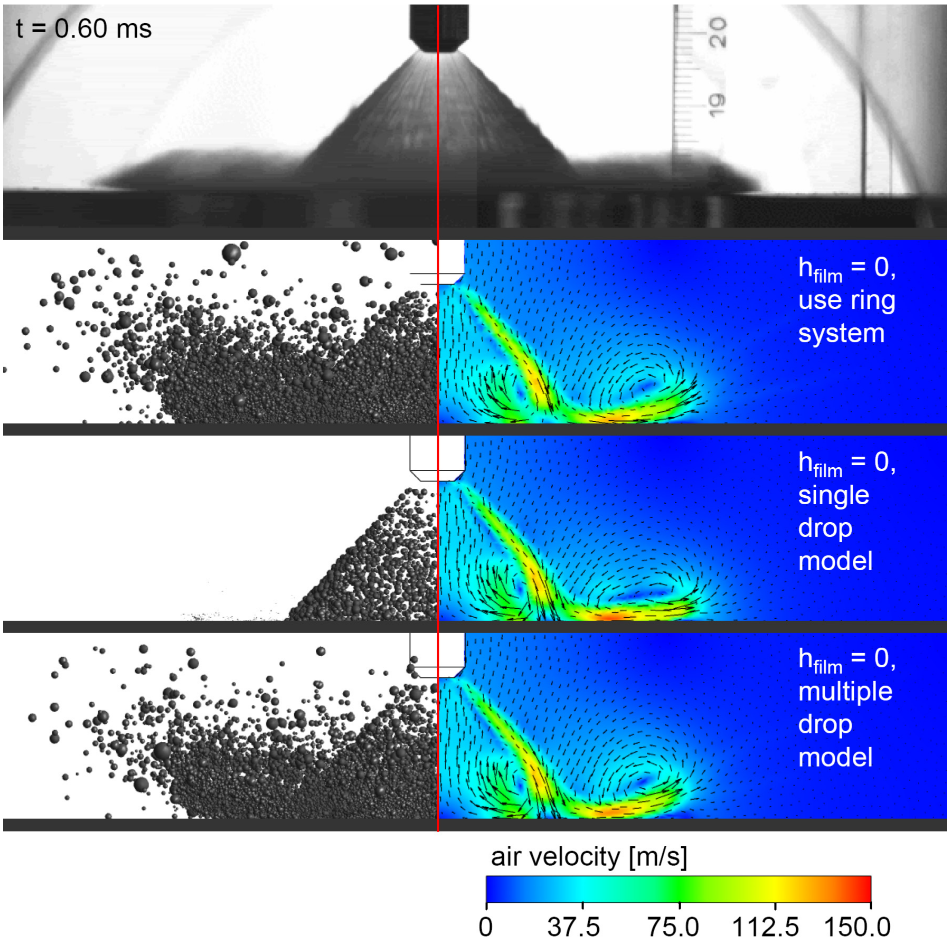

Figure 2.12: Comparison of the transmitted-light image at $t = 0.60$ ms with simulation results using Kuhnke's model with $h_{\text{film}} = 0$. Note that an application of the ring system requires the calculation of the whole cylinder, i.e. of 360°. The parcels may therefore appear more numerous in the associated side view than in the view of the single or multiple drop model results which are calculated for the usual half cylinder.

is defined as 1.5 times the value of the single drop model. Also the distribution is broader which results in a secondary spray largely dispersed.

- The secondary absolute velocity is determined in Kuhnke's model via the secondary Weber number, cf. Equation 1.84. The values for the single drop model seem rather large, yet, due to the small diameters the momentum of secondary drops is not that high. The momentum and the penetration velocity seem to be predicted rather well, see Figure 2.13.

Summarised, the results with the multiple drop model on a wetted wall seem to reproduce the transmitted-light images best. Yet, the local thickness of the secondary spray is too large, i.e. the distribution of ejection angles gives too large values. This also shows in a quantitative comparison to experimental values presented in Chapter 6.

To conclude, it is to be kept in mind that an arbitrary deviation angle Ψ is not possible in CFX yet. For ideal reflection and Elsässer's model this represents no restriction, yet Kuhnke's model (and also Roisman's/Horvat's model) in principle use a scattering in the whole range of 360°. The calculated value of Ψ in these models can only be used to

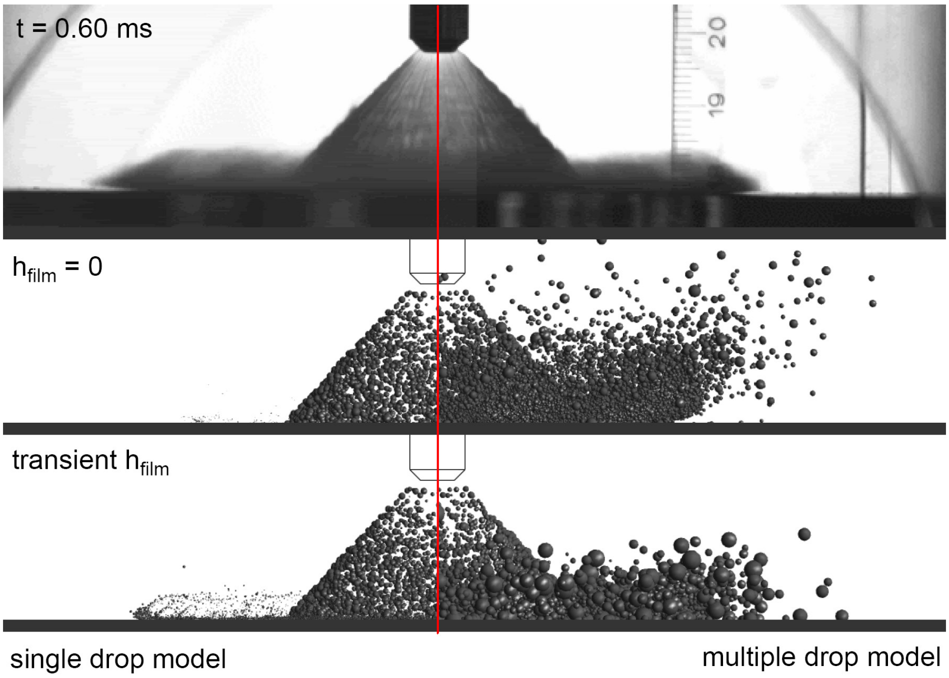

Figure 2.13: Comparison of the transmitted-light image at $t = 0.60\,\mathrm{ms}$ with simulation results using Kuhnke's model in different specifications.

decide if a child parcel is forward or backward scattered. This is actually advantageous for the models in their application to a hollow cone spray where Ψ is limited to 0° and 180°. This will be explained in more detail in Section 5.4 and Figure 5.14.

	h_{film} [μm]	D_{sec} [μm]	$v_{\mathrm{abs,sec}}$ [m/s]	β [°]	Deposited mass [mg] at $t = 0.60\,\mathrm{ms}$
Single drop correlations	0	0.36	84	21	20.7
	30	2.8	101	7.2	12.9
Multiple drop correlations	0	10.5	87	31	10.9
	30	21	37	11	8.4

Table 2.4: Outcomes of Kuhnke's model considering an impinging drop with $D_{\mathrm{prim}} = 21\,\mu\mathrm{m}$, $v_{\mathrm{abs,prim}} = 115\,\mathrm{m/s}$ and $\alpha = 45°$. The secondary mean properties are listed. SD denotes the single drop and MD the multiple drop correlations. The individual values are derived using random numbers. Note that the values for the deposited mass are the results of complete simulations of the reference case. In case of wetted wall the simulation is done with the transient value of h_{film} not with $h_{\mathrm{film}} = 30\,\mu\mathrm{m}$ fixed.

Roisman's/Horvat's model. This model is developed for the normal impact of a full cone spray. Although the spray axis is normal to the plate in the considered case, the impact of the cone-shaped shell occurs under an angle of ≈ 45° which consequently defines the impact angle. The applicability of the model in the reference case is therefore equivocal. Yet, the spray density eventually prevents it because the validity range of the secondary to primary mass ratio n_q, see Equation 1.99, is no longer met and becomes negative:
The impact area A_{impact} can be approximated as a ring of inner radius 20 mm (due to the spray angle of 90° and the distance of ≈ 20 mm between injector and plate) and 4 mm

width which is a rather large estimate. With a stationary mass flow rate of $\dot{m}_{\text{stat}} = 66.4\,\text{g/s}$, a mean impact velocity of $v_{10,\text{prim}} \approx 115\,\text{m/s}$ and $\rho_{\text{C}_7\text{H}_{16},20^\circ} \approx 685\,\text{kg/m}^3$, this leads to

$$\Gamma_V \propto 0.0011 - \frac{\dot{m}_{\text{stat}}}{\rho \cdot A_{\text{impact}} \cdot v_{10,\text{prim}}} \approx 0.0011 - 0.0015 < 0\,.$$

2.3.2.1 Summary

Although only transmitted-light images are available for the considered reference case and a quantitative comparison of drop properties such as diameters or velocity components is not possible, it becomes obvious that Elsässer's, Kuhnke's and Roisman's/ Horvat's model fail to describe the impact of a dense hollow cone spray. To the author's knowledge no other model adapted to this spray type and leading to satisfactory results exists either.

Therefore, further work both experimental and theoretical is necessary and presented in the following chapters of this thesis.

Chapter 3

Experimental methods

The previous chapters showed that modelling of spray/wall interaction is still in its infancy particularly for dense and high-pressure hollow cone sprays. Quantitative experimental data are first of all required to improve the understanding of the phenomena. To characterise spray/wall interaction in numerical simulations, diameters, wall-normal and wall-tangential velocity components and either masses or numbers of secondary relative to primary drops have to be known. Phase Doppler Anemometry is a suitable measurement technique to provide these experimentally. The setup considered is sketched in Figure 3.1. For better illustration the experimental peripherals like supply systems are omitted, see Appendix B.1 for further details.
As discussed in Section 1.2, the number of parameters influencing spray/wall interaction is enormous and any experiment has to focus on a small selection. In this case the following are chosen:

- the wall temperature T_{wall}, which is assumed very important under engine conditions.
- The adjustment of the injector relative to the target, hence a variation of impacting drop sizes and velocities. This can be expressed as a variation in Weber or Reynolds numbers for instance. The impact direction is approximately normal to the surface.
- The surface coverage. The target is considered dry or covered by an oil film with varying thickness. The influences on post-impingement spray and wall film are important with respect to the oil film on a cylinder liner to lubricate the piston motion.

All measurements are done at atmospheric conditions, i.e. $p_{\text{ambient}} \approx 1\,\text{bar}$ and $T_{\text{ambient}} \approx 20°\text{C}$.

3.1 Phase Doppler measurement technique

Laser Doppler Anemometry (LDA) and Phase Doppler Anemometry (PDA) are established non-intrusive techniques to study sprays of a transparent liquid. Velocity distributions, and in case of PDA also drop size distributions, are obtained with a very high spatial and temporal resolution.

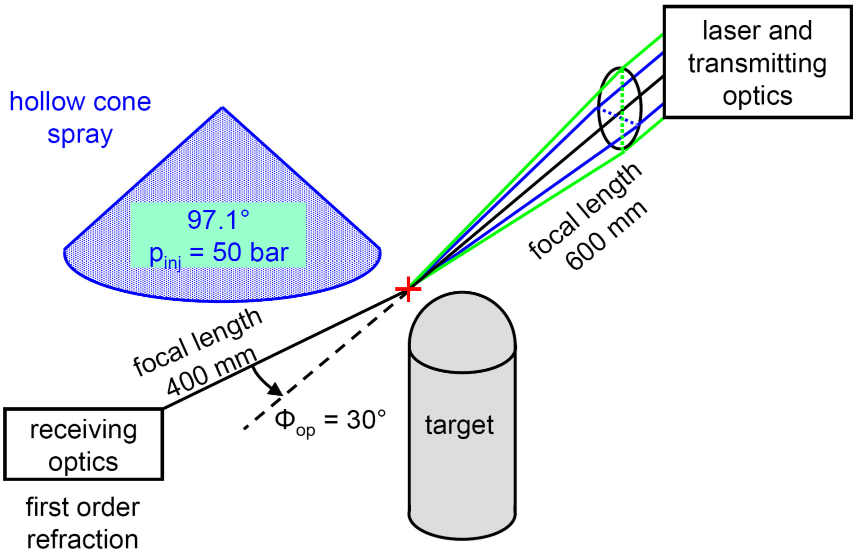

Figure 3.1: Sketch of the experimental setup.

3.1.1 Basics of Phase Doppler Anemometry

If a wave of frequency f_0 is emitted by a moving transmitter, a stationary receiver detects the wave with a frequency shift. The same is the case if the receiver moves and detects a wave from a stationary transmitter. These phenomena describe the Doppler effect which is the basic principle used in LDA and PDA and invoked twice: Monochromatic laser light is first detected by a particle which acts as a moving receiver. Then, the latter is a moving transmitter and the scattered light is received by a detector, see Figure 3.2(a). The detected frequency amounts to:

$$f_r = f_b \cdot \frac{1 - \frac{\vec{e}_b \cdot \vec{v}_p}{c}}{1 - \frac{\vec{e}_{pr} \cdot \vec{v}_p}{c}} \approx f_b \cdot \left(1 + \frac{\vec{v}_p \cdot (\vec{e}_{pr} - \vec{e}_b)}{c}\right) \qquad \text{if } v_p \equiv |\vec{v}_p| << c\,. \tag{3.1}$$

Subscripts b, r and p denote the original beam, the receiver and the particle respectively. c represents the speed of light in the medium.
The Doppler shift is proportional to the velocity of the particle. It shows an order of 1 . . . 100 MHz for typical flow systems, which is very small compared to the frequency of laser light with a size of $\approx 10^8$ MHz. Hence, it is difficult to measure.

To cope with this problem, two laser beams are used. Several possible setups are known, see [2], [20]. The following description is restricted to the so-called dual-incident beam configuration, which is used in the experiment, see Figure 3.2(b). The frequency difference between the detected frequencies in this case,

$$f_1 \approx f_b \cdot \left(1 + \frac{\vec{v}_p \cdot (\vec{e}_{pr} - \vec{e}_1)}{c}\right) \text{ and } f_2 \approx f_b \cdot \left(1 + \frac{\vec{v}_p \cdot (\vec{e}_{pr} - \vec{e}_2)}{c}\right)\,, \tag{3.2}$$

can be easily measured:

$$f_D = f_2 - f_1 \approx f_b \cdot \frac{\vec{v}_p \cdot (\vec{e}_1 - \vec{e}_2)}{c} = \frac{2 \cdot \sin(\Theta_{op}/2)}{\lambda_b} \cdot v_p \cdot \cos\alpha_p\,. \tag{3.3}$$

It is linearly proportional to the velocity component normal to the mean of both beam directions, $v_p \cdot \cos\alpha_p$. In case of the dual-incident beam configuration, it is also independent of the detector position.

The measurement principle can also be explained by the so-called "fringe model". The laser beams interfere in the measurement volume[1] where the fringe spacing of the resulting intensity pattern is given as $\frac{\lambda_b}{2 \cdot \sin(\Theta_{\mathrm{op}}/2)}$. Particles which pass through the measurement volume sample these fringes. However, this illustrative description is only valid for small particles (diameter $D_p << \lambda_b$) where the local intensity is approximately constant over its diameter. For large particles it is more complicated.

From Equation 3.3 the directional information, i.e. the sign of the measured velocity component, can obviously not be retrieved. In order to obtain it, one of the two laser beams is shifted by a frequency $\mathrm{f}_{\mathrm{shift}}$, usually with a Bragg cell. In the fringe picture, this corresponds to a movement of the interference fringes and leads to a received frequency of $\approx f_{\mathrm{shift}} \pm f_D = f_{\mathrm{shift}} \pm \frac{2 \cdot \sin(\Theta_{\mathrm{op}}/2)}{\lambda_b} \cdot v_p \cdot \cos \alpha_p$. A particle moving with (against) the fringes then results in a lower (higher) frequency.

In addition to the velocity components of a particle, the PDA measurement technique is also able to determine its diameter, for which at least two detectors are necessary. For not too small particles, i.e. when the glare points of the interfering laser beams do not merge, see Figure 3.2(c), the path lengths of both beams to both detectors differ and depend on the particle diameter. It can be shown, see [2], that the phase difference is linearly proportional to the diameter:

$$\Delta\phi_{1-2} \propto D_p \,. \tag{3.4}$$

If reflection is considered, $\Delta\phi_{1-2}$ depends only on the particle shape. If refraction is regarded, it depends also on the refractive index n_{refr}. The detectors must be adjusted such that one scattering order clearly dominates.

In a common setup, see Figure 3.2(d), the angle between the incident plane (spanned by both incident beams - the measured velocity component lies there) and the plane spanned by both detectors and the measurement volume is called off-axis angle Φ_{op}. Both detectors are usually placed symmetrically to a plane normal to the incident plane with the elevation angles $\pm\Psi_{\mathrm{op}}$.

The principle measurement technique has been presented for one measured velocity component so far. Up to three components can be measured by using three different beam pairs lying in perpendicular planes. Comparing the diameter information from several detector pairs allows then also a sphericity check on the detected particles.

3.1.2 Experimental setup

A dual PDA system instrument from Dantec Dynamics is used (BSA 2.12.05) in the measurements where first order scattering is observed under an off-axis angle of $\Phi_{\mathrm{op}} = 30^\circ$, see Figure 3.1. The focal length of the transmitting and receiving optics is 600 mm and 400 mm respectively. The latter are fitted with a mask of type A. Applying a water-cooled Ar-Kr-laser, the wavelenghts $\lambda_{\mathrm{green}} = 514.5\,\mathrm{nm}$ and $\lambda_{\mathrm{blue}} = 488\,\mathrm{nm}$ are used to determine the perpendicular velocity components $U1$ and $V1$ shown in Figure 3.3. They lie in the measurement plane which is spanned by the target and the injector axes.

---

[1] The finite expansion of the measurement and detection volumes, particularly with respect to measurements of spray/wall interaction, are discussed in more detail in Section 4.4.1.2 and Appendix B.6.

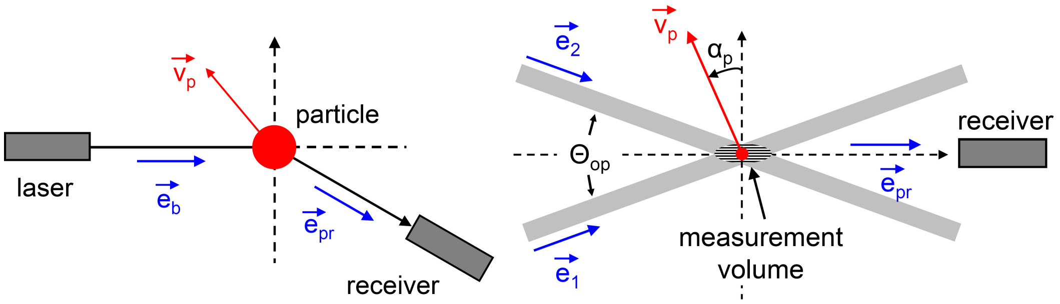

(a) Definitions to describe the Doppler effect.

(b) Dual incident-beam configuration.

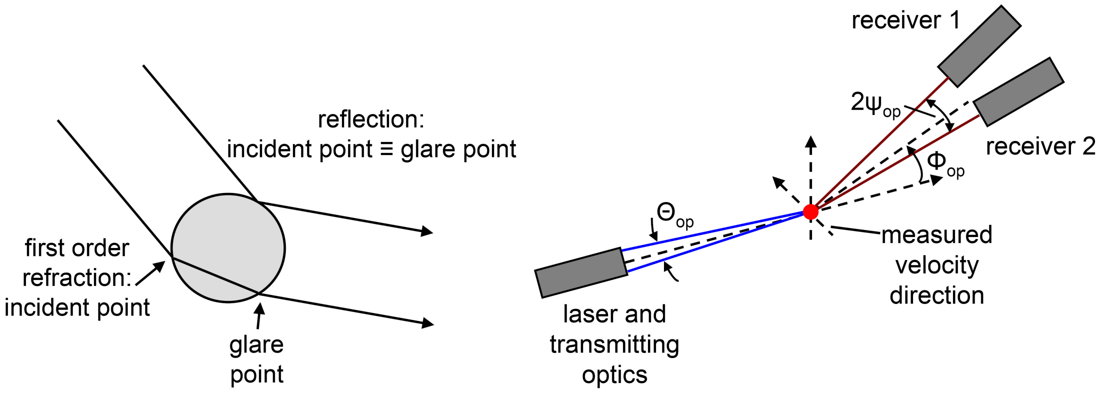

(c) Reflection and first order refraction for a particle.

(d) Definition of angles in the PDA setup.

Figure 3.2: Principles and setup of Phase Doppler Anemometry.

The third orthogonal velocity component is assumed to be zero due to the rotational symmetry of the spray.

Adapted to the two-dimensional problem the grids of measurement points[2] are positioned solely in the measurement plane, cf. Figure 3.4. On the one hand, the distance d_i of a measurement point to the target surface should not be too large as near-wall flow influences drop velocities. Moreover, in case of a hot wall, evaporation may change drop masses and diameters significantly. On the other hand, d_i must not be too small to capture all secondary drops and mainly to avoid any interference with the forming wall film where crowns and ligaments develop. Reference [31] recommends a distance of at least 1 mm-1.5 mm and in the current work 2 mm are chosen as the minimal value of d_i for an initially dry target surface. In case of an oil covered target, see below, the minimal distance is increased to 3 mm. Measurement points at different distances d_i to the target are treated separately in the evaluation. The influence of near-wall flow can hence be studied, see Appendix B.5.5.

Note that the considered setup provides two velocity components and the diameter for the counted drops. However, it is not possible to determine the oil fraction of the secondary drop liquid in case of an applied oil film which is rather complicated to achieve. A first attempt has been done by [64] who studies the impact of single water drops on a shear stress driven water film. To measure the fraction of film fluid in the

---

[2] Considering the measurement grids the small measurement volumes are denoted as measurement points in the following.

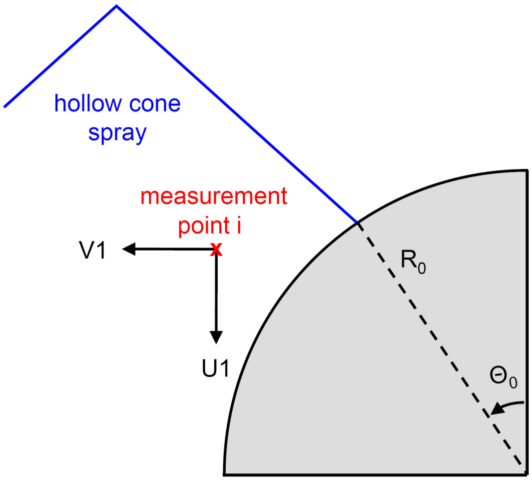

Figure 3.3: Measured velocity components $U1$ and $V1$.

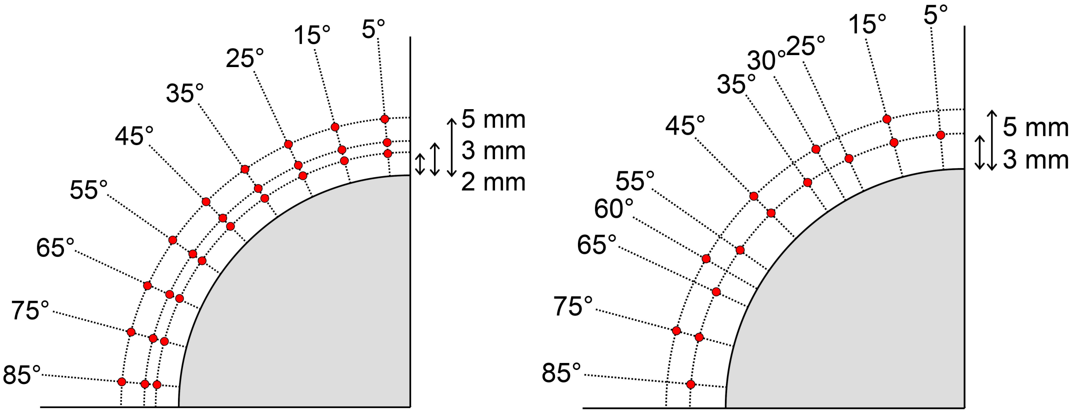

(a) Dry target.

(b) Oil covered target.

Figure 3.4: Measurement grids.

secondary drops, sodium chloride is added to the drop liquid but not to the film liquid. Concentrations are then determined in the secondary drop fluid and in the effluent film in an integral way, i.e. summed up over several drop impacts.
Using an appropriate tracer material, fluorescence measurements could also be thought of but quantitative measurements seem very difficult.

3.2 Injected spray

The dense hollow cone spray of a piezo-electric, outward opening injector is considered in the experiment, see Section 1.2. Instead of a multi-component fuel, isooctane C_8H_{18} at $\approx 25°\mathrm{C}$ is used (quality: for synthesis, min. 99.5%, water max. 0.1%), see Table 3.1. The impacting drop diameters and velocities have an order of $D_p \sim 50\,\mu\mathrm{m}$ and $v_p \sim 35\,\mathrm{m/s}$ respectively.

The applied injection parameters are described in Table 3.2. The injection duration Δt_i and the time interval Δt_{si} between successive, discrete injections, measured from injection start to injection start, are adjustable. In order to obtain good statistics,

Density ρ	695.68	kg/m^3
Refractive index n_{ref}	1.39	-
Specific heat capacity c$_P$	2.20	kJ/(kg·K)
Dynamic viscosity μ	4.46e-4	kg/(m·s)
Thermal conductivity λ	0.123	W/(m·K)
Surface tension σ	20.18e-3	N/m
Heat of vaporization Δh_{vap}	349	kJ/kg

Table 3.1: Material properties of liquid isooctane at 25°C and 1 bar, cf. [75].

Spray liquid	C_8H_{18} (isooctane)
Injection pressure p_{inj}	50 bar
Stationary mass flux (injector ring gap $\sim 30\,\mu$m)	19.4 g/s
Cone angle (determined by Mie scattering images)	97.1°

Table 3.2: Injection parameters applied in the experiment.

samples from several injections must be gathered. At the same time, Δt_{si} must be chosen large enough to ensure that the state of the target surface is restored after the precedent injection. In case of an oil covered, cold target this means $\Delta t_{si} > 30$ s. Hence, to collect sufficient data in a yet acceptable total measurement time, $\Delta t_i = 50$ ms is set although this value is larger than in an usual engine cycle where $\Delta t_i \sim 0.4$ ms - 5 ms.

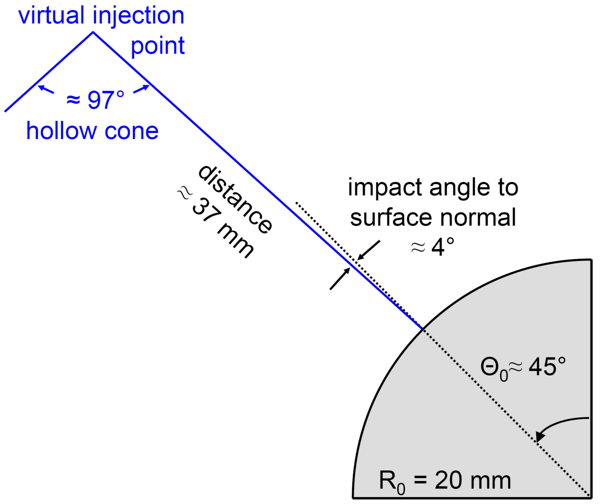

Figure 3.5: Adjustment of the injector relative to the target.

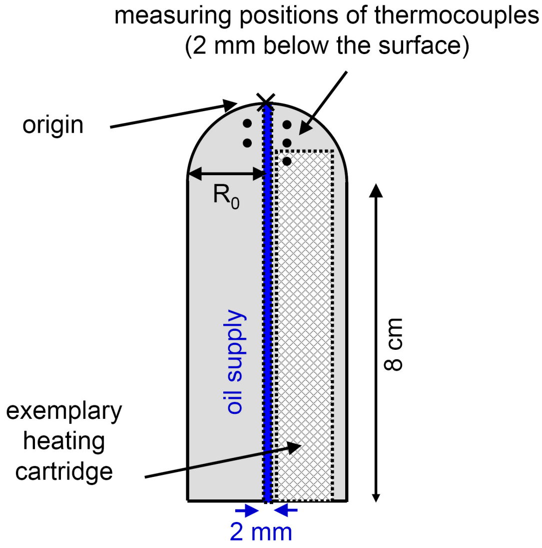

Figure 3.6: Target design.

The injector is adjusted at two different positions relative to the target with an estimated accuracy of manual adjustment of ±1 mm. Besides the alignment shown in Figure 3.5, a similar position with a distance of ≈ 21 mm between target and nozzle is considered. This causes slightly different impacting drop sizes and increased impact velocities, hence a variation in Weber and Reynolds numbers. The main impact is to occur at $\Theta_0 \approx 45°$. However, due to adjustment errors and the influence of the gaseous flow, the actual position may vary and has to be determined from data, cf. the next chapter.

3.3 Target design and oil film

To study spray/wall interaction the measurement positions should be located near the surface. At the same time two perpendicular velocity components are to be measured, each requiring the intersection of two laser beams. Hence, a target design in form of a hemisphere is advantageous, see Figure 3.6. Its radius is chosen as $R_0 = 2\,\mathrm{cm}$ and it resides on top of a cylinder with the same radius and 8 cm height. The polished surface of the copper target shows an average and peak-to-peak roughness value of $R_a \approx 0.297\,\mu\mathrm{m}$ and $R_z \approx 3.029\,\mu\mathrm{m}$ respectively.

Heating. Three heating cartridges of altogether 3 000 W, which are mounted inside the target, can heat the latter to very high temperatures T_{wall}. This value is measured at five different positions 2 mm below the surface by thermocouples. The range of the target temperature covered in the experiment amounts to:

$$T_{\mathrm{wall}} = \begin{cases} 25°\mathrm{C} - 200°\mathrm{C} & \text{(dry target)}\,, \\ 25°\mathrm{C} - 150°\mathrm{C} & \text{(oil covered target)}\,. \end{cases}$$

To account for spray cooling, data recording is started only after several spray injections when an approximately constant wall temperature is reached.
In preparation work the thermal expansion of the target has been studied by image subtraction and evaluation using customised Matlab routines, see Appendix B.2: Whereas the target radius R_0 does not change remarkably, the vertical expansion cannot be neglected. To prevent adjustment errors due to thermal expansion, the origin is readjusted at each new value of T_{wall} since all measurement positions and coordinates are adjusted relative to the target apex.

Oil film. Through a small tube of 2 mm diameter which opens up at the target apex a film fluid can be applied onto the surface, see Figure 3.7. The film of constant volume flux $\dot{Q}$ is driven solely by gravity. Under ideal conditions the resulting film thickness can be calculated as follows, cf. Appendix B.3.1:

$$h_{\mathrm{film}} = \left(\frac{3}{2 \cdot \pi \cdot R_0 \cdot g} \cdot \frac{\mu}{\rho} \cdot \frac{\dot{Q}}{(\sin\Theta)^2} \right)^{1/3} \quad , \ \Theta > 0\,. \tag{3.5}$$

Θ denotes the azimuthal position on the target and g the absolute value of gravity. The first factor on the right-hand side of the equation can be assumed constant due to the radial thermal expansion being negligible. The second equals the kinematic viscosity of the film fluid and is thus material dependent. The third factor contains the dependence on the position Θ and the volume flux $\dot{Q}$. As expected, the film becomes thinner the larger Θ and the smaller $\dot{Q}$.
An engine oil (Castrol VP1-0091-39-01, SAE 0W-30) is chosen as film liquid. Its kinematic viscosity is strongly temperature dependent with $\nu_{\mathrm{oil}}(20°\mathrm{C}) \approx 13.5 \cdot 10^{-5}\,\mathrm{m}^2/\mathrm{s}$ and $\nu_{\mathrm{oil}}(150°\mathrm{C}) \approx 0.43 \cdot 10^{-5}\,\mathrm{m}^2/\mathrm{s}$, see Figure 3.8. The film temperature is assumed to equal T_{wall}.
Two different pump settings and hence volume fluxes $\dot{Q}$ have been considered. As their value could not be measured reliably, image evaluation has been done analogously to the evaluation of thermal expansion, see Appendix B.3.2. The values $\dot{Q}_1 \approx 0.92\,\mathrm{ml/min}$

and $\dot{Q}_2 \approx 0.44\,\mathrm{ml/min}$ result.
In summary, the considered range of the oil film thickness at $\Theta = 45°$, the expected main impact region, reaches from $h_{\mathrm{film}}(\dot{Q}_2, 150°\mathrm{C}) \approx 54\,\mu\mathrm{m}$ up to $h_{\mathrm{film}}(\dot{Q}_1, 20°\mathrm{C}) \approx 216\,\mu\mathrm{m}$. Incoming droplets of $D_p \sim 50\,\mu\mathrm{m}$ diameter impact on relative film thicknesses[3] of $\delta = h_{\mathrm{film}}/D_p \sim 1-4$. The studied values h_{film} are clearly larger than those existing on the liner in an engine with a thickness of $\sim 5\,\mu\mathrm{m}$. However, smaller volume fluxes were not possible with the pump used and for a cold surface it is no longer possible to realise a stable and continuous film surface due to surface tension either.

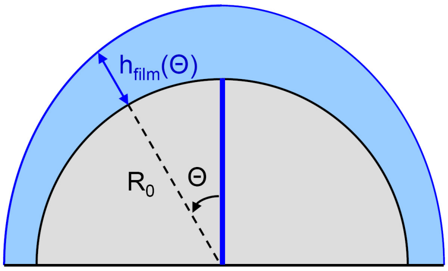

Figure 3.7: Undisturbed film on the target under ideal conditions.

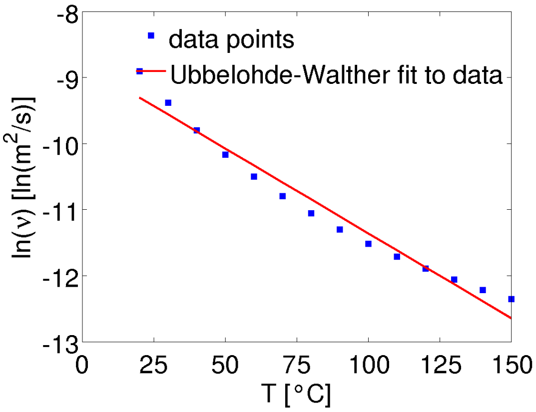

Figure 3.8: Kinematic viscosity of the used engine oil versus temperature.

---

[3] For single drops film thicknesses are often classified in several regimes. In [16], for instance, conditions of deep pool with $\delta >> 3$, of thick film with $3 > \delta > 1$, of thin film with $1 > \delta > 0.1$ and of very thin film with $\delta < 0.1$ are distinguished. Reference [39] separates only between shallow pool with $\delta < 0.5$, where roughness is still important, and deep pool with $\delta > 1.5$, where the solid wall no longer influences the impact.

Chapter 4

Data analysis

In the past, PDA data have been mainly used to characterise free sprays. Considering spray/wall interaction they have been primarily applied to validate numerical models. In both cases, experimental data and model outcome can be compared directly at the positions of the small measurement volumes. This is no longer possible for the *development* of a numerical model concerning spray/wall interaction where experimental information must be extrapolated onto the surface. The latter has only rarely been in the focus and the evaluation offered directly by the software of the PDA instrument is not suitable. A thorough treatment of the question how PDA data should be evaluated in this case still lacks.

The present chapter deals with such principle issues step by step and is supposed to give general guidelines. If not explicitly pointed out otherwise, the arbitrarily chosen measurement of Table 4.1 is used to illustrate the evaluation procedure. The latter is done by scripts written in Matlab 7.4.0 (R2007a).

Injection duration:	$\Delta t_i = 0.05\,\text{s}$,
Interval between subsequent injections:	$\Delta t_{si} = 4\,\text{s}$,
Target state:	dry, $T_{\text{wall}} = 100°\text{C}$,
Injector position	see Section 3.2 (normal impact, $\Theta_0 \approx 45°$),
Measurement grid:	see Figure 3.4(a) (measurement volumes with different distances d_i to the surface are considered separately).

Table 4.1: Exemplary measurement to illustrate the evaluation procedure.

4.1 Data of a single measurement volume

4.1.1 Raw PDA data and coordinate definitions

Each measurement (parameter setting) comprises several measurement points[1] MP_i, see Figure 3.4. Their coordinates (d_i,Θ_i) are defined with respect to the center of the target hemisphere. d_i signifies the distance to the surface and Θ_i the azimuthal angle, cf. Figure 4.1(a).

---

[1] Due to the small expansion of the measurement volumes these are often referred to as measurement points in the following, see Section 3.1.1.

For every MP_i the signal processor of the PDA instrument returns the following raw data for a detected drop:

- PDA status, i.e. if the drop is validated or not.
- Arrival time AT in the measurement volume.
- Transit time TT through the measurement volume.
- Velocity components $U1$ and $V1$, see Figure 4.1(b).
- Drop diameter D (the subscript p is omitted from now on).
- Phase differences for each detector pair, $U1_{1-2}$ and $V1_{1-2}$, which are used by the processor to calculate the diameter.

All exported raw drop data are validated in both velocity components $U1$ and $V1$ but not necessarily in the diameter D. Further evaluation concerns only the drops validated also in D. Yet, the non-validated data are necessary to calculate correction factors, see Section 4.4.2. Moreover, they will be shown in phase plots to judge data quality.

Data of a single measurement point are composed of several discrete injections. The number of the latter depends on data and validation rate which differ with the position of the considered MP_i. Data collection is stopped, if a user-defined number of validated samples has been collected or if a maximal time limit is reached. These criteria should be chosen adapted to the experiment, see Section 4.1.2.

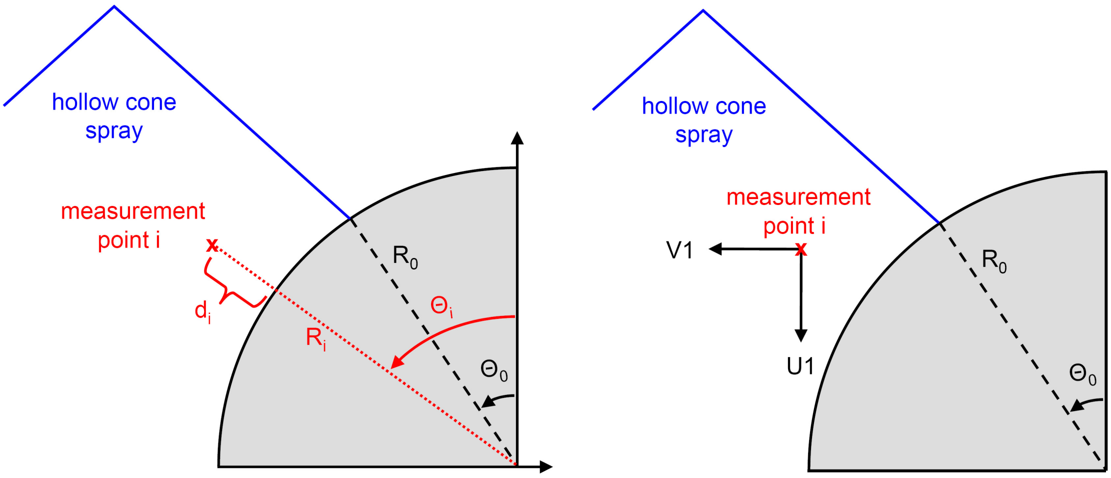

(a) Coordinates (d_i,Θ_i) of an arbitrary measurement point i.

(b) Measured velocity components U_1, V_1.

Figure 4.1: Definition of coordinates and velocity components. d_i is not drawn to scale.

4.1.2 First evaluation steps

The measured velocity components $U1$ and $V1$, see Figure 4.1(b), are not adapted to the treatment of spray/wall interactions. On a plane target geometry it is easy

to measure directly wall-normal and wall-tangential velocity components, $U2$ and $V2$. Yet, the values d_i have to be chosen larger than on the hemispherical target considered, cf. Section 3.1. For the latter and for an arbitrarily curved target in general a rotation and adjustment of the optics would be required for every measurement point anew to get $U2$ and $V2$ directly. This would be very error-prone. Therefore, the optics are fixed instead and data evaluation is to provide the velocity transformation from $U1$, $V1$ to $U2$, $V2$. The procedure is discussed in detail in the subsequent section. At this point, only the central impact area is studied and data from the measurement point at ($d_i = 2\,\text{mm}$, $\Theta_i = 45°$), part of the exemplary measurement, see Table 4.1, are used to present first evaluation steps for a single measurement point.
The coordinate system defining $U2$ and $V2$ is set up as shown in Figure 4.2(a). The value of the mean impact position Θ_0 is deduced from the injector-target alignment and the known spray cone angle. Drops with $U2 < 0$ are declared as primary, those with $U2 \geq 0$ as secondary drops, see Figure 4.2(b).
To consider impact and reflection angles, the angle between velocity vector and wall, $\Phi_{\text{vel}} \in [0°, 180°]$, is defined as explained in Figure 4.3.

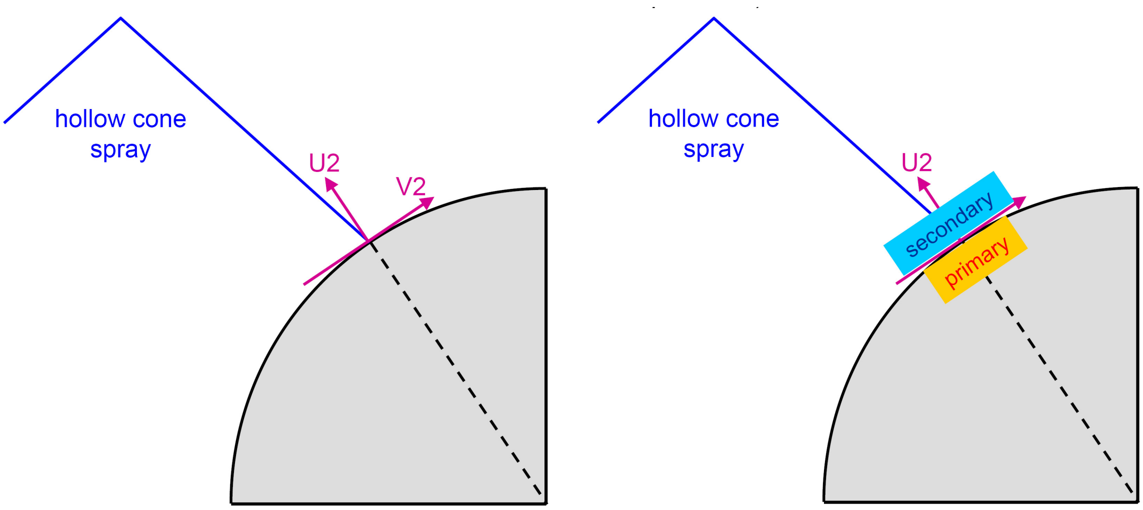

(a) Definition of $U2$ and $V2$.

(b) Distinction between primary and secondary drops.

Figure 4.2: Adapted velocity components $U2$ and $V2$ for the exemplary measurement point.

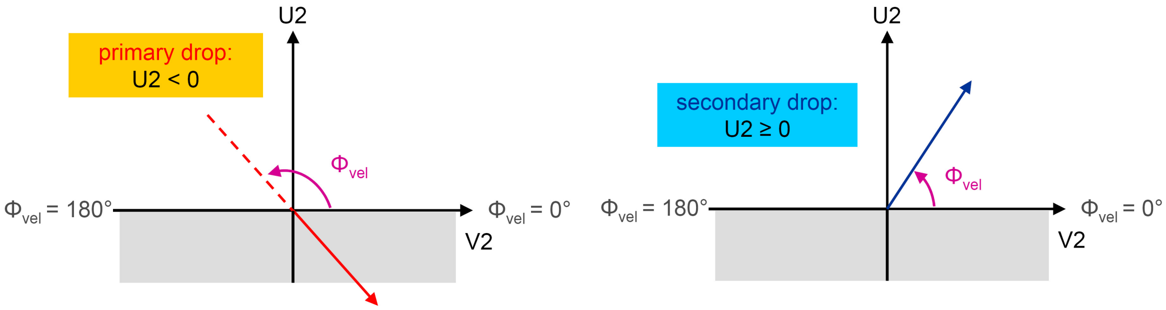

(a) Definition of Φ_{vel} for a primary drop.

(b) Definition of Φ_{vel} for a secondary drop.

Figure 4.3: Defintion of impact and reflection angles.

Data plots. Some basic plots ($V2$-$U2$, $U2$-D, $V2$-D, AT-D, D-TT, phase plot etc.) are done for a first check of the measured data:

- Misfires in the injections can be excluded as shown in Figure 4.4 because data recording has taken place in regular intervals Δt_{si} without interruptions.
- The distribution of the signs of $U2$ and $V2$ is reasonable. The exemplary measurement point lies approximately in the central impact region and the impact is almost normal. Therefore, mainly primary drops (negative $U2$) with small $V2$, distributed around zero, are expected. This is well confirmed, see Figure 4.5.
- The phase plot, cf. Figure 4.6, shows the majority of drops inside the validation band which excludes basic errors in the PDA setup and adjustment. The validation band defines the tolerance band of the phase difference, i.e. of the measured drop size, between detectors. Its width is set to 30% of the drop size range.

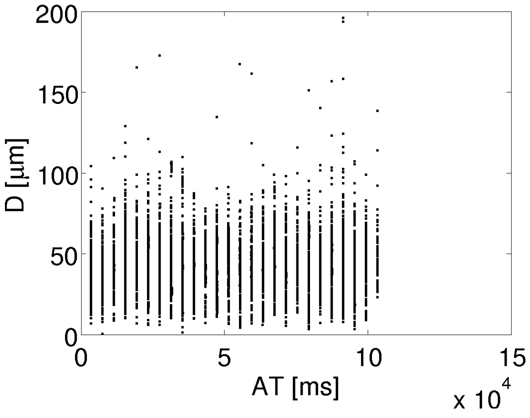

Figure 4.4: D versus AT at ($d_i = 2\,\text{mm}$, $\Theta_i = 45°$).

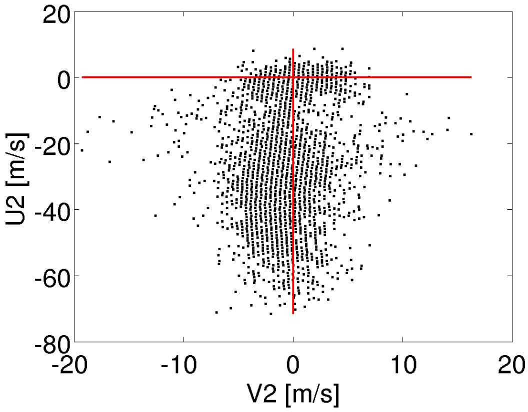

Figure 4.5: $U2$ versus $V2$ at ($d_i = 2\,\text{mm}$, $\Theta_i = 45°$).

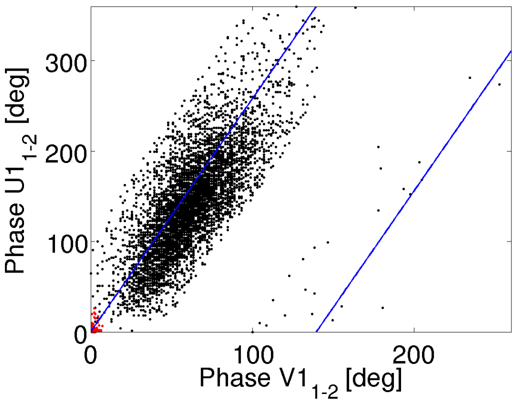

Figure 4.6: Phase plot at ($d_i = 2\,\text{mm}$, $\Theta_i = 45°$). Drops which are not validated in D are (exceptionally) also included and plotted in red.

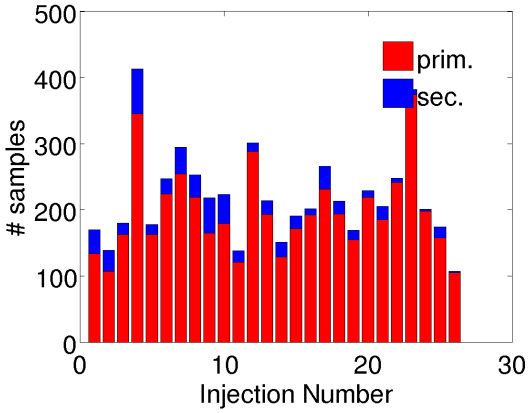

Figure 4.7: Validated sample number for separated injections at ($d_i = 2\,\text{mm}$, $\Theta_i = 45°$).

Considering single injections. Using the arrival time information AT and the fact that $\Delta t_{si} >> \Delta t_i$, data can be separated into single injections:

- The sample numbers per injection (divided in primary and secondary drops) are checked for strong fluctuations between injections, see Figure 4.7. If that had been the case, the measurement setup would have had to be revised.
- The few drops whose relative arrival time is very large, $AT_{\text{rel}} > 2 \cdot \text{t}_i$ (where the first drop of an injection sets the respective timer to zero), are filtered out as no direct correlation to the injection exists any longer.

Accumulating injections. In order to judge if enough drops are collected for reliable statistics, the single injections and thus the number of collected samples are then accumulated one by one. After every addition, arithmetic mean values of $U2$, $V2$ and D are calculated together with the standard deviations of the single values and those of the means. Presuming statistical independence of the samples, the standard deviation of the mean X_{10} of a quantity X is found as:

$$\sigma_{X_{10}} = \frac{\sigma_X}{\sqrt{N}}\,, \tag{4.1}$$

where σ_X is the standard deviation of a single value and N the sample number. The relative errors are then given as

$$\epsilon_{\text{rel}} = \frac{\sigma_{X_{10}}}{X_{10}}\,. \tag{4.2}$$

If the mean values stop to change significantly with increasing number of collected drops and if the errors reach reasonably small values compared to the overall error from adjustment, statistics are assumed well enough. Primary and secondary drops should be distinguished in the consideration. Looking at both types summed up, like done in [31] for example, does not cope with the situation.

In preparation work of the measurements considered in this work, the described method has been applied to determine that data collection at a measurement point is stopped when 12 000 validated samples have been recorded or when 400 s of measurement time have passed. Figure 4.8 presents the results for the exemplary measurement point. It is clear that at a position where primary (secondary) drops are predominant due to the impact situation, statistics are quite bad for secondary (primary) ones. This problem is weakened because data of a single measurement point will not be considered in isolation in later evaluation, but data of several measurement points will be combined. This leads to good statistics for both drop modes applying the assigned stopping criteria.

All data of one measurement point. Finally, data of all injections measured at the considered MP$_i$ are studied together again and are used to answer the following questions:

- Do the measured drops originate only from the beginning or closing interval of the injector? Or are they measured evenly distributed over the whole needle lift?
- Do the drops which originate from the beginning or closing interval of the injector have remarkably large or small diameters compared to those drops which are injected during stationary needle lift?

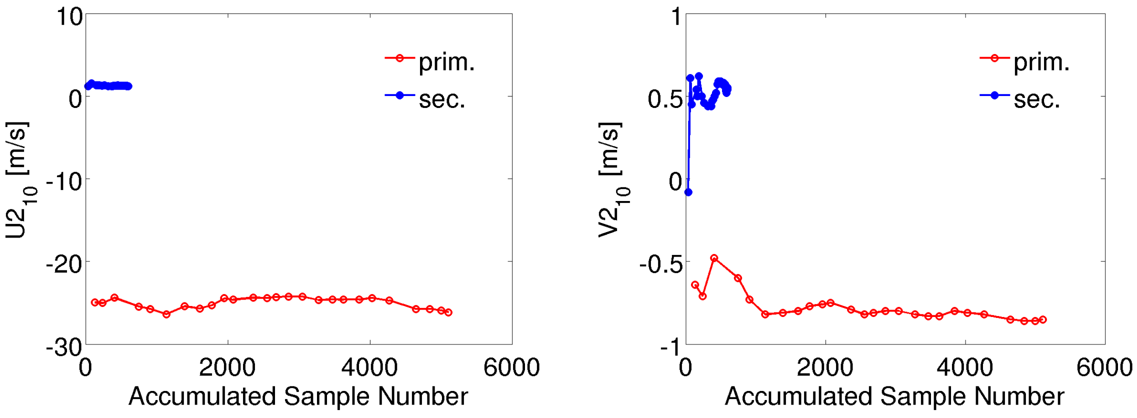

(a) $U2_{10}$. (b) $V2_{10}$.

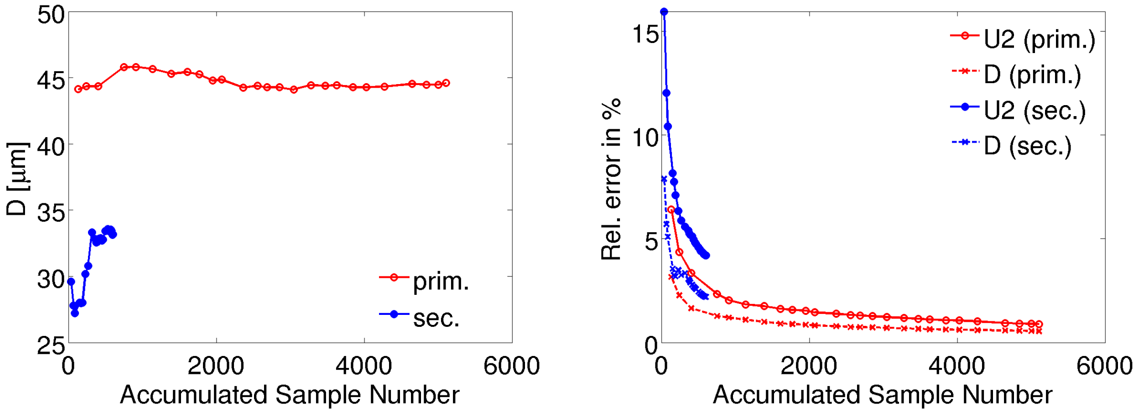

(c) D_{10}. (d) Relative errors ϵ_{rel}, see Equation 4.2, exemplarily shown for $U2_{10}$ and D_{10}.

Figure 4.8: Mean values and their relative errors versus an increasing number of validated samples at ($d_i = 2\,\text{mm}$, $\Theta_i = 45°$).

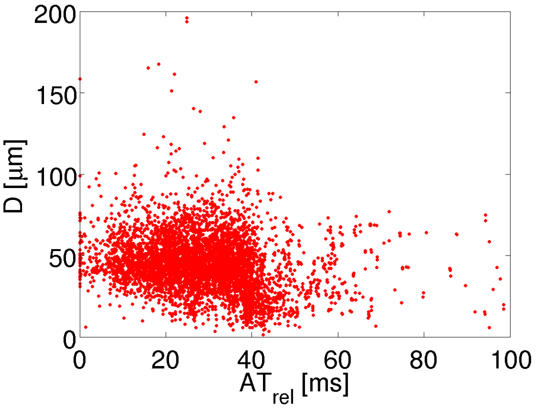

Figure 4.9: D versus AT_{rel} of all primary drops at ($d_i = 2\,\text{mm}$, $\Theta_i = 45°$).

Figure 4.9 shows that data have been quite evenly registered in time and that the diameter values of very early or very late drops are not conspicuous. A correct assignment of a drop to the opening and closing phase of an injection cannot be done, however: due to interactions with the gas phase, particularly due to the drag force, the first injected drops need not be the first arriving at the measurement point. Yet, the study of Figure 4.9 sufficiently shows, that no temporal resolution of the results with respect to the injection has to be considered in the following evaluation.

In the following, the injections are not considered separately any longer and data of all shots gathered at one measurement point are studied simultaneously.

4.2 Fundamental questions

Data of a single measurement point, which have been considered so far, cannot give sufficient information on spray impact. In order to get, for instance, a spatial resolution of the spray and the impact, data from all measurement points have to be treated together. Some of those are rather distant to the central impact region. With respect to the positions, the following fundamental questions have to be addressed:

- Is the spatial expansion of the impact decisive or is it sufficient to assume a very small impact area of the thin hollow cone spray?
- Is the distance d_i of the measurement points to the target surface significant or can it be neglected in the range of the overall error? In other words, is it allowed to assume that the wall contact points of all drops measured in an arbitrary measuring point MP_i coincide with the orthogonal projection of MP_i on the target surface?
- How is the fact that only discrete positions are measured to be dealt with, i.e. is an interpolation required? This issue is particularly important for the consideration of flux densities.

The first question is rather specific for locally restricted sprays, whereas the second and third one are of general concern. The issues will be addressed in the given order by evaluating the data with increasing levels of accuracy. These are implemented in the transformation from the measured velocity components $U1$ and $V1$ to the wall-normal and wall-tangential velocity components $U2$ and $V2$ which has to be provided by the evaluation, see the previous section.
For a short overview of the steps considered in the following cf. Table 4.2.

4.2.1 Simple approach

In a first approach, the coordinate system defining $U2$ and $V2$ is set up in a simple way: only data from measurement points with minimal d_i ($d_i = 2\,\mathrm{mm}$ in case of dry target, $d_i = 3\,\mathrm{mm}$ in case of oil-wetted target, see Section 3.1.2) are considered. Assuming that d_i can then be neglected, the evaluation is done as if the measurement points were directly located on the surface. Moreover, the thin hollow cone spray is supposed to impact on a locally rather restricted region on the target. Therefore, the adapted

Level	Spatial expansion of spray impact area	Distance d_i of MP$_i$ to target surface	Coordinate system (COSY) of transformed velocity components $U2$, $V2$
1	ignored	ignored	single COSY in the central spray impact point Θ_0
2	taken into account	ignored	local COSY for each MP$_i$ at its orthogonal projection onto the surface
3	taken into account	taken into account	local COSY for each drop at its wall contact point Θ_{con}

Table 4.2: The three different evaluation levels.

coordinate system is set up in the central spray impact point[2] at Θ_0, see Figure 4.10(a). All drops are assumed to refer to the central impact region and are hence considered in the same coordinate system no matter at which MP$_i$ they are measured. This coordinate system coincides with that already used in Section 4.1, where only one measurement point in the central impact region has been studied. As in Section 4.1, drops with $U2 < 0$ are declared as primary, those with $U2 \geq 0$ as secondary drops, see Figure 4.10(b). The definitions of impact and ejection angles Φ_{vel} are also maintained.
Note that the target is considered to be dry for the setup of the coordinate system. The question if the film surface should be taken into account is treated and negated in Appendix B.4.

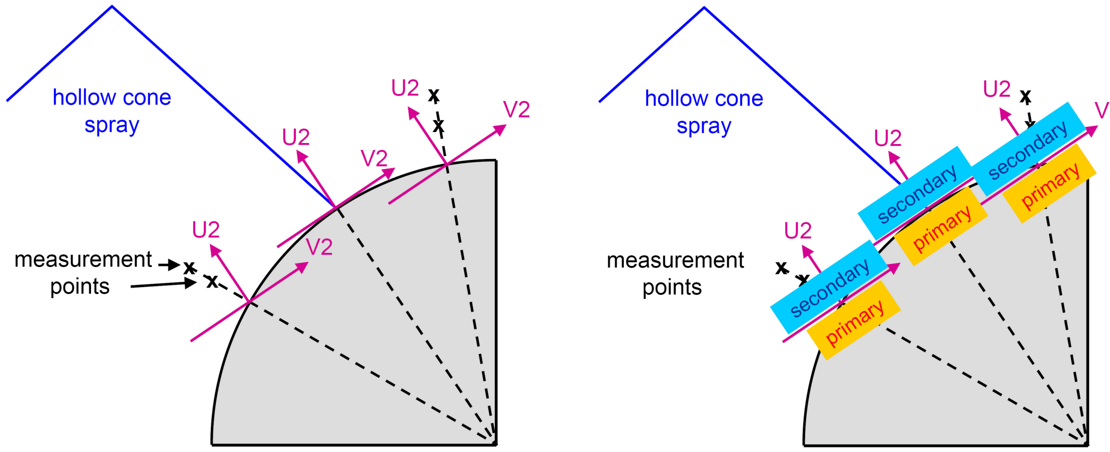

(a) Definition of $U2$ and $V2$. (b) Distinction of primary and secondary drops.

Figure 4.10: Adapted coordinates $U2$ and $V2$ in the basic evaluation level 1.

To combine the data of all measurement points with the same distance d_i to the target surface, arithmetic mean values D_{10}, $U2_{10}$, $V2_{10}$ and $\Phi_{\text{vel},10}$ are calculated for primary

---

[2] As the problem can be considered two-dimensional, i.e. restricted to the measurement plane, the small impact area is often referred to as central impact "point" in the following.

and secondary drops at every MP_i. The arithmetic mean value of any scalar quantity X of primary (secondary) drops is defined as

$$X_{10} = \frac{\sum_j X_j}{\sum_k 1} \,, \tag{4.3}$$

where the sum runs over all primary (secondary) drops j and k respectively. The results are plotted at the respective values of Θ_i in Figure 4.11.

The sign of $V2_{10}$, which might appear strange at first glance, is explained in Figure 4.11(f). Together with $U2$, the curve progression of $\Phi_{\mathrm{vel},10}$ can then be deduced.
Considering the sample number in Figure 4.11(a) it gets clear that the results are not coherent: The position of the main peaks of primary and secondary drops do not coincide with the expected $\Theta_0 \approx 45°$. Moreover, a minimum of primary drops around the expected central impact region and a high number of primary drops in the outer regions ($\Theta << \Theta_0$ and $\Theta >> \Theta_0$) are completely implausible. Consequently, the classification of primary and secondary drops has to be wrong. High-speed images, see Chapter 5, reveal that the secondary spray moves rather tangentially to the surface. This can explain the poor behaviour of the current evaluation, see Figure 4.12: Secondary drops are partly assigned erroneously as primary drops.
Summarised, the evaluation done so far is not accurate enough and improvements are necessary.

4.2.2 Influence of the spatial expansion of the spray impact area

The assumption of a locally restricted impact area, which allows the definition of a single coordinate system in Θ_0, is given up in this step of evaluation. Instead the coordinate system defining $U2$ and $V2$ is set up at the individual Θ_i of a measurement point, cf. Figure 4.13. The distance d_i is still ignored, i.e. data are treated as if the measurement points lay directly on the target surface.

In principle the same evaluation steps as in the previous subsection are performed. Mean values in dependence on Θ_i for all measurement points with the same distance d_i to the target surface are used to compare results, see Figure 4.14. As expected, the differences to Figure 4.11 of evaluation level 1, e.g. with respect to $V2$, are most significant for $\Theta_i >> \Theta_0$ and $\Theta_i << \Theta_0$.
Looking at the distribution of the sample numbers, a dominant peak of primary drops appears in Figure 4.14(a) near the expected $\Theta_0 \approx 45°$ in contrast to Figure 4.11(a). The wrong classification of secondary as primary drops is avoided now in contrast to the basic evaluation. Figure 4.15 compared to Figure 4.12 illustrates this. Note that the finite width of the peak at Θ_0 is another hint that the assumption of a point-like spray impact area in the first basic evaluation does not hold.
Besides the primary peak in Figure 4.14(a), also the distribution of secondary drops looks plausible at first. It is symmetrical to Θ_0 as expected for an almost normal impact. However, it shows a minimum in the central impact region which must not be the case if the evaluation is correct: The distance d_i is still assumed negligible and the wall contact points of all drops measured at the same MP_i are approximated at (R_0,Θ_i), i.e. at the orthogonal projection of MP_i on the surface. In this case, primary and the associated secondary drops should be assigned to approximately the same Θ_i and the

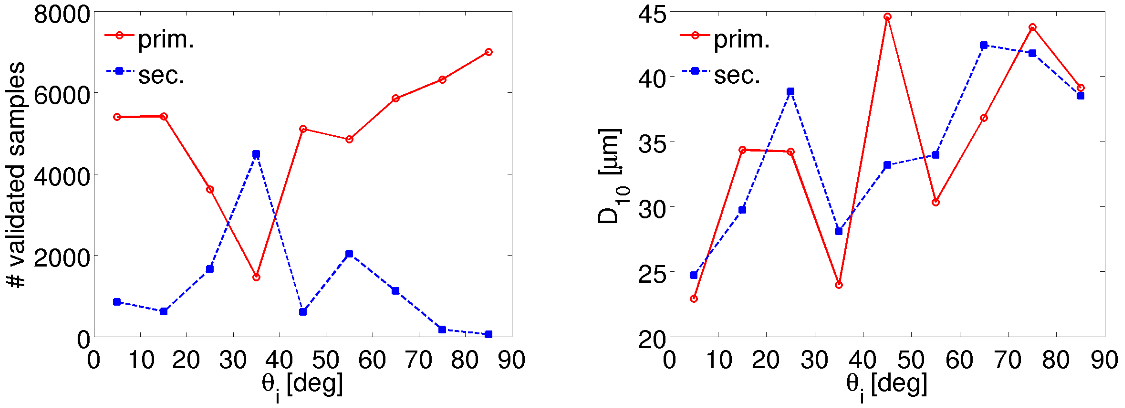

(a) Number of validated samples versus Θ.

(b) $D_{10}(\Theta)$.

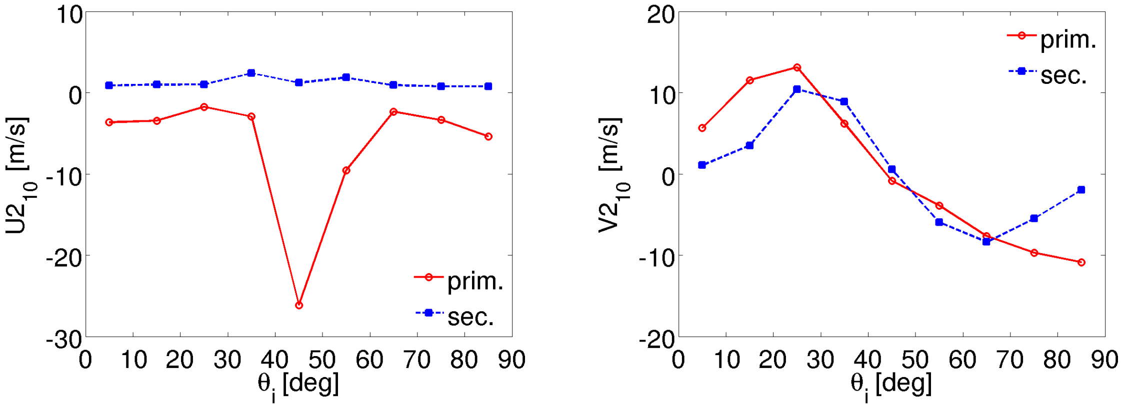

(c) $U2_{10}(\Theta)$.

(d) $V2_{10}(\Theta)$.

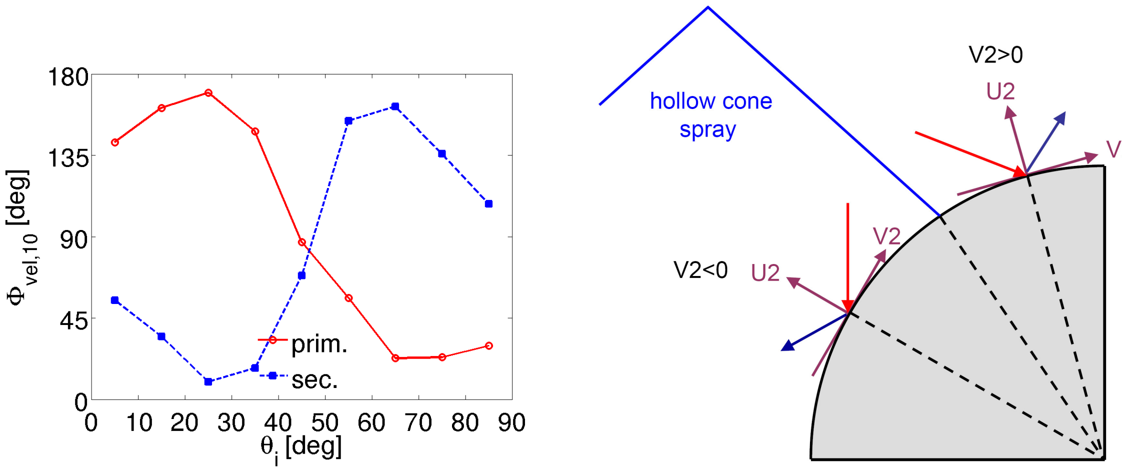

(e) $\Phi_{\mathrm{vel},10}(\Theta)$.

(f) Expected sign of $V2$.

Figure 4.11: Arithmetic mean values versus Θ for $d_i = 2\,\mathrm{mm}$ and explanation of the sign of $V2$ (evaluation level 1).

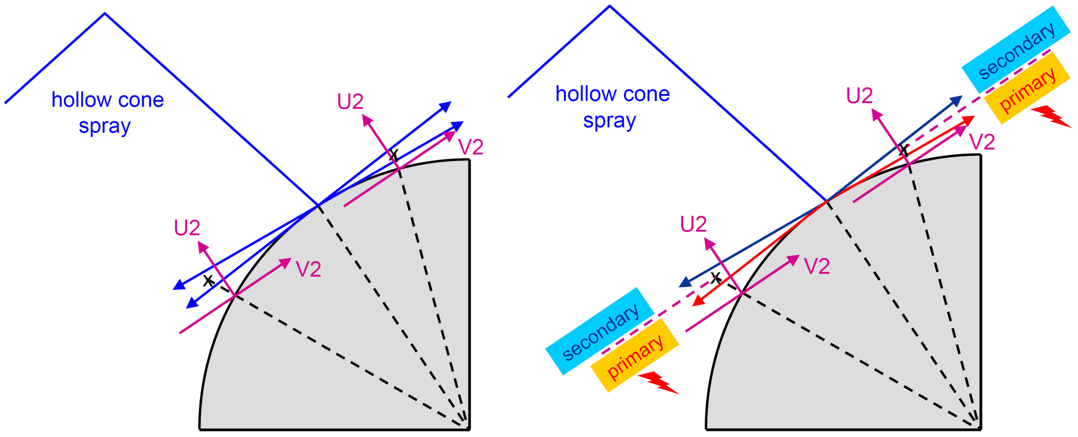

(a) Tangentially reflected secondary spray. (b) Erroneous declaration of secondary drops as primary ones.

Figure 4.12: Problem of the first evaluation approach.

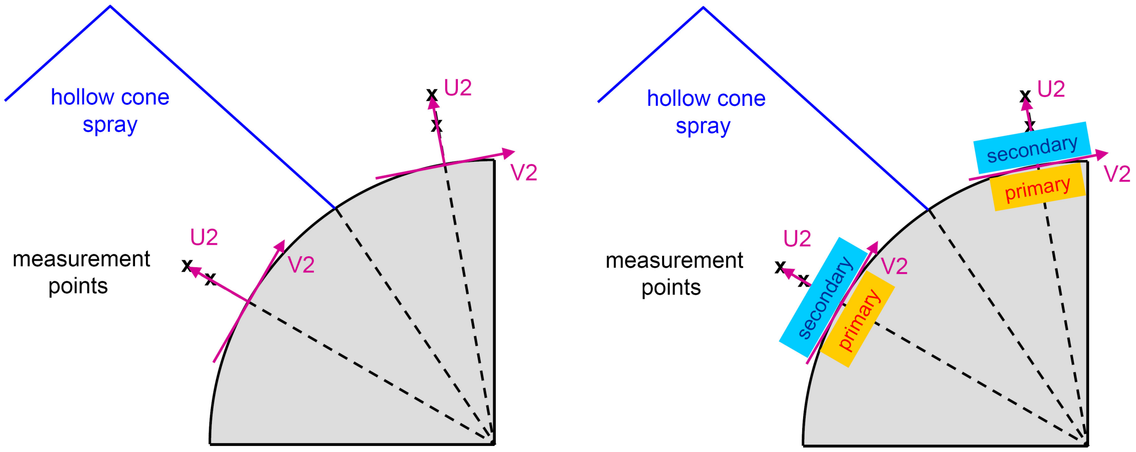

(a) Definition of $U2$ and $V2$. (b) Distinction of primary and secondary drops.

Figure 4.13: Declaration of the adapted coordinate system in evaluation level 2 where the spatial expansion of the impact region is taken into account.

distributions of their sample numbers should more or less agree. This is not fulfilled which leads to the conclusion that this evaluation level is still not sufficient.

4.2.3 Influence of the finite distance between measurement points and wall

In this third and most advanced evaluation level also the distance d_i of a measurement point to the target surface is no longer neglected: Each drop is projected from its MP_i along its velocity vector onto the surface, see Figure 4.16(a). At its individual wall contact point $\Theta_{\mathrm{con},i}$, a local coordinate system is established. The classification as primary or secondary drop is done according to the sign of $U2$ as usual, cf. Figure 4.16(b). Note that the few drops which cannot be assigned to a surface point by projection are discarded. In addition, the determination of the wall contact point of a drop may bear errors because the velocity vector could change between an MP_i and the surface due to

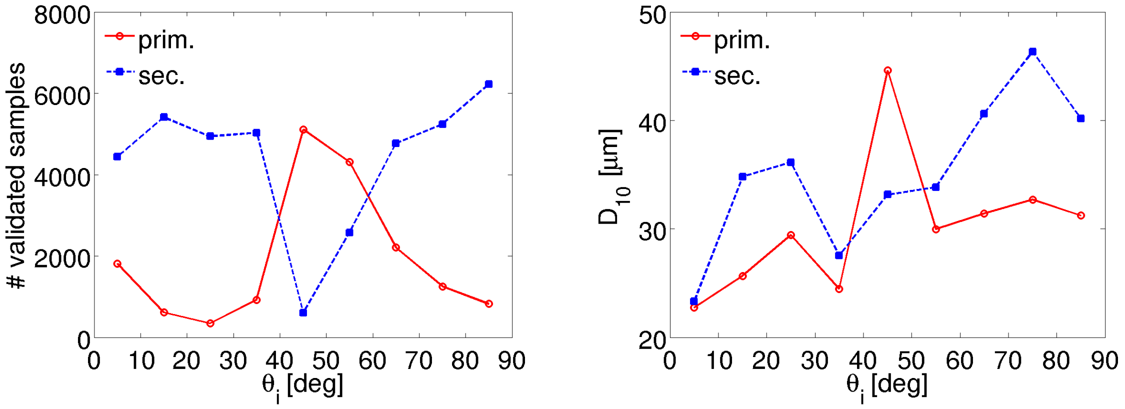

(a) Number of validated samples versus Θ. (b) $D_{10}(\Theta)$.

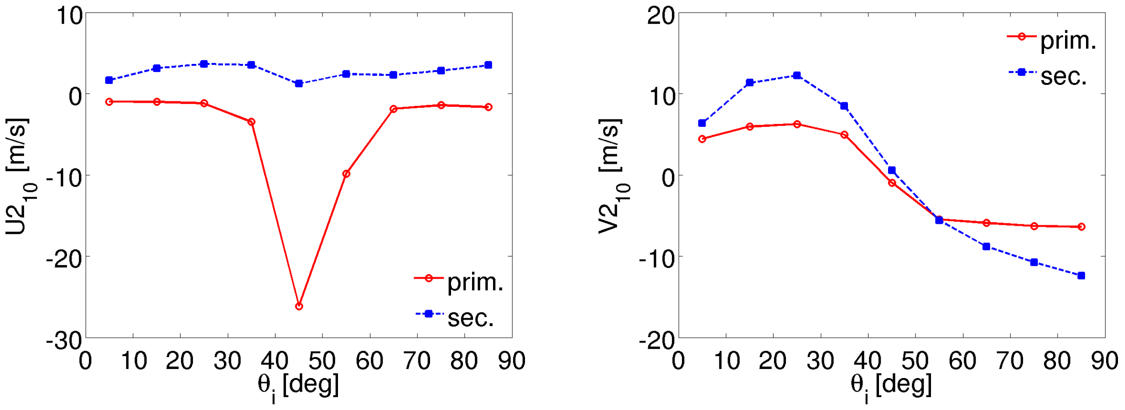

(c) $U2_{10}(\Theta)$. (d) $V2_{10}(\Theta)$.

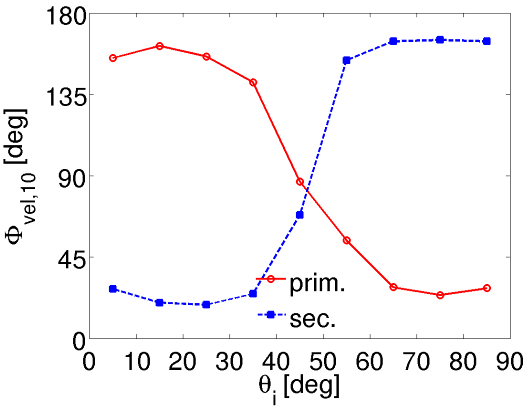

(e) $\Phi_{\mathrm{vel},10}(\Theta)$.

Figure 4.14: Arithmetic mean values versus Θ for $d_i = 2\,\mathrm{mm}$ where the spatial expansion of the impact region is taken into account (evaluation level 2).

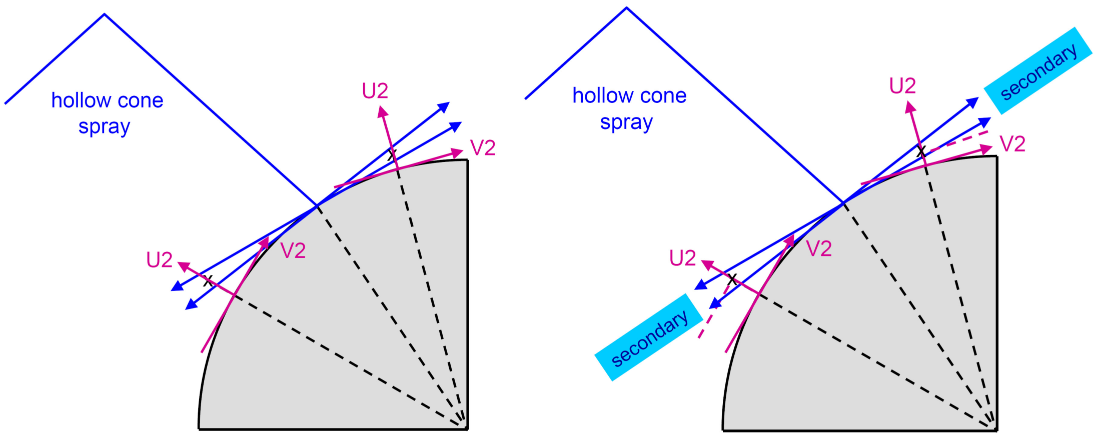

(a) Coordinate system of $U2$, $V2$.

(b) Assignment of primary and secondary drops in level 2.

Figure 4.15: Improved declaration of primary and secondary drops when the spatial expansion of the impact region is taken into account (evaluation level 2).

drop collisions or the influence of near-wall flow. Yet, this possible problem is studied in Appendix B.5.5 and shown to have only minor effects.

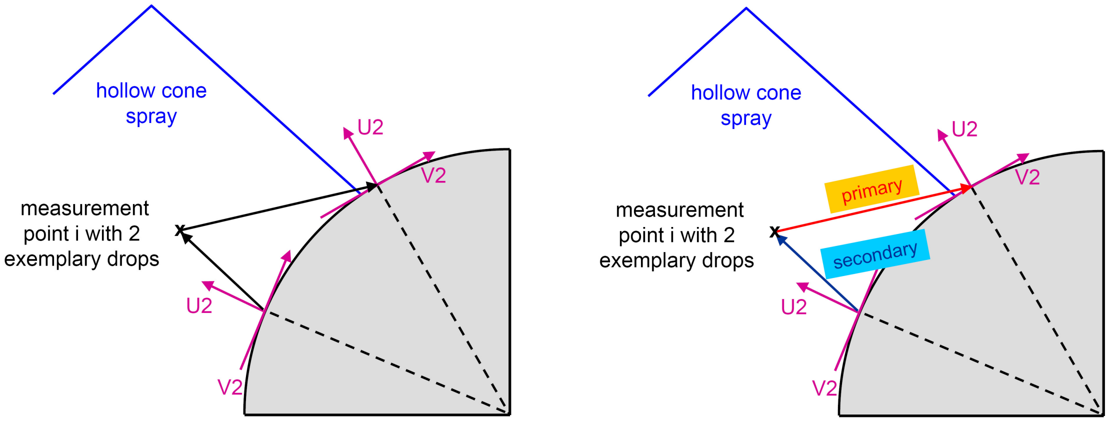

(a) Definition of $U2$ and $V2$.

(b) Distinction of primary and secondary drops.

Figure 4.16: Adapted coordinate system with the spatial expansion of the impact region and the distance d_i taken into account (evaluation level 3).

All drops measured at the same MP_i have different wall contact points in contrast to the previous evaluation steps and the assignment of the drops to the MP_i is no longer relevant. Therefore, it no longer makes sense to calculate mean values of primary and secondary quantities for every measurement point and to plot them in dependence on Θ_i. Instead, Θ-classes have to be established on the target surface. In a first approach, they are defined with a step width of $\Delta\Theta = 10°$ and oriented on the surface, starting at the target apex, $\Theta = 0°$. The mean impact area around $\Theta_0 \approx 45°$ is thus expected in the center of a Θ-class. The step width $\Delta\Theta = 10°$ is chosen intuitively, as this is also the distance in the Θ_i values of neighboured measurement points. The drops are sorted to the classes due to their individual wall contact point $\Theta_{\mathrm{con},i}$. At this point, the evaluation is rather detached from the raw data.

Mean values are finally calculated for every Θ-class and plotted versus the mean wall contact point $\Theta_{\mathrm{con},10}$ per Θ-class, see Figure 4.17. The difference to evaluation level 2, which did not take d_i into account, is most significant comparing Figures 4.14(a) and 4.17(a): While the distributions of primary drops quite agree, those of the secondary drops differ significantly. In Figure 4.14(a) secondary drops are predominantly found distant from Θ_0 in contrast to the primary drops, which has been discussed to contradict the assumptions of evaluation level 2. In Figure 4.17(a), the wall contact points of the secondary drops coincide much better with those of the primary drops and with the impact region. The symmetric distributions of primary and secondary drops around Θ_0 also fulfil the expectations of a rather normal impact.

The diameters of secondary drops reflected to the inside of the spray cone ($\Theta > \Theta_0$) seem to be larger than those reflected to the outside ($\Theta < \Theta_0$), see Figure 4.17(b). This could be due to coalescence of smaller drops. Furthermore, measurements at the inside of the spray cone are more difficult due to the dense spray. Note also that the numbers of validated drops impacting at angles which deviate strongly from Θ_0 are small and that the local mean values bear larger errors in these regions.

4.2.4 Discrete measurement positions

In the previous subsections, it showed that the drops have to be projected from their respective measurement point onto the target surface if spray/wall interaction is to be evaluated. They are sorted to Θ-classes and data from all measurement points MP_i (with same d_i) are summed up. Especially when considering flux densities of mass, number etc., see Section 4.5, which is critical from PDA data a priori, a biased collection of secondary or primary drops in the Θ-classes and the associated large errors must be avoided. Therefore, the measurement grid should be defined such that primary and secondary spray are approximately equally captured. A grid symmetric to the mean impact area is also to be preferred.

But even for a fine grid, not all drops are detected due to the point-wise measurement technique. Hence, one could think of an interpolation. Yet, this is difficult even when free sprays are considered because there is no indication or reasoning which function is to be applied. Therefore, it is omitted in this work. To account for the non-measured drops, only relative flux densities, secondary to primary, will be regarded, cf. Section 4.5 for more details.

4.2.5 Conclusion on the evaluation procedure

It can be resumed that the spatial expansion of the spray impact area must not be ignored although the hollow cone of the spray is quite thin. For plane target geometries, the differences are presumably small, but for any kind of curved surface, where the impact angles may vary significantly, this refinement is important.

The finite distance d_i between measurement points and target surface must also be taken into account by projecting every drop along its velocity vector onto the target. Else the spatial distribution of the drop impacts is predicted in a wrong way even in case of a plane target surface. The coordinate system used to define $U2$ and $V2$ is set up at the wall contact point $\Theta_{\mathrm{con},i}$ for every drop individually.

Primary and secondary drops cannot be compared in a single measurement point but have to be collected from several, reasonably positioned measurement points (with the

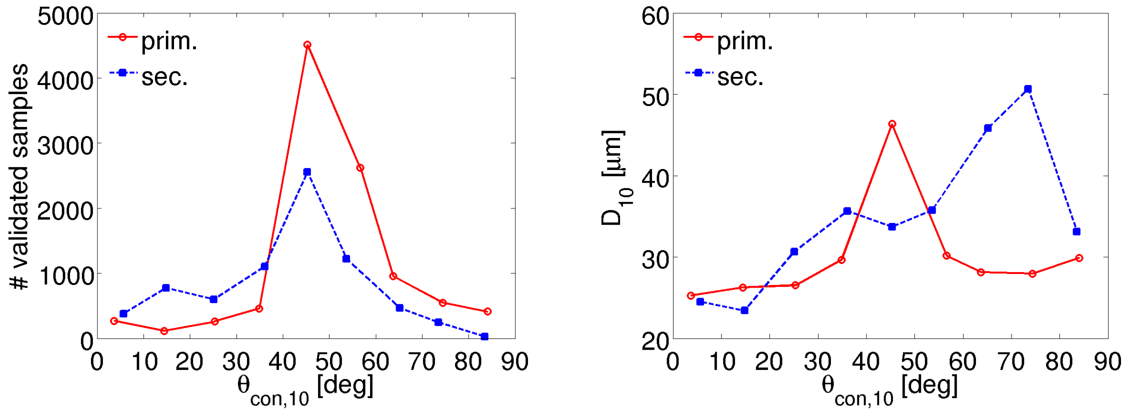

(a) Number of validated samples versus Θ. (b) $D_{10}(\Theta)$.

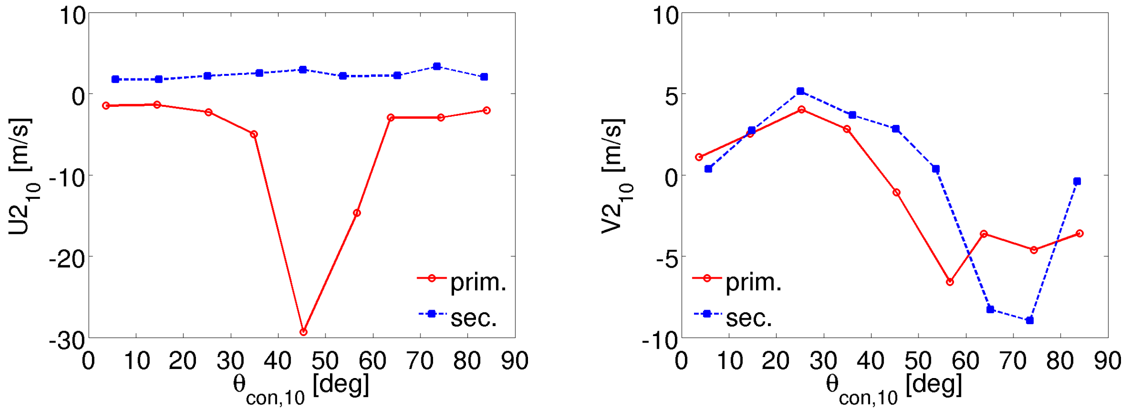

(c) $U2_{10}(\Theta)$. (d) $V2_{10}(\Theta)$.

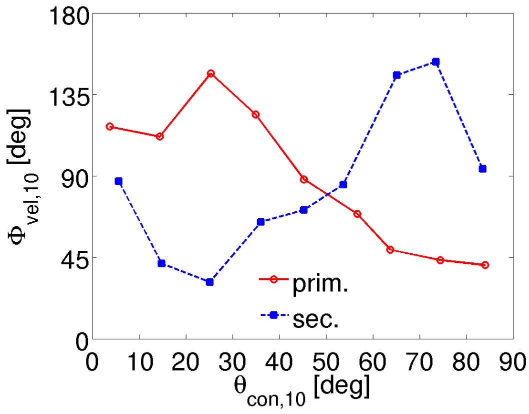

(e) $\Phi_{\mathrm{vel},10}(\Theta)$.

Figure 4.17: Arithmetic mean values versus Θ for $d_i = 2\,\mathrm{mm}$ where the spatial expansion of the impact region and the distance d_i are taken into account (evaluation level 3).

same d_i) in Θ-classes, which are established on the target surface.
Due to the discreteness of the measurement points, only relative flux densities should be considered.

All further studies will be done as shown in Section 4.2.3 and summarised above. Only one generalisation is added: So far, the Θ-classes are simply oriented on the target geometry. Beginning at the target apex, they have been set with a width $\Delta\Theta = 10°$. The central spray impact region ($\Theta_0 \approx 45°$) is expected approximately in the center of a Θ-class. However, for other step widths than $\Delta\Theta = 10°$ this might no longer be true and results for different $\Delta\Theta$ might differ strongly. Therefore, the Θ-classes are redefined and grouped around the central impact region with a user-defined step width $\delta\Theta$, see Figure 4.18: The original classes with $\Delta\Theta = 10°$ are searched for the one with the maximal number of validated primary drops. For this central class, the mean wall contact point $\Theta_{\mathrm{con},10}$ of the primary drops is calculated and defines the center of the new central Θ-class with step width $\delta\Theta$. The other new Θ-classes are then evenly established on both sides of the latter.
Figure 4.19 shows the arithmetic mean values calculated in the new classes with $\delta\Theta = \Delta\Theta = 10°$. As assumed, the differences to Figure 4.17 are not remarkable for this chosen step width.
The value of $\delta\Theta$ can in principle be chosen freely now. In Appendix B.5.3 a sensitivity analysis on the step width is shown. Throughout the following work, the intuitive value of $\delta\Theta = 10°$ is maintained.

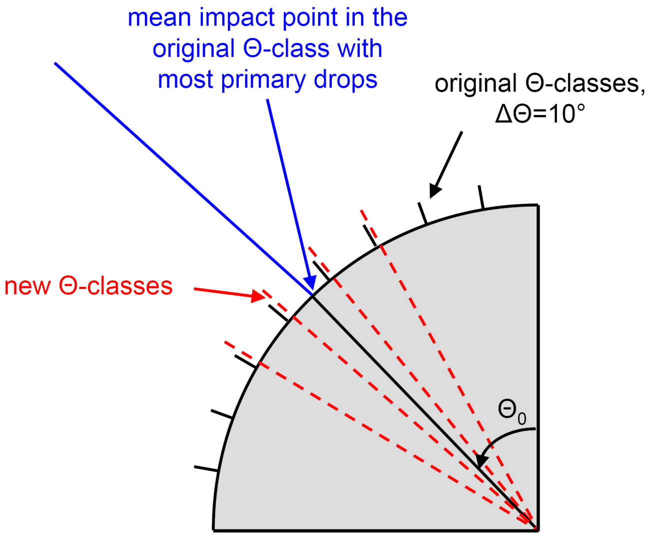

Figure 4.18: Definition of new Θ-classes.

4.3 Further examination of the data

Using the principal evaluation procedure developed in the previous section, some basic examinations of the data concerning sensitivities and robustness still have to be done. In contrast to Section 4.1, where data of one measurement point have been considered, they address the data of a complete measurement, i.e. those from all measurement points taken together.
Moreover, only mean values per Θ-class have been studied so far. Equally important

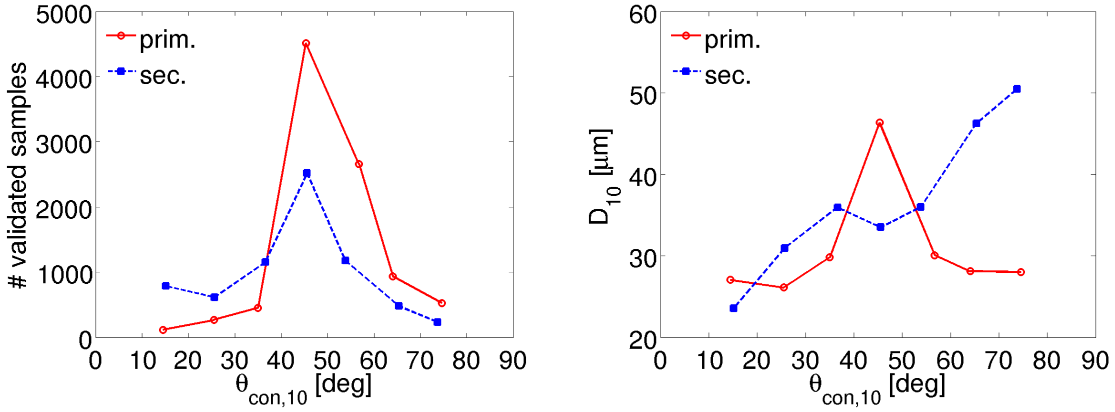

(a) Number of validated samples versus Θ. (b) $D_{10}(\Theta)$.

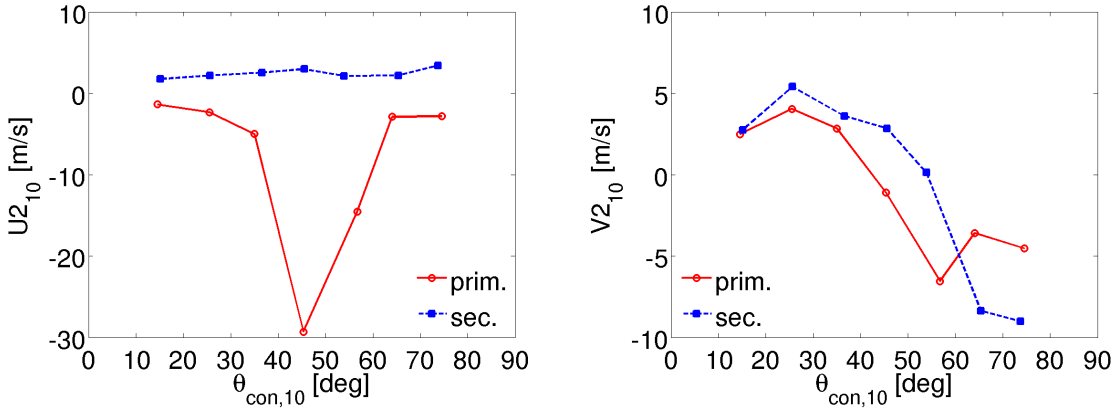

(c) $U2_{10}(\Theta)$. (d) $V2_{10}(\Theta)$.

Figure 4.19: Arithmetic mean values versus Θ for $d_i = 2\,\mathrm{mm}$ where the new Θ-classes are used with $\delta\Theta = 10°$.

and still lacking is a consideration of the distribution functions. It results in reasonable filtering of primary drops and the distinction of secondary drops in those reflected towards the outside of the hollow cone spray and those reflected to the inside.

4.3.1 Basic tests

For any measurement it is essential to perform tests on the data to estimate their quality and the reliability of the results. In Appendix B.5 the following issues are treated:

- data reproducability, which is confirmed.
- Influence of the target on the primary spray. The properties of primary drops are studied with the target adjusted and without target. The differences appear to be minor.
- Sensitivity on the width $\delta\Theta$ of the Θ-classes. Differences can be seen, yet the overall statements are the same for different values of $\delta\Theta$.
- Data robustness towards small measurement and adjustment errors, which is affirmed.

- Influence of near-wall flow. Different distances d_i between measurement points and surface are considered and slight deviations are found. It is decided to consider the minimal values ($d_i = 2\,\mathrm{mm}$ in case of dry target, $d_i = 3\,\mathrm{mm}$ in case of oil-wetted target) in further evaluations.

4.3.2 Histograms and further data treatment

So far, mean values for each Θ-class have been considered. Yet, they do not extract all the information of the data and the same mean values can be obtained by entirely different distributions, cf. [37]. Therefore, it is necessary to regard also the underlying measured histograms. In the following, these are discussed for the quantities D, $U2$, $V2$ and Φ_{vel} for the exemplary measurement, see Table 4.1, in the central Θ-class with $40.3° \leq \Theta_{\mathrm{con}} < 50.3°$.

4.3.2.1 Primary drops and filtering

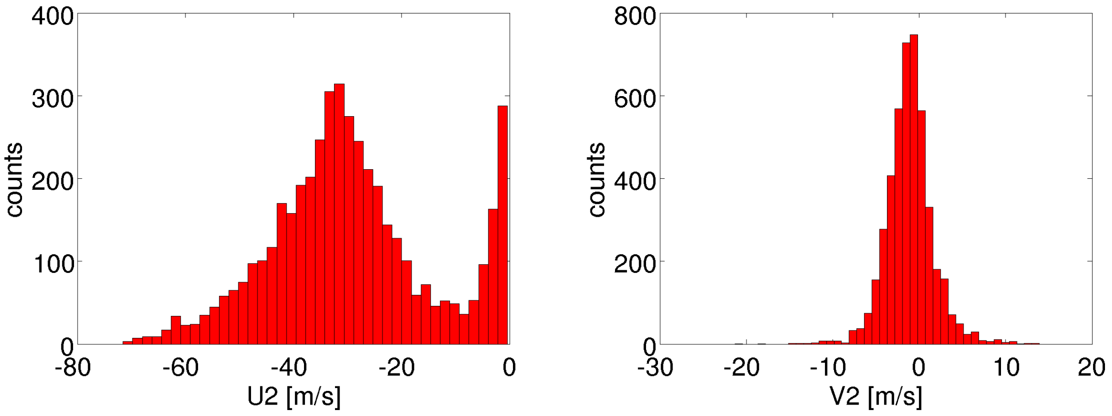

(a) Wall-normal velocity component.

(b) Wall-tangential velocity component.

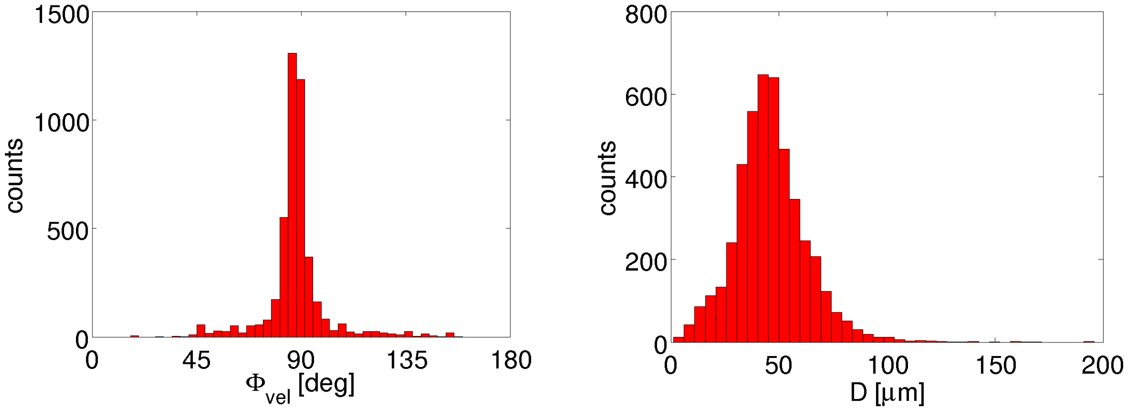

(c) Impact angle.

(d) Diameter.

Figure 4.20: Primary drops in the central spray impact class for the exemplary measurement ($40.3° \leq \Theta_{\mathrm{con}} < 50.3$, $d_i = 2\,\mathrm{mm}$).

In Figure 4.20 which shows the histograms of the primary drops, the bimodal distribution of the wall-normal velocity component $U2$ and in particular the slim peak near

zero seem wrong. The drops belonging to the latter could be part of the recirculation zone of the spray. Or they could be falsely assigned secondary drops carried by the flow in an eddy-like trajectory back onto the surface. To characterise the conspicuous drops some tests are performed: A look at the diameter distribution shows that these drops do not have remarkably small or large diameters. An additional filter in the transit time also reveals no distinctive features. The drops are not late with respect to the start of injection either, as their value of the relative arrival time proves. Finally, it is found that they impact in a very flat angle onto the target, i.e. that they are identical to those drops with very small/large values of Φ_{vel} compared to the expected value of $\approx 90°$ in the central impact area, cf. Figure 4.20(c).
Also in the outer Θ-classes with $\Theta_{\mathrm{con}} << \Theta_0$ ($\Theta_{\mathrm{con}} >> \Theta_0$), where only few primary drops are detected, arguable values of the impact angle appear. Some drops show negative (positive) values of $V2$ and are connected to impact angles $\Phi_{\mathrm{vel}} << 90°$ ($\Phi_{\mathrm{vel}} >> 90°$). Some show negative (positive) values of $V2$ and are connected to impact angles $\Phi_{\mathrm{vel}} << 90°$ ($\Phi_{\mathrm{vel}} >> 90°$). This is rather peculiar with respect to the experimental setup and the injector-target alignment.

For directly impacting drops, the values of Φ_{vel} should lie in a well-defined, relatively limited range due to the hollow cone shape of the spray. Primary drops with much smaller/larger angles are most probably not impacting for the first time. Therefore, these are to be filtered out and the following procedure is applied:
The mean direction of the primary spray is described by $\tilde{\Phi}_{\mathrm{vel},10}$ and the widening of the hollow cone by a diversification angle $\Delta\tilde{\Phi}_{\mathrm{vel}}$, see Figure 4.21. Primary drops in any Θ-class are only further taken into account if

$$\tilde{\Phi}_{\mathrm{vel},10} - \Delta\tilde{\Phi}_{\mathrm{vel}} \;\leq\; \tilde{\Phi}_{\mathrm{vel},i} \;\leq\; \tilde{\Phi}_{\mathrm{vel},10} + \Delta\tilde{\Phi}_{\mathrm{vel}}\,, \tag{4.4}$$

else they are filtered out. $\tilde{\Phi}_{\mathrm{vel},i}$ is calculated for every drop i using the directly measured velocity components $U1$ and $V1$. The impact angles $\Phi_{\mathrm{vel},i}$, which are calculated as the angles between $U2$ and $V2$ and which are addressed in the histograms, cannot be used for the filtering because a unique coordinate system for all drops with reference to the injector has to be considered. And the values of $U2$, $V2$ and consequently $\Phi_{\mathrm{vel},i}$ depend on the respective wall contact points.
The value of $\tilde{\Phi}_{\mathrm{vel},10}$ is evaluated as the arithmetic mean angle $\tilde{\Phi}_{\mathrm{vel},10,\mathrm{central\ class}}$ in the central Θ-class, where the maximal number of validated primary drops is counted.
In order to determine a reasonable value of $\Delta\tilde{\Phi}_{\mathrm{vel}}$, the widening of the spray hollow cone is estimated under the assumption of a normal impact. Considering Figure 4.21, $\Delta\tilde{\Phi}_{\mathrm{vel}}$ can be found via the relation:

$$2\cdot\tan(\Delta\Theta_{\mathrm{prim}}/2)\cdot(R_0 + d_i) = 2\cdot\tan(\Delta\tilde{\Phi}_{\mathrm{vel}})\cdot(d_{\mathrm{inj.point}} - d_i)\,. \tag{4.5}$$

The relative distance between the virtual injection point and the target surface is adjusted to $d_{\mathrm{inj.point}} \approx 37\,\mathrm{mm}$ for the exemplary measurement. $\Delta\Theta_{\mathrm{prim}}$, a measure for the spatial expansion of the impact area, is not known. For an estimation, the data at different measurement points with $d_i = 2\,\mathrm{mm}$ are studied and it shows that the primary spray is observed at $\Theta_i = 35°$, $\Theta_i = 45°$ and $\Theta_i = 55°$ but hardly any more at $\Theta_i = 25°$ or $\Theta_i = 65°$. It can be deduced that $\Delta\Theta_{\mathrm{prim}}$ should lie in a range of 20°-30°.
Using these estimations, $\Delta\tilde{\Phi}_{\mathrm{vel}}$ can be calculated and the results are shown in Table 4.3. It is decided to use the mean value of $\Delta\tilde{\Phi}_{\mathrm{vel}} = 9°$ to filter primary drops in the following. This filtering does not impose a very restrictive criterion compared to a beam diversification angle of 2°-3° which is the approximate value assumed by the manufacturer of the injector.

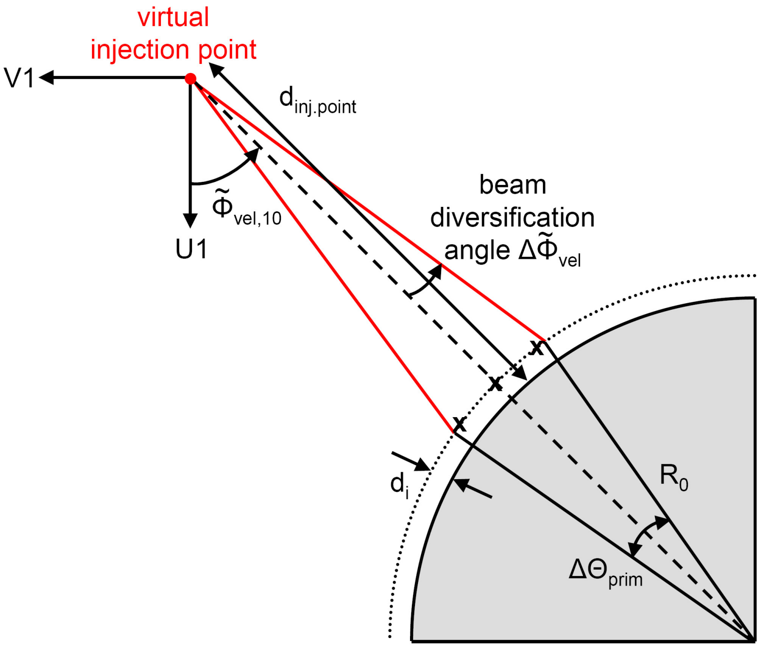

Figure 4.21: Widening of the spray cone, presentation not in scale.

$d_{\text{inj.point}}$ [mm]	$\Delta\Theta_{\text{prim}}$ [°]	$\Delta\tilde{\Phi}_{\text{vel}}$ [°] ($d_i = 2\,\text{mm}$)	$\Delta\tilde{\Phi}_{\text{vel}}$ [°] ($d_i = 3\,\text{mm}$)	$\Delta\tilde{\Phi}_{\text{vel}}$ [°] ($d_i = 5\,\text{mm}$)
37	20	6.3	6.8	7.8
37	25	7.9	8.5	9.8
37	30	9.6	10.3	11.8
35	25	8.4	9.1	10.5
39	25	7.5	8.1	9.3

Table 4.3: Beam diversification angle of the spray.

Figure 4.22 presents the histograms in the central Θ-class now including the described filter. The peak of almost zero wall-normal velocity $U2$ is strongly reduced. No other significant changes result, as expected.

4.3.2.2 Secondary drops and distinction of two directions

In contrast to primary drops, no filtering of secondary drops must be done. All directions are possible due to surface roughness, drop/drop and drop/wall film interactions.

In the central impact area, cf. the histograms in Figure 4.23, the wall-tangential velocity component $V2$ and consequently also Φ_{vel} show an almost symmetrical, bimodal distribution. The reflection is not broadly distributed in all directions but two main directions are clearly defined. The determination of one mean value for $V2$ and Φ_{vel} in this class, as done so far, is therefore not sufficient. It leads erroneously to approximately zero tangential velocity in the central impact region.
Hence, the reflection (which is not meant in its strict physical sense here) towards the outside and towards the inside of the spray cone are distinguished from now on, see Figures 4.24 and 4.25: The mean impact angle $\Phi_{\text{vel,10,central area}}$ of all primary drops

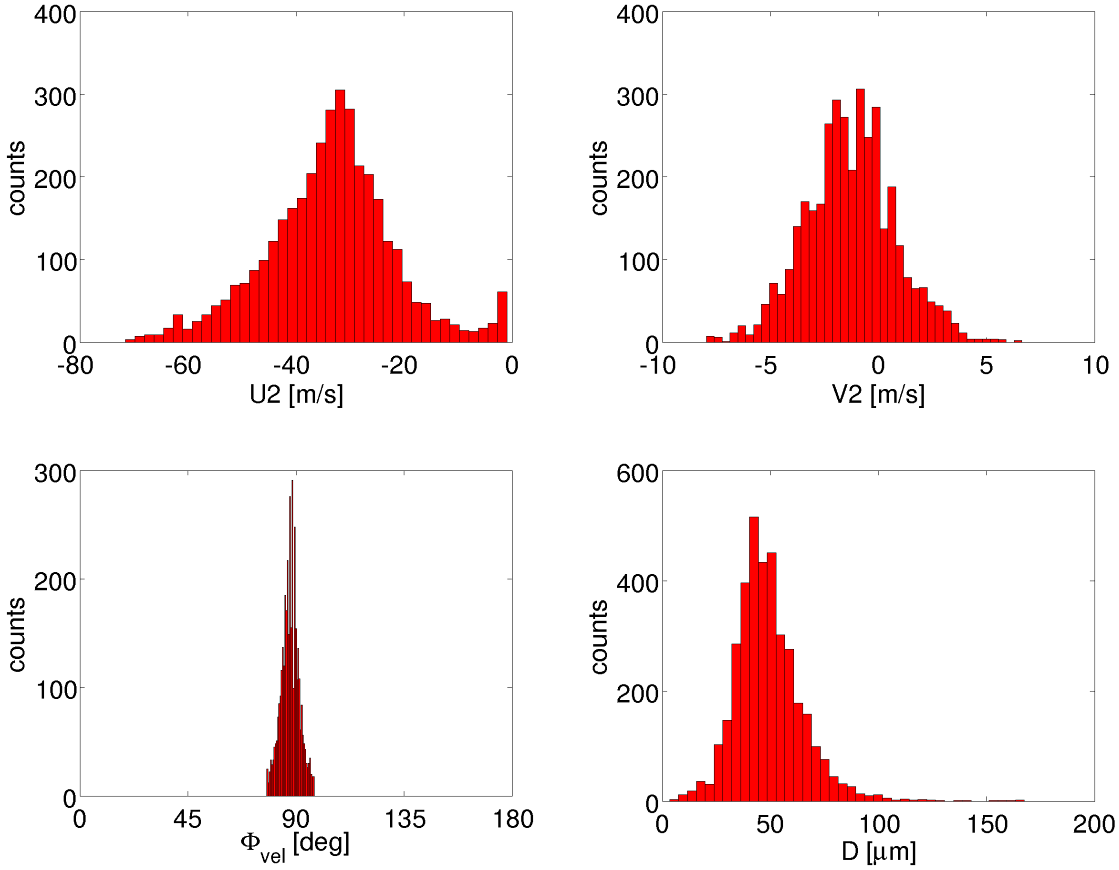

Figure 4.22: Primary drops in the central spray impact class including a filter with $\Delta\tilde{\Phi}_{\mathrm{vel}} = 9°$ for the exemplary measurement ($40.3° \leq \Theta_{\mathrm{con}} < 50.3$, $d_i = 2\,\mathrm{mm}$).

assigned to the central impact area is calculated. The latter comprises the central class (maximum number of primary drops) as well as the directly neighbouring class on each side. A secondary drop in the central impact area is sorted to the outside if $\Phi_{\mathrm{vel}} \leq \Phi_{\mathrm{vel,10,central\ area}}$ else to the inside. For secondary drops outside the central impact area the assignment is obvious.

4.3.2.3 Changes in the mean values

Figure 4.26 shows the mean values per Θ-class where primary drops are filtered with $\Delta\tilde{\Phi}_{\mathrm{vel}} = 9°$ and secondary drops are distinguished in two modes. For primary drops the maximal value of $U2$ is increased compared to Figure 4.19 because the peak near zero is filtered out.

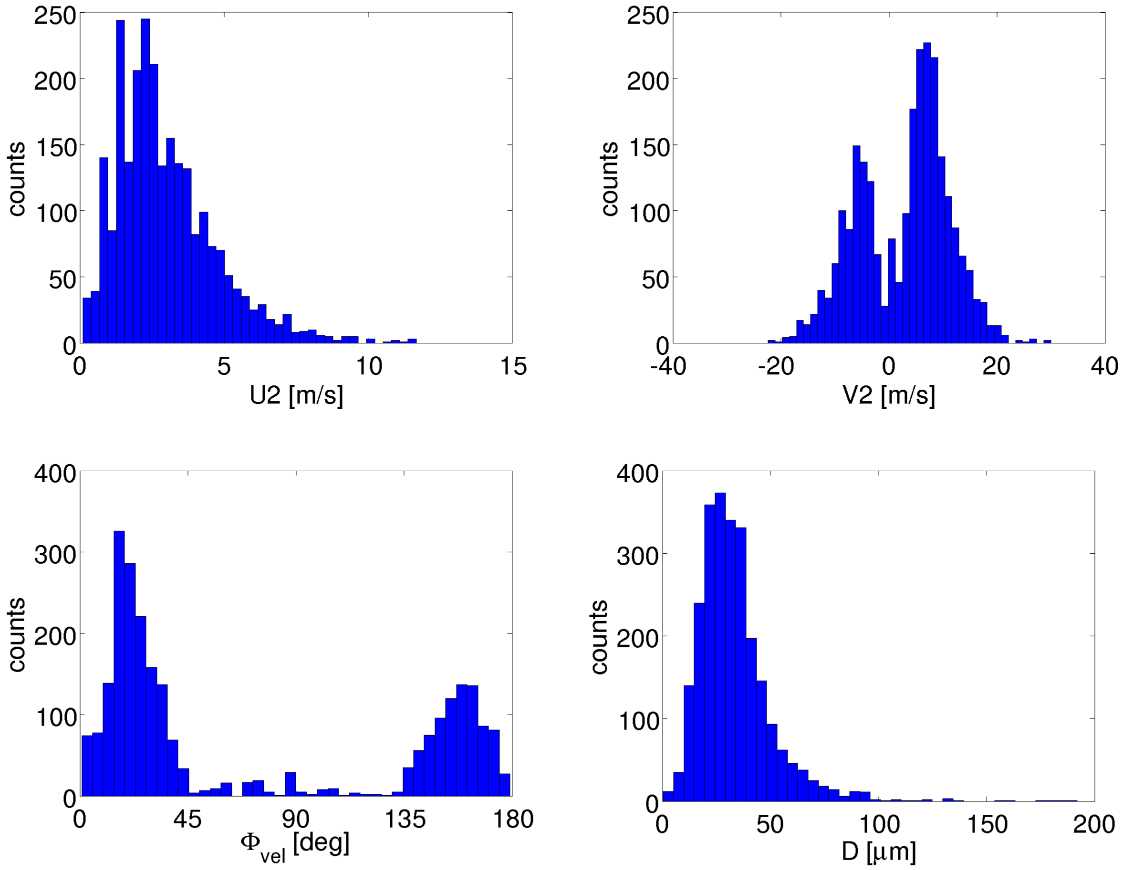

Figure 4.23: Secondary drops in the central spray impact class for the exemplary measurement ($40.3° \leq \Theta_{con} < 50.3$, $d_i = 2\,\text{mm}$).

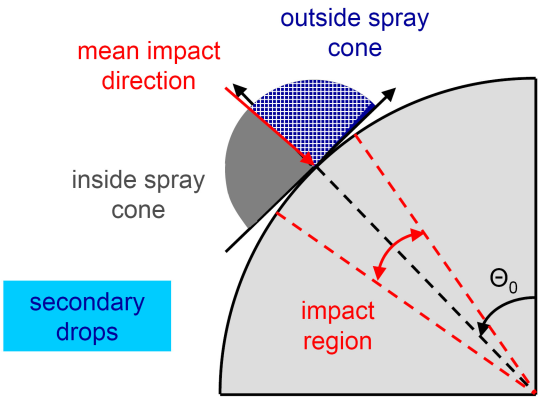

Figure 4.24: Separating two modes of secondary drops in the central impact area.

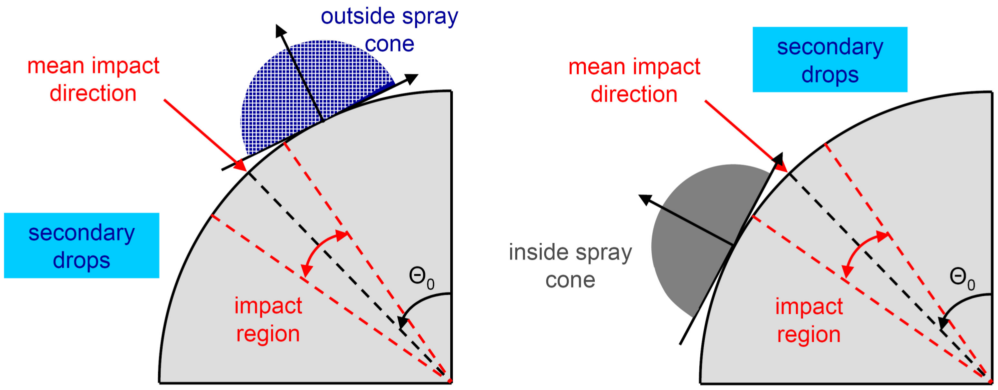

Figure 4.25: Assignment of secondary drops outside the central impact area.

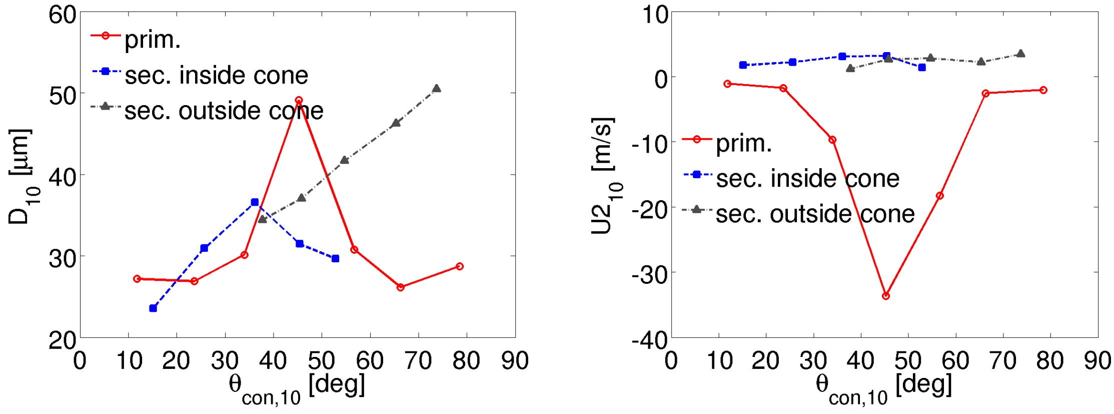

(a) $D_{10}(\Theta)$.

(b) $U2_{10}(\Theta)$.

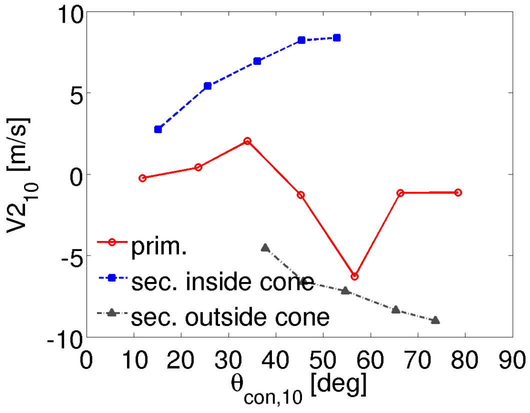

(c) $V2_{10}(\Theta)$.

Figure 4.26: Arithmetic mean values versus Θ for data of the exemplary measurement ($d_i = 2\,\mathrm{mm}$). Primary data are filtered with $\Delta\tilde{\Phi}_{\mathrm{vel}} = 9^\circ$ and secondary drops are distinguished in those reflected to the outside and inside of the hollow cone respectively.

4.4 Refined best values

Up to this point, the mean values for diameters, wall-normal and wall-tangential velocity components of primary and secondary drops considered in every Θ-class n have been of a simple arithmetic type, cf. Equation 4.3. However, the same mean values could be obtained by entirely different distributions, see [37]. More reliable values for any scalar quantity X could be calculated by fitting its respective distribution $pdf_{k,\mathrm{class}\,n}(X)$ and by using the general definition, cf. [2]:

$$X_{ab,k,\mathrm{class}\,n} = \left(\frac{\int X^a \cdot pdf_{k,\mathrm{class}\,n}(X)\, dX}{\int X^b \cdot pdf_{k,\mathrm{class}\,n}(X)\, dX} \right)^{1/(a-b)} . \tag{4.6}$$

a and b are integers, k denotes if primary ($k = 1$) or secondary drops ($k = 2, 3$) are considered.
However, $pdf_{k,\mathrm{class}\,n}(X)$ usually has to be chosen by a trial-and-error procedure as the distribution function best fitting the data, because no physical reasoning exists which function is to be used. Therefore, arithmetic mean values are retained in this work. To improve their definition additional weighting and correction factors are introduced.

Due to limitations in numerical modelling some additional definitions of mean values become necessary and are also addressed in this section: In the simulations considered, spray impact is represented by the impacts of individual Lagrangian parcels. These ignore each other during the impact and do not know if they impact in the central region or on the borders. A system of ellipses like in Kuhnke's model to get this information, cf. Section 1.4.2, is not possible for arbitrary target geometries. Hence, the spatial information in Θ resulting from the evaluation cannot be continued to simulations and final representative values, which do no longer contain a Θ-dependence, have to be conceived instead.
This does not question the broad evaluation done so far but is understood as a necessary step to use the results in simulations and to cope with the limited description of spray impact there.

4.4.1 Correction and weighting factors

4.4.1.1 Multiple or non-validated drops in the detection volume

If two or more drops pass simultaneously through the probe volume, their overlapping signals are registered as one event and probably rejected by the validation procedure of the system. Drops with a diameter below the detection threshold of the system are not counted at all. Hence, the number of validated signals $N_{S,\mathrm{val}}$ is smaller than the number of detected signals N_S, which is itself smaller than the actual number of drops N_D, passing through the detection volume in a given time span Δt: $N_{S,\mathrm{val}} < N_S < N_D$. For flux measurements and the calculation of improved mean values, it is necessary to conclude from $N_{S,\mathrm{val}}$ to N_D. In [61], see also [2], the factor $\eta_{\mathrm{val},i}$ is developed to provide this:

$$\eta_{\mathrm{val},i} = \frac{2 + \frac{\lambda_A}{\epsilon_S} \cdot \frac{N_D}{\Delta t} \cdot \tau_i}{2 \cdot \frac{N_{S,\mathrm{val}}}{N_D} + \lambda_A \cdot \frac{\epsilon_{S,\mathrm{val}}}{\epsilon_S}} \quad \text{with} \quad N_D = \frac{N_S}{1 + \ln(1 - \epsilon_S)} . \tag{4.7}$$

τ_i denotes the signal duration, $\epsilon_S = \sum_{i=1}^{N_S} \frac{\tau_i}{\Delta t}$ the relative signal presence of all detected signals, $\epsilon_{S,\text{val}} = \sum_{i=1}^{N_{S,\text{val}}} \frac{\tau_i}{\Delta t}$ the relative signal presence restricted to all validated signals and $\lambda_A = -\ln(1-\epsilon)$ the probability of a drop appearance. It is assumed that overlapping signals are not validated.

Using the value $\eta_{\text{val},i}$ for every drop as a weighting factor then accounts for measurement errors due to multiple and non-validated drops.

To calculate the values $\eta_{\text{val},i}$, all data of a measurement point are considered, where every measurement point is treated separately. To estimate the time span Δt, the intervals between the first and the last measured drop of each injection are summed up. Figure 4.27 shows the resulting values for the exemplary measurement point. It can be seen that most validated drops are weighted with a factor $\eta_{\text{val},i} \approx 2.2$, i.e. that one out of approximately 2.2 drops is detected and validated on average.

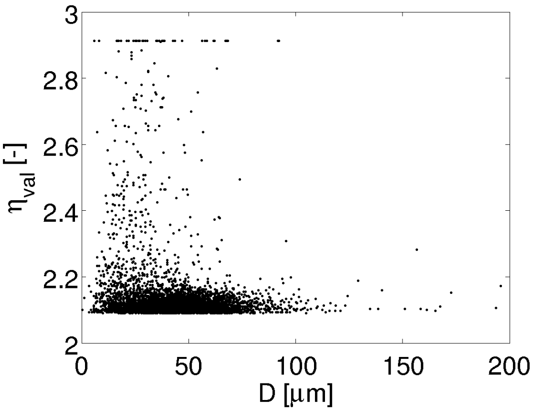

Figure 4.27: Values of $\eta_{\text{val},i}$ at (d_i = 2 mm, $\Theta_i = 45°$) for the exemplary measurement, see Table 4.1.

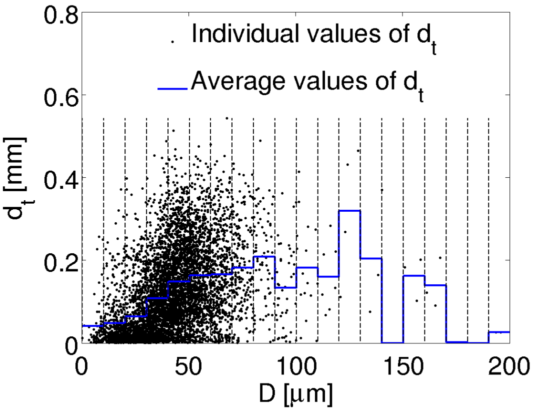

Figure 4.28: Values of d_t at (d_i = 2 mm, $\Theta_i = 45°$) for the exemplary measurement, see Table 4.1.

4.4.1.2 Uncertainty of a wall contact point

Another aspect which has not been taken into account yet is the spatial uncertainty $\Delta\Theta_{\text{con},i}$ of every wall contact point $\Theta_{\text{con},i}$ which is not due to measurement errors but due to the finite diameter $d_{t,i}$ of the detection volume in PDA measurements. In Appendix B.6.2, some general remarks on measurement and detection volumes are given with a particular stress on the drop-size dependent diameter $d_{t,i}$ of the detection volume.

$d_{t,i}$ can be considered as the spatial uncertainty of the position of a drop when it is detected at a measurement point. The values resulting for the exemplary measurement point are shown in Figure 4.28. The average expansion of the detection volume amounts to approximately 0.2 mm.

Unless free spray propagation but spray/wall interaction is of interest, however, the spatial uncertainty is not needed at the measurement position but on the target surface. Hence, $d_{t,i}$ must be transferred onto the latter which is done analogously to the determination of $\Theta_{\text{con},i}$: $d_{t,i}$ is projected along the velocity vector of the considered drop i. The calculation of the spatial uncertainty $d_{w,i}$ on the surface is described in detail in Appendix B.6.3. The angle $\Delta\Theta_{\text{con},i}$, associated to the arc $d_{w,i}$ is interpreted as the uncertainty of $\Theta_{\text{con},i}$. Due to the hemispherical target, the values of $d_{w,i}$ and $\Delta\Theta_{\text{con},i}$

depend strongly on the direction of the velocity vector and the position (d_i,Θ_i) of the measurement point, see Figure 4.29.

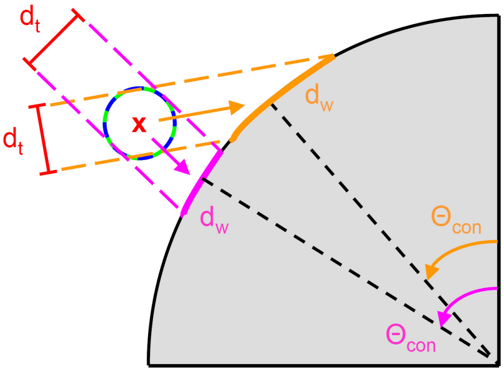

Figure 4.29: Dependence of $d_{w,i}$ on the velocity direction and the position of the measurement point.

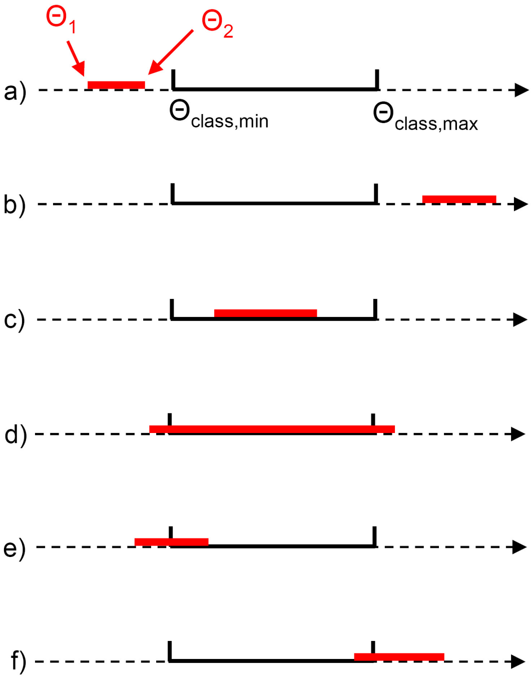

Figure 4.30: Different situations in the determination of $w_{n,i}$. Θ_1 and Θ_2 denote the boundaries of the uncertainty band $\Delta\Theta_{\mathrm{con},i}$ of an arbitrary drop i. Its fraction in a Θ-class n, reaching from $\Theta_{\mathrm{class,min}}$ to $\Theta_{\mathrm{class,max}}$, is defined as the weighting factor $w_{n,i}$, cf. Table 4.4.

Case	Situation	Weight $w_{n,i}$
a	$\Theta_2 < \Theta_{\mathrm{class,min}}$	0
b	$\Theta_1 > \Theta_{\mathrm{class,max}}$	0
c	$\Theta_1 \geq \Theta_{\mathrm{class,min}} \wedge \Theta_2 \leq \Theta_{\mathrm{class,max}}$	1
d	$\Theta_1 < \Theta_{\mathrm{class,min}} \wedge \Theta_2 > \Theta_{\mathrm{class,max}}$	$\frac{\Theta_{\mathrm{class,max}}-\Theta_{\mathrm{class,min}}}{\Delta\Theta_{\mathrm{con}}}$
e	$\Theta_1 < \Theta_{\mathrm{class,min}} \wedge \Theta_2 \leq \Theta_{\mathrm{class,max}}$	$\frac{\Theta_2-\Theta_{\mathrm{class,min}}}{\Delta\Theta_{\mathrm{con}}}$
f	$\Theta_1 \geq \Theta_{\mathrm{class,min}} \wedge \Theta_2 > \Theta_{\mathrm{class,max}}$	$\frac{\Theta_{\mathrm{class,max}}-\Theta_1}{\Delta\Theta_{\mathrm{con}}}$

Table 4.4: Values of $w_{n,i}$ associated to Figure 4.30.

There are two possibilities to employ the uncertainties $\Delta\Theta_{\mathrm{con},i}$: First, drops with a large value of $\Delta\Theta_{\mathrm{con},i}$ could be excluded. However, this would affect particularly secondary drops because these are reflected in a very small angle from the target and therefore have larger uncertainty values a priori. Therefore, the second possibility is chosen, which means a weighting of drop data: So far, each drop has been put with weight 1 to the Θ-class where its wall contact point $\Theta_{\mathrm{con},i}$ is situated and with weight 0 to all other classes. Now, the uncertainty band $\Delta\Theta_{\mathrm{con},i}$ is distributed over the Θ-classes and $w_{n,i}$ amounts to the fraction of $\Delta\Theta_{\mathrm{con},i}$ in the Θ-class n, $w_{n,i} \in [0;1]$ for each class n and

$\sum_{\text{class}\,n} w_{n,i} = 1$. Every drop can contribute to the means of several classes. Figure 4.30 shows the six possible cases and Table 4.4 gives the associated values of $w_{n,i}$. If parts of the uncertainty band of a drop lie outside all defined classes, these parts are discarded. Apart from that, no drops are "lost".

Note that the class in which $\Theta_{\text{con},i}$ is located need not be the class where the weight of the considered drop is maximal because $\Theta_{\text{con},i}$ is usually not the center of the uncertainty band due to the hemisperical target geometry.

4.4.2 Improved mean values

So far, pure arithmetic mean values of a quantity X per Θ-class have been applied:

$$X_{10,k,\text{class}\,n} = \frac{\sum_{i(k,\text{class}\,n)} X_i}{\sum_{j(k,\text{class}\,n)} 1} \,. \tag{4.8}$$

$\sum_{i(k,\text{class}\,n)}$ signifies the summation over all drops i of direction k in the Θ-class n, where $k = 1$ for primary drops and $k = 2, 3$ for secondary drops.

The definition of mean values is now generalised and replaced by

$$X_{ab,k,\text{impro},\text{class}\,n} = \left(\frac{\sum_{i(k,\text{class}\,n)} X_i^a \cdot w_{n,i} \cdot \eta_{\text{val},i}}{\sum_{j(k,\text{class}\,n)} X_j^b \cdot w_{n,j} \cdot \eta_{\text{val},j}} \right)^{1/(a-b)} \,, \tag{4.9}$$

where a, b are integers and in case of arithmetic means chosen as $a = 1$, $b = 0$.

Figure 4.31 presents the relative differences

$$\left| \frac{X_{10,k,\text{impro},\text{class}\,n} - X_{10,k,\text{class}\,n}}{X_{10,k,\text{impro},\text{class}\,n}} \right| \tag{4.10}$$

for the diameters, wall-normal and wall-tangential velocity components of the exemplary measurement, see Table 4.1. In the mean impact area the deviations are not very large in contrast to the outer areas where the sample numbers are lower and where the secondary drops which move almost tangentially to the target show large values of $\Delta\Theta_{\text{con},i}$.

Restriction to numerical modelling. As explained in the introduction of the current section, the spatial resolution over the target cannot be transferred to numerical modelling. This means that the mean values which have been considered for every Θ-class so far have to be condensed to one representative value per quantity for that application.

In a first attempt, the averages obtained in the central impact class could be used. Yet, this does not hold because especially secondary drops are distributed over a certain Θ-range with non-constant properties. And it has to be the aim to represent the properties of all drops in the mean values, i.e. to represent the whole distribution of all drops and not just of those in the center.

Finally, all measured primary and secondary drops are summed up over the different Θ-classes and means are defined analogously to Equation 4.9, except that sums run over all drops of one direction k, not only over those of a single Θ-class:

$$X_{ab,k,\text{impro}} = \left(\frac{\sum_{i(k)} X_i^a \cdot \eta_{\text{val},i}}{\sum_{j(k)} X_j^b \cdot \eta_{\text{val},j}} \right)^{1/(a-b)} \,. \tag{4.11}$$

Concerning numerical input and output, secondary drop directions are oriented only relative to the primary drop directions. Wall-normal and wall-tangential velocity components defining the latter are always given as positive arguments in the interaction routines. The impact angle which is defined relative to the wall in CFX is consequently restricted to the range $[0°, 90°]$. Therefore, some definitions and naming conventions are eventually slightly changed:

- The wall-normal velocity component is defined positively for both primary and secondary drops i:
$$v_{\mathrm{N},ab,k} := |U2_{ab,k,\mathrm{impro}}| \; . \tag{4.12}$$
- The wall-tangential velocity component is defined positively for primary drops; secondary drops keep their relative sign as compared to primary drops:
$$\begin{aligned} v_{\mathrm{T},ab,1} &:= |V2_{ab,1,\mathrm{impro}}| \;, \\ v_{\mathrm{T},ab,2/3} &:= \mathrm{sign}\left(\frac{V2_{ab,2/3,\mathrm{impro}}}{V2_{ab,1,\mathrm{impro}}}\right) \cdot v_{\mathrm{T},ab,1} \; . \end{aligned} \tag{4.13}$$

In the following Chapter 5, every mean value is understood in the way presented and the index "impro" is omitted. The distributions associated to the mean values are those of all drops of the considered direction taken together - independent of the individual wall contact points.

4.5 Flux densities

The evaluation procedure for a single measurement is concluded with the declaration of mass and number ratios of secondary to primary drops necessary for modelling. This is connected with a general look on the declaration of flux density[3] values. These have to be defined with respect to spray/wall interaction, hence differently from those of a free spray.

Generally, the flux density of an arbitrary scalar quantity X in a free spray can be written as, see [2], [61]:

$$\vec{q}_X = \frac{1}{t_{\mathrm{meas}}} \cdot \sum_i \frac{\eta_{\mathrm{val},i} \cdot X_i}{A_{\mathrm{val},i}} \cdot \vec{e}_i \,, \tag{4.14}$$

where t_{meas} denotes the total measurement time. $A_{\mathrm{val},i}$ signifies the so-called validation area, which is the projection of the detection volume in the direction of the drop motion. It depends on the drop size D_i and the drop trajectory. $\vec{e}_i$ is a unit vector pointing in the direction of the drop velocity. The sum includes all validated samples i.
The flux density in a specific direction $\vec{e}_\gamma$ becomes

$$q_{X,\gamma} = \vec{q}_X \circ \vec{e}_\gamma = \frac{1}{t_{\mathrm{meas}}} \cdot \sum_i \frac{\eta_{\mathrm{val},i} \cdot X_i}{A_{\mathrm{val},i}} \cdot \vec{e}_i \circ \vec{e}_\gamma \,. \tag{4.15}$$

Typical examples for the scalar property X are

---

[3] As the term "flux" is sometimes restricted to a flow rate (unit [J/s]), the term "flux density" is used in this work to underline that a quantity per time and area is denoted (unit [J/(m^2·s)]).

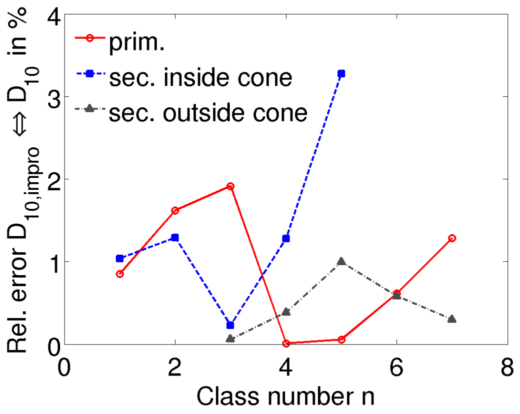

(a) D.

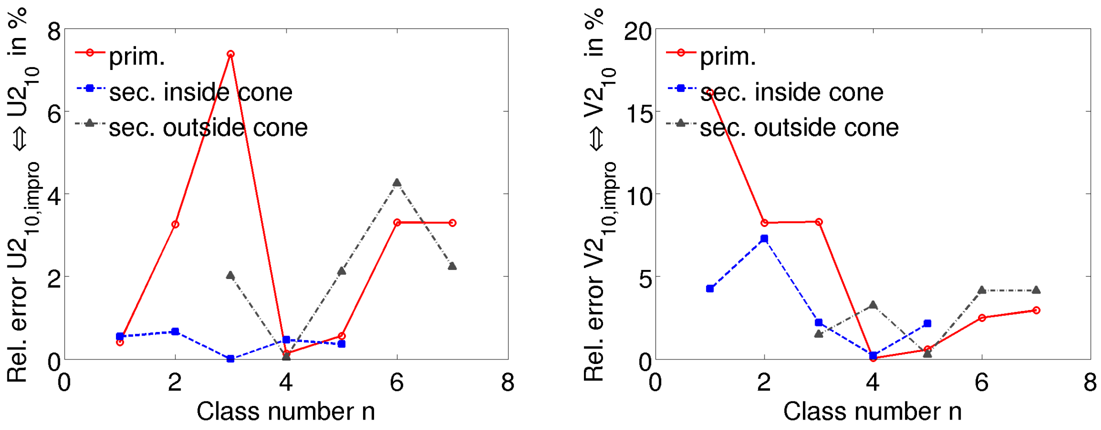

(b) U2. (c) V2.

Figure 4.31: Relative deviations between the purely arithmetic and the improved mean values in percent. Class number 4 marks the central class, class number 1 the region of smallest Θ and class number 7 the region of largest Θ considered.

- $X_i = 1$ for the number flux density, $q_{\mathrm{Nr},\gamma}$,
- $X_i = \frac{\pi}{6} \cdot D_i^3$ for the volume flux density, $q_{V,\gamma}$,
- $X_i = \frac{\pi \cdot \rho}{6} \cdot D_i^3$ for the mass flux density, $q_{m,\gamma}$,
- $X_i = \frac{\pi \cdot \rho}{12} \cdot D_i^3 \cdot v_{\mathrm{abs},i}^2$ for the kinetic enery flux density, $q_{\mathrm{E_{kin}},\gamma}$,
- $X_i = \frac{\pi \cdot \rho}{12} \cdot D_i^3 \cdot v_{\mathrm{abs},i}^2 + \pi \cdot D_i^2 \cdot \sigma$ for the total mechanical energy flux density, $q_{\mathrm{E_{tot}},\gamma}$,
- $X_i = \frac{\pi \cdot \rho}{6} \cdot D_i^3 \cdot v_{j,i}$ for the j-momentum flux density, $q_{j\text{-mom},\gamma}$.

In case of spray/wall interaction the definitions of Equations 4.14 and 4.15 used for free sprays have to be modified:

- Primary and secondary droplets have to be treated separately which is expressed by the additional index k ($k = 1$ for primary and $k = 2, 3$ for secondary drops assigned to the outside, inside the hollow cone).

- An accurate determination of absolute flux densities from PDA data is in general difficult: Due to the point-like measurement technique only a small fraction of all drops is measured at all. Furthermore, some drops might lie outside the measurable diameter range also for a well-adjusted setup. Inhomogeneous drop densities, e.g. in case of an applied oil film where secondary drops might bear oil fractions, lead to errors in mass flux densities.
  Therefore, flux density values must be treated very carefully and only the ratios of secondary to primary values in an arbitrary direction $\overrightarrow{e}_\gamma$ should be used if spray/wall interactions are considered. It is assumed that problems concern primary and secondary drops equally and therefore are reduced[4] when expressed in relative values.

- Considering spray/wall interaction where flux densities on the target are of interest, it does not make sense to employ the validation area $A_{\mathrm{val},i}$ in the measurement point as the reference area. Instead, the projection of $A_{\mathrm{val},i}$ on the target should be used. For the considered hemispherical target its calculation is not easy. But, as the problem is reduced to two dimensions and only ratios of secondary to primary flux densities are considered, the already calculated values $d_{w,i}$ can be applied instead.

Summarised, the following ratio of secondary ($k = 2, 3$) to primary ($k = 1$) flux densities of a scalar quantity X in direction $\overrightarrow{e}_\gamma$ is considered in the treatment of spray/wall interaction:

$$\Gamma_{X,k=2/3,\gamma} = \frac{q_{X,k=2,3,\gamma}}{q_{X,k=1,\gamma}} = \frac{\sum_{i(k=2,3)} \frac{\eta_{\mathrm{val},i} \cdot X_i}{d_{w,i}} \cdot \overrightarrow{e}_i \circ \overrightarrow{e}_\gamma}{\sum_{j(k=1)} \frac{\eta_{\mathrm{val},j} \cdot X_j}{d_{w,j}} \cdot \overrightarrow{e}_j \circ \overrightarrow{e}_\gamma} \,. \tag{4.16}$$

If the direction does not matter and if only an overall ratio is of interest, the equation reduces to:

$$\Gamma_{X,k=2/3} = \frac{q_{X,k=2,3}}{q_{X,k=1}} = \frac{\sum_{i(k=2,3)} \frac{\eta_{\mathrm{val},i} \cdot X_i}{d_{w,i}}}{\sum_{j(k=1)} \frac{\eta_{\mathrm{val},j} \cdot X_j}{d_{w,j}}} \,. \tag{4.17}$$

For numerical modelling without a resolution in Θ, the definitions of overall, relative flux densities in Equations 4.16 and 4.17 can be directly used. For the exemplary measurement the mass and number flux ratios $\Gamma_{m,2} \approx 44.8\%$, $\Gamma_{\mathrm{Nr},2} \approx 71.7\%$ and $\Gamma_{m,3} \approx 36.5\%$, $\Gamma_{\mathrm{Nr},3} \approx 28.4\%$ result for the secondary drops assigned to the outside and inside of the hollow cone respectively. In contrast to relative mass flux densities, relative number flux densities may exceed 100% also on a dry target.

---

[4] Note that a small fraction of measured drops could not be assigned to a wall contact point and has been neglected. Presumably, this fraction consists predominantly of secondary drops due to their small reflection angle. It is assumed that this fraction is approximately equal to the primary drops filtered out, see Section 4.3.2. For confirmation some tests have been performed with positive results.

Sometimes overall flux densities are used to calculate mean values, e.g. [28], [59], instead of definining them as in Equation 4.11:

$$\begin{aligned}
v_{\mathrm{N},10,k,\mathrm{flux},\gamma} &= \frac{q_{\text{N-mom.},k,\gamma}}{\rho \cdot q_{V,k,\gamma}}\,, \qquad (4.18)\\
v_{\mathrm{T},10,k,\mathrm{flux},\gamma} &= \frac{q_{\text{T-mom.},k,\gamma}}{\rho \cdot q_{V,k,\gamma}}\,,\\
\mathrm{D}_{30,k,\mathrm{flux},\gamma} &= \left(\frac{6 \cdot q_{V,k,\gamma}}{\pi \cdot q_{\mathrm{Nr},k\gamma}}\right)^{1/3},\\
v_{\mathrm{abs},20,k,\mathrm{flux},\gamma} &= \left(\frac{2 \cdot q_{\mathrm{E}_{kin},k,\gamma}}{\rho \cdot q_{V,k,\gamma}}\right)^{1/2} \quad \text{etc.}\,.
\end{aligned}$$

The direction $\overrightarrow{e}_\gamma$ is commonly chosen normal to the target, which gives $\overrightarrow{e}_i \circ \overrightarrow{e}_\gamma = |U2_i|/\sqrt{U2_i^2 + V2_i^2}$.
As only relative flux densities enter the defintions of Equations 4.18, such mean values can also be considered reliable. However, the use of direct means is preferred in the following because flux densities are only indirectly measured PDA data and therefore in general less accurate.

A spatial resolution in Θ, i.e. a distinction of Θ-classes, is not accounted for in Equations 4.16 and 4.17. This is sufficient for the application of the results in numerical modelling. Yet, if the Θ-dependence of diameters and velocity components is of interest, also the number or mass flux densities have to be resolved in Θ. Moreover, it is useful to consider number flux densities per Θ-class to find out where mean values are reliable and where they are not due to small sample numbers:

$$\Gamma^*_{X,k,\mathrm{class}\,n} = \frac{q_{X,k,\mathrm{class}\,n}}{q_{X,k}} = \frac{\sum_{i(k,\mathrm{class}\,n)} \frac{w_{n,i}\cdot\eta_{\mathrm{val},i}\cdot X_i}{d_{w,i}}}{\sum_{j(k)} \frac{\eta_{\mathrm{val},j}\cdot X_j}{d_{w,j}}}\,. \qquad (4.19)$$

The weighting factor $w_{n,i}$ must be included in this declaration, which focuses on one Θ-class, in contrast to the definitions where all drops, i.e. all Θ-classes, are summed up (the weights sum up to unity there).
If secondary and primary values are to be compared per Θ-class, the same reference value, for example $q_{X,k=1}$, is to be used:

$$\Gamma_{X,k,\mathrm{class}\,n} = \frac{q_{X,k,\mathrm{class}\,n}}{q_{X,k=1}} = \frac{\sum_{i(k,\mathrm{class}\,n)} \frac{w_{n,i}\cdot\eta_{\mathrm{val},i}\cdot X_i}{d_{w,i}}}{\sum_{j(k=1)} \frac{\eta_{\mathrm{val},j}\cdot X_j}{d_{w,j}}}\,, \qquad (4.20)$$

where $\sum_{\mathrm{class}\,n} \Gamma_{X,k,\mathrm{class}\,,n} = \Gamma_{X,k}$.

For the exemplary measurement $\Gamma^*_{m,k,\mathrm{class}\,n}$, $\Gamma^*_{\mathrm{Nr},k,\mathrm{class}\,n}$ and $\Gamma_{m,k,\mathrm{class}\,n}$, $\Gamma_{\mathrm{Nr},k,\mathrm{class}\,n}$ are shown in Figure 4.32. Primary drops are found locally restricted to the central impact region in comparison to secondary drops which show a broader distribution over several Θ-classes. This is due to the fact, that secondary drops can also be torn off the forming wall film in some distance to the central impact region, cf. Figure 4.33. As $q_{X,k=1,\mathrm{class}\,n}$ tends to zero in such distant classes n, it becomes clear that the possibly first idea to consider $q_{X,k,\mathrm{class}\,n}/q_{X,k=1,\mathrm{class}\,n}$ instead of Equation 4.20 is not reasonable for a comparison of different directions (including a spatial resolution).

It has to be added that the measurement grid and the resulting resolution in Figure 4.32 should be finer, if spatially resolved fluxes and best values were to be used further which is not the case here.

In summary, it has to be stressed that representative values extracted from a measurement usually differ if different definitions are chosen. Comparisons to other experimental data or to simulations should be based on the same definitions. This is also true for the calculation of derived quantities like Reynolds or Weber numbers: Values calculated with mean values like D_{10} deviate from those averaged over the single drop values, which are to be preferred und which are used in this work. Table 4.5 illustrates these aspects.

Mean values based on		Relative error
Equation 4.11	flux definitions of Equations 4.18	
$v_{\mathrm{N},10,1}$ 32.30 m/s	$v_{\mathrm{N},10,1,\mathrm{flux},\mathrm{N}}$ 36.84 m/s	14.4%
$D_{30,1}$ 52.20 μm	$D_{30,1,\mathrm{flux},\mathrm{N}}$ 52.59 μm	0.18%
$\mathrm{Re}_{\mathrm{N},10,1}$ (single values are averaged) 2373	$\mathrm{Re}_{\mathrm{N},10,1}$ (calculated with means derived from fluxes) 2885	21.6%

Table 4.5: Differences of mean values due to different definitions. The underlying data of primary drops are taken from the exemplary measurement, see Table 4.1. The errors are calculated relative to the values in the first column.

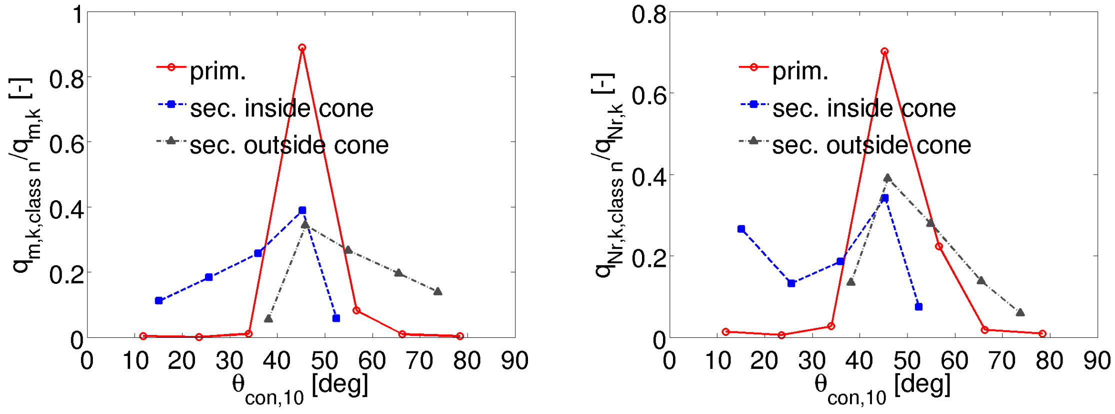

(a) $\Gamma^{*}_{m,k,\mathrm{class}\,n} = q_{m,k,\mathrm{class}\,n}/q_{m,k}$.

(b) $\Gamma^{*}_{\mathrm{Nr},k,\mathrm{class}\,n} = q_{\mathrm{Nr},k,\mathrm{class}\,n}/q_{\mathrm{Nr},k}$.

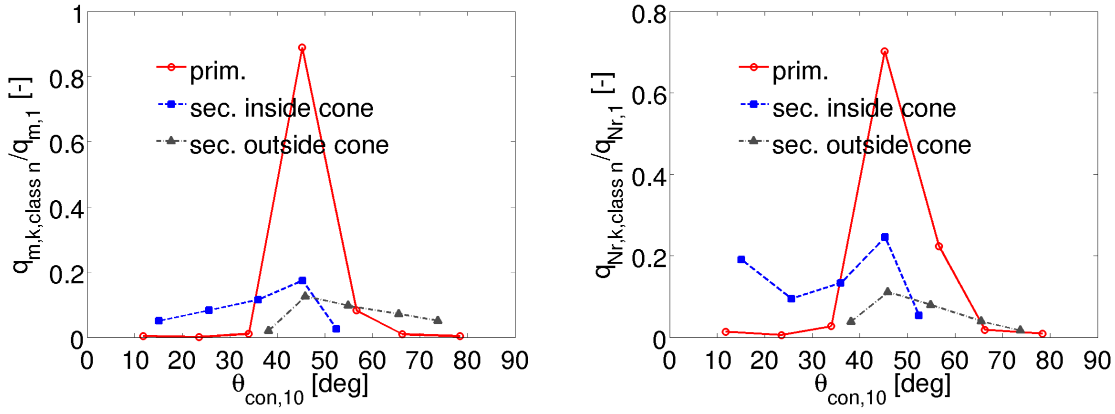

(c) $\Gamma_{m,k,\mathrm{class}\,n} = q_{m,k,\mathrm{class}\,n}/q_{m,k=1}$.

(d) $\Gamma_{m,k,\mathrm{class}\,n} = q_{m,k,\mathrm{class}\,n}/q_{m,k=1}$.

Figure 4.32: Relative mass and number flux densities resolved in Θ.

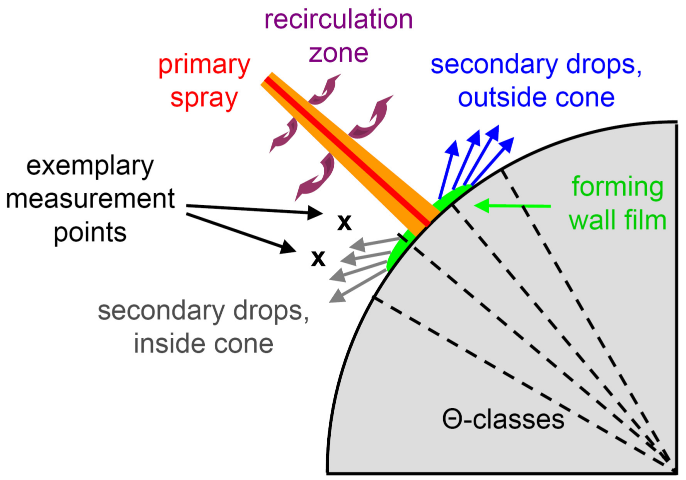

Figure 4.33: Secondary drops may be torn off the forming wall film distant from the central impact region. The wall film itself has not been directly captured in the measurements.

Chapter 5

Empirical model of spray impact

Having developed the evaluation procedure concerning data of an individual measurement, i.e. of one parameter setting, the focus is now cast on a variation of parameters. Different values of the wall temperature T_{wall} and of the mean primary Reynolds number $\text{Re}_{\text{N,10,prim}}$ are considered for an impact on an initially dry target. The influence of an oil film on the surface is addressed separately.
After an analysis of the impact mechanism, a new empirical model is finally formulated describing the normal impact of dense and high-pressure hollow cone sprays where existing models have been shown to be inadequate. An extrapolation to oblique impacts is suggested.

5.1 Influence of wall temperature and mean Reynolds number

Measurements have been performed for varied wall temperatures T_{wall} and for two different injector positions leading to different impacting drop sizes and velocities. To characterise the latter, the averaged normal Reynolds number $\text{Re}_{\text{N,10,prim}}$ of the primary drops is considered (see Section 4.5 for its definition). This choice is more or less arbitrary and e.g. the Weber number could also be selected.
The influences of T_{wall} and $\text{Re}_{\text{N,10,prim}}$ on the secondary spray properties are discussed in this section for an initially dry target[1].

High-speed images are used to confirm and interprete the results qualitatively. They are captured with a Photron high-speed video camera (Fastcam Sa1.1, model 675K-M1) at 54 000 frames per second and a shutter speed of 10^{-6} s. The injection duration is set to $\Delta t_i = 10\,\text{ms}$, which is short compared to $\Delta t_i = 50\,\text{ms}$ in PDA measurements where the large value is chosen to collect enough drop data for good statistics. The rail pressure remains at 50 bar. Due to the large spray density only the secondary drops outside of the spray hollow cone can be observed.

---

[1] Tests on the primary data have been performed to confirm that the impacting spray properties did not change notably for fixed injector position.

5.1.1 Experimental results

In order to study the parameter influences, relative mean values from every measurement, i.e. from every parameter setting, are compared. Secondary to primary ratios of averaged wall-normal and wall-tangential velocity components, diameters and mass flux densities

$$\frac{v_{\mathrm{N,10,sec}}}{v_{\mathrm{N,10,prim}}}\,,\quad \frac{v_{\mathrm{T,10,sec}}}{v_{\mathrm{T,10,prim}}}\,,\quad \frac{D_{\mathrm{10,sec}}}{D_{\mathrm{10,prim}}} \text{ and } \frac{q_{m,\mathrm{sec}}}{q_{m,\mathrm{prim}}}\,, \tag{5.1}$$

defined as described in Section 4.4, are considered. Secondary droplets assigned to the outside and to the inside of the spray hollow cone respectively are distinguished.
As the same mean values can be obtained from totally different distribution functions, see [37], it is not sufficient to consider only mean values but the underlying distributions have to be tested on parameter influences, too. However, a separate presentation is omitted at this point, because the same results are obtained as for the mean values, cf. Section 5.4 for more details.

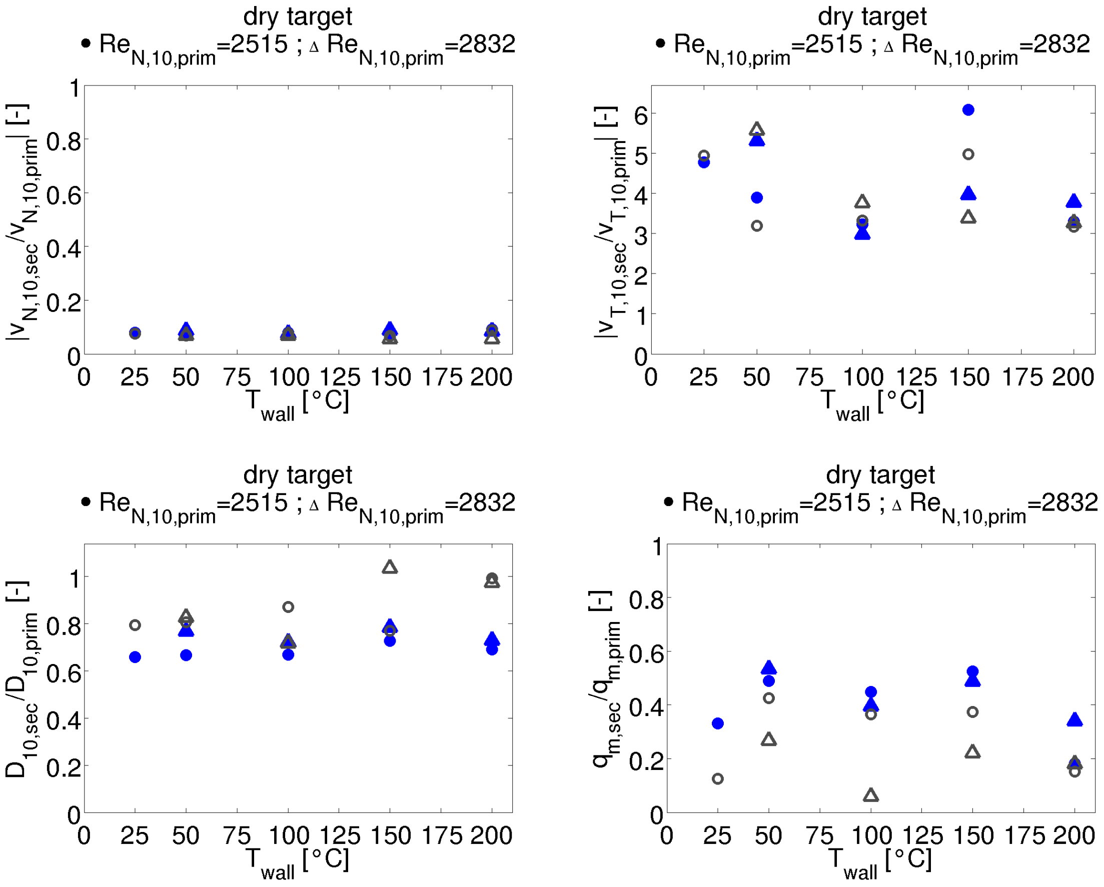

Figure 5.1: Influence of T_{wall} for a dry target. Secondary drops outside the hollow cone are drawn in blue, full symbols, secondary drops inside the hollow cone in grey, empty symbols.

In Figures 5.1 and 5.2 the secondary to primary mean values of Equation 5.1 are shown for a variation in T_{wall} and $\mathrm{Re}_{\mathrm{N,10,prim}}$. The influences of both parameters are revealed to be very weak. In every case the following statements can be made:

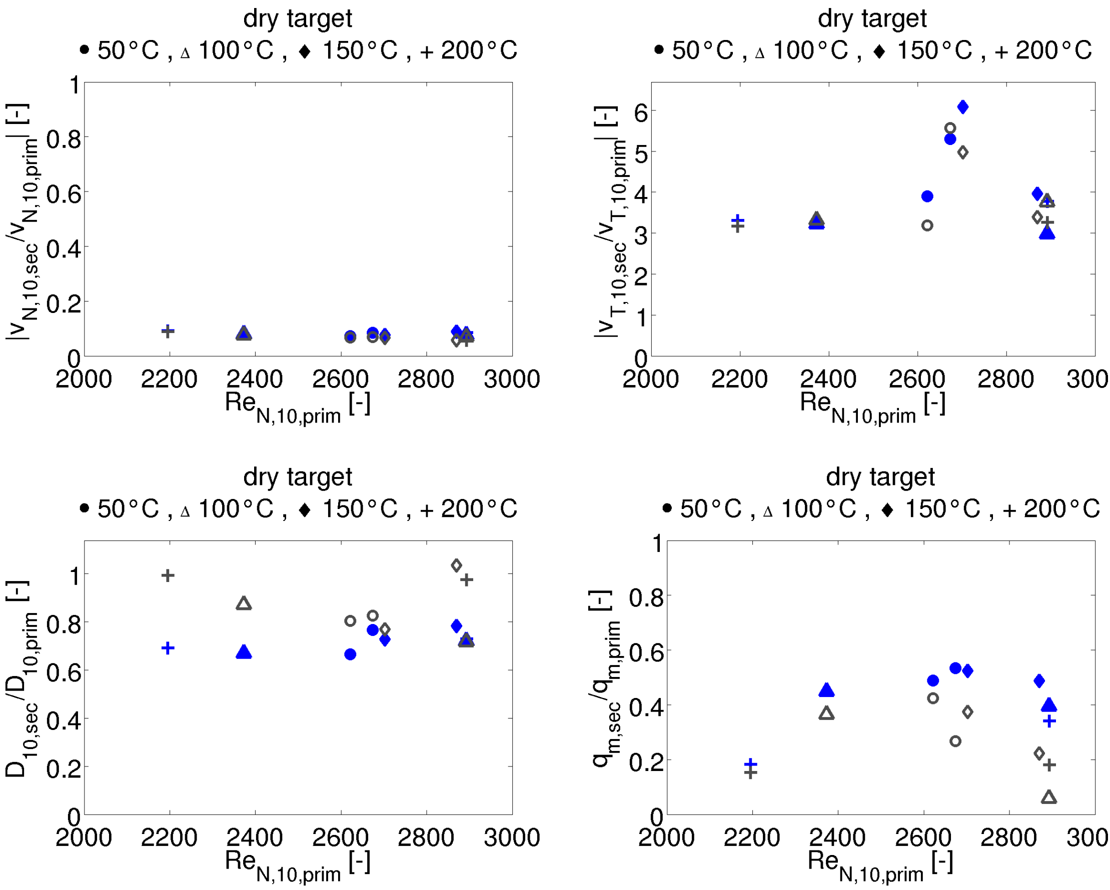

Figure 5.2: Influence of $Re_{N,10,prim}$ for a dry target. Secondary drops outside the hollow cone are drawn in blue, full symbols, secondary drops inside the hollow cone in grey, empty symbols.

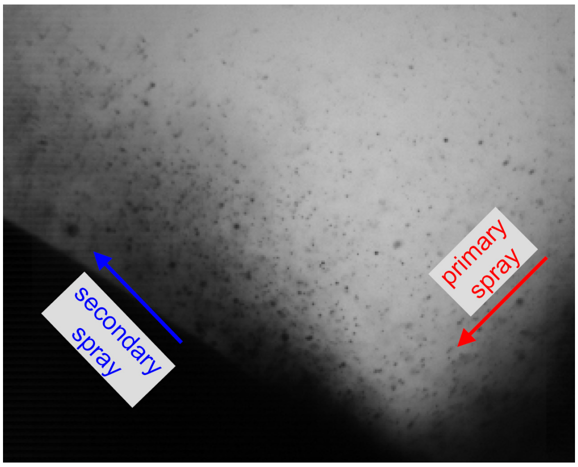

Figure 5.3: High-speed image for a dry target ($T_{wall} \approx 30°C$). In the bottom left corner a sector of the target can be seen with the secondary spray drops moving rather tangentially to the surface.

- The secondary spray propagates in a rather tangential direction relative to the target, i.e. primary wall-normal momentum is transformed to secondary wall-tangential momentum. This is confirmed by high-speed images, see Figure 5.3. The wall-normal velocity components of secondary drops are reduced to about 10% of the primary values whereas the wall-tangential velocity components are increased to about 3 to 6 times the primary values which are very small due to the almost normal impact. Secondary drops outside and inside the spray cone show approximately the same values.

- The secondary drop diameters are reduced to approximately 70% of the primary values. Inside the spray cone secondary drops tend to be larger than outside.

- The overall ratio of secondary to primary mass flux densities, which comprises secondary drops inside as well as outside the hollow cone, amounts to 50% to 80% percent. The fraction measured inside tends to be smaller than that outside which could be due to the impact being not ideally normal. But, as diameters are at the same time slightly larger inside the spray cone, it is more probable that less drops are registered and validated there, where measurements are more difficult due to the high spray density.
  Compared to the velocity components or the diameters, the values of the mass ratios fluctuate strongly. This reflects that measuring flux densities is in general less accurate[2].

5.1.2 Comparison to Elsässer's single drop impact model

The minor parameter influence of T_{wall} and $\text{Re}_{\text{N,10,prim}}$ observed in the experiment leads to the conclusion that the impact phenomena of the considered dense, high-pressure spray differ completely from those of single drop impacts. For these, the influence of wall temperature and impacting drop properties are decisive and entirely different post-impingement characteristics may occur, see Section 1.4. To illustrate that this would be the case for the parameter ranges considered in the experiments, the wall temperature variation is studied exemplarily for Elsässer's single drop model, see Section 1.4.2.1. The variation in $\text{Re}_{\text{N,10,prim}}$ does not produce new ideas.
The mean properties of the measured, impacting drops, $v_{\text{N,10,prim}}$, $v_{\text{T,10,prim}}$ and $D_{\text{10,prim}}$, are put as arguments into the model calculation. The thickness h_{film} of the forming and accumulating wall film on spray impact, which is another argument of Elsässer's model, is set to zero because its time-dependence cannot be accounted for at this point.

Figure 5.4 shows that the values of T_{wall}, considered in the experiments performed in this work, range from the cold wetting to the hot non wetting regime. The small hot wetting regime in-between is not directly addressed by one of the measurements. Changing the regimes, Elsässer's model predicts a jump in the ratio of the wall-normal velocity components in contrast to the measured results. The diameter ratio is predicted much smaller. And the mass ratios, which have to be compared to the sum of the mass ratios measured inside and outside the spray cone in the experiment, are underestimated in the cold wetting regime and overestimated in the hot non wetting regime, where all impacting mass is transferred to the secondary spray.

---

[2] Even for single drop impacts the determination of secondary to primary mass ratios is usually problematic, see [50].

In summary, the measured results and the outcome of Elsässer's model disagree, as expected.

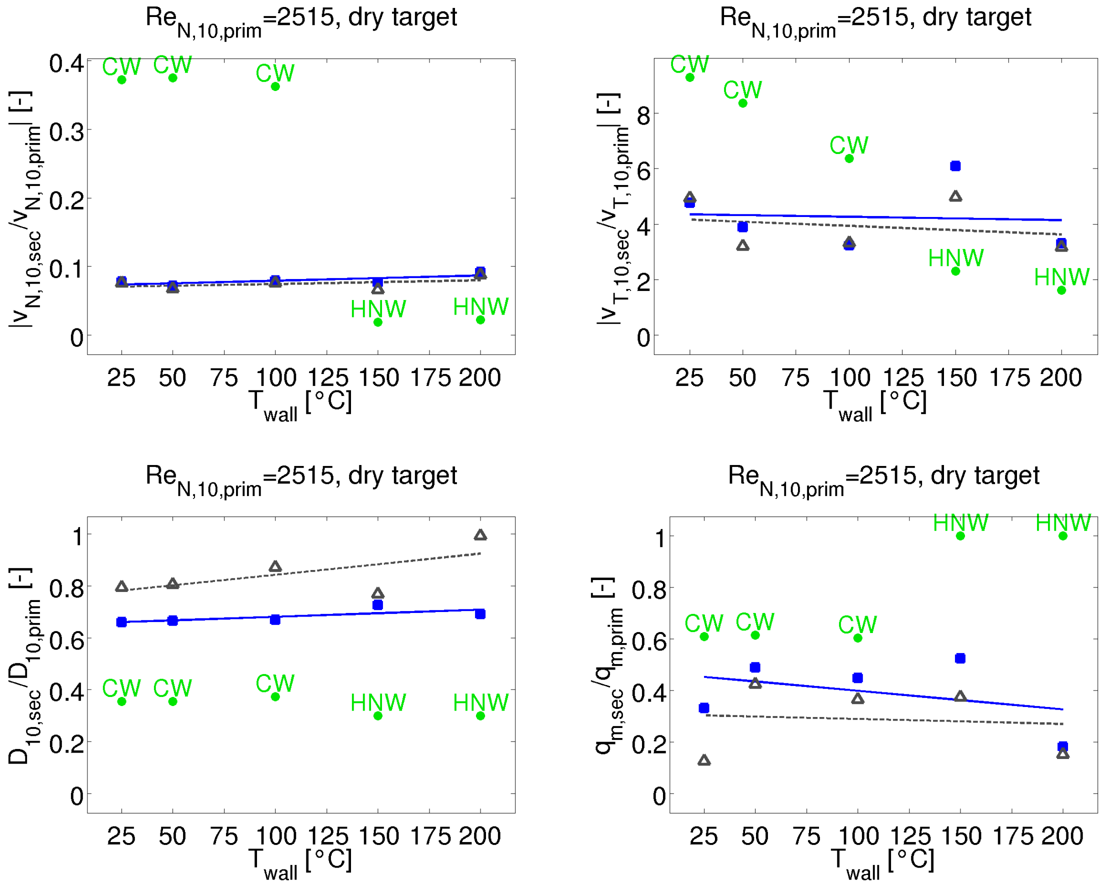

Figure 5.4: Influence of T_{wall}: comparison of measured results (secondary drops outside the hollow cone are drawn in blue, full symbols, secondary drops inside the hollow cone in grey, empty symbols) with Elsässer's model (green symbols, CW denotes the cold wetting regime with splashing and HNW the hot non wetting regime with one boiling parcel.)

5.1.3 Comparison to Roisman's/Horvat's data and interpretation

The fact that single drop models fail supports the importance of drop/drop interactions for dense sprays. Kuhnke's and especially Roisman's/Horvat's model should provide better results. Both models are not deterministic as Elsässer's single drop model but depict secondary distributions using random numbers. Consequently, individual single outcomes can vary significantly and a comparison with measured mean values, analogous to Figure 5.4, is rather restricted. Therefore, a more meaningful comparison of the distributions is postponed to the simulation of the experiment in Section 6.2.

Yet, for Roisman's/Horvat's model not only the final model correlations, which could be applied to the respective conditions, are available but also the underlying data, which have been used to build the model, see [59] and courtesy of Priv.-Doz. Dr.-Ing. habil. I. Roisman. These refer to the normal impingement of a relatively sparse full cone spray of water on a cold and initially dry surface for Reynolds numbers smaller than 2000 on impact. Corona splash is identified as main impact phenomenon.

In order to analyse the impact mechanisms for dense and high-pressure hollow cone sprays, the data gathered in this work are compared to those of Roisman/Horvat in a first step. The latter extracted mean values based on flux values, i.e. $v_{\mathrm{N},10,k,\mathrm{flux},\gamma}$ and $D_{30,k,\mathrm{flux},\gamma}$ ($k = 1,2$ for primary, secondary droplets) are defined as in Equations 4.18 with $\overrightarrow{e}_\gamma$ being normal to the target surface. For convenience, these quantities are renamed to U_b, D_b and U_a, D_a where the subscripts b and a denote "before" and "after" impact, i.e. primary and secondary drops. Derived quantities are calculated using the means, e.g. $\mathrm{Re}_b = \frac{\rho \cdot U_b \cdot D_b}{\mu}$.

For the comparison in this section, the current experimental data are exceptionally evaluated in the same way as Roisman's/Horvat's data, which is important for a reasonable analysis as described in Section 4.5. U_a and D_a are determined for secondary drops assigned to the outside of the spray cone. All measurements are included in the comparison due to the insignificant influences of the wall temperature and the mean primary Reynolds number.

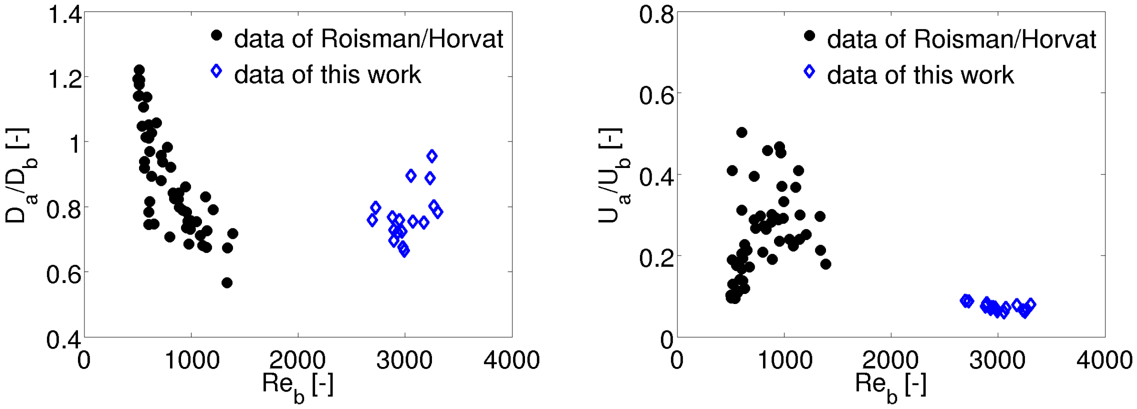

(a) Diameter ratio.

(b) Ratio of wall-normal velocity components.

Figure 5.5: Comparison of Roisman's/Horvat's data with the measured data.

Figure 5.5 shows the secondary to primary ratios of diameters and wall-normal velocity components versus the mean impinging Reynolds number for Roisman's/Horvat's data ($\mathrm{Re}_b > 500$) in comparison to the new data obtained in this work:

- The behaviour of the diameter ratio is different although the values are of the same order.
- Especially the normal velocity values[3] of Roisman's/Horvat's data scatter over a large range in contrast to the new values which only display a negligible parameter influence.
- The data sets refer to different ranges of the Reynolds numbers with higher values for the new measurements. A gap around $\mathrm{Re}_b = 2000$ contains no data points.

---

[3] Note that these are not used directly for modelling in Roisman's/Horvat's model. Instead a relation between the volume flux ratio Γ_V and the energy flux ratio $\Gamma_{\mathrm{E_{tot}}}$ is considered, see Section 1.4.2.

It is deduced that the impact phenomena are different for both data sets. In Roisman's/Horvat's model, corona splash is stated: Finger-like jets are created at unstable crown rims and break up into secondary drops. Their diameters are assumed to scale in the same way as the finger radius, which finally gives $D_a/D_b \propto \mathrm{Re}_b^{-0.5}$, see Section 1.4.2. This presumes an undisturbed crown formation for an individual spray drop, i.e. a small spray density. In contrast to the relatively sparse full cone spray considered by Roisman/Horvat, the disturbance of crown formation by neighbouring drops cannot be neglected for the dense hollow cone spray addressed in this work. This can be proven by a rough estimation which shows that the necessary time and space are not available:

- Using the non-dimensional time $\tau = t \cdot v_{\mathrm{prim}}/D_{\mathrm{prim}}$, reference [82] describes the maximum time of crown propagation as

  $$\tau_{\max} = 5.44 \cdot Z \qquad \text{with} \qquad Z = \frac{\mathrm{We}_{\mathrm{prim}}}{\mathrm{Re}_{\mathrm{prim}}^{0.5}} = \frac{D_{\mathrm{prim}}^{0.5} \cdot v_{\mathrm{prim}}^{1.5} \cdot \rho^{0.5} \cdot \mu^{0.5}}{\sigma}. \tag{5.2}$$

  Inserting the liquid properties of isooctane from Table 3.1 and approximating the mean spray impact properties of the experiment as $v_{\mathrm{prim}} \approx 35\,\mathrm{m/s}$ and $D_{\mathrm{prim}} \approx 50\,\mu\mathrm{m}$, one gets $\tau_{\max} \approx 220$ and $t_{\max} \approx 0.31\,\mathrm{ms}$ respectively.
  Note that a lot of parameters, like the wall film thickness, are known to influence the crown formation, cf. [39], [43]. They are neglected at this point.

- Equation 5.2 is based on a mass and momentum balance in the axial crown direction and some results from [95] and [10]. These references also give estimates for the crown expansion in form of its radius R_{crown}:

  - In [95] the growth of crowns formed on the normal impact of an ethanol drop chain on a thinly wetted wall is described. $R_{\mathrm{crown}}(\tau)/D_{\mathrm{prim}} = K \cdot (\tau - \tau_0)^n$ is obtained with the non-dimensional time $\tau = t \cdot 2 \cdot \pi \cdot f$. f denotes the drop frequency and τ_0 a constant, equivalent to a virtual time origin. The exponent is set to $n = 0.5$.
  - In [10] this behaviour is confirmed for the impact of single water drops. Using $\tau = t \cdot v_{\mathrm{prim}}/D_{\mathrm{prim}}$, $n \approx 0.4$ is found. This exponent is shown to be independent of the film thickness and of the impact velocity in contrast to K which is found to depend on the impacting Weber number ($\mathrm{We}_{\mathrm{prim}} < 1000$).

  However, the fits cannot be used to calculate the maximal radius $R_{\mathrm{crown,max}}$ because the values of K and τ_0 are not known in the current case. Therefore, an intuitive and possibly rather small estimate is chosen with $R_{\mathrm{crown,max}} = 1.5 \cdot D_{\mathrm{prim}}/2$. The area occupied by the crown is then given as $R_{\mathrm{crown,max}}^2 \cdot \pi$.

- The injected mass flux $\dot{m}_{\mathrm{inj}} = 19.4\,\mathrm{g/s}$ in the experiments is known from the injector characteristics. For a distance between target and injector of $d_{\mathrm{inj.point}} \approx 37\,\mathrm{mm}$ and a main impact Θ-area of $\Delta\Theta_{\mathrm{prim}} \approx 15°$ on the target, see Figure 4.21 in Section 4.3.2.1, the impinging mass flux density can be estimated as $q_{m,\mathrm{prim}} \approx 21\,\mathrm{kg/(s \cdot m^2)}$. Assuming spherical drops of uniform drop size $D_{\mathrm{prim}} \approx 50\,\mu\mathrm{m}$, this value leads to a number flux density $q_{\mathrm{Nr,prim}} \approx 4.6 \cdot 10^{11}\,/(\mathrm{s \cdot m^2})$.

- Finally, the number of drops which impact during crown formation can be assessed as $N_{\mathrm{impact}} = q_{\mathrm{Nr,prim}} \cdot t_{\max} \cdot R_{\mathrm{crown,max}}^2 \cdot \pi \approx 0.6$. This means, that approximately

> three out of five crowns are disturbed by newly impinging drops. This estimate is careful, as the time span $t_{\max}$ only comprises the crown propagation and not the lamella spread or the corona collapse. The number flux density is also rather underestimated in the dense spray core which probably takes less then $\Delta\Theta_{\mathrm{prim}} = 15°$. Moreover, even if a corona is not hit directly by other drops, film fluctuations may transport the influence of impingements over a large distance.

Due to this assessment ideal corona splash is ruled out as main source of secondary atomisation in case of dense spray impact. Yet, spray density is not the only important parameter where Roisman's/Horvat's and the new data sets differ: As can be seen in Figure 5.5, they also cover considerably different values of the Reynolds number that describes the ratio between inertial and viscous forces.

For Roisman's/Horvat's spray, viscous forces are important which becomes obvious in the scaling $D_a/D_b \sim \mathrm{Re}_b^{-0.5}$. An increase in the Reynolds number is equivalent to a decrease of viscosity, i.e. to an increase in the tendency to break up into smaller drops. For the data gathered in this work, however, the viscous forces do no longer play a role and inertial forces strongly dominate, which is expressed in negligible influence of Re_b. Inertial forces also outweigh other forces, e.g. surface tension, which can be seen if other characteristic numbers, e.g. the Capillary number (which shows a size of ≈ 1) or the Weber number, are considered, see Section 1.4.1. The overall weighting of forces is changed and inertial forces clearly represent the decisive forces in the spray impact. As a consequence, large parameter influences are no longer to be expected in this regime. This explains well the results observed in the present experiment.

Summarised, spray impacts considered by Roisman/Horvat and those regarded in this work differ due to the mutual influence of a different spray density and of a changed force weighting. Due to the former, undisturbed corona splash cannot represent the impact phenomena in the measurements of this work and due to the latter, inertial forces dominate strongly and cause negligible parameter influences.

Unfortunately, no data could be found in literature to close the gap around $\mathrm{Re}_b \approx 2000$ in Figure 5.5. Further experiments are hence necessary to catch the transition from low to high Reynolds numbers as well as from sparse to dense sprays and to finally formulate a global model.

5.2 Oil film on the target

Besides the wall temperature and the impinging Reynolds number, the initial target coverage has also been varied in the experiments, see Chapter 3: The surface has been considered in a dry state or covered by an oil film of non-dimensional depth $\delta = h_{\mathrm{film}}/D_{10,\mathrm{prim}}$. To the author's knowledge, the impact on a film of different material properties than the spray has not been studied quantitatively in literature yet, not even for single drop impacts.

Secondary drops might carry an unknown amount of oil film mass. The refractive index is then different from that of pure isooctane, and the diameter and consequently mass flux determination with the PDA system includes additional errors which are considered to be small, though.

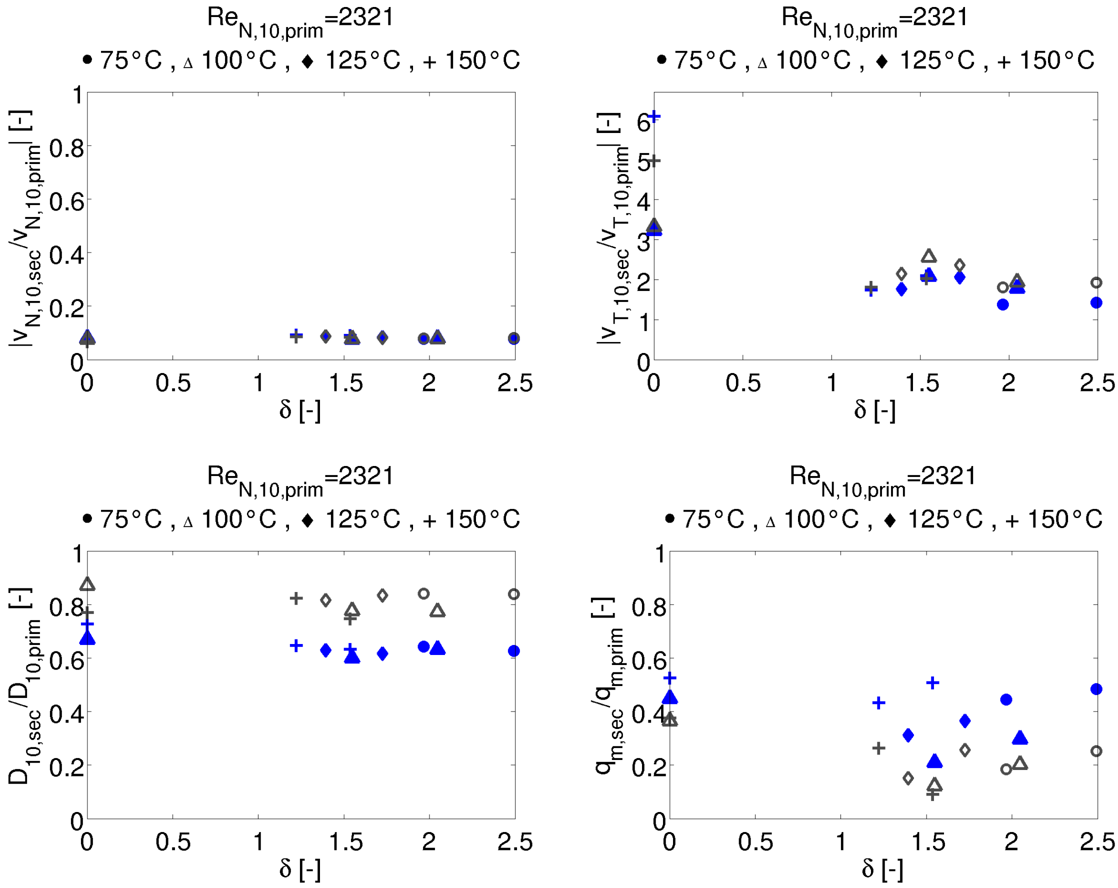

Figure 5.6: Influence of δ. Secondary drops outside the hollow cone are drawn in blue, full symbols, secondary drops inside the hollow cone in grey, empty symbols.

In order to analyse the influence of an oil coverage on the post-impingement characteristics, relative mean values (cf. Equation 5.1) for different values of δ are compared in Figure 5.6. The same statements as for the variation in T_{wall} and $\text{Re}_{\text{N,10,prim}}$ can be drawn for the wall-normal and wall-tangential velocity components. The differences between secondary drop diameters inside and outside the spray cone seem slightly more significant.

Considering the overall trends, the influence of the oil film is very weak. High-speed images, see Figure 5.7, show the reason: The first impacting spray drops remove the oil film very quickly. After at most 2 ms the central impact area seems to be devoid of oil. The majority of subsequent primary drops no longer contacts the oil film but experiences the same situation as if the target had been initially dry which leads to secondary drops with the same properties. Spray density and inertial forces dominate the impact as described in the previous section.

For higher wall temperatures the surface of the driven oil film shows a very chaotic structure with distinct ligaments in contrast to smaller temperatures where it appears rather smooth, see Figure 5.7. Yet, this affects at most the first secondary drops, which may result from impacts on the oil film. Possibly, these secondary drops show different properties than later ones but they do not influence the overall distributions and mean values notably.

The result that the oil film is quickly driven away by the impacting spray is very important for spray targeting in engine development. Although the injection duration Δt_i

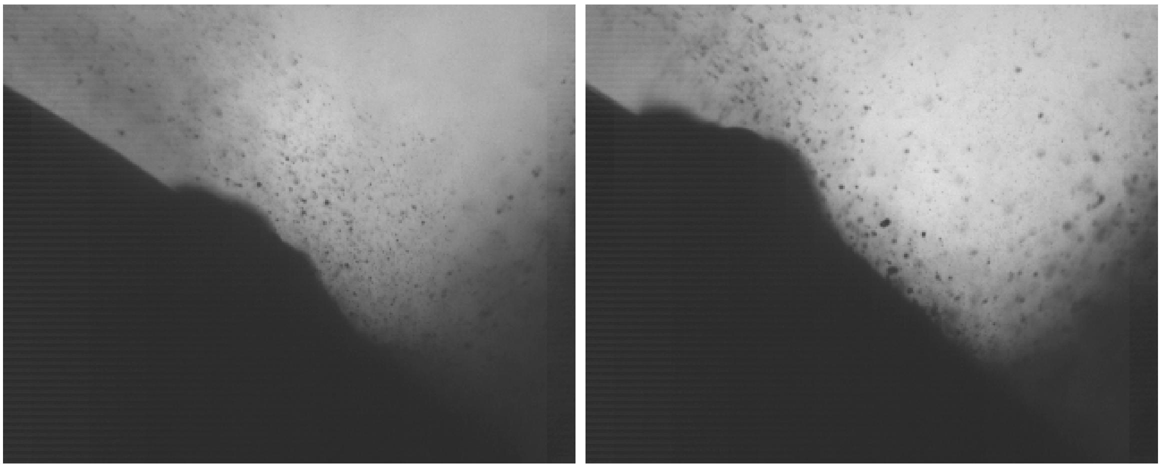

(a) $T_{\mathrm{wall}} \approx 30°\mathrm{C}$, shortly after start of impact.

(b) $T_{\mathrm{wall}} \approx 30°\mathrm{C}$, oil film is driven away.

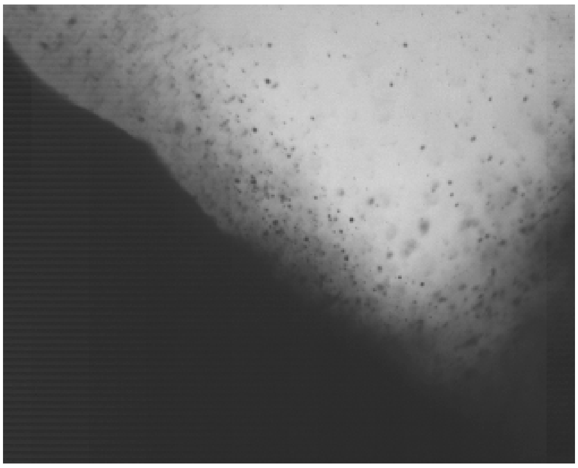

(c) $T_{\mathrm{wall}} \approx 30°\mathrm{C}$, stationary state.

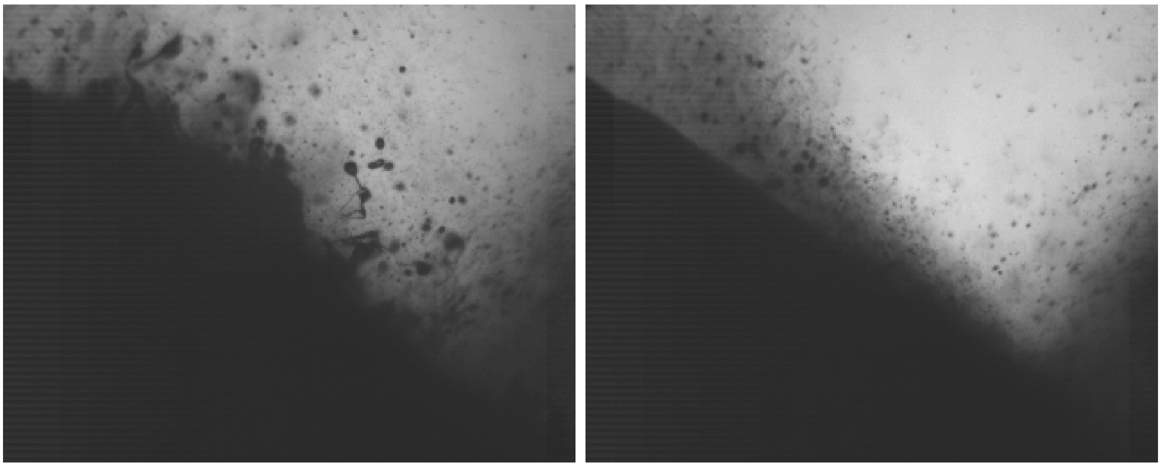

(d) $T_{\mathrm{wall}} \approx 150°\mathrm{C}$, shortly after start of impact.

(e) $T_{\mathrm{wall}} \approx 150°\mathrm{C}$, stationary state.

Figure 5.7: High-speed images for the target initially covered by an oil film, $\dot{Q}_1 \approx 0.92\,\mathrm{ml/min}$.

is smaller in an engine cycle than in the experiment (0.4 ms - 5 ms compared to 10 ms in the high-speed images and 50 ms in the PDA measurements), the timescale of the oil film removal proved to be of the same size as Δt_i. Moreover, the injection pressure is often higher (up to 200 bar compared to 50 bar in the experiments), which means even larger impacting momentum favouring the removal. This underlines that direct spray impact on the liner should be avoided to maintain the lubricating oil film.

5.3 Impact mechanism

So far, the negligible influence of T_{wall} and $\text{Re}_{\text{N,10,prim}}$ could be explained by dominant inertial forces. Moreover, undisturbed corona splash has been excluded as main phenomenon underlying impacts of a dense spray. Yet, the actual impact mechanisms still have to be clarified.
It is shown in this section that fluctuations in the forming wall film are supposed to determine the impact process for a dense, high-pressure spray. The fluctuations probably lead to ligaments which are stripped off the film and break up in secondary droplets.

5.3.1 Film fluctuations

Reference [63] states that film fluctuations are decisive for the impact of a dense spray and provides first length and velocity scales, see Equations 1.47. These can also be expressed as

$$\Lambda = D_b \cdot \left(\frac{U_b}{36 \cdot q_{V,\text{prim}}} \right)^{1/6} , \quad \tau = \frac{D_b}{\left(6 \cdot q_{V,\text{prim}}^2 \cdot U_b\right)^{1/3}} , \quad \Upsilon = \left(q_{V,\text{prim}} \cdot U_b\right)^{1/2} . \tag{5.3}$$

In that reference it is found that secondary diameters and velocities concerning the impact of a dense Diesel spray are of the same order as the associated scales.
Also for the data gathered in the present work, it can be confirmed that the scales are of the same order as the secondary diameter and velocity values, cf. Figure 5.8. It is therefore deduced that film fluctuations determine the impact.
However, the scales do not reveal correlations which could be used for modelling, and a profound understanding and description of film fluctuations still lacks.

5.3.2 Breakup of ligaments.

In the approach of [87], [21], [86] it is stated that atomisation is due to the breakup of ligaments, also called threads or fingers, which result from primary instabilities in a liquid bulk. The ligaments are defined as approximately columnar objects attached by their foot to the liquid volume from which they are stripped, cf. Figure 5.9. During that process, a ligament of initial volume $V_L = D_{L,0}^3$ is first elongated and stretched, i.e. its transverse diameter becomes smaller than $D_{L,0}$. Capillary forces try to break up the ligament in blobs, see Figure 5.10, whereas the Laplace pressure difference between the blobs, which is proportional to $\sigma \cdot (1/D_{B,1} - 1/D_{B,2})$ for two blobs of diameters $D_{B,1}$ and $D_{B,2}$, tries to coalesce them during their detachment. Due to this interplay, the final mean drop size separating from the ligament is larger than the average ligament diameter before breakup and scales with $D_{L,0}$.

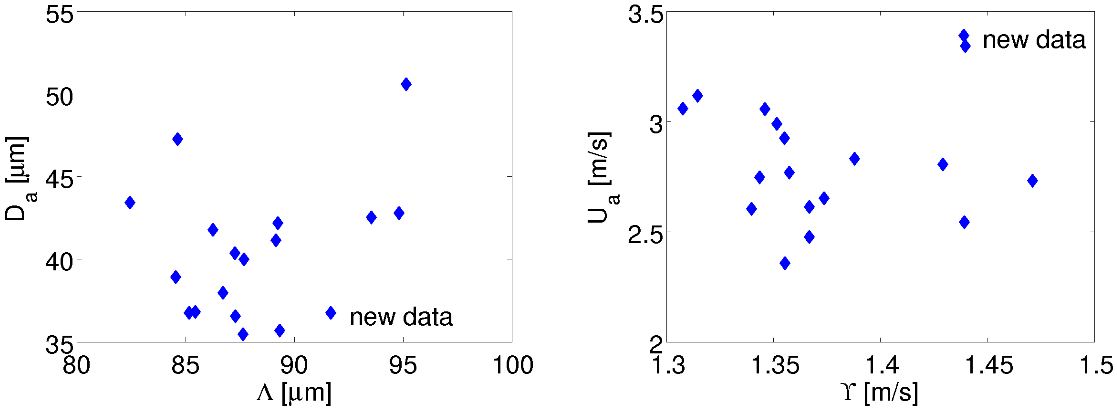

Figure 5.8: Scales for film fluctuations according to [63], calculated for the new data.

Figure 5.9: Destabilised water jet in a coaxial, fast air stream, [87]. Shear instabilities lead to the formation of ligaments whose diameter upon stretching is smaller than the final drop sizes after fragmentation.

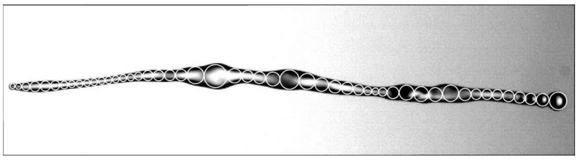

Figure 5.10: Ligament constitutive of blobs, [40].

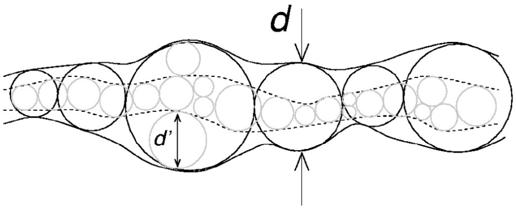

Figure 5.11: Modelling of the liquid motion and perturbations in a ligament by layers of subblobs of diameter d', [40]. The superposition of the latter gives the average size d of the blobs along the ligament.

The liquid motion in a ligament is influenced by complex perturbations due to remnant motion of the bulk or the surrounding gas stream. The associated overlapping waves are modelled by considering the sizes of the blobs as results from a superposition of several independent layers of blobs. Their widths are determined by the mean free path associated to radial motions of a fluid particle across the ligament and they interact randomly (with no correlation to the blob sizes), cf. Figure 5.11. From this notion a gamma distribution is deduced for the probability density function pdf_B describing the correlation of blob sizes before breakup of a single ligament and of drop sizes afterwards:

$$pdf_B(x) = \frac{n^n}{\Gamma(n)} \cdot x^{n-1} \cdot \exp(-n \cdot x) \quad \text{with} \quad x = \frac{D}{D_{B,0}} \,. \tag{5.4}$$

$D_{B,0}$ denotes the average blob diameter. For a smooth and uniform ligament the only parameter n of the distribution is large and a narrow size distribution results. For a very corrugated ligament n becomes small and yields a broad size distribution. The

gamma distribution is found to describe well drop sizes in various examples: from the disintegration of ligaments in a liquid sheet or a jet, drops impacting on a pool or colliding with other drops to spume and rain.
To quantify the final drop size distribution, the distribution pdf_L, characterising the ensemble of ligament sizes $D_{B,0}$ has to be considered and one gets

$$pdf(D) = \int_0^\infty pdf_L(D_{B,0}) \cdot pdf_B\left(\frac{D}{D_{B,0}}\right) dD_{B,0} \,. \tag{5.5}$$

Usually, the distribution of the ligament sizes pdf_L is narrower than the gamma distributions of the blob sizes resulting from the ligaments. The exponential tail of the gamma distributions is then maintained in the drop size distribution and has often been stated by fits of empirical data.

In the high-speed images taken in this work, where an oil film is applied on the target surface, see Figure 5.7(d), ligaments can be clearly identified. For an originally dry target, the breakup of the ligaments probably occurs closer to the impact center which cannot be seen in the high-speed images.
To test if ligament breakup actually determines the impact process observed in the experiment, the secondary size distribution of every measurement would have to be fitted to Equation 5.5. Yet, the distribution pdf_L of the ligament sizes is unknown and the argument of the gamma distribution in Equation 5.4 also depends on $D_{B,0}$. Hence, only a rough estimate can be done by fitting a general gamma distribution to the distribution of $\frac{D_\text{sec}}{D_{10,\text{sec}}}$ of every measurement:

$$pdf_\text{gamma}(x) = \frac{b^a}{\Gamma(a)} \cdot x^{a-1} \cdot \exp\left(-b \cdot x\right) \,. \tag{5.6}$$

In Figure 5.12 the results are shown for the secondary drops assigned to the outside of the spray hollow cone for two arbitrary parameter settings. The fits describe the distributions very well, which confirms the role of ligaments in the considered impacts. Only the maximum is underestimated by the fits which is most probably due to the omitted distribution pdf_L. It is striking that approximately equal values are assigned to the fit parameters a and b in every case which is a predicted restriction of the gamma distribution of Equation 5.4 describing ligament breakup.

5.3.3 Summary

In the impingement of a dense, high-pressure spray with its large insertion of momentum into the forming wall film, fluctuations of the latter probably constitute the first step of the impact mechanism. They are supposed to lead to ligaments being stripped off the film. Secondary droplets are ejected from the ligaments. The situation is summarised in Figure 5.13. For one ligament the drop size distribution can be described as a gamma distribution in dependence of the ligament size. To derive the size distribution of the entire secondary spray, the size distribution pdf_L of the ligaments would have to be known. This is not the case because the distribution pdf_L is determined by the film fluctuations and these cannot be described yet.

In Section 5.1 the influence of the wall temperature and the mean impacting Reynolds number on the secondary spray droplets has been discussed and found to be very weak

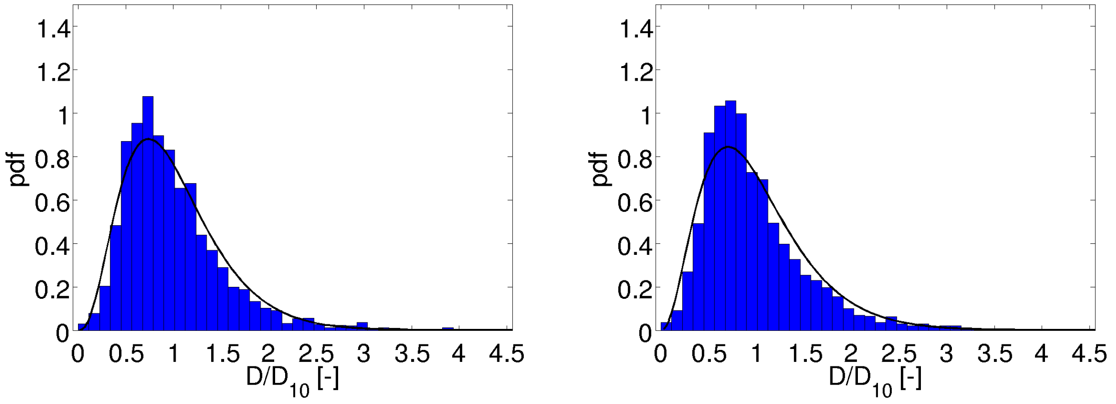

(a) $T_{\text{wall}} = 100°\text{C}$, $\delta = 0$, $\text{Re}_{N,10,\text{prim}} \approx 2370$. $a_{\text{fit}} \approx 3.817$, $b_{\text{fit}} \approx 3.815$.

(b) $T_{\text{wall}} = 150°\text{C}$, $\delta \approx 1.48$, $\text{Re}_{N,10,\text{prim}} \approx 2290$. $a_{\text{fit}} \approx 3.379$, $b_{\text{fit}} \approx 3.378$.

Figure 5.12: $D_{\text{sec}}/D_{10,\text{sec}}$ fitted by a gamma distribution for two arbitrary measurements.

due to dominant inertial forces. As the gamma distribution which describes the secondary droplet sizes for one ligament size does not depend on further parameters, it can be inferred that the parameter independence and dominance of inertial forces actually refer to the film fluctuations and hence the ligament size distribution pdf_L.

The comparison of Roisman's/Horvat's data with the data gathered in this work can also be focused. In both cases secondary drops are due to ligament/finger breakup - also for Roisman's/Horvat's data the fitted size distribution of Equation 1.98 shows an exponential tail like the gamma distribution. Yet, the ligament size distributions have to be very different: For Roisman's/Horvat's data the ligaments are produced at the rims of undisturbed coronas whose formation is influenced by viscous forces. By contrast, the film fluctuations in the measurements of this work with larger Reynolds numbers on impact are dominated by inertial forces. They are furthermore characterised by a strong disturbance between closely impacting drops due to the high spray density.

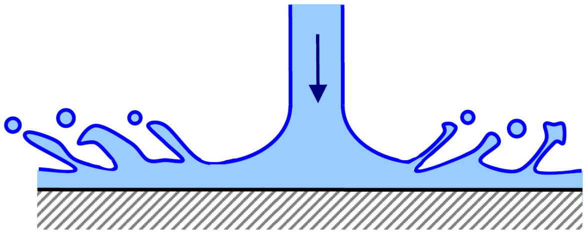

Figure 5.13: Film fluctuations and ligament breakup for the impact of a dense, high-pressure spray.

5.4 Development of an empirical model

At the moment, no model exists to describe satisfactorily wall interactions of the considered dense hollow cone sprays impacting with high Reynolds numbers. As shown in the previous subsections, physical understanding is growing. Yet, it is still not sufficient to form the foundation of a complete model. Therefore, as a first step which provides at least a successful description of the impact, empirical correlations are proposed in the following, based on the experimental data gathered in this work.

5.4.1 Normal spray impact

For the modelling only evaluated data from secondary drops assigned to the outside of the spray hollow cone are used, because their measurement is considered more reliable and more accurate with respect to the high spray density. The impacts in the experiment are approximately normal and spray/wall interaction is assumed to be symmetric in the ideal case. This is supported by the observation of only small differences between the mean values of secondary drops assigned to the outside and those assigned to the inside of the hollow cone in Sections 5.1 and 5.2. Also the distributions are confirmed to coincide well.
With respect to the negligible parameter influences due to dominant inertial forces, averages over all measurements are addressed for modelling - no matter which individual parameter setting is adjusted. The averaging concerns mean values as well as distribution shapes.

Mean values. The definitions according to Equation 4.11 (and not the flux-related ones of Equations 4.18) are addressed to calculate mean values of the primary and secondary spray for every measurement. Averaging the relative values yields:

$$\begin{aligned}
\overline{\frac{D_{10,\text{sec}}}{D_{10,\text{prim}}}} &\approx 0.673\,(\pm 0.013)\,, \\
\overline{\frac{v_{\text{N},10,\text{sec}}}{v_{\text{abs},10,\text{prim}}}} &\approx 0.0811\,(\pm 0.0015)\,, \\
\overline{\frac{v_{\text{T},10,\text{sec}}}{v_{\text{abs},10,\text{prim}}}} &\approx f_{\text{dev}} \cdot 0.203\,(\pm 0.010) \text{ with } f_{\text{dev}} = \pm 1, \\
0.5 \cdot \overline{\frac{q_{m,\text{sec total}}}{q_{m,\text{prim}}}} = \overline{\frac{q_{m,\text{sec}}}{q_{m,\text{prim}}}} &\approx 0.399\,(\pm 0.026)\,. \qquad (5.7)
\end{aligned}$$

The mean errors of the means, given in brackets, are defined as $\sigma_X/\sqrt{N}$, where σ_X is the standard deviation of a single value and N is the number of measurements. Their small values demonstrate again the minor parameter influences. For the diameter and the wall-normal velocity component, the values are below 2%. For the wall-tangential velocity component and the mass ratio, the mean errors are larger with values below 5% and 7% respectively. Yet, they are still in an acceptable range considering the overall uncertainties[4].
In contrast to the previous sections, the secondary velocity components are considered relative to the primary absolute velocity and not to the respective primary velocity *component*, which becomes zero in the wall-tangential direction for an ideally normal impact.

Assuming a symmetric impact, the total reflected mass ratio is set to twice the measured one outside the spray hollow cone. This is characteristic for a hollow cone spray:

---

[4] As random numbers will be used in the implementation of the model, see Section 6.1, the error values will not be considered in the following.

- In case of the normal impact of a single drop, the deviation angle of an exemplary secondary drop may take values $\in [0°, 360°[$. The same range is applied in modelling a spray jet or a full spray cone, where normal impact refers to an angle of 90° between spray axis and surface, see Figure 5.14(a). The problem is three-dimensional and three velocity components have to be measured to capture the full information on secondary drops.

- In case of an impacting hollow cone spray, an intersection through the spray reveals that the impact ressembles locally the impact of a liquid sheet, cf. Figure 3.3 in Section 3.1.2 and Figure 5.14(b). The deviation angle is restricted to either 0° or 180° and, due to rotational symmetry, modelling is reduced to a two-dimensional problem. This is reflected in the two signs f_{dev} of the mean, relative wall-tangential velocity component in Equation 5.7. The measurement of only two velocity components as done in the experiments is sufficient because the third is approximately zero. The mass ratio caught in the experiment outside the spray cone corresponds to half the total reflected mass ratio.

Note that the restriction of the deviation angle to the impact plane for a hollow cone spray is advantageous for an implementation in CFX, where arbitrary angles are not possible yet[5], see Section 1.4.3.

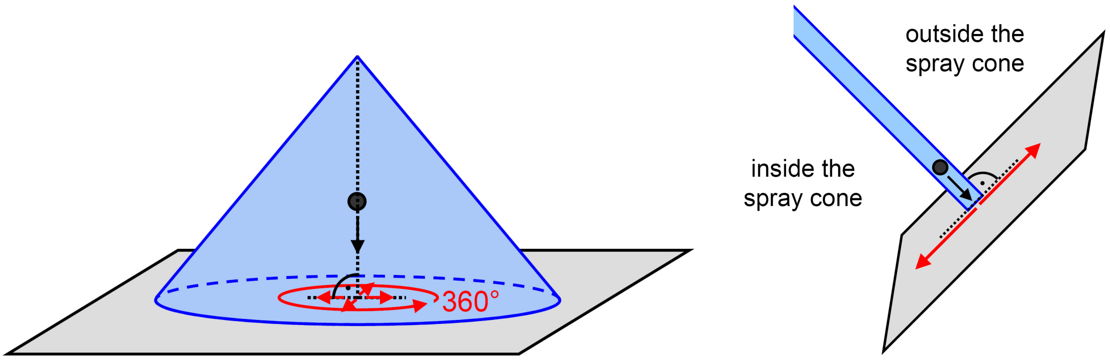

(a) Impact of a full cone spray.

(b) Impact of a hollow cone spray which can be locally approximated by the impact of a liquid sheet.

Figure 5.14: Deviation angles.

Shapes of distribution. To represent the spread of the secondary spray properties, the relative distributions

$$\frac{D_{\text{sec}}}{D_{10,\text{sec}}}, \quad \frac{v_{\text{N,sec}}}{v_{\text{N,10,sec}}}, \quad \frac{v_{\text{T,sec}}}{v_{\text{T,10,sec}}} \tag{5.8}$$

are considered where the data of every measurement are separately fitted.

The choice of the distribution functions is still a weak point in modelling because it is a common and often the only possible procedure, see [37], to select functions which provide satisfactory fits but which are not further justified:

---

[5] Also Kuhnke's and Roisman's/Horvat's model profit from this limitation in CFX if they are applied to hollow cone sprays. Originally, they refer to full cone sprays with varying deviation angles.

- The size distributions in fragmentation processes have been considered several times, cf. [21], [86] and references therein. Some authors consider the fragmentation of an initial liquid volume as a sequential cascade of breakups, using e.g. random numbers smaller than unity to describe the child volumes per step of the cascade. This leads to a log-normal distribution in the limit of an infinite number of steps. Other approaches apply purely combinatoric methods to describe the breakup in one step. Aiming at maximal entropy, a Poisson distribution of the volumes is found. In contrast to the mentioned approaches, which do not account for the physics underlying the breakup on spray impact, references [87], [21], [86] suggest a gamma distribution in case of the breakup of one ligament, see Section 5.3. The results are very promising, yet the size distribution of the ligaments resulting from spray impact is unknown and a pure gamma distribution underestimates the maximal values of the secondary size distribution.
  Therefore, a generalised extreme value distribution, which fits the secondary diameters best and which comprises the combination of the size distribution of the ligaments and of the associated gamma distributions, is used in the following:
  $$pdf_{\mathrm{gev}}\left(x=\frac{D_{\mathrm{sec}}}{D_{10,\mathrm{sec}}}\right)=\frac{1}{\sigma}\cdot\exp\left(-\left(1+k\cdot\frac{x-\mu}{\sigma}\right)^{-1/k}\right)\cdot\left(1+k\cdot\frac{x-\mu}{\sigma}\right)^{-1-1/k}, \tag{5.9}$$
  with k, σ and μ being shape, scale and location parameters.
- For the velocity components no theoretical reasoning for a special distribution shape could be found in literature and Weibull distributions are addressed:
  $$pdf_{\mathrm{Weibull}}(x)=\frac{b}{a}\cdot\left(\frac{x}{a}\right)^{b-1}\cdot\exp\left(-\left(\frac{x}{a}\right)^{b}\right), \tag{5.10}$$
  with $x=\frac{v_{\mathrm{N,sec}}}{v_{\mathrm{N,10,sec}}}$ and $x=\frac{v_{\mathrm{T,sec}}}{v_{\mathrm{T,10,sec}}}$ respectively and a, b two parameters.

Figures 5.15-5.17 show the fits for two arbitrary measurements. In comparison to the distributions of the diameters and the wall-normal velocity components, those of the wall-tangential velocity components are not described as well by the associated fits. Yet, other distribution shapes than Weibull have been found to be worse. It might seem as if two peaks, one with $v_{\mathrm{T,sec}}/v_{\mathrm{T,10,sec}}$ near zero and one around unity, were superimposed. Yet, there is no argument to either evaluate two peaks or to filter the secondary drops, as done for the primary ones in Section 4.3.2, and the presented Weibull fits are therefore chosen.

The fit parameters vary only slightly among different measurements, and mean fit parameters are determined from all measurements:

$$\begin{aligned}
\frac{D_{\mathrm{sec}}}{D_{10,\mathrm{sec}}} &: \; k\approx 0.111\,(\pm 0.009),\ \sigma\approx 0.367\,(\pm 0.002),\ \mu\approx 0.737\,(\pm 0.004)\,,\\
\frac{v_{\mathrm{N,sec}}}{v_{\mathrm{N,10,sec}}} &: \; a\approx 1.100\,(\pm 0.002),\ b\approx 1.416\,(\pm 0.015)\,,\\
\frac{v_{\mathrm{T,sec}}}{v_{\mathrm{T,10,sec}}} &: \; a\approx 1.076\,(\pm 0.005),\ b\approx 1.302\,(\pm 0.033)\,.
\end{aligned} \tag{5.11}$$

The small errors show that the distribution shapes coincide well for different parameter settings, i.e. parameter influences are negligible like already shown for the relative mean values.

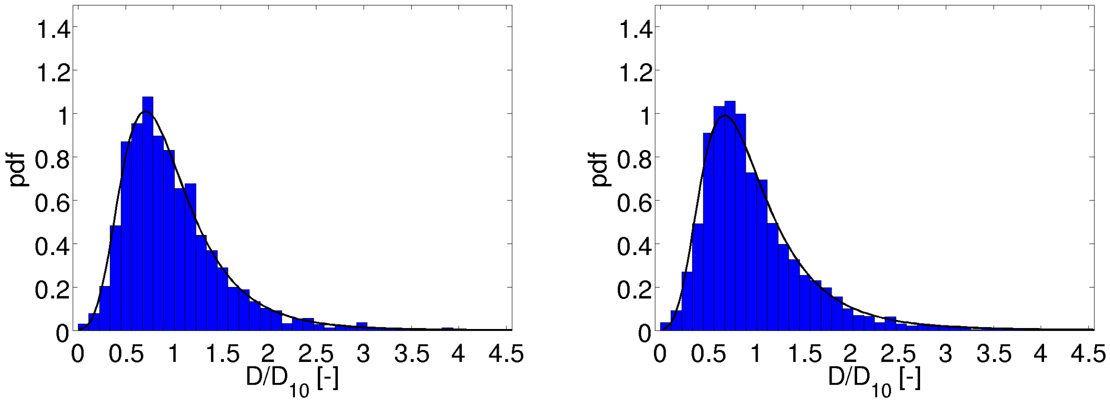

(a) $T_{\text{wall}} = 100°\text{C}$, $\delta = 0$, $\text{Re}_{\text{N,10,prim}} \approx 2370$.

(b) $T_{\text{wall}} = 150°\text{C}$, $\delta \approx 1.48$, $\text{Re}_{\text{N,10,prim}} \approx 2290$.

Figure 5.15: $D_{\text{sec}}/D_{10,\text{sec}}$ fitted by a generalised extreme value distribution.

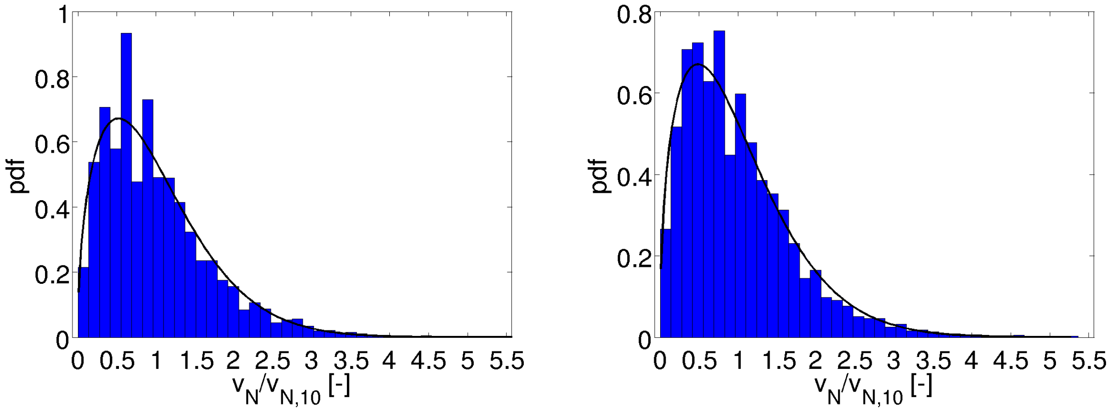

(a) $T_{\text{wall}} = 100°\text{C}$, $\delta = 0$, $\text{Re}_{\text{N,10,prim}} \approx 2370$.

(b) $T_{\text{wall}} = 150°\text{C}$, $\delta \approx 1.48$, $\text{Re}_{\text{N,10,prim}} \approx 2290$.

Figure 5.16: $v_{\text{N,sec}}/v_{\text{N,10,sec}}$ fitted by a Weibull distribution.

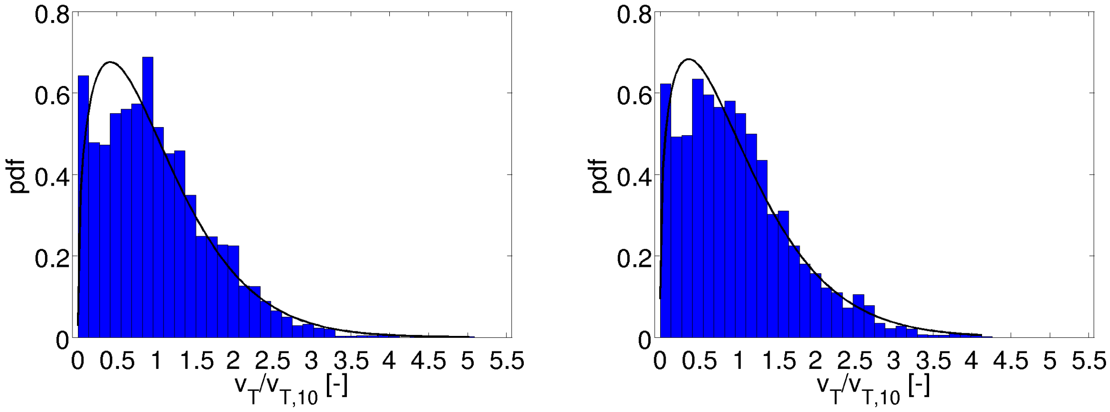

(a) $T_{\text{wall}} = 100°\text{C}$, $\delta = 0$, $\text{Re}_{\text{N,10,prim}} \approx 2370$.

(b) $T_{\text{wall}} = 150°\text{C}$, $\delta \approx 1.48$, $\text{Re}_{\text{N,10,prim}} \approx 2290$.

Figure 5.17: $v_{\text{T,sec}}/v_{\text{T,10,sec}}$ fitted by a Weibull distribution.

Coupling between D_{sec}, $v_{\mathrm{N,sec}}$ and $v_{\mathrm{T,sec}}$. In principle, Equations 5.7 and 5.11 bear all information to describe the averaged secondary spray. D_{sec}, $v_{\mathrm{N,sec}}$ and $v_{\mathrm{T,sec}}$ are treated as independent quantities. Yet, it must still be clarified if this is correct or if a significant relation between diameter and velocity components exists and has to be accounted for.

For this purpose, data are split in small ranges of diameter and velocity component values. A large number of raw data points are necessary for good statistics. Therefore, in contrast to the usual approach where data from every measurement are evaluated separately and where means and fit parameters are averaged afterwards, all raw drop data of all measurements are assembled in a first step. As expected due to the negligible parameter influence, the resulting distributions are very similar to the averaged distributions of Equations 5.7 and 5.11:

$$\begin{aligned}
\left(\frac{D_{10,\mathrm{sec}}}{D_{10,\mathrm{prim}}}\right)_{\mathrm{all\,data}} &\approx 0.649\,, \\
\left(\frac{v_{\mathrm{N},10,\mathrm{sec}}}{v_{\mathrm{abs},10,\mathrm{prim}}}\right)_{\mathrm{all\,data}} &\approx 0.0804\,, \\
\left(\frac{v_{\mathrm{T},10,\mathrm{sec}}}{v_{\mathrm{abs},10,\mathrm{prim}}}\right)_{\mathrm{all\,data}} &\approx 0.193\,, \\
0.5\cdot\left(\frac{q_{m,\mathrm{sec\,total}}}{q_{m,\mathrm{prim}}}\right)_{\mathrm{all\,data}} &\approx 0.387\,, \\
\frac{D_{\mathrm{sec}}}{D_{10,\mathrm{sec}}} &: \quad k\approx 0.120,\ \sigma\approx 0.370,\ \mu\approx 0.731\,, \\
\frac{v_{\mathrm{N,sec}}}{v_{\mathrm{N},10,\mathrm{sec}}} &: \quad a\approx 1.100,\ b\approx 1.407\,, \\
\frac{v_{\mathrm{T,sec}}}{v_{\mathrm{T},10,\mathrm{sec}}} &: \quad a\approx 1.070,\ b\approx 1.251\,.
\end{aligned} \tag{5.12}$$

The data are sorted in diameter classes of 5 μm width. The mean values of $v_{\mathrm{N,sec}}$ and $v_{\mathrm{T,sec}}$ per bin are shown in Figure 5.18 together with the raw data points. They hardly vary but the ranges of the velocity components seem to be dependent on the secondary drop size.

To analyse this in more detail, discrete distribution functions of $v_{\mathrm{N,sec}}$ and $v_{\mathrm{T,sec}}$ respectively are determined per diameter bin. Some are exemplarily plotted in Figure 5.19. The differences seem negligible, i.e. the distribution functions seem to be independent of the diameter class. It is therefore deduced that the ranges of the velocity components in Figure 5.18 are in fact not different: If the drop diameters were equally distributed over all values, i.e. if as many drops existed for large diameter values as around 20 μm, approximately the same ranges could be observed. A coupling of D_{sec} with $v_{\mathrm{N,sec}}$ or $v_{\mathrm{T,sec}}$ is neglected and it is concluded that a coupling between $v_{\mathrm{N,sec}}$ and $v_{\mathrm{T,sec}}$ can also be ignored, which is confirmed by Figure 5.20.

In summary, the averaged distributions of D_{sec}, $v_{\mathrm{N,sec}}$ and $v_{\mathrm{T,sec}}$ can be modelled independently as done in Equations 5.7 and 5.11.

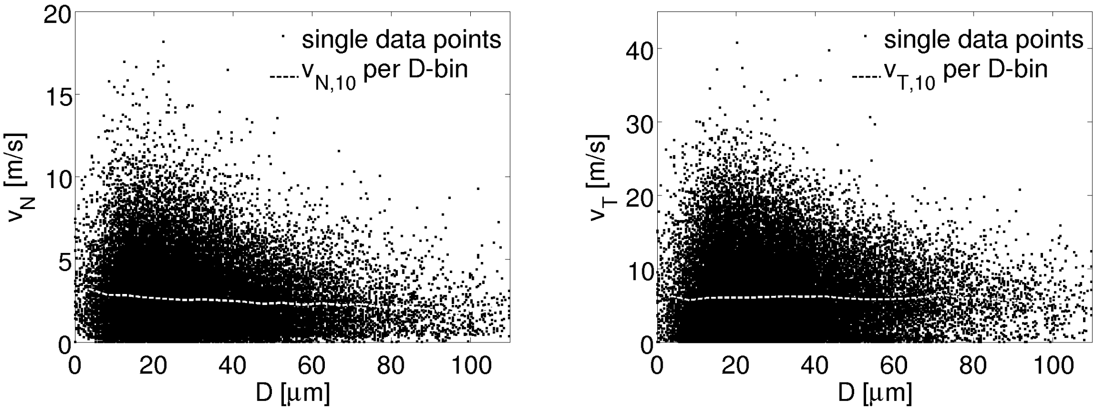

(a) $v_{\text{N,sec}}$ versus D_{sec}.

(b) $v_{\text{T,sec}}$ versus D_{sec}.

Figure 5.18: Dependence of $v_{\text{N,sec}}$ and $v_{\text{T,sec}}$ on the diameter D_{sec} for single drops of all measurements. Mean values per bin of width 5 μm are also shown.

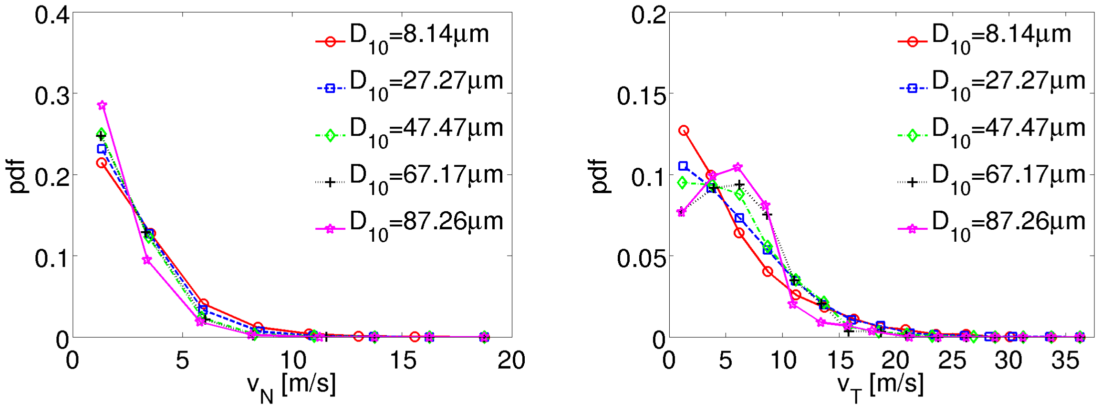

(a) Wall-normal component.

(b) Wall-tangential component.

Figure 5.19: Several discrete distribution functions of secondary drops describing the velocity components per diameter bin of width 5 μm. D_{10} denotes the mean secondary diameter in the respective bin.

5.4.2 Oblique spray impact

The experiment performed in this work focused on normal spray impact. From literature it is not possible either to retrieve sufficient quantitative information to extend the empirical correlations of the previous section from normal to oblique impact. Yet, this is necessary for their application in engine calculations and simple correlations are proposed in the following. They are ajusted to describe correctly the reference case in Chapter 2, where an impact under 45° is considered.
The secondary to primary mean values

$$\frac{D_{10,\text{sec}}}{D_{10,\text{prim}}}\ ,\ \frac{v_{\text{N,10,sec}}}{v_{\text{abs,10,prim}}}\ ,\ \frac{v_{\text{T,10,sec}}}{v_{\text{abs,10,prim}}}\ \text{and}\ \frac{q_{m,\text{sec total}}}{q_{m,\text{prim}}}\ , \tag{5.13}$$

are modified when indicated, but the secondary distributions

$$\frac{D_{\text{sec}}}{D_{10,\text{sec}}}\ ,\ \frac{v_{\text{N,sec}}}{v_{\text{N,10,sec}}}\ \text{and}\ \frac{v_{\text{T,sec}}}{v_{\text{T,10,sec}}} \tag{5.14}$$

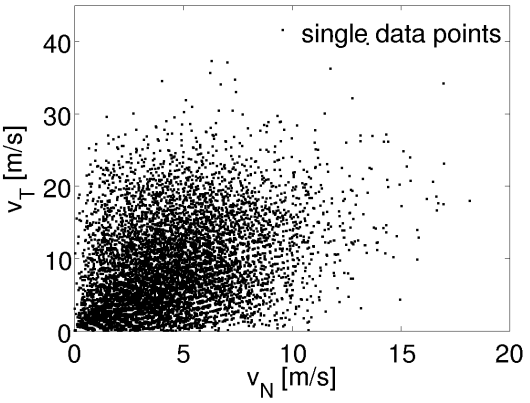

Figure 5.20: $v_{\mathrm{N,sec}}$ versus $v_{\mathrm{T,sec}}$ for single drops of all measurements.

Figure 5.21: Endoscopy image of the impact of a hollow cone spray in a one-cylinder test bench at BMW. The rail pressure is set to 100 bar and the ambient temperature lies around 70°C. Courtesy Peter Helmetsberger.

are maintained for any value of the impact angle.

Secondary diameters. Presumably, film motion changes considerably with the impact angle. However, these changes in the film fluctuations and resulting ligaments are not known and it is therefore assumed in this work that the relation between secondary and primary mean diameters does not depend on the impact angle.

Secondary velocities. From the transmitted-light images of the reference case in Chapter 2 with an impact angle of $\approx 45°$ and from endoscopy images taken at BMW, see Figure 5.21, it can be inferred that the direction of the secondary spray does not change significantly compared to the case of normal impact: The motion is still rather tangential to the wall.
To extrapolate the correlations from normal impact to values $\alpha_{10} \neq 90°$, cf. Equations 5.7, a momentum consideration is applied. The absolute primary momentum is generally transferred to:

- momentum carried by secondary drops in forward and backward direction,
- momentum transferred to the wall film,
- losses.

Only the first point is of interest at this point. The associated momentum fraction is unknown and the following assumptions are made:

$$\begin{aligned} p_{\mathrm{N,10,sec\,forward}} &= f_{\mathrm{N,forward}}(\alpha_{10}) \cdot p_{\mathrm{abs,10,prim}} \,, \\ p_{\mathrm{T,10,sec\,forward}} &= f_{\mathrm{T,forward}}(\alpha_{10}) \cdot p_{\mathrm{abs,10,prim}} \,, \\ p_{\mathrm{N,10,sec\,backward}} &= f_{\mathrm{N,backward}}(\alpha_{10}) \cdot p_{\mathrm{abs,10,prim}} \,, \\ p_{\mathrm{T,10,sec\,backward}} &= f_{\mathrm{T,backward}}(\alpha_{10}) \cdot p_{\mathrm{abs,10,prim}} \,. \end{aligned} \tag{5.15}$$

The momentum p and the associated mass do not refer to a single secondary or primary drop here - several children are created per impact on average - but to the total primary mass fraction which is reflected in forward and backward direction respectively:

$$\begin{aligned} p_{\mathrm{N/T,10,sec\,forward/backward}} &\approx q_{m,\mathrm{sec\,forward/backward}} \cdot v_{\mathrm{N/T,10,sec\,forward/backward}} \, , \\ p_{\mathrm{abs,10,prim}} &\approx q_{m,\mathrm{sec\,forward/backward}} \cdot v_{\mathrm{abs,10,prim}} \, . \end{aligned} \tag{5.16}$$

Therefore, the velocity components, which are directly measured quantities in the experiments for normal impact, can be considered instead of the momentum:

$$\begin{aligned} v_{\mathrm{N,10,sec\,forward}} &= f_{\mathrm{N,forward}}(\alpha_{10}) \cdot v_{\mathrm{abs,10,prim}} \, , \\ v_{\mathrm{T,10,sec\,forward}} &= f_{\mathrm{T,forward}}(\alpha_{10}) \cdot v_{\mathrm{abs,10,prim}} \, , \\ v_{\mathrm{N,10,sec\,backward}} &= f_{\mathrm{N,backward}}(\alpha_{10}) \cdot v_{\mathrm{abs,10,prim}} \, , \\ v_{\mathrm{T,10,sec\,backward}} &= f_{\mathrm{T,backward}}(\alpha_{10}) \cdot v_{\mathrm{abs,10,prim}} \, . \end{aligned} \tag{5.17}$$

From the experiment $f_{\mathrm{N,forward/backward}}(90°) \approx 0.0811$ and $f_{\mathrm{T,forward/backward}}(90°) \approx 0.203$ result, cf. Equation 5.7.
In Figure 5.22 it is shown that the reference case with $\alpha_{10} \approx 45°$ cannot be described correctly with constant functions $f_{\mathrm{N,forward/backward}}(\alpha_{10}) = f_{\mathrm{N,forward/backward}}(90°) = \mathrm{const.}$ and $f_{\mathrm{T,forward/backward}}(\alpha_{10}) = f_{\mathrm{T,forward/backward}}(90°) = \mathrm{const.}$: The tangential penetration is much too slow. This cannot be explained by an unaccounted change in secondary diameters with the impact angle: Assuming $0.75 \cdot D_{\mathrm{10,prim}}$ or $1.25 \cdot D_{\mathrm{10,prim}}$ in the correlations does not lead to sufficient tangential penetration either. A consideration of $v_{\mathrm{N/T,10,sec\,forward/backward}}$ relative to $v_{\mathrm{N,10,prim}}$ instead of $v_{\mathrm{abs,10,prim}}$ would even decrease the penetration.

The functions are therefore chosen intuitively as follows:

- With decreasing mean impact angle α_{10}, i.e. for flatter impact, the secondary normal momentum is expected to decrease. Assuming that especially the normal component of the primary momentum contributes to the secondary normal component, the decrease is set proportional to it with no difference between forward and backward direction:

  $$f_{\mathrm{N,forward/backward}}(\alpha_{10}) = f_{\mathrm{N,forward/backward}}(90°) \cdot \sin \alpha_{10} \, . \tag{5.18}$$

  The sensitivity of this function on α_{10} is limited as the value $f_{\mathrm{N,forward/backward}}(90°)$ is very small.

- The secondary tangential momentum in forward direction is expected to increase with decreasing α_{10}. Assuming that the increase is proportional to the primary tangential momentum yields:

  $$f_{\mathrm{T,forward}}(\alpha_{10}) = f_{\mathrm{T,forward/backward}}(90°) + k_{\mathrm{T}} \cdot \cos \alpha_{10} \, . \tag{5.19}$$

  The parameter k_{T} denotes the fraction of the primary tangential momentum which is transferred to the secondary one, additionally to the general transformation of absolute momentum. It is determined in simulating the reference case and in adapting the tangential penetration to the transmitted-light images. It shows that $v_{T,\mathrm{10,sec\,forward}}(45°) \approx 0.4 \cdot v_{\mathrm{abs,10,prim}}$ describes these best, see

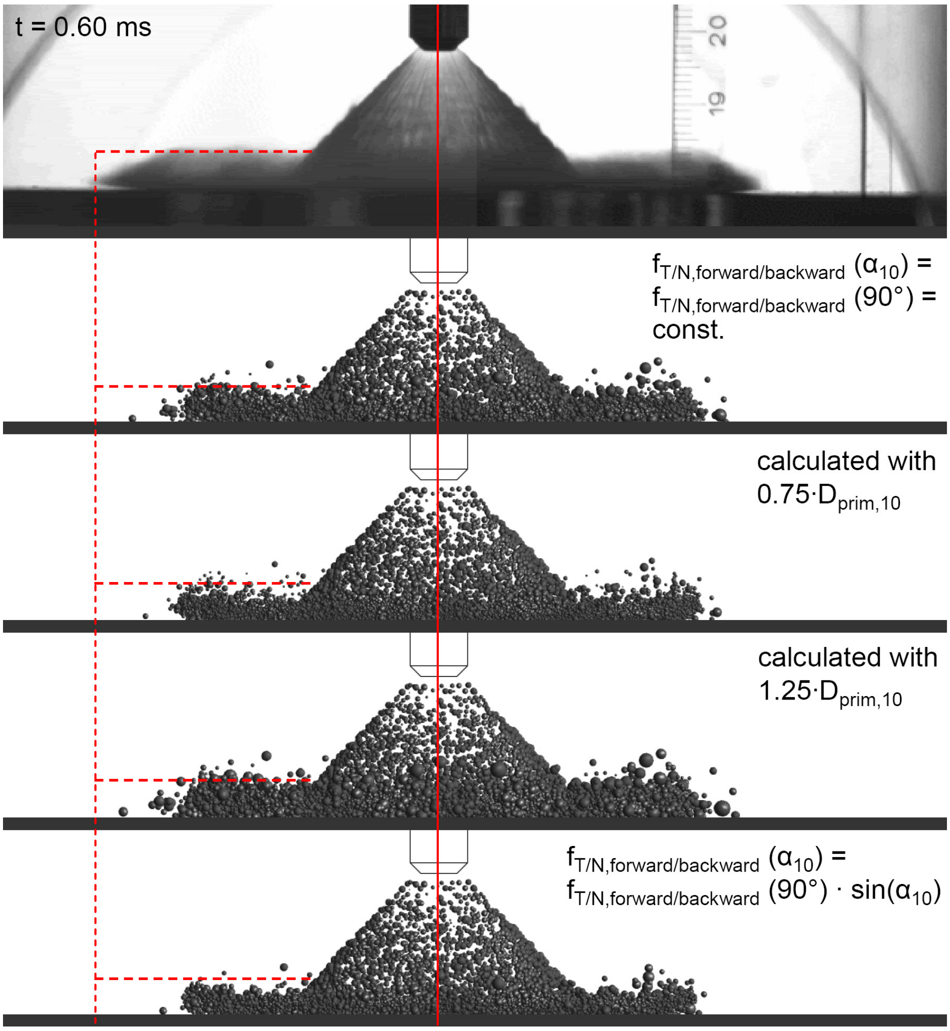

Figure 5.22: Reference case at $t = 0.60\,\text{ms}$ with constant functions $f_{\text{N,forward/backward}}(\alpha_{10})$ and $f_{\text{T,forward/backward}}(\alpha_{10})$. The sensitivity on the primary diameter is also presented. The results with the mean secondary velocity components considered relative to $v_{\text{N,10,prim}}$ instead of $v_{\text{abs,10,prim}}$ are shown at the bottom.

Figures 5.23 and 5.24. This gives $k_{\text{T}} \approx 0.28$. Note that the reference case with an injection pressure of 200 bar and an oblique impact angle of 45° differs noteworthy from the experimental conditions.

The backward direction, i.e. the reflection towards the inside of the spray cone cannot be adjusted considering transmitted-light images and no additional information is available. Therefore, no contribution from the primary tangential momentum is accounted for:

$$f_{\text{T,backward}}(\alpha_{10}) = f_{\text{T,forward/backward}}(90°)\,. \tag{5.20}$$

The presented functions are used for modelling oblique impacts in the following. A quantitative validation is not possible due to a lack of data. Yet, in Chapter 6 a case is presented where mean impact angles in an approximate range of $30° < \alpha_{10} < 60°$ are considered. Together with $\alpha_{10} \approx 90°$ from the experiment, it can be presumed that the correlations cover also the angle range in-between with $60° < \alpha_{10} < 90°$ and that they can therefore be used in an estimated range of $30° < \alpha_{10} \leq 90°$ in engine calculations.

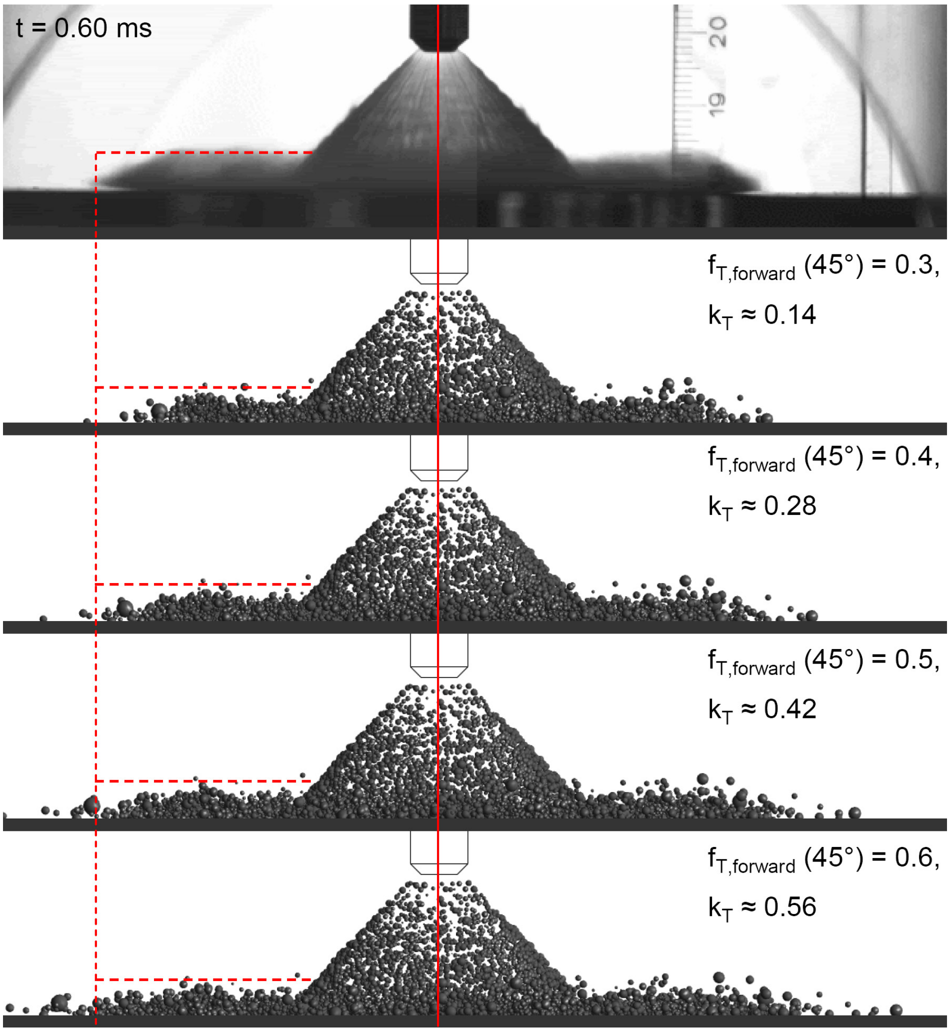

Figure 5.23: Reference case for different values of $f_{\mathrm{T,forward}}(45^\circ)$ at $t = 0.60\,\mathrm{ms}$, $f_{\mathrm{N,forward/backward}}(\alpha_{10}) = f_{\mathrm{N,forward/backward}}(90^\circ) \cdot \sin\alpha_{10}$ and $f_{\mathrm{T,backward}}(\alpha_{10}) = f_{\mathrm{T,forward/backward}}(90^\circ)$.

This meets the conditions occuring in in-cylinder calculations rather well: Except very rarely on the spark plug, impacts under even smaller angles do not occur.

Secondary mass. In case of normal impact, half the total secondary mass is reflected on either side of the impacting spray which can be locally approximated by an impacting liquid sheet, see above. For an extrapolation to oblique angles, a simple analogy to the stationary impact of a liquid volume flux onto a plane is considered, see Figure 5.25. Applying Bernoulli's equation one gets, see e.g. [19]:

$$\frac{q_{m,\mathrm{sec\,forward}}}{q_{m,\mathrm{prim}}} = \frac{1}{2} \cdot \frac{q_{m,\mathrm{sec\,total}}}{q_{m,\mathrm{prim}}} \cdot (1 + \cos\alpha_{10}) \ , \tag{5.21}$$

$$\frac{q_{m,\mathrm{sec\,backward}}}{q_{m,\mathrm{prim}}} = \frac{1}{2} \cdot \frac{q_{m,\mathrm{sec\,total}}}{q_{m,\mathrm{prim}}} \cdot (1 - \cos\alpha_{10}) \ , \tag{5.22}$$

where α_{10} is defined relative to the wall tangent[6].

---

[6] The analogy cannot be used to give correlations for the secondary velocity as the latter is maintained in the secondary sheets (viscosity is neglected), which does not hold for the measured data.

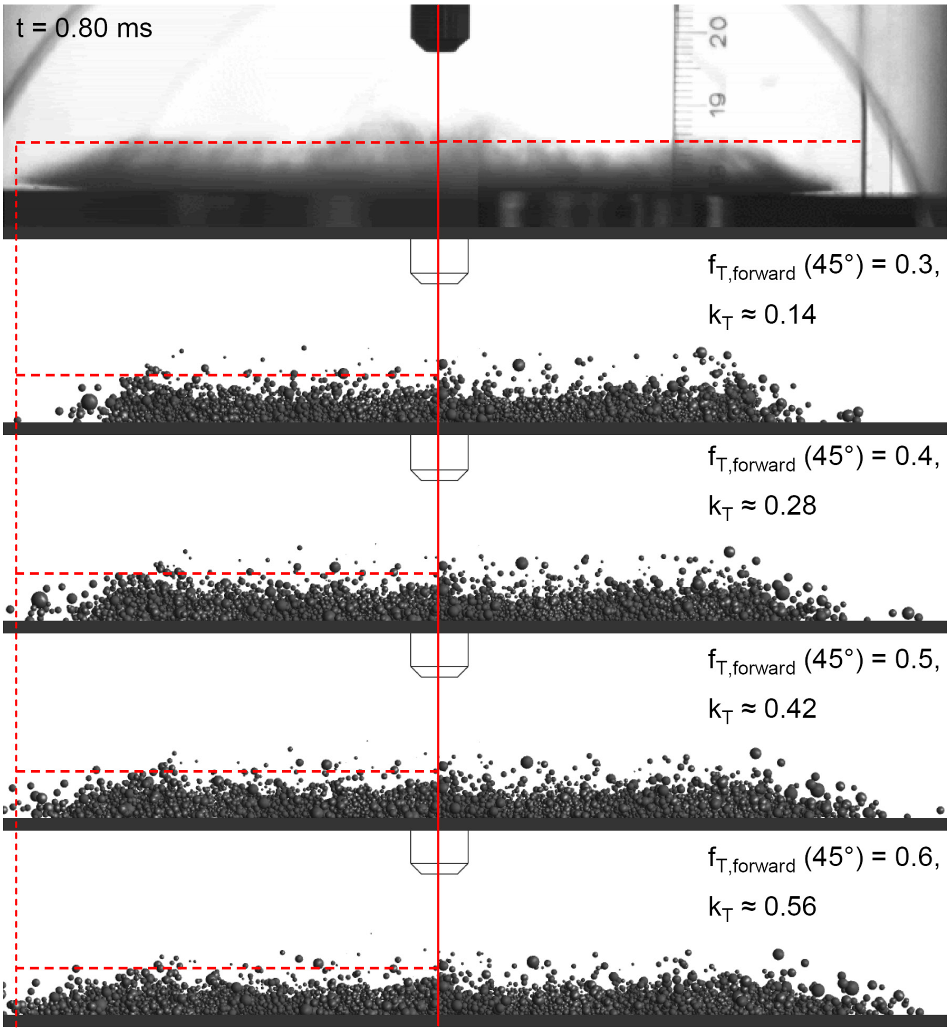

Figure 5.24: Reference case for different values of $f_{\mathrm{T,forward}}(45^\circ)$ at $t = 0.80\,\mathrm{ms}$, $f_{\mathrm{N,forward/backward}}(\alpha_{10}) = f_{\mathrm{N,forward/backward}}(90^\circ) \cdot \sin\alpha_{10}$ and $f_{\mathrm{T,backward}}(\alpha_{10}) = f_{\mathrm{T,forward/backward}}(90^\circ)$.

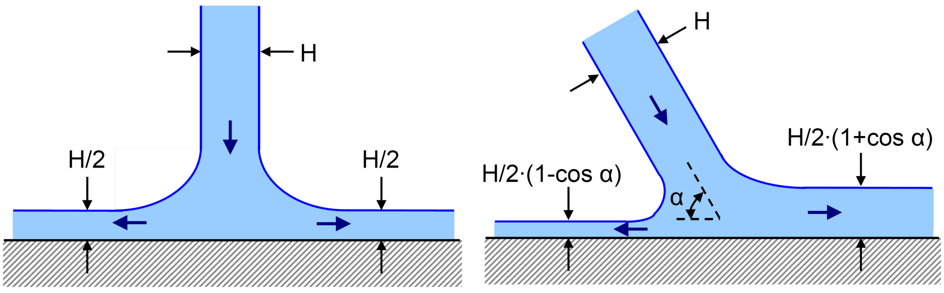

(a) Normal impact. (b) Oblique impact.

Figure 5.25: Impact of a liquid sheet onto a plane. Gravity and viscosity are neglected.

5.4.3 Summary of the modelling

The secondary spray created in the impacts of a dense hollow cone spray with high Reynolds numbers is described by the following relative mean values, see Equations 5.7, and the averaged shapes of distribution, cf. Equations 5.11:

- secondary diameters:

$$\begin{aligned}\overline{\frac{D_{10,\text{sec}}}{D_{10,\text{prim}}}} &\approx 0.673\,,\\ pdf_{\text{gev}}\left(\frac{D_{\text{sec}}}{D_{10,\text{sec}}}\right) &\approx \frac{1}{0.367}\cdot\exp\left(-z^{-1/0.111}\right)\cdot z^{-1-1/0.111}\\ &\qquad \text{with } z = 1 + 0.111\cdot\frac{\frac{D_{\text{sec}}}{D_{10,\text{sec}}} - 0.737}{0.367}\,.\end{aligned} \tag{5.23}$$

- Wall-normal velocity components:

$$\begin{aligned}\overline{\frac{v_{\text{N},10,\text{sec}}}{v_{\text{abs},10,\text{prim}}}} &\approx 0.0811\cdot\sin\alpha_{10}\,,\\ pdf_{\text{Weibull}}\left(\frac{v_{\text{N},\text{sec}}}{v_{\text{N},10,\text{sec}}}\right) &\approx \frac{1.416}{1.100}\cdot z^{0.416}\cdot\exp\left(-z^{1.416}\right)\\ &\qquad \text{with } z = \frac{v_{\text{N},\text{sec}}}{v_{\text{N},10,\text{sec}}}/1.100\,.\end{aligned} \tag{5.24}$$

- Wall-tangential velocity components:

$$\begin{aligned}\overline{\frac{v_{\text{T},10,\text{sec forward}}}{v_{\text{abs},10,\text{prim}}}} &\approx +1\cdot(0.203 + 0.42\cdot\cos\alpha_{10})\,,\\ \overline{\frac{v_{\text{T},10,\text{sec backward}}}{v_{\text{T},10,\text{prim}}}} &\approx -1\cdot 0.203\,,\\ pdf_{\text{Weibull}}\left(\frac{v_{\text{T},\text{sec}}}{v_{\text{T},10,\text{sec}}}\right) &\approx \frac{1.302}{1.076}\cdot z^{0.302}\cdot\exp\left(-z^{1.302}\right)\\ &\qquad \text{with } z = \frac{v_{\text{T},\text{sec}}}{v_{\text{T},10,\text{sec}}}/1.076\,.\end{aligned} \tag{5.25}$$

- Mass ratios:

$$\overline{\frac{q_{m,\text{sec forward}}}{q_{m,\text{prim}}}} = 0.399\cdot(1 + \cos\alpha_{10})\,, \tag{5.26}$$

$$\overline{\frac{q_{m,\text{sec backward}}}{q_{m,\text{prim}}}} = 0.399\cdot(1 - \cos\alpha_{10})\,. \tag{5.27}$$

The correlations are empirical and not universally valid. If they are applied to other spray nozzles, the probability density functions, i.e. the *pdf*s, should be adapted if known. It is vital to gather further quantitative data for different volume fluxes, Reynolds numbers and impact angles in future work in order to extend and confirm

the correlations, especially the extrapolation to oblique impacts.
Yet, the empirical correlations represent the first successful attempt to describe the impact of the considered spray type, which can furthermore be easily implemented in numerical code, see the following section. The correlations describe the experiment and the reference case very well, where it has to be emphasized that the conditions of both cases differ strongly, e.g. a different injector is used and the injection pressure differs by a factor of four. Another case in Chapter 6 leads to the conclusion that the correlations are presumably applicable in a range of $30^\circ < \alpha_{10} < 90^\circ$.

Chapter 6

Validation of the new empirical model

In the previous chapter an empirical model describing the wall interaction of a dense hollow cone spray with high Reynolds numbers on impact has been defined. Its implementation in numerical code is discussed in the following. For validation, especially with respect to the extrapolation to oblique impacts, three cases are then considered:

- For a basic test of the correlations, the experiment in which the spray cone hits the target in an approximately normal angle is simulated and a detailed quantitative comparison of the resulting distribution functions for diameters and velocity components is done with those measured.
- A modification of the reference case in Chapter 2 is addressed with the plate tilted by 13°.
- Finally, a target in form of a generic piston geometry is treated. The case refers to experiments carried out in engine development at BMW to adjust the design of the spray and the piston in a combustion chamber. Previous models could not describe spray/wall interactions satisfactorily in associated CFD simulations.

Unstructured grids constituted of tetrahedral cells with maximal 1 mm edge length are used in every case. Five prism layers with a total height of 1 mm are applied on rigid surfaces. Numerical parameters are set per default as for the reference case in Chapter 2, cf. Table 2.2. Deviations will be stated when indicated.

6.1 Implementation of the model

In the Lagrangian approach of numerical simulations, a primary parcel i represents $n_{\mathrm{prim},i}$ drops, see Section 1.3.2. Spray/wall interaction is to be defined individually for each primary parcel in such a manner that the ensemble describes the secondary spray correctly in means and shapes of distribution. In the following the implementation of the new empirical model which fulfills this criterion and which has been used for the validation cases is shown.

The $n_{\mathrm{prim},i}$ drops of a primary parcel are characterised by a diameter $D_{\mathrm{prim},i}$ and wall-normal and wall-tangential velocity components $v_{\mathrm{N,prim},i}$ and $v_{\mathrm{T,prim},i}$. For every child parcel $j = 1, \ldots, N_{\mathrm{sec},i}$, the secondary diameter $D_{\mathrm{sec},j}$, the velocity restitution coefficients $c_{\mathrm{N},j} = v_{\mathrm{N,sec},j}/v_{\mathrm{N,prim},i}$ and $c_{\mathrm{T},j} = v_{\mathrm{T,sec},j}/v_{\mathrm{T,prim},i}$ and the number of represented drops $n_{\mathrm{sec},j}$ have to be declared. The number of secondary parcels $N_{\mathrm{sec},i}$ per primary parcel and impact can be user-defined in Fortran code in CFX.

6.1.1 Secondary diameters and restitution coefficients

In a first step, random values for $D_{\mathrm{sec},j}/D_{10,\mathrm{sec}}$, $v_{\mathrm{N,sec},j}/v_{\mathrm{N,10,sec}}$ and $v_{\mathrm{T,sec},j}/v_{\mathrm{T,10,sec}}$, which are distributed according to the probability density functions specified in Equations 5.23, 5.24 and 5.25, are determined. The following, general procedure to get a random number x_{rand}, distributed according to an arbitrary probability density function $\mathit{pdf}(x)$, is applied:

- Determine the associated cumulative distribution function $\mathit{cdf}(x)$ analytically if possible, else by numerical integration. Due to the normalisation of $\mathit{pdf}(x)$, i.e. $\int_0^\infty \mathit{pdf}(x)dx = 1$, it follows by definition that $\mathit{cdf}(x) \in [0,1]$.
- Choose a linear distributed random number $p_{\mathrm{rand}} \in [0,1]$.
- Determine x_{rand} which fulfils $\mathit{cdf}(x_{\mathrm{rand}}) = p_{\mathrm{rand}}$.

In combination with the relative mean values given in Equations 5.23, 5.24 and 5.25, the secondary diameter, the wall-normal and wall-tangential restitution coefficient of child j can be calculated as follows:

$$\begin{aligned}
D_{\mathrm{sec},j} &= \frac{D_{\mathrm{sec},j}}{D_{10,\mathrm{sec}}} \cdot \overline{\frac{D_{10,\mathrm{sec}}}{D_{10,\mathrm{prim}}}} \cdot D_{10,\mathrm{prim}}\,, \\
c_{\mathrm{N,sec},j} &= \frac{v_{\mathrm{N,sec},j}}{v_{\mathrm{N,10,sec}}} \cdot \overline{\frac{v_{\mathrm{N,10,sec}}}{v_{\mathrm{abs,10,prim}}}} \cdot \frac{v_{\mathrm{abs,10,prim}}}{v_{\mathrm{N,prim},i}}\,, \\
c_{\mathrm{T,sec},j} &= f_{\mathrm{dev}} \cdot \frac{v_{\mathrm{T,sec},j}}{v_{\mathrm{T,10,sec}}} \cdot \overline{\frac{v_{\mathrm{T,10,sec}}}{v_{\mathrm{abs,10,prim}}}} \cdot \frac{v_{\mathrm{abs,10,prim}}}{v_{\mathrm{T,prim},i}} \\
&\quad \text{with } f_{\mathrm{dev}} = \begin{cases} +1 & \text{if the parcel is forward scattered}\,, \\ -1 & \text{if the parcel is backward scattered}\,. \end{cases}
\end{aligned} \tag{6.1}$$

It is important that the last terms in the given equations, $D_{10,\mathrm{prim}}$, $\frac{v_{\mathrm{abs,10,prim}}}{v_{\mathrm{N,prim},i}}$ and $\frac{v_{\mathrm{abs,10,prim}}}{v_{\mathrm{T,prim},i}}$, must not be substituted by $D_{\mathrm{prim},i}$, $\frac{v_{\mathrm{abs,prim},i}}{v_{\mathrm{N,prim},i}}$ and $\frac{v_{\mathrm{abs,prim},i}}{v_{\mathrm{N,prim},i}}$ respectively: The model correlations have been obtained using mean impacting values and not individual ones. If those were applied, the primary distributions would be superimposed on the actual secondary distributions leading to different results.

To determine the mean primary properties, information from the previous timestep is evaluated, cf. the discussion in Section 1.4.3. Only if all spray drops experience approximately the same impact conditions like in the reference case, it is possible to do the averaging over all impacting drops. Else, e.g. for the impact on an oblique plate in Chapter 6, the rotationally symmetric spray has to be divided in sectors with approximately homogeneous impact conditions, and the averaging has to be done for every sector separately. Depending on the sector in which a parcel impinges, different means are then used in the calculations. For very asymmetric and spatially diversified surfaces, where it is no longer possible to do an averaging at all, the individual primary properties have to be used although this is known to comprise errors.

6.1.2 Numbers and number rates of child parcels

The number of secondary parcels generated per impact is a user-defined quantity and should be chosen not too large with respect to computational effort. In case of a mean impact angle $60° \leq \alpha_{10} \leq 90°$ ($\alpha = 90°$ signifies normal impact), it is suggested to define two child parcels per impinging parcel i, i.e. $N_{\mathrm{sec},i} = 2$. For smaller α_{10}, three child parcels are proposed, i.e. $N_{\mathrm{sec},i} = 3$: two in forward direction and one in backward direction. An adaption to other values of $N_{\mathrm{sec},i}$ can be easily done.
The jump from $N_{\mathrm{sec},i} = 2$ to $N_{\mathrm{sec},i} = 3$ at a mean impact angle of $\alpha_{10} = 60°$ is rather arbitrary at the moment. It may have an influence on a graphical presentation when simulations are post-processed and a sufficient number of Lagrangian parcels is required. It has to be stressed, however, that any model suffers from a similar problem, which is inherent to Lagrangian particle tracking where the multitude of physical spray droplets has to be represented by a small number of discrete parcels, see Section 1.3.2.

The definition of the number $n_{\mathrm{sec},j}$ of physical drops associated to every child parcel is an important aspect in the implementation of a model, because the values strongly influence the diameter and velocity distributions: The number rates[1] present a weighting factor of a drop value - analogously to the factors $w_{n,i} \cdot \eta_{\mathrm{val},i}$ used in Equation 4.9 for the measured values.
Two different ways can be chosen to define the number rates, see Figure 6.1. Consider exemplarily a drop size distribution:

- Dividing the diameter range in a finite number of discrete size values/classes, the same number of parcels can be chosen for every size value/class. The number rates of the parcels then have to represent the mass/number fractions per size value/class to obtain the correct distribution.
- If the diameter values for the child parcels are chosen according to the associated distribution function, the distribution is already represented. The number rates then have to be equal for all parcels.

A mixture of both ways is in principle also possible but rather error-prone. In this work the second possibility is chosen and for each secondary direction a constant value for the child number rates is determined such that the averaged secondary to primary mass ratio from the measurements, see Equation 5.26, is accounted for:

$$\begin{aligned}
&N_{\mathrm{sec},i} = 2 : \\
&n_{\mathrm{sec},1} = \frac{\overline{q_{m,\mathrm{sec\,forward}}}}{q_{m,\mathrm{prim}}} \cdot \frac{\overline{m}_{\mathrm{prim,parcel}}}{\overline{m}_{\mathrm{sec,single\ drop}}} \quad (f_{\mathrm{dev},1} = +1)\,, \\
&n_{\mathrm{sec},2} = \frac{\overline{q_{m,\mathrm{sec\,backward}}}}{q_{m,\mathrm{prim}}} \cdot \frac{\overline{m}_{\mathrm{prim,parcel}}}{\overline{m}_{\mathrm{sec,single\ drop}}} \quad (f_{\mathrm{dev},1} = -1)\,, \\
&N_{\mathrm{sec},i} = 3 : \\
&n_{\mathrm{sec},1/2} = 0.5 \cdot \frac{\overline{q_{m,\mathrm{sec\,forward}}}}{q_{m,\mathrm{prim}}} \cdot \frac{\overline{m}_{\mathrm{prim,parcel}}}{\overline{m}_{\mathrm{sec,single\ drop}}} \quad (f_{\mathrm{dev},1} = +1)\,, \\
&n_{\mathrm{sec},3} = \frac{\overline{q_{m,\mathrm{sec\,backward}}}}{q_{m,\mathrm{prim}}} \cdot \frac{\overline{m}_{\mathrm{prim,parcel}}}{\overline{m}_{\mathrm{sec,single\ drop}}} \quad (f_{\mathrm{dev},1} = -1)\,.
\end{aligned} \tag{6.2}$$

---

[1] $n_{\mathrm{prim},i}$ and $n_{\mathrm{sec},j}$ respectively are scaled with the timestep value of the continuous phase in CFX and thus denoted also as number rate.

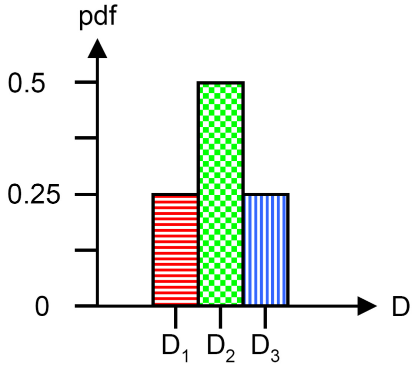

Figure 6.1: Illustration of the two methods to define the number rates. Consider a simplified, discrete diameter distribution with three values. On the one hand, the distribution could be presented by three parcels - one per size value - with weights (number rates) of 0.25, 0.5 and 0.25. On the other hand, it is also possible to choose four parcels - one for size D_1 and D_3 and two for size D_2 - with equal weights of 0.25.

The ratio between the mean primary parcel mass and the mean mass of a single secondary drop can be approximated as

$$\frac{\overline{m}_{\text{prim,parcel}}}{\overline{m}_{\text{sec,single drop}}} \approx \overline{n}_{\text{prim}} \cdot \left(\frac{D_{30,\text{prim}}}{D_{30,\text{sec}}} \right)^3 , \tag{6.3}$$

where the evaluation of the measurement gives

$$\frac{D_{30,\text{prim}}}{D_{30,\text{sec}}} \approx 0.789 \,. \tag{6.4}$$

The averaged primary number rate can be calculated for a specific simulation as

$$\overline{n}_{\text{prim}} = \frac{\text{total injected mass flow}}{\text{total number of Lagrangian primary parcels} \cdot \pi/6 \cdot \rho \cdot D_{30,\text{prim}}^3} \,. \tag{6.5}$$

It is also possible to evaluate $\overline{n}_{\text{prim}}$ directly from the previous timestep like the value $D_{30,\text{prim}}$ if unknown[2].

Remarks on Kuhnke's and Roisman's/Horvat's model In these models, described in Section 1.4.2, diameters of secondary parcels are chosen in the same way as in the new model, i.e. random numbers distributed according to the respectively given distribution function are used. As discussed above, number rates then have to be set to a constant value (which has to be determined in such a manner that the overall secondary to primary mass ratio is respected). Yet this is not done. Instead a rather intuitive but imprecise procedure is carried out in both models:

- In Kuhnke's model, see Equation 1.83, the child number rates are determined as

$$n_{\text{sec},j} = \frac{\overline{q_{m,\text{sec}}}}{q_{m,\text{prim}}} \cdot m_{\text{prim},i} \cdot F \,. \tag{6.6}$$

---

[2] The experiment yields $D_{30,\text{prim}} \approx 52.9\,\mu\text{m}$.

$m_{\mathrm{prim},i} = \pi/6 \cdot \rho \cdot D^3_{\mathrm{prim},i} \cdot n_{\mathrm{prim},i}$ is the total mass of the impacting parcel and F is a function which divides the secondary mass between the child parcels generated for the considered impact

$$F = \frac{pdf_{\mathrm{Weibull}}(D_{\mathrm{sec},j})}{\sum_{k=1,2,3} D^3_{\mathrm{sec},k} \cdot pdf_{\mathrm{Weibull}}(D_{\mathrm{sec},k})} \,. \tag{6.7}$$

Even if the primary spray was set up in such a way that all primary parcels carried the same mass m_{prim}, the function F would not be constant for all parcel impacts, because it depends on the randomly chosen values of the secondary diameters. Also the secondary to primary mass ratio $\overline{q_{m,\mathrm{sec}}/q_{m,\mathrm{prim}}}$ is calculated using a random number, see Equation 1.79. The secondary number rates are therefore not set to a constant value.

- In Roisman's/Horvat's model, see Equation 1.100 the child number rates are also defined as in Equation 6.6. The function F is different but depends on the secondary diameters, which are random numbers distributed according to the size distribution, too. Analogously to Kuhnke's model, the values of $n_{\mathrm{sec},j}$ are thus not constant.

Summarised, the definition of the child number rates is arguable in both models: If the parcels were considered with equal weights, the distributions of the drop diameters and velocities would be correctly represented, because the values are chosen randomly according to the distributions. Yet, the distributions must not be evaluated for the parcels but for the actual drops, i.e. every parcel has to be weighted with its number rate. Since these are not constant in this case, the distributions are incorrectly deformed.

6.2 Simulation of the experiment

For a first verification of the new empirical model given in Section 5.4, the experiment is repeated in simulation and the results are compared with the measurements. Elsässer's, Kuhnke's and Roisman's/Horvat's model are also addressed and, in contrast to the reference case of Chapter 2, the present case allows a quantitative consideration of drop size and velocity distributions.

6.2.1 Setup

6.2.1.1 Geometry, mesh and settings

The injector position with a distance of $\approx$ 37 mm between nozzle exit and target, see Figure 3.5, is studied in the simulations. Figure 6.2 shows the geometry of the computational domain. The associated mesh consists of $\approx 6.45 \cdot 10^4$ nodes and $\approx 3.5 \cdot 10^5$ elements.

In order to gain sufficient statistics within a reasonable measurement time, an injection duration of $\Delta t_i = 50\,\mathrm{ms}$ has been set in the experiment. Compared to the computational effort, the benefit from simulating this long time span is rather small, especially since opening and closing phase of the injector are not resolved in data evaluation,

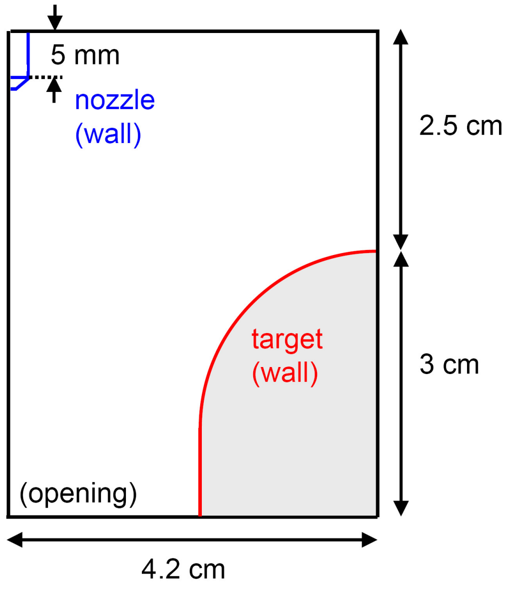

(a) Side view.

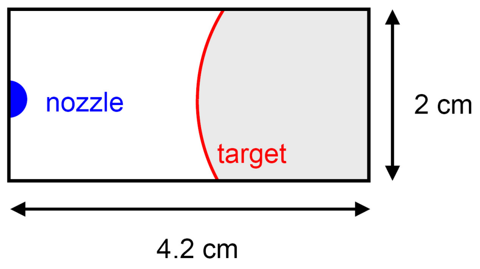

(b) Top view.

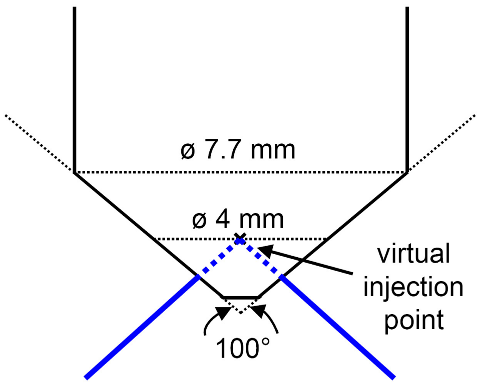

(c) Details of the nozzle.

Figure 6.2: Geometry used in the simulation of the experiment.

cf. Section 4.1: In principle, a single momentary state would give a sufficient result of a simulation. A steady state calculation cannot be done, however, due to the accumulating and stationary wall parcels in CFX version 12, see Section 2.3.1. Finally, a time interval of $\Delta t_{\text{run}} = 8.5\,\text{ms}$ is considered. The choice is based on the evaluation procedure, see Section 6.2.2, and the time span of approximately 5.0 ms which the air flow takes to reach approximately a steady state after start of injection, cf. Section 6.2.3 and Appendix C.1. The Eulerian time step is set to $DT = 1.0 \cdot 10^{-5}\,\text{s}$.

6.2.1.2 Initialisation of the primary spray

To enable a reasonable comparison of the secondary spray properties resulting in simulation with those measured, it is necessary to provide the same primary spray on impact. To achieve this, the following settings are initialised via user Fortran at the injection region, which is defined as a small ring area near the nozzle exit analogously to the reference case in Chapter 2:

- mass flow rate:
  According to the characteristic line of the injector, which gives the injected mass per injection duration depending on the injection pressure, the total mass for a pulse width of $\Delta t_i = 50\,\text{ms}$ and an injection pressure of $p_{\text{inj}} = 50\,\text{bar}$ amounts to $m_{\text{inj}} = 970\,\text{mg}$. This is equivalent to a stationary mass flow rate of $19.4\,\text{g/s}$. As opening and closing phase of the injector are not of interest here, they are not modelled and no ramping functions are impressed on the mass flow rate.

- Drop size distribution:
  For a fixed injector position the measured distributions of primary drop sizes

near the target surface agree very well for different parameter settings, and the distributions of the exemplary measurement, see Table 4.1, are finally initialised at the nozzle exit. The individual diameter values for the parcels are chosen randomly according to the distribution, cf. Section 5.4. No breakup model is applied and evaporation is assumed to change drop sizes only slightly till wall interaction.

- Injection velocity:
  Its definition at the injection region is rather difficult because the velocity resulting on the target is strongly influenced by drag, turbulent dispersion etc.. Therefore, the measured distributions of wall-normal and wall-tangential velocity components on the target cannot be used directly for initialisation.
  In a trial-and-error method it became apparent that the setting of a single value for the absolute velocity at nozzle exit does not reproduce the measured distributions on the target correctly. A coupling between diameter and velocity values showed to be unnecessary (in Section 5.4 it proved negligible in modelling the secondary spray, too). Finally, the absolute velocity of an initialised Lagrangian parcel is determined as $1.2 \cdot [v_{\mathrm{abs,10,prim}} + p_{\mathrm{rand}} \cdot (v_{\mathrm{abs,max,prim}} - v_{\mathrm{abs,10,prim}})]$ with $p_{\mathrm{rand}} \in [0, 1[$ a random number. $v_{\mathrm{abs,10,prim}} \approx 35\,\mathrm{m/s}$ and $v_{\mathrm{abs,max,prim}} \approx 72\,\mathrm{m/s}$ are the mean and maximal values observed in the experiment at the target respectively.
  To complete the definition of the velocity vector, the known hollow cone angle of $\approx 97°$ in combination with a random dispersion angle $\in [-2.5°, +2.5°]$ is used. This variation together with turbulent dispersion leads to approximately the same finite expansion of the impact area on the target as in the experiment, see Section 4.3.2.

- Number of injected Lagrangian parcels:
  It is set to 45 000 parcels injected per 1 ms, i.e. per 19.4 mg. With respect to the computational effort the net number of parcels, which is decreased by parcels leaving the domain but strongly increased by parcels created on wall interaction, is still manageable. The mass flow fraction carried by every parcel is deduced from its diameter value.

In Figure 6.3 the measured primary drop distributions are compared to those resulting in the simulation on the target (for the evaluation of the latter see the subsequent section). The agreement for drop size and wall-normal velocity components is rather good. For the wall-tangential velocity components the values below $-10\,\mathrm{m/s}$ are underestimated in the simulation. These correspond probably to primary drops moving on the inside of the spray hollow cone with a relatively small injection angle. As their number is small, the error is acceptable.

6.2.2 Evaluation procedure

In order to evaluate the simulation, the track file is used where the information about all parcel trajectories is stored in regular distances - in this case whenever a parcel crosses the face between two mesh elements. The target-nearest position of every parcel is extracted with Perl scripts. It is stored together with the associated parcel properties if the wall contact point lies in a distance of at most 2 mm to the measurement plane,

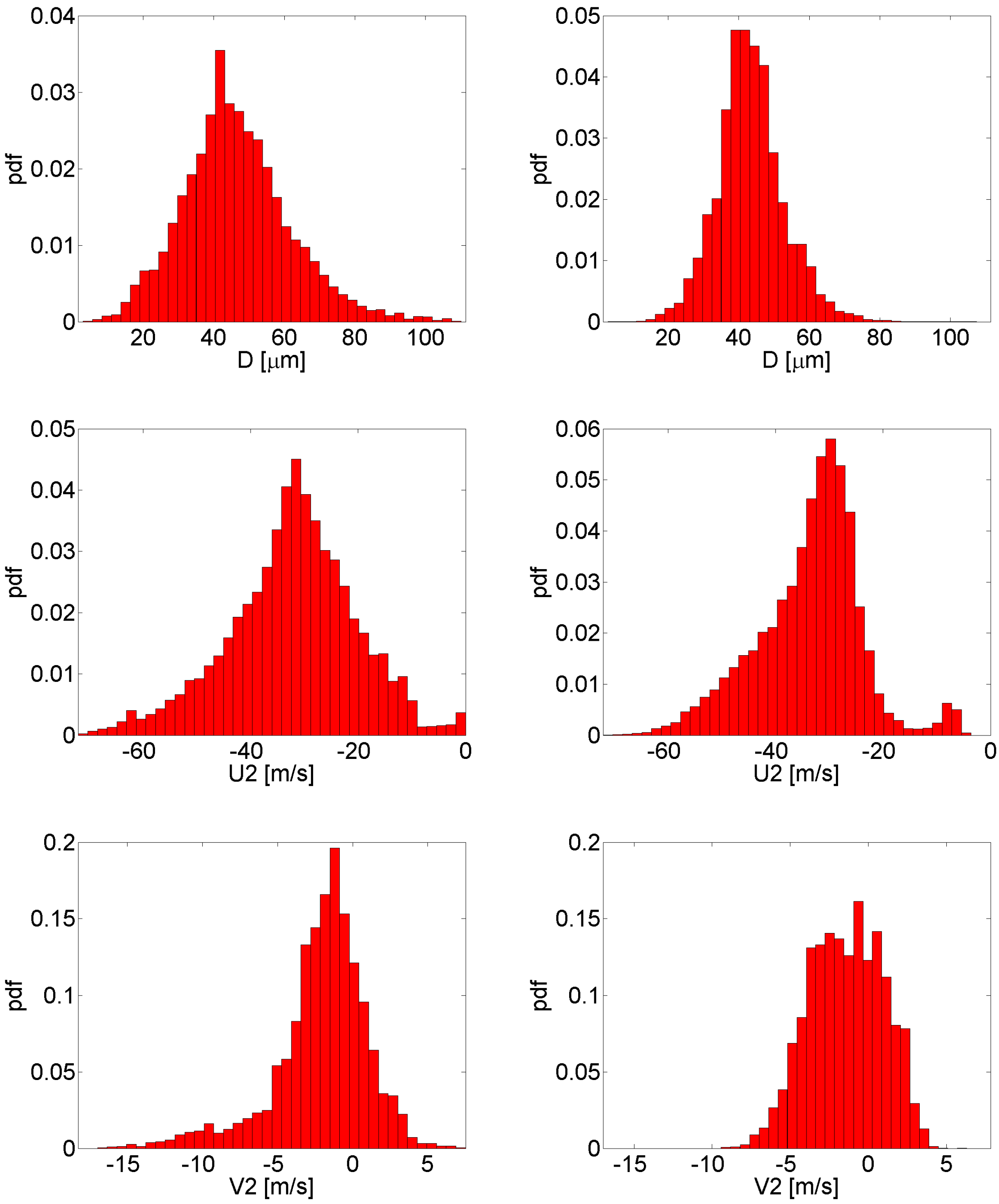

Figure 6.3: Comparison of the impacting spray in measurement (left) and simulation (right).

which corresponds to the middle plane of the geometry in the simulation. These data are then input to the Matlab scripts which have been written for the evaluation of the measured data and which are only slightly modified: Instead of the weighting and correction factors $w_{n,i}$ and $\eta_{\text{val},i}$, see Section 4.4, the number rates of the Lagrangian parcels now are the weights of the individual drop properties represented in a parcel. The same plots as in the evaluation of the experiment are finally generated and a comparison of the distribution functions can be done, cf. Figure 6.3, for instance.

As mentioned in the introduction to this validation case, the interest in the simulation results only concerns the quasi steady state but not the start of injection. This has to be accounted for in the evaluation: It takes almost 1.0 ms for the first primary drops to reach the target. The initially quiescent air flow takes an even longer time, up to approximately 5.0 ms, to reach a steady state, see Appendix C.1. Although it is also shown there that the influence of the flow formation on the evaluated drop distributions is minor, only parcels which attain their wall-nearest position at $t \geq 5$ ms are considered in the distribution functions extracted from a simulation as described above.

6.2.3 Comparison of spray/wall interaction models

To assess different spray/wall interaction models, the experimental results for the secondary spray will be drawn in the same plots as the respective simulation results in the following. For that purpose, the averaged distribution functions evaluated from the measured data will be used. These have also been employed to formulate the empirical model, see Section 5.4. For secondary drops assigned to the inside of the spray cone the function for the wall-tangential velocity component is mirrored to negative values. To complete the description of the secondary spray, the parcel tracks within a distance of at most 2 mm from the measurement plane will be shown at $t = 8.0$ ms after start of injection.

6.2.3.1 Ideal Reflection

Figure 6.4 illustrates the poor results with ideal reflection calculated on the target. As the impact is not ideally normal, the direction towards the inside of the spray cone is preferred and the lack of a collision model is obvious. A comparison of Figures 6.4 and 6.3 reveals that the secondary distributions resemble the primary ones, as expected. For the wall-normal velocity component this is rather difficult to see due to the scaling in Figure 6.4 which accounts for the measured secondary distribution.

The same results are in principle found for the secondary drops assigned to the outside of the hollow cone. The histograms only appear more sparse, as these drops are very few.

6.2.3.2 Elsässer's model

A comparison of this model with the experimental data has already been done in Section 5.1 restricted to the ratio of secondary to primary mean values. It showed that two different regimes of the model are captured in the experiment by the variation of the target temperature, namely the cold wetting and the hot non wetting regime. For both, the comparison is now extended from the mean values to the distribution functions.

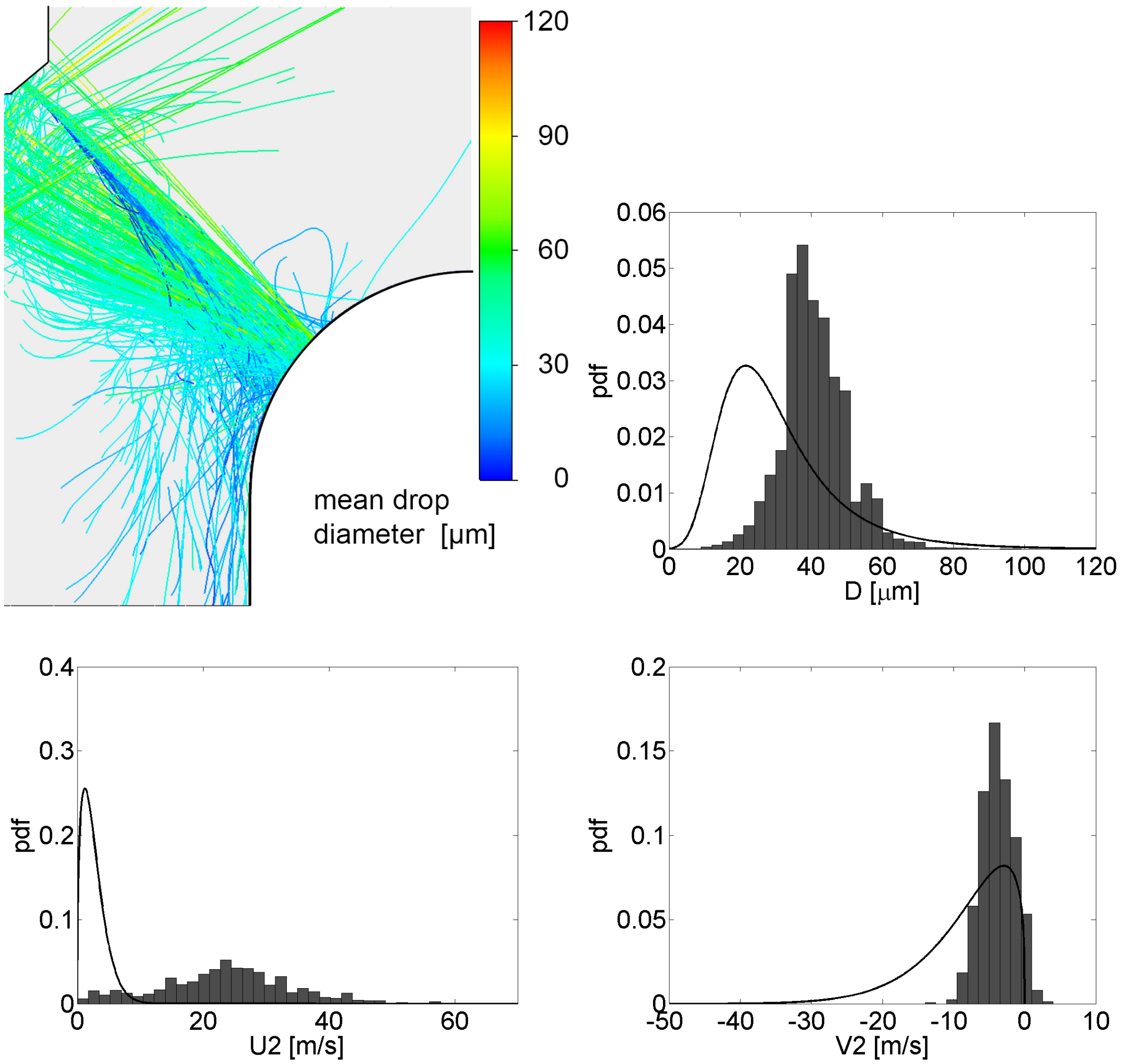

Figure 6.4: Results using ideal reflection. The distributions refer to the secondary drops assigned to the inside of the spray hollow cone. The continuous black lines present the experimental results.
In the figure on the upper left, the reflection of secondary parcel trajectories on the left boundary is an unwanted consequence of the symmetry definition.

Model	h_{film} [μm]	T_{wall} [°C]	D_{sec} [μm]	$v_{\text{abs,sec}}$ [m/s]
Elsässer	0	25	18	19
Elsässer	30	25	21	22
Elsässer	0	200	15	4.7

Table 6.1: Results of Elsässer's model considering an impinging drop with $D_{\text{prim}} = 50\,\mu\text{m}$, $v_{\text{abs,prim}} = 35\,\text{m/s}$ and $\alpha = 85°$. The reflection angle is not presented because it depends on a random number.

Figure 6.5 shows the results for a wall temperature of $T_{\text{wall}} = 25°\text{C}$, which lies in the cold wetting regime. The outcomes are mainly splash and partly spreading, rebound does not occur. As for ideal reflection fewer secondary drops are predicted outside the spray cone than inside, i.e. the reflection is weighted towards the inside. Although the experimentally observed motion of the secondary drops tangentially to the target surface seems to be reproduced, the distribution functions do not agree well. The diameter distribution is much too narrow and the normal velocity components are still too large. The distribution function of the wall-tangential velocity component shows the wrong shape.
Due to the lack of a model for the wall film transport in CFX version 12, the formation of a stationary wall film on the target in the cold wetting regime cannot be simulated. Hence, the results would depend on the time span Δt_{run} considered in the simulation, if the film thickness was included as a transient argument in Elsässer's model. Therefore, the calculations associated to Figure 6.5 are done as if the target was dry, i.e. with $h_{\text{film}} = 0$. To get a notion of the changes in Elsässer's predictions if the target was wetted instead, Figure 6.6 presents the results for a constant value of $h_{\text{film}} = 30\,\mu\text{m}$, which is arbitrarily chosen. The distributions are slightly shifted, else no significant differences arise.

For a wall temperature of $T_{\text{wall}} = 200°\text{C}$, which lies in the hot non wetting regime, the comparison of the simulation results to the experimental data is hardly better than in the cold wetting regime, see Figure 6.7. The distribution of the wall-normal velocity components is now too narrow and shifted to too small values. The diameter distributions and those of the wall-tangential velocity components are also too narrow with the large values of the distribution missing. A wall film does not form in this regime and the value of the model argument h_{film} is not addressed.

Table 6.1 complements the consideration of Elsässer's model with a short overview of the results for an exemplary primary drop. In summary, the agreement of the predictions with the measurements is not satisfactory.

6.2.3.3 Kuhnke's model

The system of ellipses which is used in this model to determine the spray density cannot be defined on the hemispherical target. Therefore, the linear interpolation between single and multiple drop correlations is not possible in this case and either pure single (κ set to a very large value) or pure multiple (κ set to value smaller than unity) drop correlations are considered.
As in Elsässer's model, the film thickness h_{film} and the wall temperature T_{wall} are arguments of the model:

- The actual value of the film thickness is only used to calculate regime distinctions for the single drop model, i.e. $K_{\text{crit},SD}$, in case of a wetted wall, as well as to determine the secondary to primary mass ratio in the splashing regime. Else Kuhnke's model only distinguishes the general state of dry or wetted wall and the transient character and actual value of h_{film} are hence not important in the calculation of the outcome which is predominantly splashing. Thus, only fixed values of $h_{\text{film}} = 0$ and $h_{\text{film}} = 30\,\mu\text{m}$ are considered in the simulations.

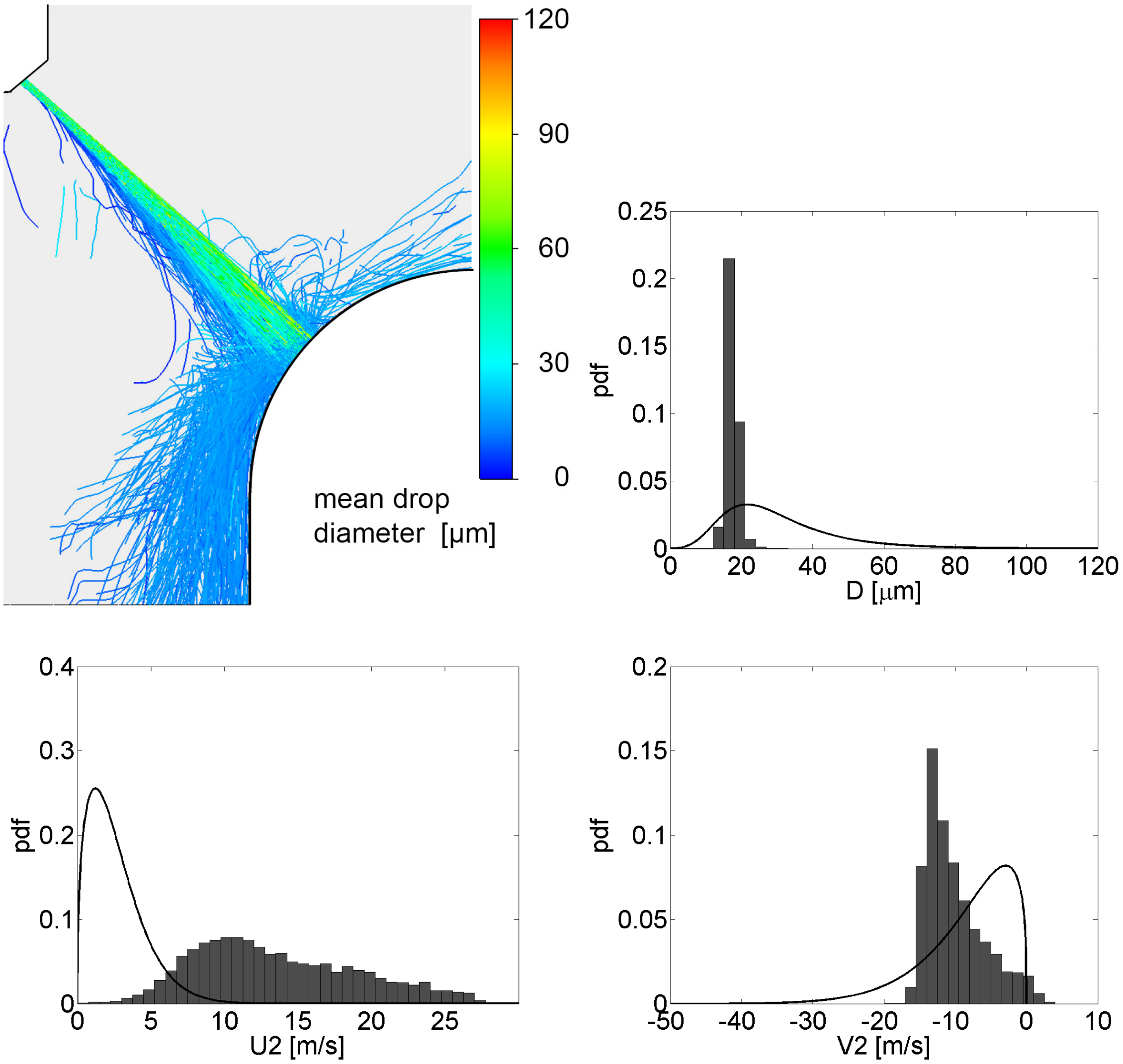

Figure 6.5: Results using Elsässer's model with $T_{\text{wall}} = 25°\text{C}$ (cold wetting regime) and $h_{\text{film}} = 0$. The distributions refer to the secondary drops assigned to the inside of the spray hollow cone. The continuous black lines present the experimental results.

- The value of the wall temperature is addressed in the calculation of regime boundaries, which does not play a role in the considered case because splashing is chosen due to droplet kinematics no matter what value T_{wall} takes. Moreover, it is applied in the splashing regime to calculate the ejection angle for single drop impact in case of a dry wall. But it is only distinguished between a cold and a hot state there - the exact value is not of influence. In the following, values of $T_{\text{wall}} = 25°\text{C}$ and $T_{\text{wall}} = 200°\text{C}$ are regarded.

A comparison of the results using Kuhnke's model is rather confusing concerning different specifications with respect to single/multiple drop correlations and the value of h_{film} and T_{wall}. Therefore, Table 6.2 gives a first overview in presenting the mean secondary properties for an exemplary primary drop:

The secondary diameters are smaller for dry than for wetted surfaces and smaller for the single drop correlations than for the multiple drop correlations as already seen in Chapter 2. The mean ejection angle in case of the multiple drop model is 1.5 times the value of the single drop model (the distribution width is also broader) which gets very

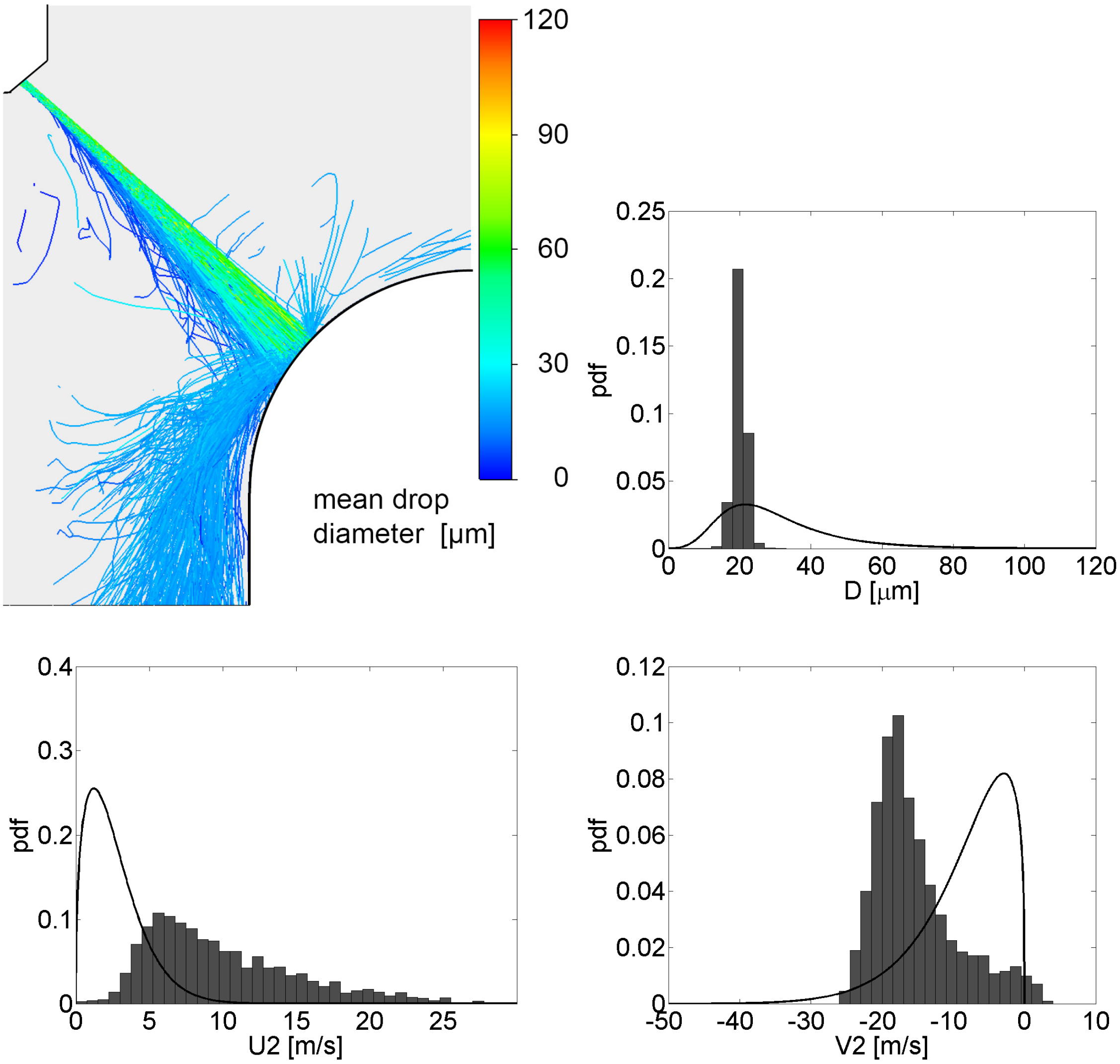

Figure 6.6: Results using Elsässer's model with $T_{\text{wall}} = 25°\text{C}$ (cold wetting regime) and $h_{\text{film}} = 30\,\mu\text{m}$. The distributions refer to the secondary drops assigned to the inside of the spray hollow cone. The continuous black lines present the experimental results.

small for hot and dry target. It is affirmed that the wall temperature value is of no influence in case of a wetted wall, neither for single nor for multiple drop correlations.

For a wetted target, which better meets the situation of a spray impact than a dry target because only the very first impinging drops actually see a dry surface, the results of Kuhnke's model are presented in Figure 6.8 for the single drop correlations and in Figure 6.9 for the multiple drop correlations. In the reference case, see Chapter 2, it showed that the latter were addressed for the dense, high-pressure sprays when the system of ellipses was used.
It shows that the secondary diameters are predicted mainly too small especially with the single drop correlations. In contrast to the wall-normal velocity components, the range of the wall-tangential velocity components is not well predicted with the large values missing. Considering the parcel trajectories, the reflection seems slightly weighted towards the outside of the spray cone in contrast to the predictions of ideal reflection or Elsässer's model, where the inside of the hollow cone is preferred. This impression is mainly due to the air flow which disperses the small secondary drops outside the

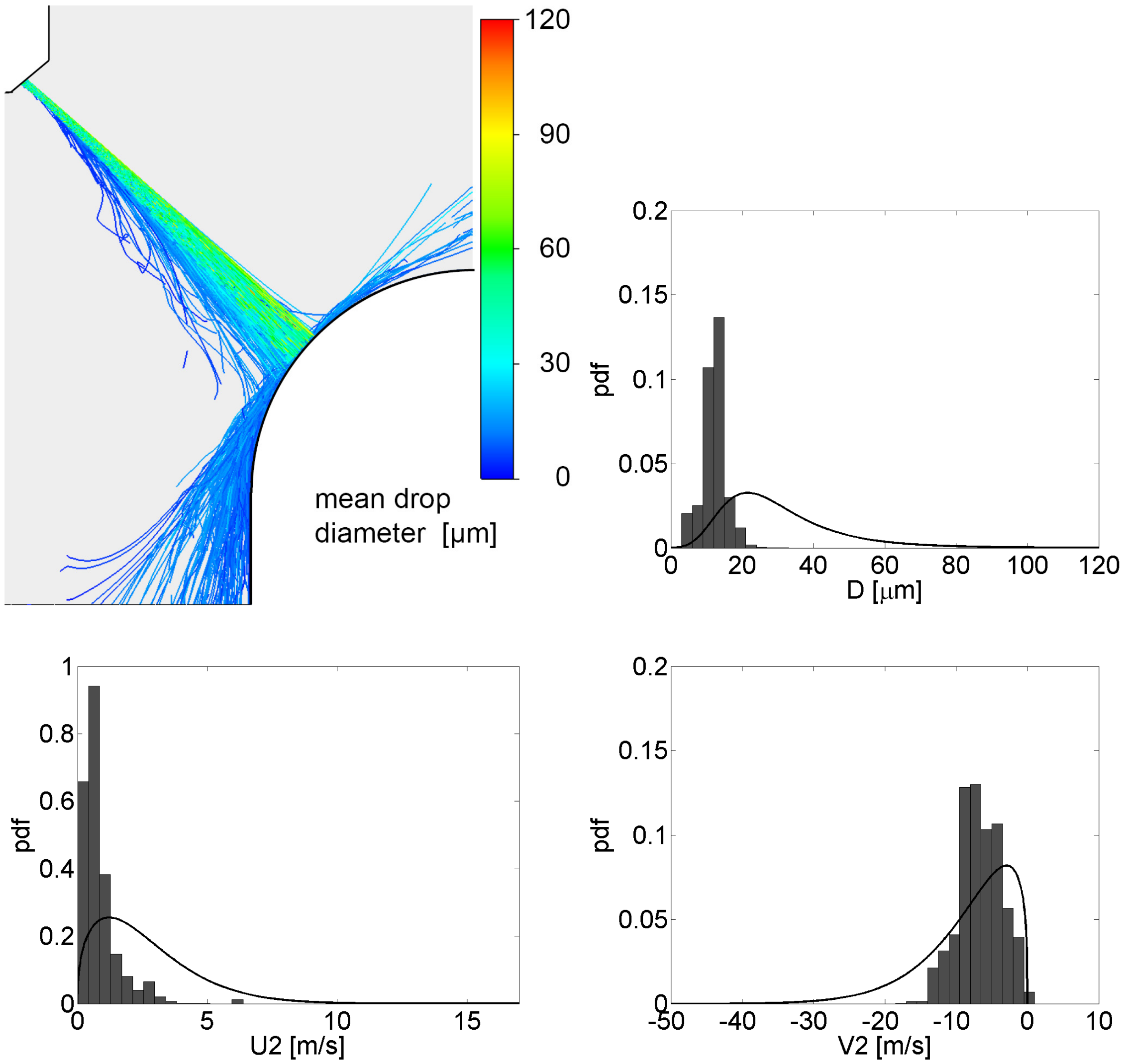

Figure 6.7: Results using Elsässer's model with $T_{\text{wall}} = 200°\text{C}$ (hot non wetting). The distributions refer to the secondary drops assigned to the inside of the spray hollow cone. The continuous black lines present the experimental results.

	h_{film} [μm]	T_{wall} [°C]	D_{sec} [μm]	$v_{\text{abs,sec}}$ [m/s]	β [°]
Single drop correlations	0	25	2.6	11	27
	0	200	2.6	11	0.0065
	30	25	16	7.3	53
	30	200	16	7.3	53
Multiple drop correlations	0	25	25	14	41
	0	200	25	14	0.0098
	30	25	50	4.1	79
	30	200	50	4.1	79

Table 6.2: Outcomes of Kuhnke's model considering an impinging drop with $D_{\text{prim}} = 50\,\mu\text{m}$, $v_{\text{abs,prim}} = 35\,\text{m/s}$ and $\alpha = 85°$. The secondary mean properties are listed. (The individual values are derived using random numbers.)

spray cone in a wider range of directions than inside the spray cone. In principle, however, forward and backward scattering should occur equally frequent in case of normal impact[3].

In Figures 6.8 and 6.9 the results of Kuhnke's model are shown with the original definition of the number rates, cf. Equation 1.83. In Section 6.1 it has been discussed that the latter is arguable and that constant number rates should be used. Evaluating the parcel trajectories in the simulation with such values (the constant value itself does not matter due to the normalisation of the distribution functions), some differences arise which is exemplarily shown for the secondary drop diameters outside of the spray cone in case of the single drop correlations, see Figure 6.10. Large diameters are weighted more strongly.

6.2.3.4 Roisman's/Horvat's model

As for the reference case, cf. Chapter 2, this model cannot be applied with its original correlation describing the secondary to primary mass ratio Γ_V, see Equation 1.99. In Section 5.1 the primary mass flux is estimated as $q_{m,\mathrm{prim}} \approx 21\,\mathrm{kg/(s \cdot m^2)}$ and the mean impact velocity is found as $v_{10,\mathrm{prim}} \approx 35\,\mathrm{m/s}$. Together with the liquid density of $\rho = 696\,\mathrm{kg/m}^3$, cf. Table 3.1, this leads to

$$\Gamma_V \propto 0.0011 - \frac{q_{m,\mathrm{prim}}}{\rho \cdot v_{10,\mathrm{prim}}} \approx 0.0011 - 0.00086 \approx 0.00024\,. \tag{6.8}$$

The value is not negative as for the reference case. Yet, $q_{V,\mathrm{prim}}/v_{10,\mathrm{prim}}$ is far beyond the validity range of $4.6 \cdot 10^{-5} < q_{V,\mathrm{prim}}/v_{10,\mathrm{prim}} < 5.3 \cdot 10^{-4}$ given by Roisman / Horvat, and the correlation of the mass ratio Γ_V cannot be used. Therefore, the value of Γ_V observed in the experiment and used in the new model, see Equation 5.26, is applied by way of trial. Note that this change in the model affects also the calculated secondary velocities, cf. Equation 1.101.

The model is limited to cold walls and Figure 6.11 shows the simulation results for a target temperature of $T_{\mathrm{wall}} = 25°\mathrm{C}$ (the value itself is not an argument of the model). The dominant outcome is splash where the secondary drop diameters show to be too small in general. The wall-normal velocity components prove to be too large but the wall-tangential components are rather well represented. Yet, as mentioned above, the comparison of the velocity distributions has to be considered very carefully as these are influenced by the change in the mass ratio.
The simulation has been done with the original number rates defined in Equation 1.100. As for Kuhnke's model, their definition is questionable.
The target is considered wetted in the calculations associated to Figure 6.11, i.e. h_{film} is set to $30\,\mu\mathrm{m}$. The results for a dry target are identical because the film thickness is only used to calculate the criterion for splashing, see Equations 1.93. The correlations which describe splashing are not affected.

---

[3] As already mentioned in Section 2.3, Kuhnke's and also Roisman's/Horvat's model predict the deviation angle Ψ in a range of $[0°, 360°[$, but the implementation in CFX is restricted to values of $\Psi = 0°$ and $\Psi = 180°$ (forward and backward scattering). This limitation is rather advantageous for the models in their application to a hollow cone spray, see Section 5.4 and Figure 5.14.

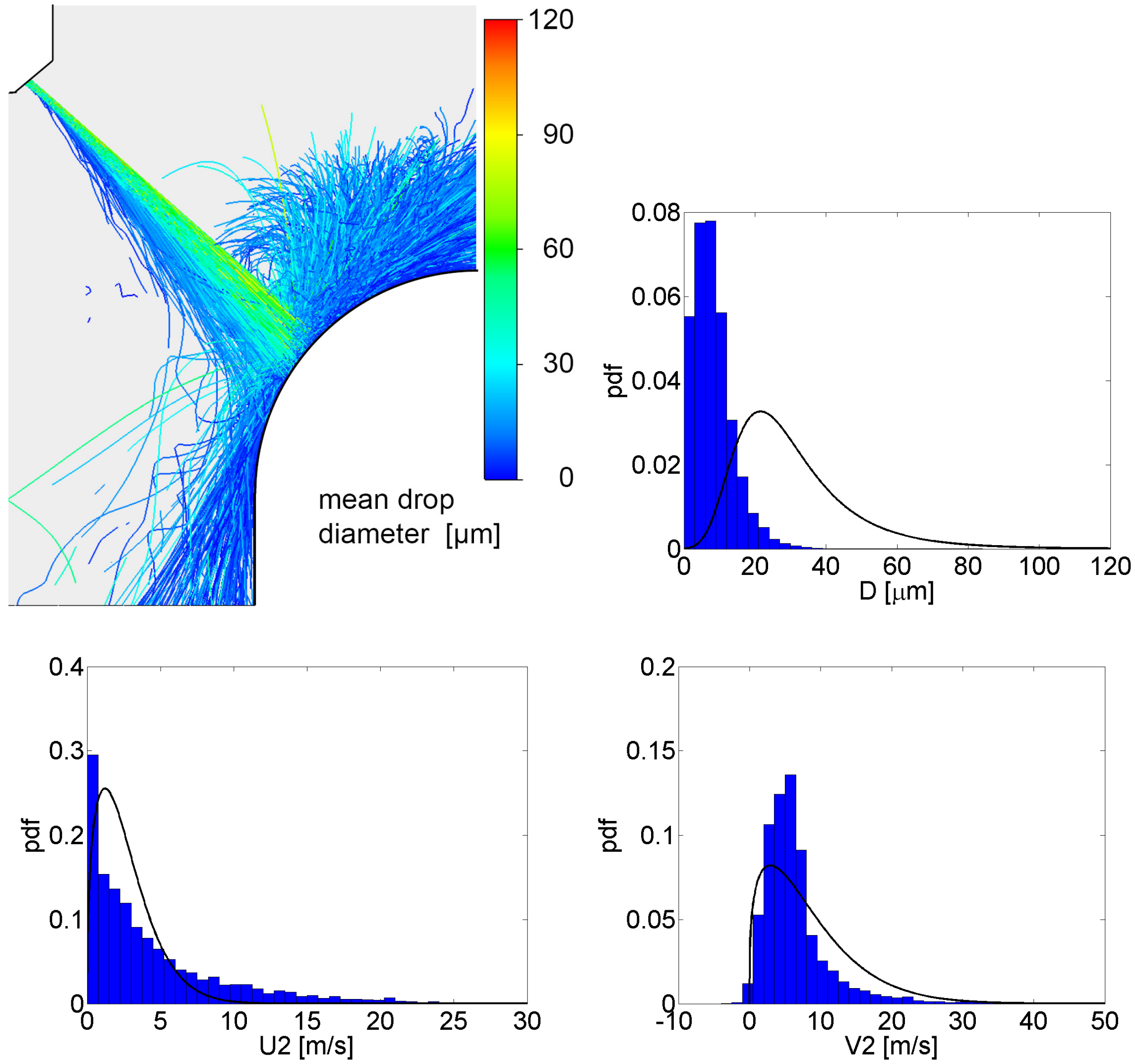

Figure 6.8: Results using Kuhnke's model with single droplet correlations and $h_{\text{film}} = 30\,\mu\text{m}$ ($T_{\text{wall}} = 25°\text{C}$). The distributions refer to the secondary drops assigned to the outside of the spray hollow cone. The continuous black lines present the experimental results.

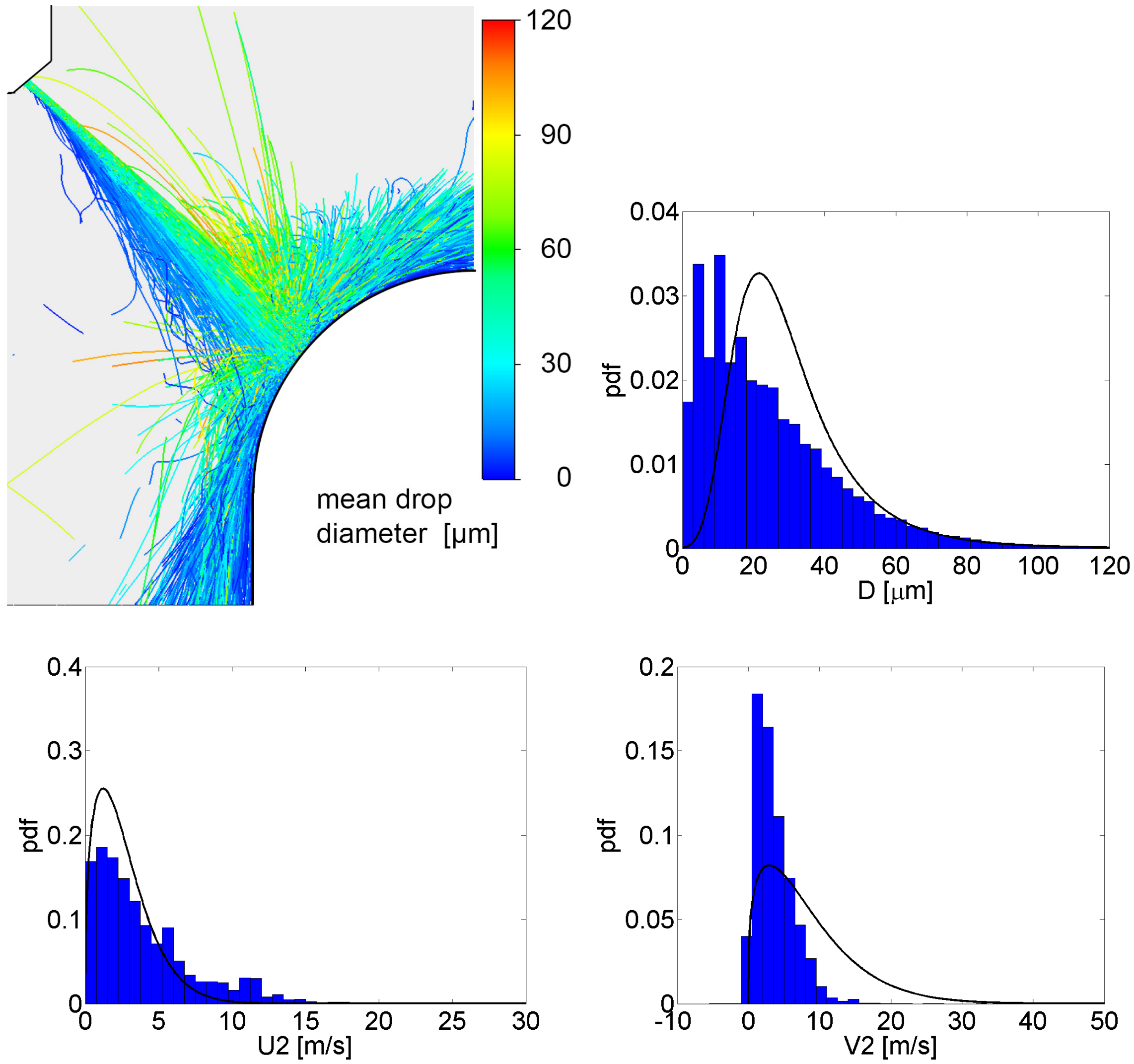

Figure 6.9: Results using Kuhnke's model with multiple droplet correlations and $h_{\mathrm{film}} = 30\,\mu\mathrm{m}$ ($T_{\mathrm{wall}} = 25°\mathrm{C}$). The distributions refer to the secondary drops assigned to the outside of the spray hollow cone. The continuous black lines present the experimental results.

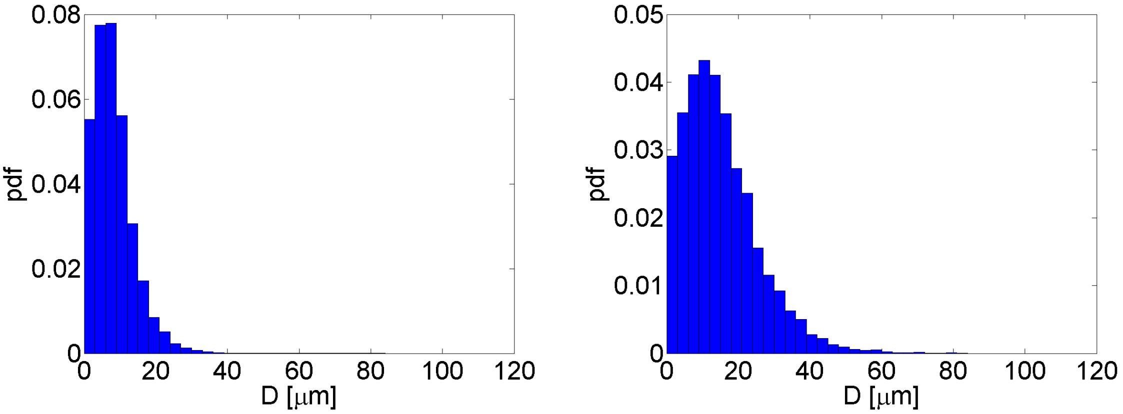

Figure 6.10: Comparing the simulation results for Kuhnke's model (single droplet correlations, $h_{\text{film}} = 30\,\mu\text{m}$, $T_{\text{wall}} = 25°\text{C}$) using the original (left) and constant (right) number rate definitions. Secondary drops assigned to the outside of the spray cone are considered.

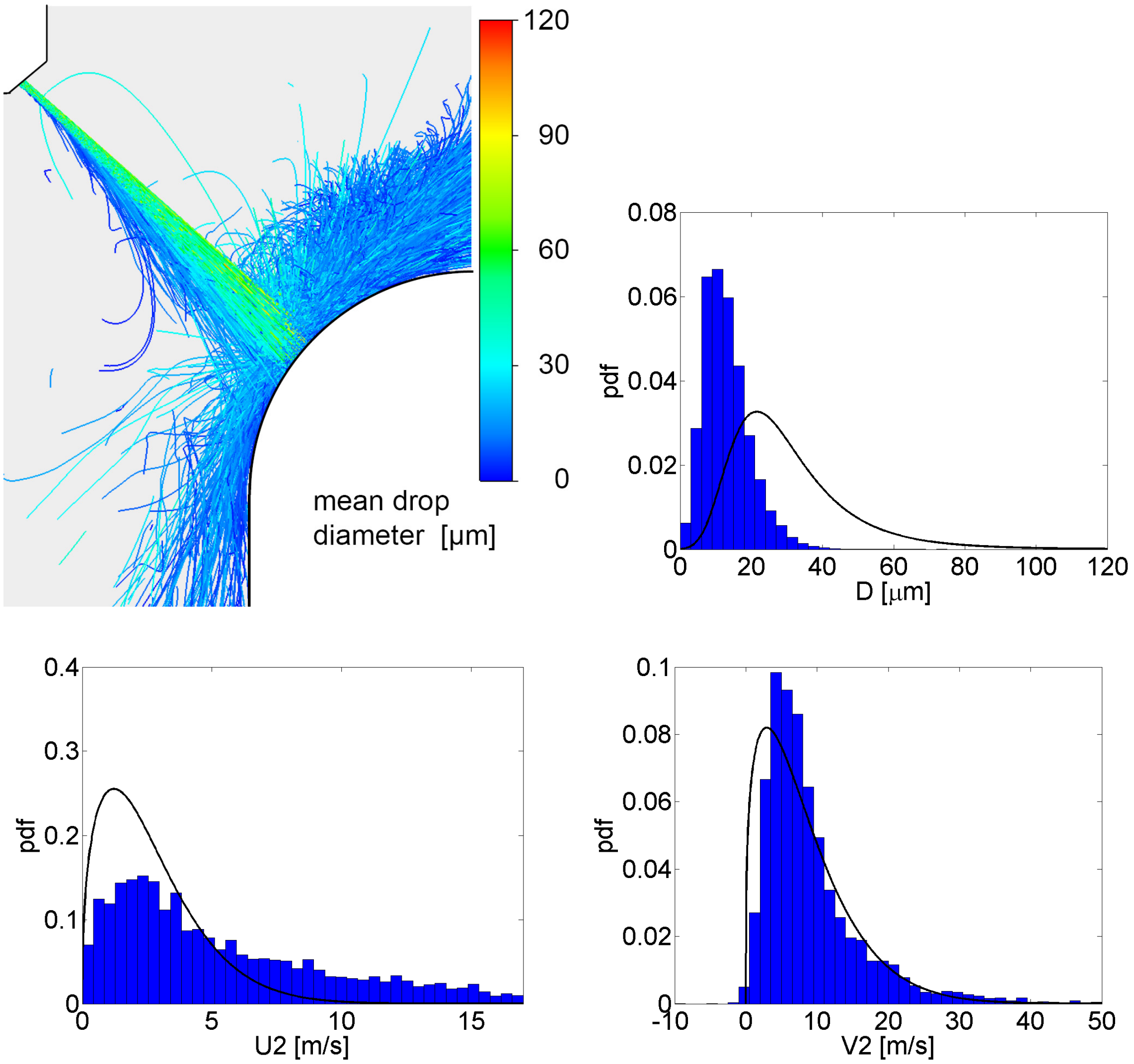

Figure 6.11: Results using Roisman's/Horvat's model ($h_{\text{film}} = 30\,\mu\text{m}$). The distributions refer to the secondary drops assigned to the outside of the spray hollow cone. The continuous black lines present the experimental results.

6.2.3.5 New model

In Figure 6.12 the simulation results applying the new model are exemplarily presented for $T_{\text{wall}} = 25°\text{C}$. The results can be transferred to other conditions, as the target temperature and the film height are no arguments of the wall interaction correlations. The agreement with the measured distribution functions is very good for diameters as well as for both velocity components. The parcel trajectories are evenly distributed towards the inside and outside of the spray cone.

As the correlations have been developed using the measured data, this presents a basic verification of the model correlations and their implementation.

In the following sections the validation and application of the empirical model under different conditions and for varied properties of the impacting spray are studied.

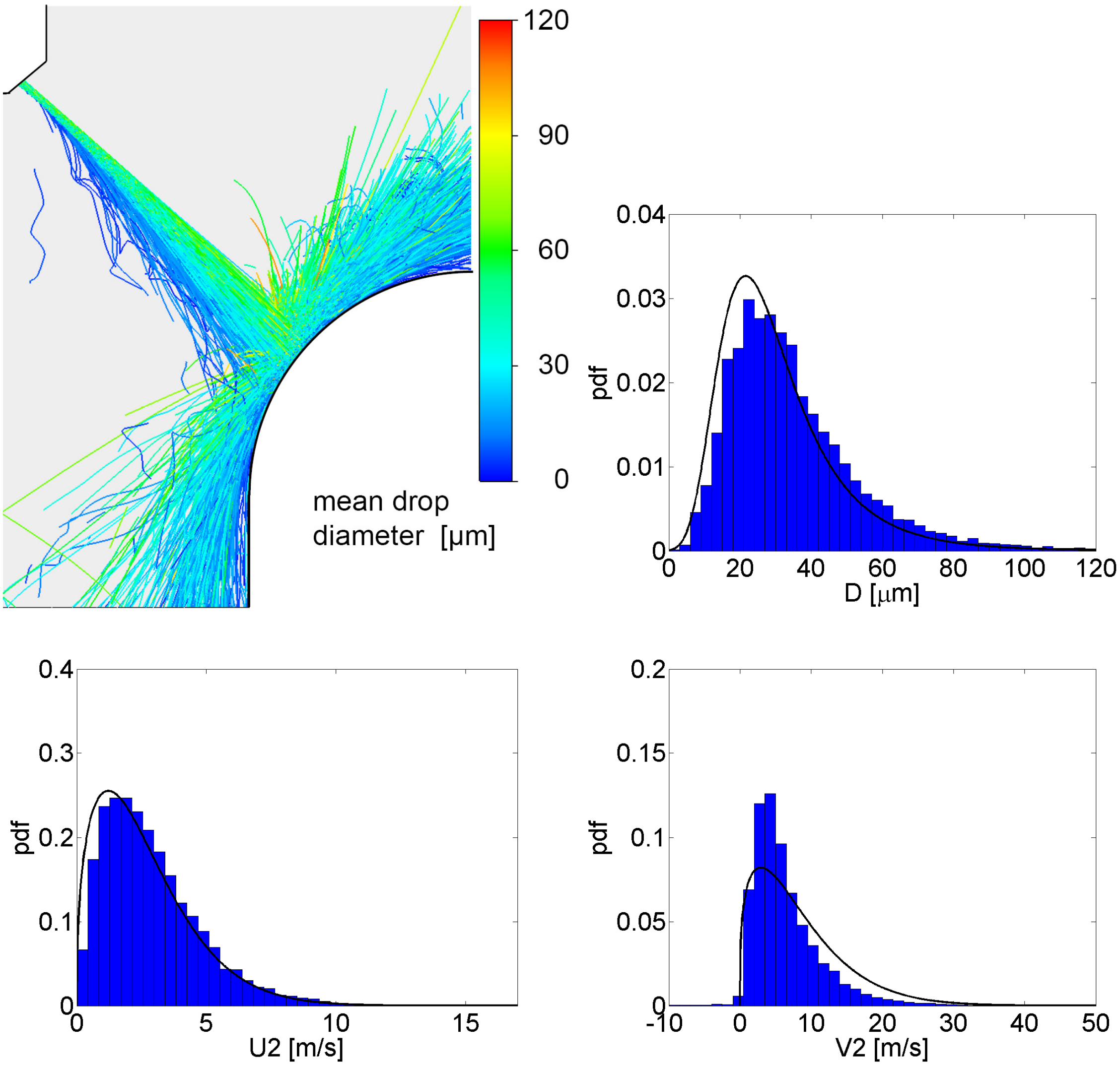

Figure 6.12: Results using the new empirical model. The distributions refer to the secondary drops assigned to the outside of the spray hollow cone. The continuous black lines present the experimental results.

6.3 Impact on an oblique plate

As the experimental data are restricted to an approximately normal impact, the extrapolation of the empirical model correlations to oblique impact angles has been deduced with simple assumptions. These have been adapted to describe correctly the reference case of Chapter 2 with a mean impact angle of $\alpha_{10} \approx 45°$, see Section 5.4.2 and also Appendix C.2 for additional remarks.
A validation of the correlations for oblique impact still lacks and, unfortunately, no quantitative data are available for that purpose. However, transmitted-light images can be used. These refer to a case almost identical to the reference case in Chapter 2 - yet, the plate is tilted by 13° to the horizontal which leads to impact angles in a range from 32° to 58°, see Figure 6.13, and a loss of the axial symmetry. The distance between injector and plate in the direction of the spray axis is 20 mm. The same ambient conditions and spray settings as in the reference case apply. These differ from those of the experiment performed in this work: A different injector is used and the injection pressure is 200 bar instead of 50 bar.
The spray propagation till wall impact is not changed notably by the different position of the plate compared to the reference case.

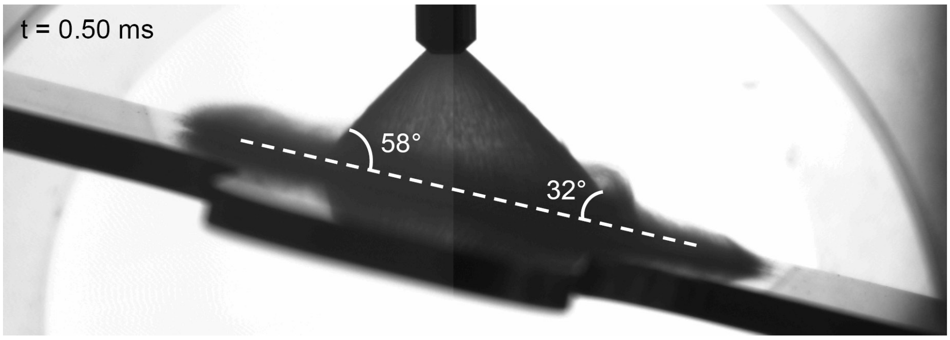

Figure 6.13: Impact on an oblique plate, tilted by an angle of 13° to the horizontal, at $t = 0.50\,\text{ms}$ ($\approx 0.45\,\text{ms}$ after start of injection).

For the sake of completeness, Figures 6.14 and 6.15 compare transmitted-light images with the results applying ideal reflection, Elsässer's and Kuhnke's model at $t = 0.60\,\text{ms}$ (start of injection at $t \approx 0.05\,\text{ms}$). The images are analogous to those in Figures 2.11 and 2.13 for the impact on a horizontal plate. Roisman's/Horvat's model is restricted to normal impacts and furthermore cannot be applied due to the secondary to primary mass ratio becoming negative, see Section 2.3.2. It is again affirmed that the presented models cannot describe the wall interaction of a dense hollow cone spray satisfactorily.

In comparison, the simulation results with the new empirical model agree very well with the transmitted-light images, cf. Figures 6.16 and 6.17 for exemplary time values of $t = 0.60\,\text{ms}$ and $t = 0.80\,\text{ms}$. Besides the shape of the secondary spray, also the velocity of propagation is reproduced correctly. This is very promising for the applicability of the empirical model to oblique impacts.
In contrast to the reference case, it is not possible to calculate the mean drop properties on impact for all primary drops of the previous timestep and to use these values in the model calculations of the current timestep, because they depend on the position on

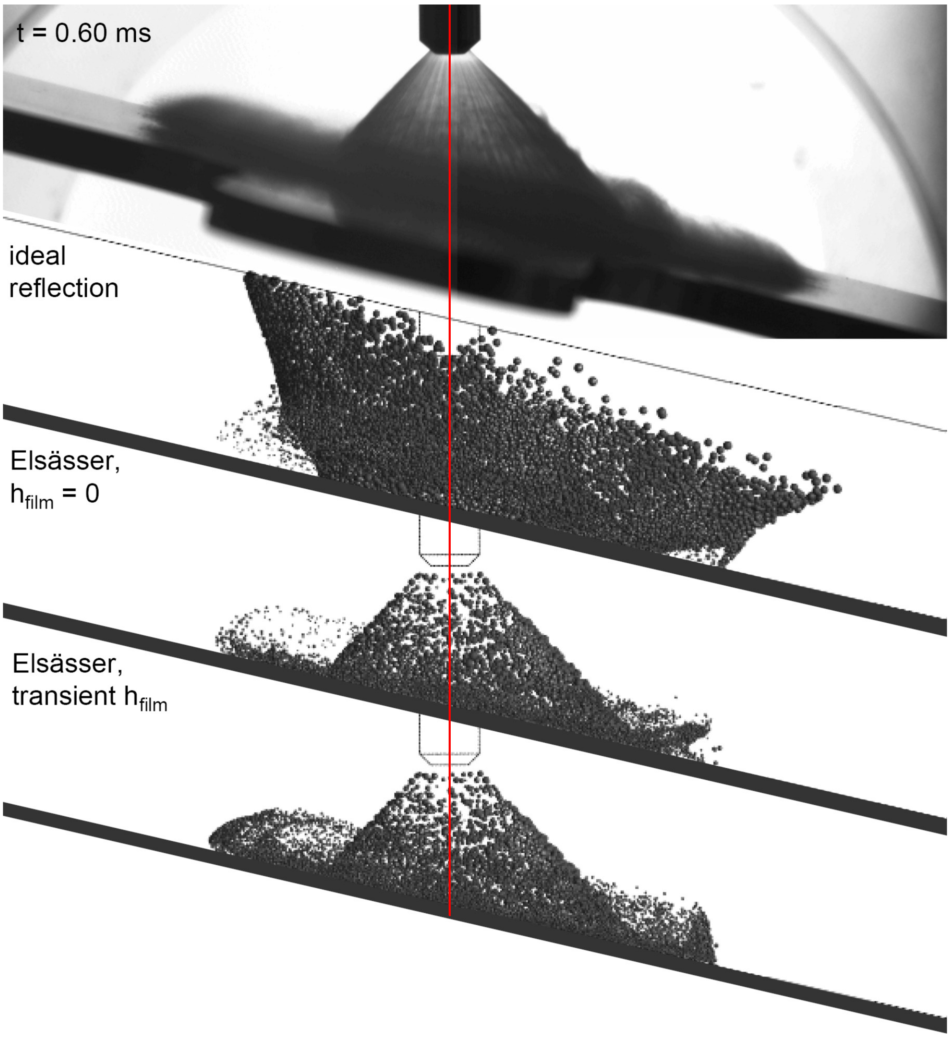

Figure 6.14: Comparison of a transmitted-light image with the predictions of ideal reflection and Elsässer's model at $t = 0.60\,\mathrm{ms}$.

the plate (the case is not rotationally symmetric to the spray axis). Therefore, the averaging is done for sectors of 10° around the spray axis.

In Figures 6.16 and 6.17 the results are also shown with the averaging carried out over sectors of width 20° instead of 10° which only leads to negligible differences. Moreover, the results are presented for the case without any averaging, i.e. where the individual properties of primary parcels are applied in the correlations. This procedure will usually have to be chosen for diversified surface curvatures occuring in an engine, although it entails errors: The primary distribution functions are superimposed on the secondary ones, which leads, for instance, to too large maximal diameters and velocity components. The differences in Figures 6.16 and 6.17 between results with/without averaging seem insignificant, though. Yet, it has to be kept in mind that the number rates of the secondary parcels are also affected which changes the drop weighting and hence the shape of the distribution functions.

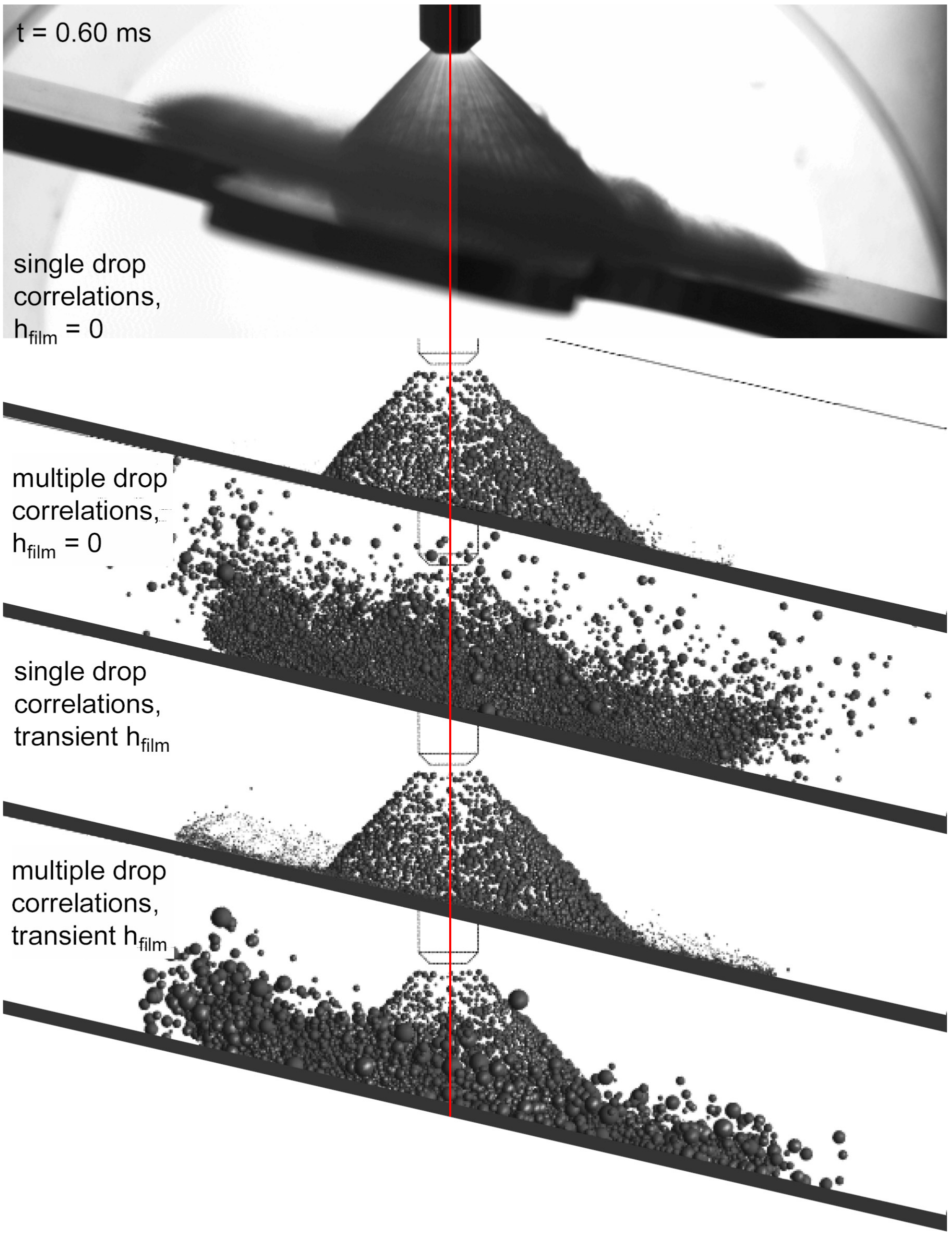

Figure 6.15: Comparison of a transmitted-light image with the predictions of Kuhnke's model at $t = 0.60\,\mathrm{ms}$. The system of ellipses to determine the spray density and hence to find out if single or multiple drop correlations apply, can be used in this case. As in the reference case it leads to multiple drop correlations.

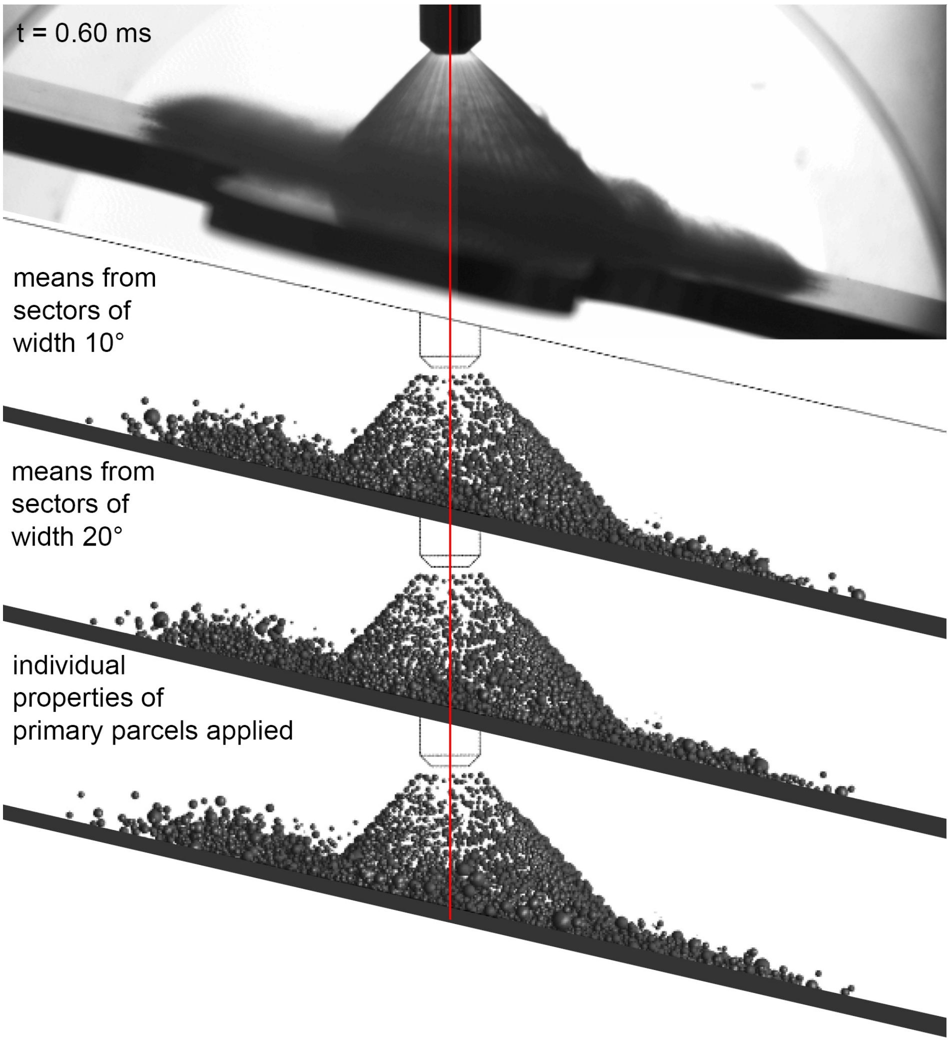

Figure 6.16: Comparison of a transmitted-light image with the predictions of the new model at $t = 0.60\,\mathrm{ms}$.

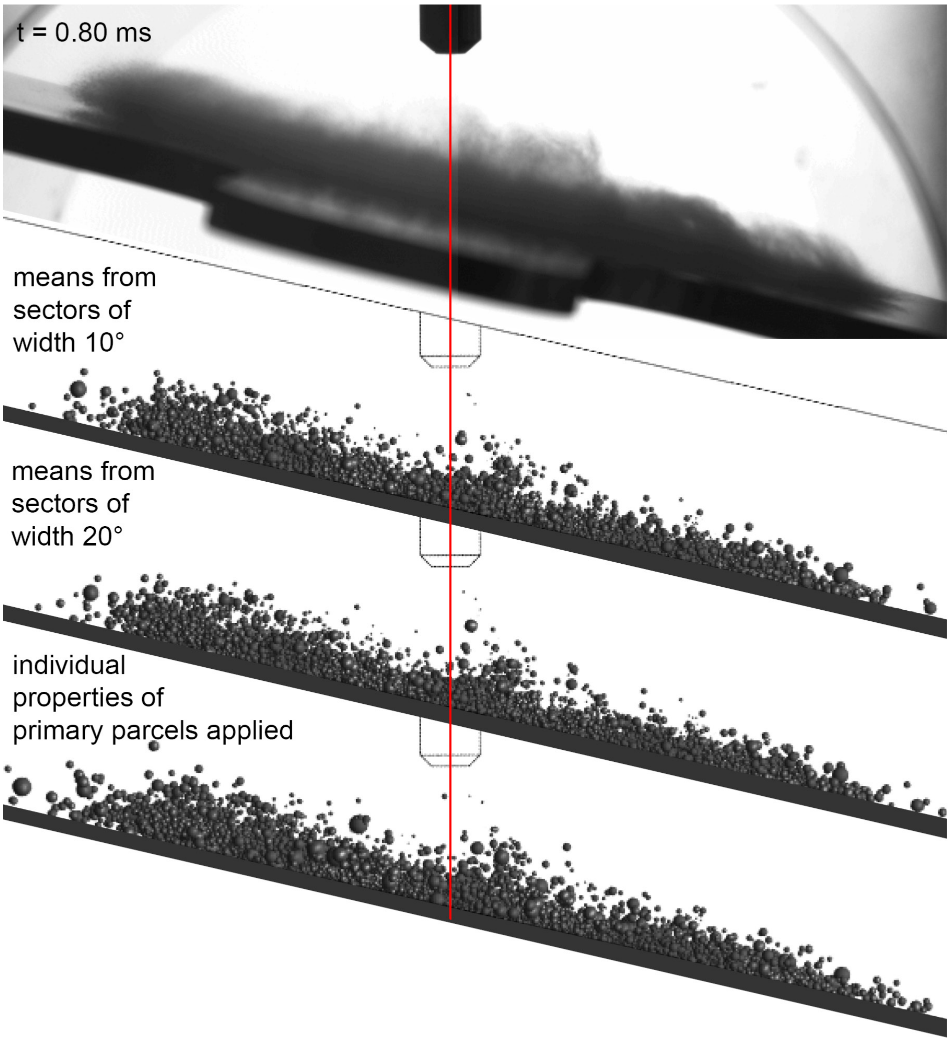

Figure 6.17: Comparison of a transmitted-light image with the predictions of the new model at $t = 0.80\,\mathrm{ms}$.

6.4 Impact on a piston dummy

Finally, the new empirical model is applied to a case taken from engine development. In order to adapt the spray design to the piston geometry in a combustion chamber, the impact on a generic piston geometry is studied.

6.4.1 Definition

A dense hollow cone spray with isooctane as spray liquid is injected at a pressure of $p_{\mathrm{inj}} = 50\,\mathrm{bar}$ into atmospheric conditions. It impacts on a piston dummy in a close distance of $\approx 11\,\mathrm{mm}$ to the injector, which corresponds to an engine situation where the piston is situated near the top dead center, see Figure 6.18. The injection settings and ambient conditions are summarised in Table 6.3.

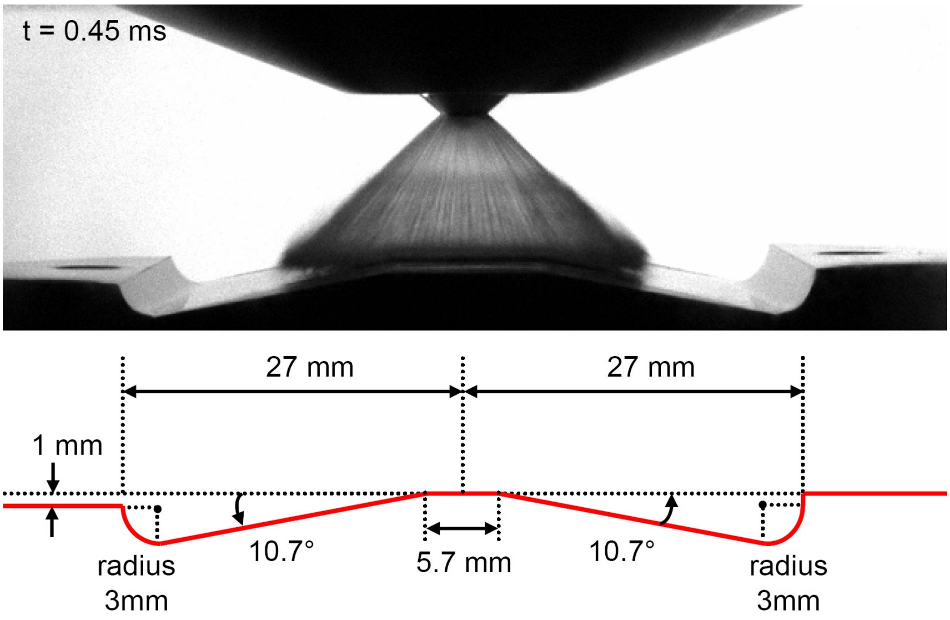

Figure 6.18: Transmitted-light image showing the spray impact on the piston dummy at $t = 0.45\,\mathrm{ms}$, i.e. $\approx 0.35\,\mathrm{ms}$ after start of injection. Details of the piston geometry are also presented.

The piston is not considered in a usual shape but as a “two-dimensional” variant where an intersection through the centre plane of a real piston is simply translated in space to define the dummy surface, cf. Figure 6.19. Thus, transmitted-light images can be taken including a look into the bowl and the deflection of the spray in the radii can be studied. The impact angle varies in a range from $\approx 38°$ to $45°$ (obtained on the horizontal middle part of the piston).

On one side of the piston an additional height of 1 mm is added on top of the radius to find out if such a procedure helps in guiding the secondary spray, e.g. to avoid later impact on the cylinder liner.

Surface material	aluminium, anodised
Wall temperature T_{wall}	20°C
Gas fluid	air, initially quiescent
Ambient pressure p_{ambient}	1 bar
Ambient temperature T_{ambient}	20°C
Spray liquid	C_8H_{18} (isooctane)
Full spray cone angle	97.1°
Injection pressure p_{inj}	50 bar
Injection duration Δt_i	1.0 ms
Injected mass m_{inj}	19.4 mg
Liquid temperature $T_{C_8H_{18}}$	20°C

Table 6.3: Ambient conditions and injection settings for the impact on the piston dummy.

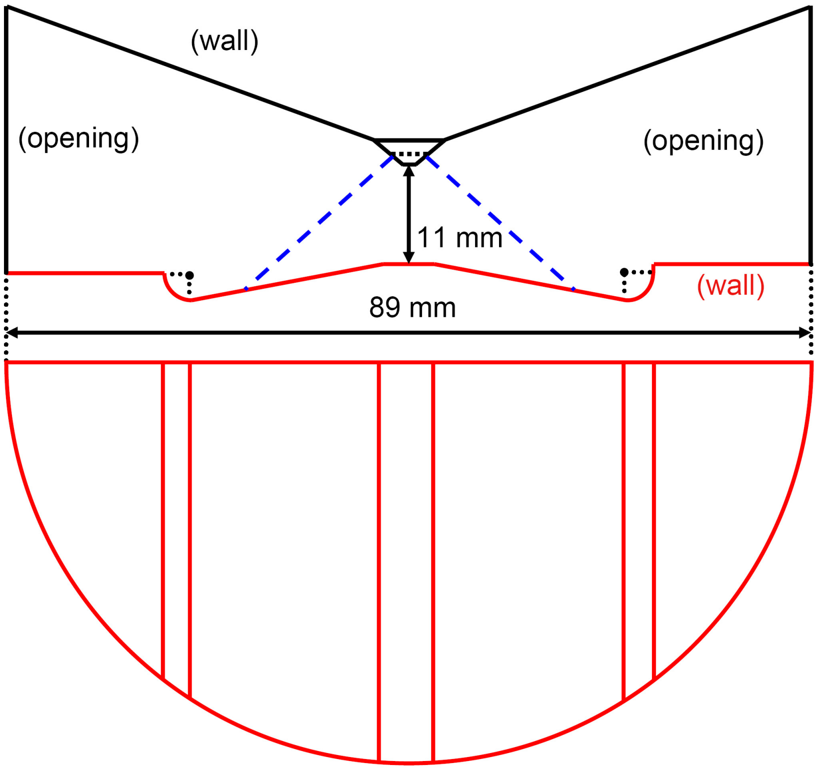

Figure 6.19: Geometry including the boundary conditions considered in the simulation.

6.4.2 Setup of the simulation

Due to the symmetry of the problem towards the centre plane, only half the geometry is calculated. The associated mesh of tetrahedra and prisms on rigid walls consists of $\approx 1.6 \cdot 10^5$ nodes and $\approx 7.9 \cdot 10^5$ elements. The timestep size is set to $5.0 \cdot 10^{-6}$ s.
Since the same injector and the same injection pressure are considered as in the experiment, cf. Chapter 3, the spray initialisation is taken from the simulation of the experiment, see Section 6.2.1.2. There, the diameter and velocity distributions are adjusted to reproduce the measured distributions near the target surface. However, the opening and closing phase of the injector have not been of interest and hence no ramping functions have been considered in the initialised mass flow or velocity functions.
In the present case, this leads to a propagation of the first spray drops which is too fast compared to the transmitted-light images. Instead of modifying the initialisation of the first and last injected spray drops, which would have to be done based solely on assumptions, the initialisation is kept without changes and the images are slightly shifted by altogether 0.10 ms till wall impact. The resulting spray propagation is shown in Figures 6.20 and 6.21. Before the impact, see Figure 6.21(b), the transmitted-light images and the simulation results are synchrone and no shifting is done afterwards.
The uncertainty of spray initialisations is a general problem which affects also spray/wall interaction. Yet, a detailed treatment is beyond the scope of this work and the common procedure applied at BMW is used. In order to assess the performance of spray/wall interaction models, it is anticipated to make no difference whether the intialisation of the first and last drops is adjusted to fit the images, as done for the reference case in Chapter 2, or whether the images are slightly shifted.

6.4.3 Spray impact

In Figures 6.22, 6.23 and 6.24 the simulation results applying the new empirical spray/ wall interaction model are compared with the transmitted-light images. The agreement is very good. The secondary spray propagates rather tangentially to the surface and the velocity is predicted correctly. The thickness of the secondary spray above the surface is also well reproduced.
Considering the predictions of Elsässer's and other models for the impact on a horizontal plate, cf. chapter 2, it gets clear that the new correlations present a major improvement. They predict the deflection in the piston bowl very well and can hence be used to assess the effects of different piston geometries and spray designs[4].

---

[4] It has to be added that the model has not been designed to characterise the secondary drops which are created only at the top of the radii due to a detachment and breakup of the forming wall film. The mechanisms for the ejection of such drops are probably very different from those on direct spray impact and they are no subject of this work.

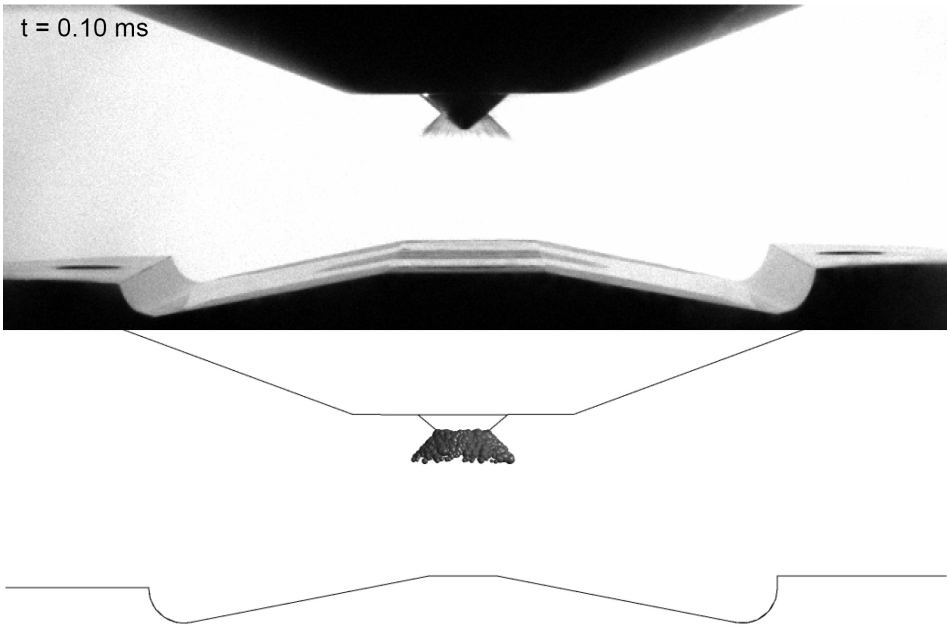

(a) $t = 0.10\,\mathrm{ms}$.

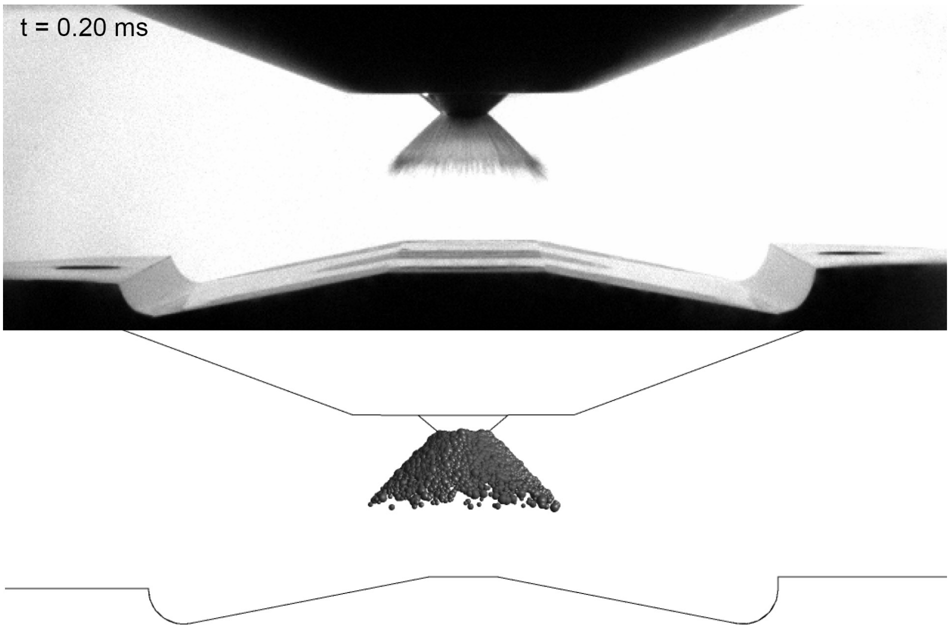

(b) $t = 0.20\,\mathrm{ms}$.

Figure 6.20: Spray propagation before the impact on the piston dummy at $t = 0.10\,\mathrm{ms}$ and $t = 0.20\,\mathrm{ms}$.

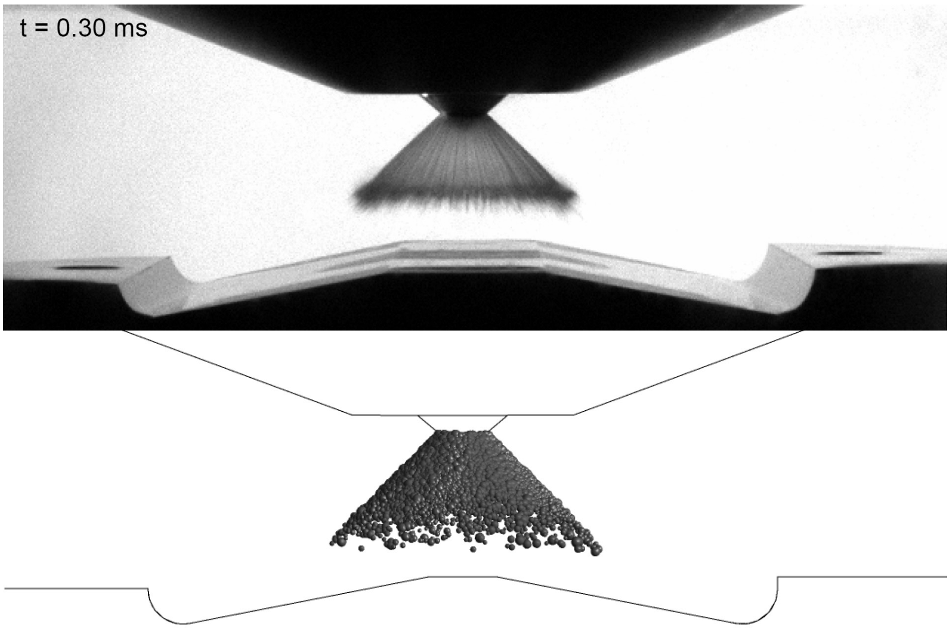

(a) $t = 0.30\,\mathrm{ms}$.

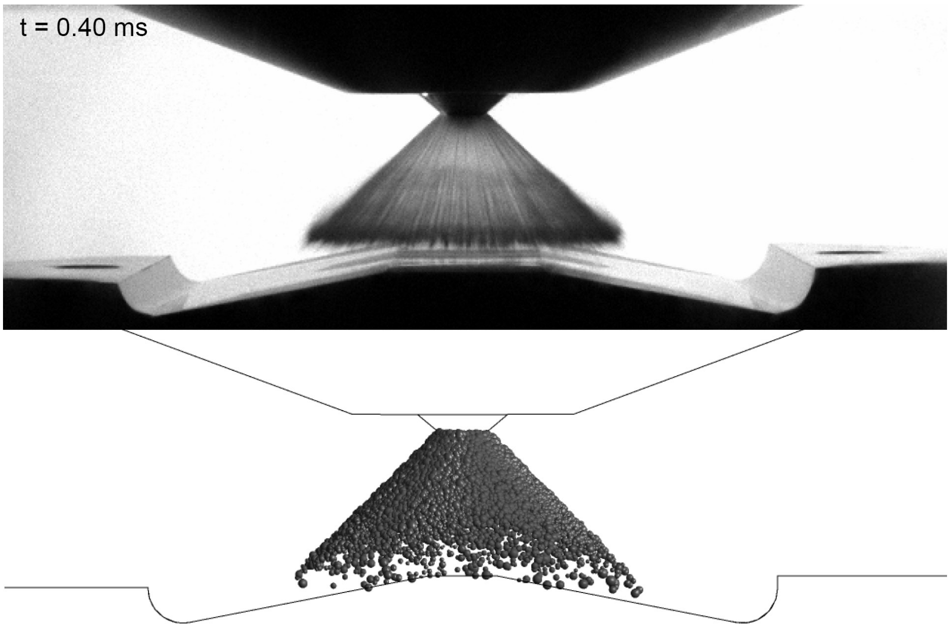

(b) $t = 0.40\,\mathrm{ms}$.

Figure 6.21: Spray propagation before the impact on the piston dummy at $t = 0.30\,\mathrm{ms}$ and $t = 0.40\,\mathrm{ms}$.

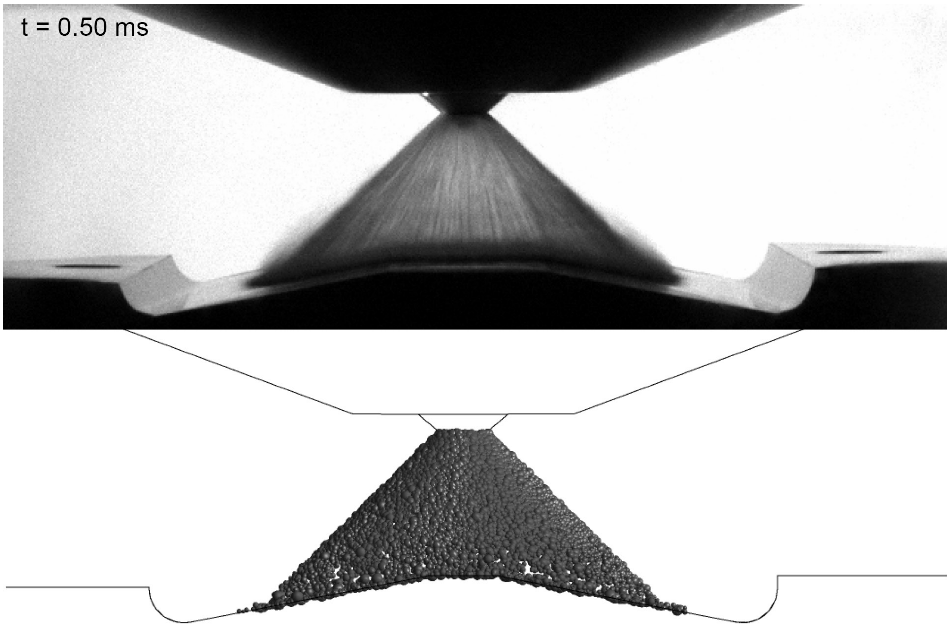

(a) $t = 0.50\,\mathrm{ms}$.

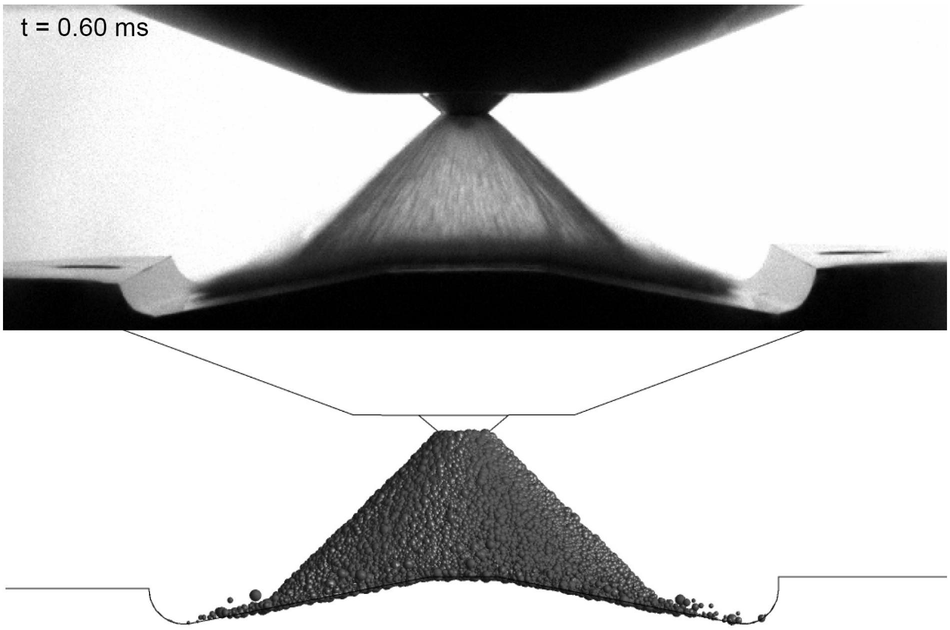

(b) $t = 0.60\,\mathrm{ms}$.

Figure 6.22: Spray/wall interaction on the piston dummy at $t = 0.50\,\mathrm{ms}$ and $t = 0.60\,\mathrm{ms}$.

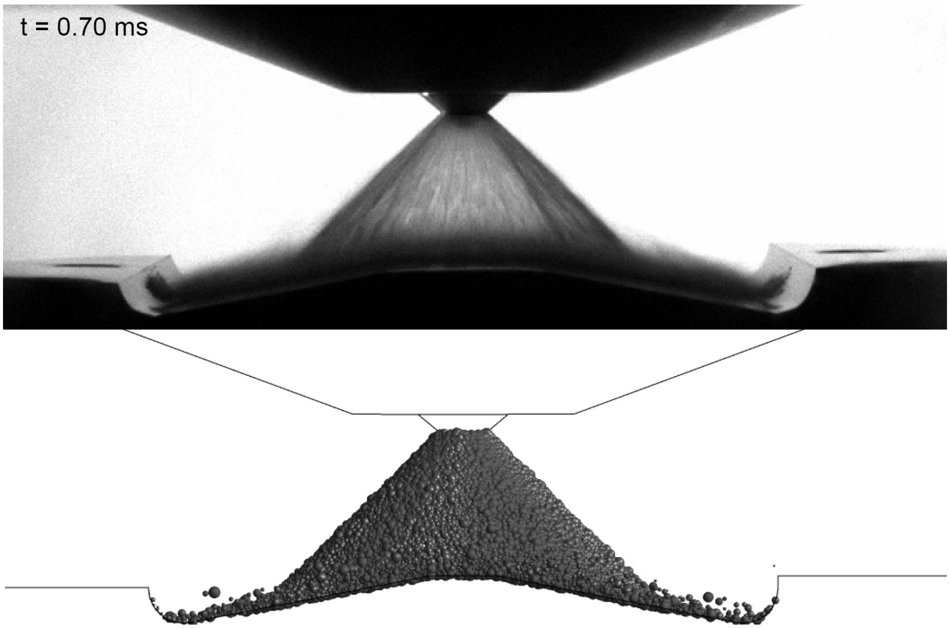

(a) $t = 0.70\,\mathrm{ms}$.

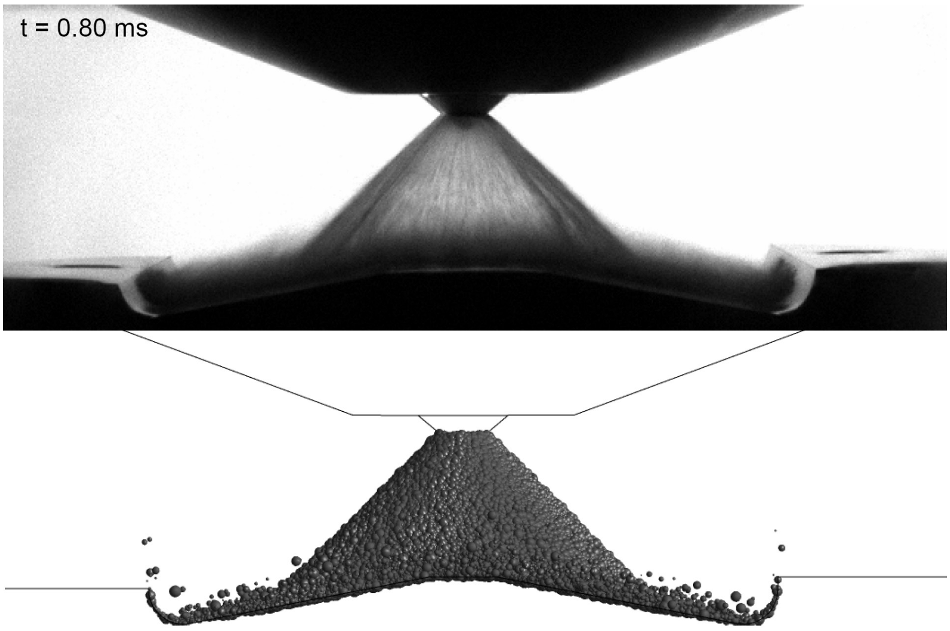

(b) $t = 0.80\,\mathrm{ms}$.

Figure 6.23: Spray/wall interaction on the piston dummy at $t = 0.70\,\mathrm{ms}$ and $t = 0.80\,\mathrm{ms}$.

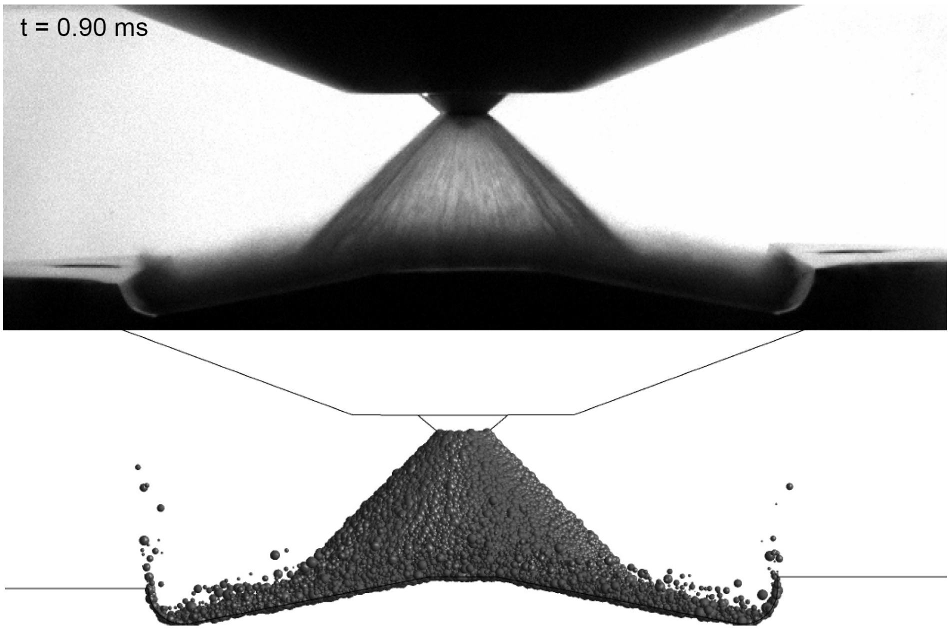

Figure 6.24: Spray/wall interaction on the piston dummy at $t = 0.90\,\mathrm{ms}$.

Chapter 7

Summary and outlook

Spray/wall interactions significantly influence air/fuel mixing and thus fuel consumption and emissions in modern spark-ignited direct injection engines. Yet, the complex phenomena are not well understood and their description is rather limited so far - especially for the large number of parameters and the associated wide ranges occuring in an engine. Modelling spray/wall interactions therefore presents a major drawback in numerical simulations which play an important role in engine development.
This thesis focuses on modelling wall interactions of dense and high-pressure hollow cone sprays - a spray type which is often applied in direct injection engines due to a good and reliable spray quality and a fast opening/closing mechanism of the piezo-driven injectors.

In a first step, Elsässer's single drop model, previously employed at BMW, has been implemented in the commercial CFD code ANSYS CFX which is used after a software change. This required in advance an extended data structure in CFX, where new Lagrangian child parcels can be generated on impact, and the implementation of a first wall film model. In the framework of this thesis numerous tests have been carried out in cooperation with CFX.

Considering the impact of a dense hollow cone spray onto a horizontal plate, it is demonstrated in a comparison to transmitted-light images that Elsässer's model does not describe the interaction correctly. Also Kuhnke's model, which includes an extrapolation from single to multiple drop impact based on the spray density, as well as Roisman's/Horvat's model, which refers to data of sparse full cone sprays, have been shown to be unsuitable. To the best of the author's knowledge no wall interaction model adapted to the impact of dense, high-pressure sprays existed.

This is associated to a general lack of quantitative, experimental data concerning wall interaction of the fuel sprays considered. To overcome this deficiency, data were gathered using Phase Doppler Anemometry and addressing the approximately normal impact of an isooctane spray, injected with 50 bar, onto a hemispherical copper target. In order to investigate the effect of the wall temperature on the parameters of the secondary spray, the target temperature has been varied in the range from 25° to 200°. Moreover, an oil film has been applied on the surface to simulate the thin oil layer on a cylinder liner lubricating the piston motion. Variations in the Reynolds number of the impinging drops have been achieved in the range from 2000 to 3000 by changing the distance between injector and target.

As the evaluation procedure of PDA data concerning spray/wall interactions had not been studied thoroughly so far, fundamental analysis has been carried out and presented in this thesis. It showed that it is important, even for a spray with small spatial expansion, to account for the finite size of the impact area when defining coordinate systems on a curved surface. Moreover, it is necessary for any surface curvature to consider the small distance between measurement points and surface by projecting drop data onto the surface along the respective drop velocity vectors. The definition of fluxes has been revised with the reference area determined on the target surface in contrast to free sprays.
The results of the studies apply to PDA data of spray/wall interaction in general and are not limited to dense and high-pressure hollow cone sprays. They may serve as general guidelines for future work.

The outcome of the evaluated measurements proved to be very different from single drop impacts. Analysing the impact mechanisms of very dense sprays with high Reynolds numbers, film fluctuations have been found decisive. They lead to ligaments which finally break up into secondary drops. A theoretical description of film fluctuations is not available yet, but it could be stated that inertial forces dominate all other forces like viscous forces and surface tension for the considered high Reynolds numbers on impact. As a consequence, parameter influences have shown to be negligible and different values of the Reynolds number or the wall temperature have yielded approximately the same results.
Furthermore, it could be observed that a thin oil film on the target is quickly driven away by the impacting spray which points out that spray/wall interaction on a cylinder liner may seriously affect the operability of an engine.

Finally, the gathered data have been used to develop empirical correlations which describe the typical average and integral parameters of the secondary spray based on those of the primary spray. An extrapolating model for oblique impacts has been suggested and validated in an approximate range from 30° to 90° of the impact angle, measured relative to the wall, and for injection pressures of 50 bar and 200 bar. Details concerning the implementation of this first empirical model adapted to dense, high-pressure hollow cone sprays in a Lagrangian approach have been given. An application from engine development has been presented.

In spite of all achievements, there remain open questions, and suggestions for future work have also been raised by this thesis:
It is necessary to gather data for Reynolds numbers around 2000 on impact and hence to fill the gap between spray data of Roisman, see [59], with Reynolds numbers up to around 1500 where viscous forces still play a significant role, and the present data, where inertial forces clearly dominate. Additional data for Reynolds numbers above 3000 are also desirable.
Moreover, measurements with varied injection pressures and hence spray densities are needed. Only with a broader experimental data base will it be possible to achieve a more profound understanding of the mechanisms on spray impact, i.e. of the film

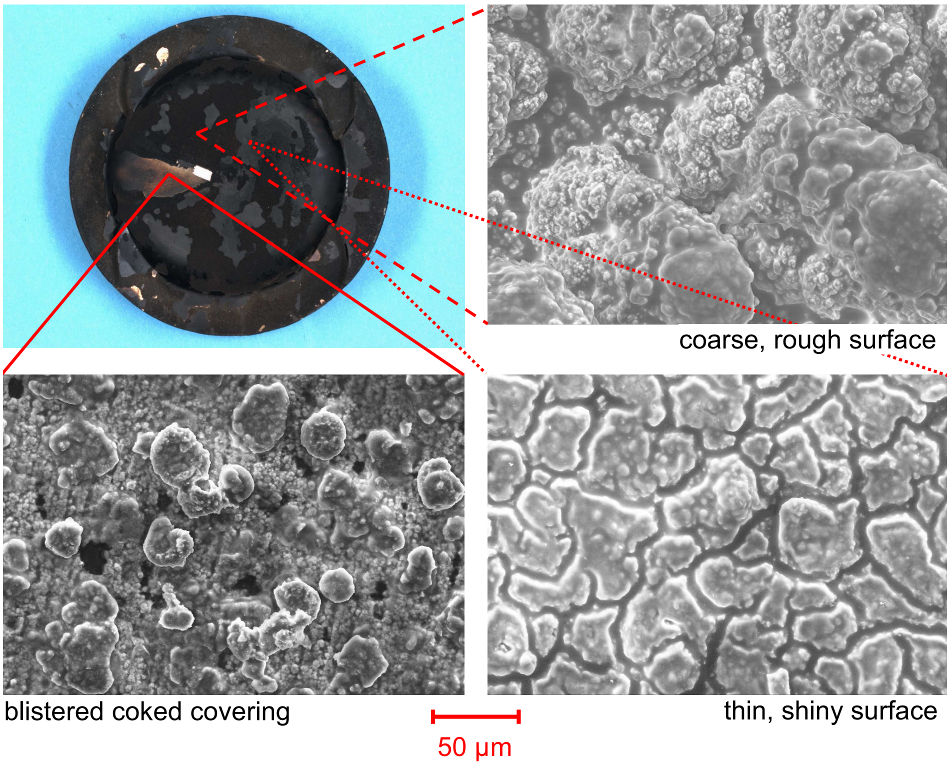

Figure 7.1: Example of a coked piston in a DI engine with SEM (Scanning Electron Microscope) images of different surface areas.

fluctuations, and to replace the empirical model by correlations which are theoretically deduced.

In order to further validate the developed empirical model with respect to oblique impact, data associated to different impact angles have to be gathered. To cover the conditions in a running engine, experiments with increased ambient temperature and pressure are furthermore required, and different surface roughnesses and coked coverings should also be considered. The latter may vary significantly over operating time and for different fuels and their additives. Different specifications can occur on one and the same piston, see Figure 7.1. In some cases the coked surface covering ressembles a porous medium being able to store fuel mass which leads to increased emissions.
For questions like these, it will be necessary to improve the measurement of mass and number fluxes of primary and secondary sprays. These are in general rather inaccurate for the point-wise measurement technique of Phase Doppler Anemometry, where it is not possible either to distinguish film fluid and primary fluid mixed in the secondary drops.

Apart from experimental challenges, also the CFD codes face necessary improvements concerning sprays and spray/wall interactions in industrial applications. For dense sprays a Lagrangian approach is generally questionable because it is only valid if liquid volume fractions are very small. Near injection regions or wall impact areas this condition is often not fulfilled. In this context spray initialisation at the nozzle by the definition of independent Lagrangian parcels is also very problematic, because the spray liquid enters in form of a liquid sheet which breaks up only subsequently after several millimeters of propagation.

Collision models as well as an exchange of information between parcels, e.g. to estimate the spray density on impact, will become more and more important. Appropriate models are often not provided by common commercial codes yet.
Modelling wall films is another difficult task where the momentum transfer between impacting spray and film liquid should be accounted for. A stable handling of large source terms, e.g. due to strong film evaporation on very hot surfaces, is also indispensable but often not yet accounted for.

The considered aspects clearly point out that sprays and spray/wall interactions will remain a very interesting object of research for several years, both in experiment and theory.

Appendix A

Reference case of chapter 2

A.1 Parameter influences

As mentioned in Chapter 2, numerical and modelling parameters set in a simulation may exert a strong influence on the results. This is studied shortly in this appendix, not least because it was furthermore shown in Section 2.2 that the initialisation of the primary spray is based on a scant experimental data base (cf. also [22], [35] where only free spray propagation is considered).

Variations and deviations from the default setup presented in Section 2.2 are marked. Elsässer's model with the film thickness set to zero, $h_{\text{film}} = 0$, is considered exemplarily for wall interaction unless otherwise specified.

Mesh resolution. The influence of the chosen cell size is noteworthy, see Figure A.1. The coarser the mesh, the slower the spray propagation: The expansion of the spray front is very small and in principle the mesh should resolve the associated scales properly - under the restriction that the Lagrangian approach is still valid. For a coarser mesh the spray front is resolved worse and the mean gaseous velocity in a cell in that region is smaller. Hence, the slip velocity is increased and the drag force is larger which leads to a larger deceleration of the spray.

The gradients in the flow are in general dampened for a coarser mesh and the changed vortex behaviour results in a different appearance of the secondary spray whose smaller and slower drops follow the vortex.

As clearly no independence of the mesh resolution prevails for the default mesh with a tetrahedron edge length of maximal 1 mm, it is necessary to compare different simulations always for the same mesh.

Eulerian timestep size DT. The Eulerian timestep is often oriented at the Courant-Friedrichs-Lewy number, CFL= $(v_f \cdot DT)/(\text{measure for the cell size})$, where v_f is the fluid speed. This number classifies the transport of information through the mesh[1]. The default value of $DT = 5.0 \cdot 10^{-6}\,\text{s}$ for the standard mesh with maximal 1 mm cell size corresponds to values of CFL≤ 1, i.e. the information is not transported further than one cell per timestep.

---

[1] The discretisation is done by a fully implicit scheme in CFX which is unconditionally stable. In explicit methods, a Courant number CFL≤ 1 often provides conditional stability.

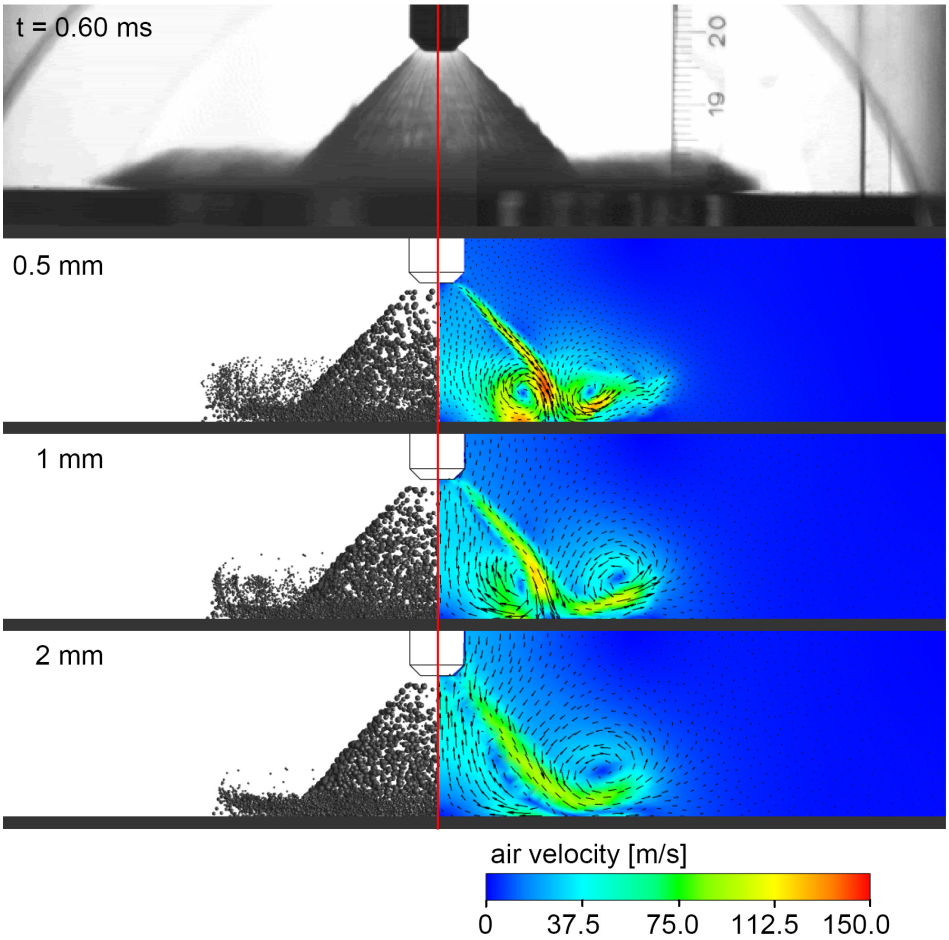

Figure A.1: Influence of the mesh resolution at $t = 0.60\,\mathrm{ms}$.

In Figure A.2 the effects of a timestep with half and double the value appear minor. As the solution converges already with few iterations for a timestep of $DT = 5.0 \cdot 10^{-6}\,\mathrm{s}$, smaller values only increase the computational time without much benefit. Larger values than $DT = 1.0 \cdot 10^{-5}\,\mathrm{s}$ worsen convergence considerably.

Total number of Lagrangian parcels. The total injected mass of $m_{\mathrm{inj}} = 26.6\,\mathrm{mg}$ is distributed per default on 40 000 parcels. The larger the number, the smaller the number rate per parcel. Particle source terms are directly proportional to the latter and with respect to convergence alone it is generally advisable to calculate not too small a number. Yet, the computational cost also increases considerably and in case of wall interaction with real droplet breakup the number may be multiplied on wall contact. Figure A.3 shows the simulation results for a varied total number of parcels. The air flow seems unchanged even for only 20 000 parcels. In case of 80 000 parcels injected, the number after wall contact is still feasible as only one child is created per impact (splash in Elsässer's model).

Discretisation of convective terms. Per default the high-resolution scheme is used in the calculations which is of second oder if gradients are not too large. Figure A.4 shows a comparison to the results using only an upwind first order scheme. Similar to a coarse mesh resolution, the gradients and fine structures of the flow are dampened. Free spray propagation is also slowed down.

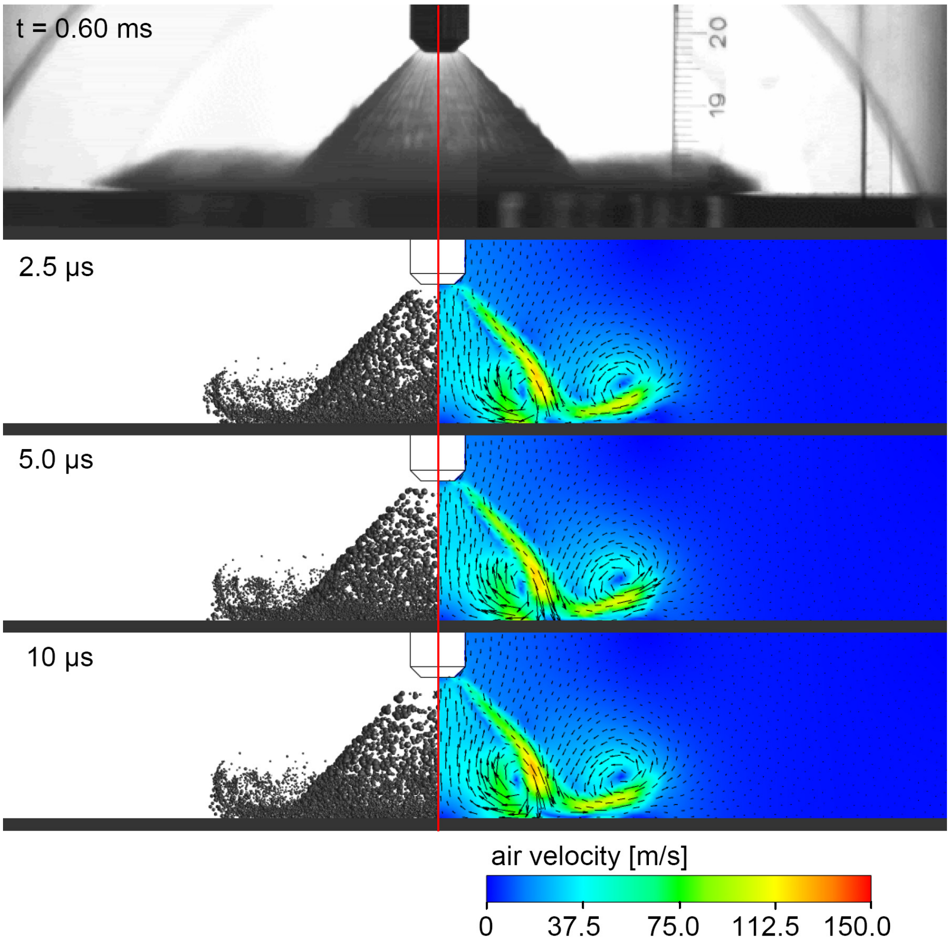

Figure A.2: Influence of the timestep size at $t = 0.60\,\mathrm{ms}$.

Turbulence modelling. Throughout this work, Reynolds-averaged Navier Stokes equations are considered with two-equation models for closure. Per default the Shear-Stress-Transport model is activated which differs from the standard k-ε model only near rigid surfaces. Figure A.5 presents this influence.

Turbulent dispersion. To account for the turbulence of the Eulerian phase in the calculation of the Lagrangian phase, the parcels are assumed to move in virtual eddies whose properties are defined with k, ε and random numbers. The differences of the results with this coupling between the phases considered or ignored are presented in Figure A.6. They appear negligible.

Number of the particle integration time steps per element. Increasing this number equals a decrease in the timestep δt of the Lagrangian phase. Per default a value of 10 is set. A changed value shows no noticable influence.

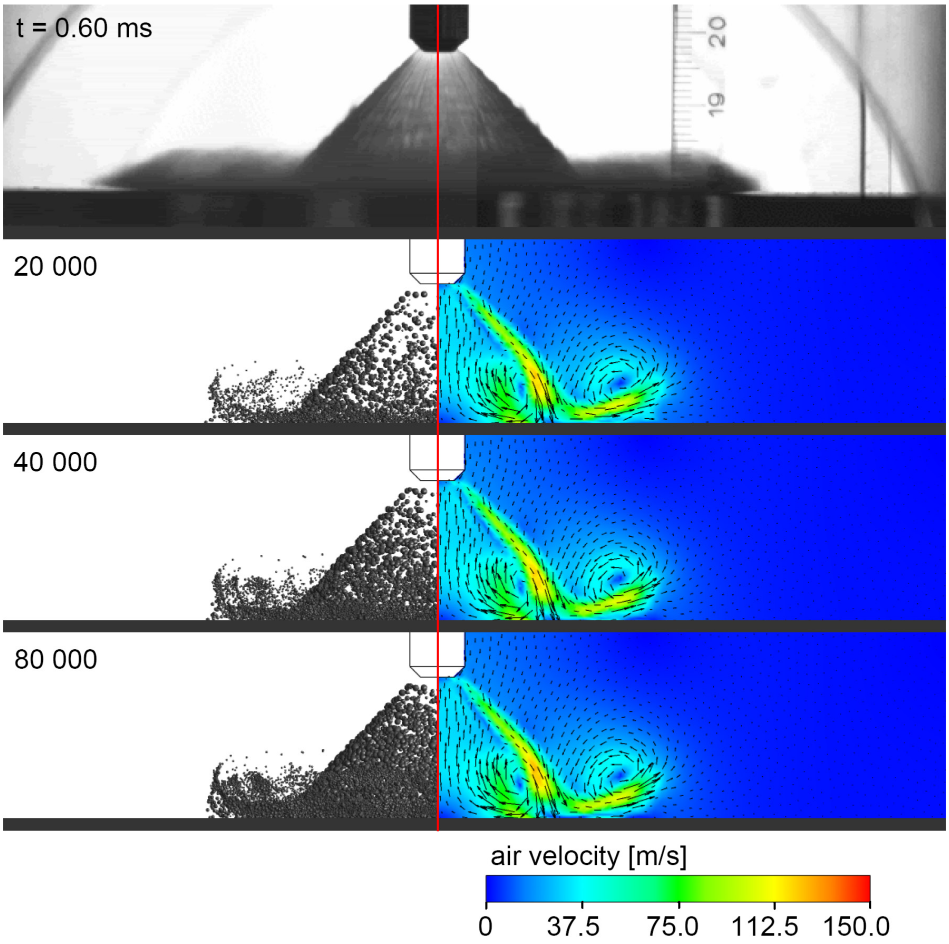

Figure A.3: Influence of the total parcel number at $t = 0.60\,\mathrm{ms}$.

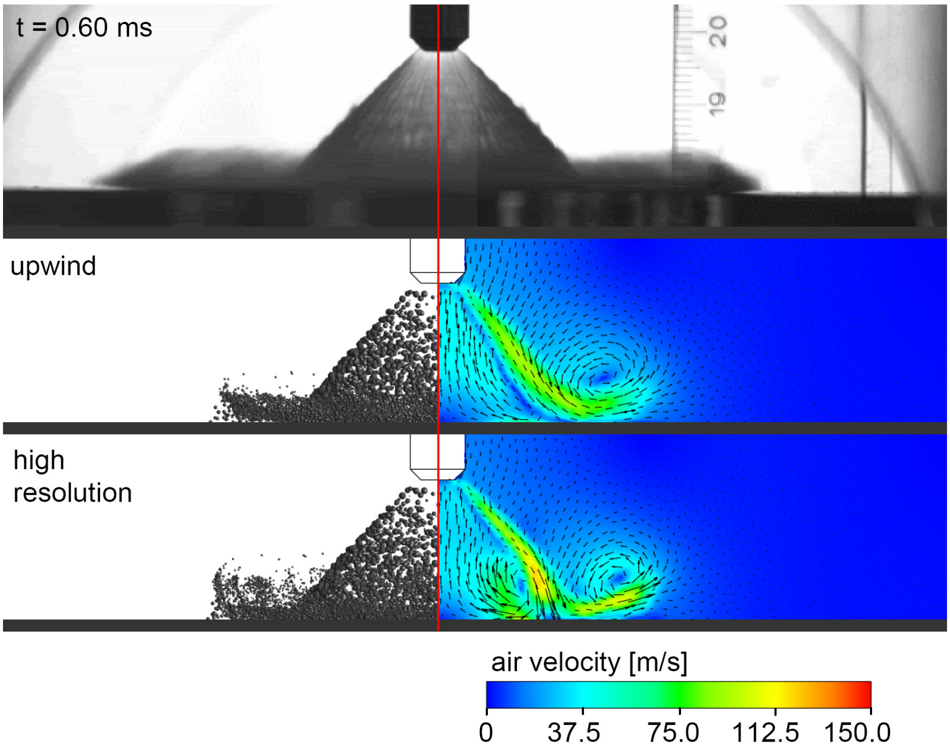

Figure A.4: Results with different discretisations of the convective terms at $t = 0.60\,\mathrm{ms}$.

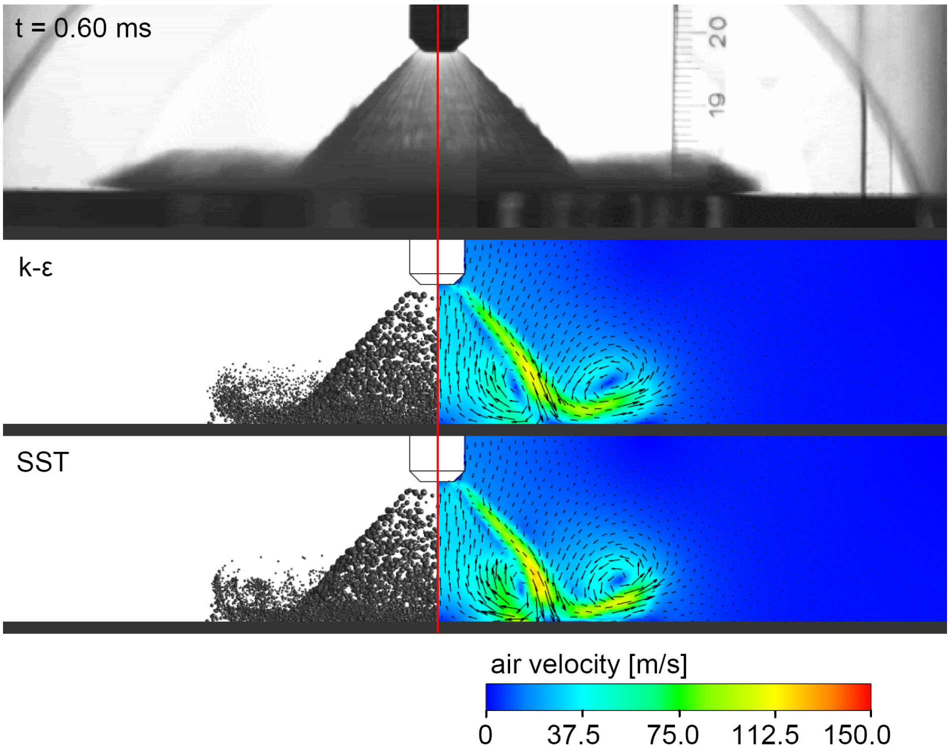

Figure A.5: Results with different turbulence models at $t = 0.60\,\mathrm{ms}$.

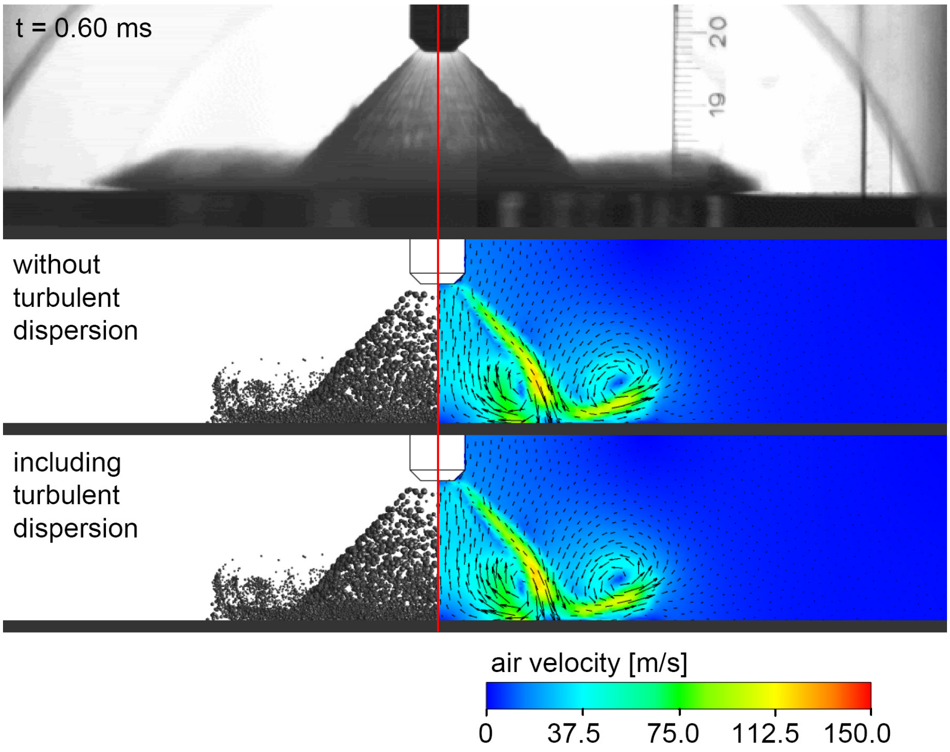

Figure A.6: Influence of turbulent dispersion at $t = 0.60\,\mathrm{ms}$.

Appendix B

Experimental work of chapters 3 and 4

B.1 Peripherals of the experimental setup

Chapter 3 presents the experimental setup in detail. However, supply and control systems are omitted for purposes of clarity. Figure B.1 catches up on an overview of such peripherals.

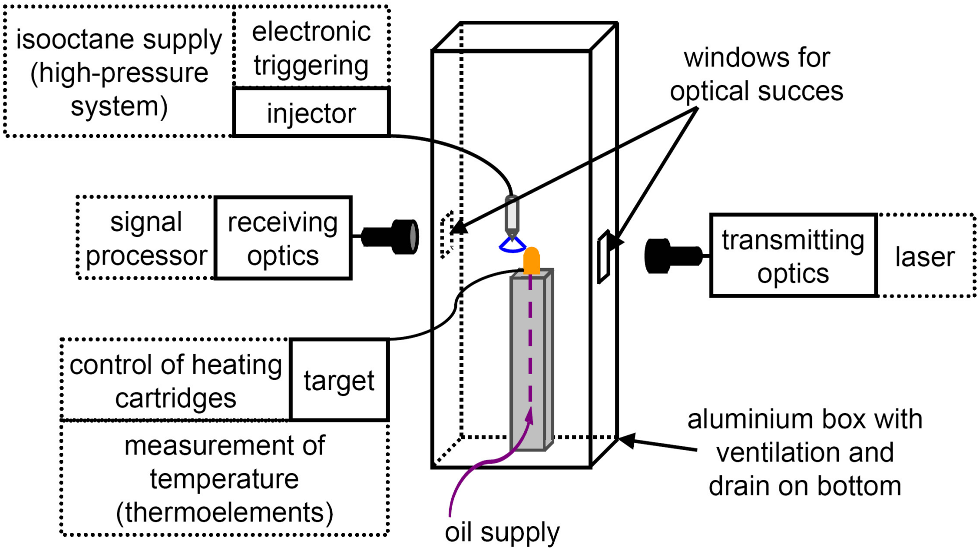

Figure B.1: Sketch of the experimental setup including supply and control systems.

The whole experiment is carried out in an aluminium box because isooctane is noxious and hazardous to the environment. The box measures about $180 \times 60 \times 50\,\mathrm{cm}^3$ and it is equipped with a drain on the bottom to collect remaining isooctane and film oil. Moreover, a small ventilation system prevents the possible formation of explosive gas mixtures of isooctane and air. It has been checked that this ventilation does not affect the properties of the spray drops noticeably. Two openings in the side faces of the box provide optical access for the transmitting and receiving optics.

In order to generate the spray, an electronic triggering as well as an isooctane supply are necessary. The latter comprises a rather complex high-pressure system including a control of the injection pressure. The surface temperature of the target is measured by thermocouples, see Section 3.3. In case of heated target the heating cartridges have to be controlled and in order to realise an oil film on the surface a feed line for the oil is provided.

B.2 Thermal expansion of the target

This appendix complements Section 3.3 and presents the procedure to determine the thermal expansion of the dry target. The image evalution is carried out using customised Matlab software and comprises the following steps:

- A long-distance microscope is adjusted with the plane containing the target axis in focus. The alignment is unchanged throughout the observations.
- A zero image (reference image) is taken at $T_{\text{wall},0} = 19.3°\text{C}$, see Figure B.2(a). It contains a scale where each point is known to have a diameter of 1.5 mm. The boundary of a scale point is tracked, fitted to a circle and the resulting diameter establishes a correspondence between pixels and millimeters for all further images, see Figure B.2(b).
- Images at various temperatures up to $T_{\text{wall}} = 200°\text{C}$ are then taken. A first impression of the importance of thermal expansion can be obtained by subtracting the reference image, see Figure B.2(c).
- To get a quantitative notion of the thermal expansion, every image is converted to black and white. The boundary of the target is fitted assuming the segment of a circle, see Figure B.2(d). The center and radius of the fit are read.

No significant thermal expansion could be seen in the radial direction, in contrast to the direction of the target axis. Assuming a simple linear thermal expansion with a constant coefficient, one obtains, see Figure B.2(e):

$$\frac{L - L_0}{L_0} = \alpha_T \cdot (T_{\text{wall}} - T_{\text{wall},0}) \qquad \text{with } \alpha_T \approx 2.12 \cdot 10^{-5}/°\text{C}.$$

L_0 signifies the length of the target at the reference temperature $T_{\text{wall},0} = 19.3°\text{C}$, L its value at T_{wall}. For comparison pure copper at 20°C shows $\alpha_T \approx 1.65 \cdot 10^{-5}/°\text{C}$ which is notably different. Yet, the approximation of a linear thermal expansion can hardly be correct as the target is not a full solid of copper but supplied with heating cartridges and the oil pipe. Nevertheless, it becomes obvious that the thermal expansion must be taken into account. This is done by readjusting the coordinates to the target apex for every wall temperature.

B.3 Oil film thickness on the target

At the apex of the target an oil film can be applied on the target with a small, constant volume flux $\dot{Q}$ through a thin supply pipe. The flow is driven solely by gravity. This appendix to Section 3.3 derives Equation 3.5 for the film thickness h_{film} on the target under ideal and undisturbed conditions. To complement the calculations, image evaluation is done analogously to Appendix B.2.

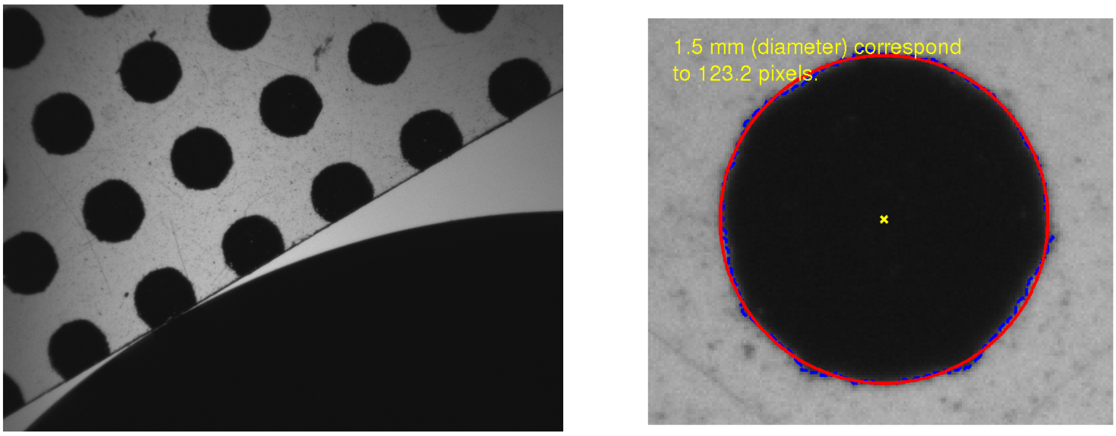

(a) Reference image at $T_{\text{wall},0} = 19.3°\text{C}$ including a scale.

(b) Evaluated scale point.

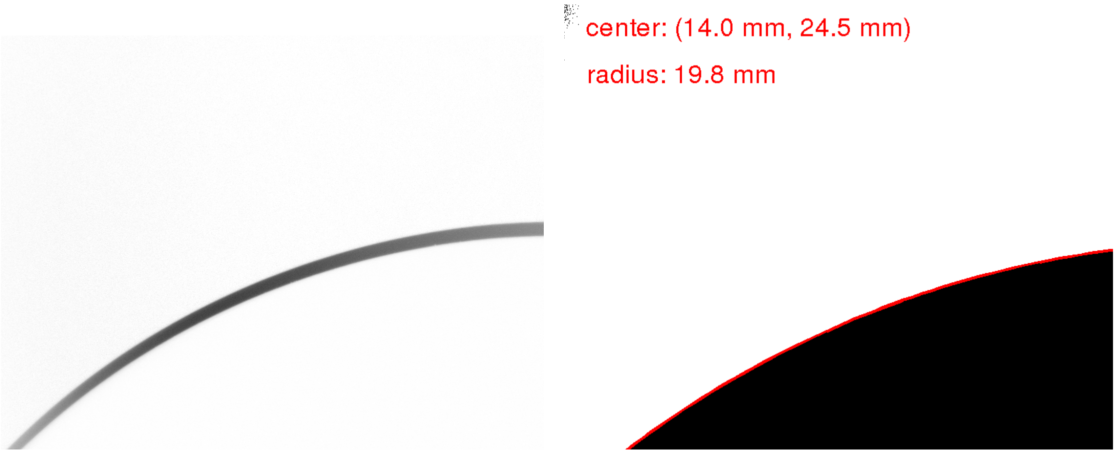

(c) Image at $T_{\text{wall}} = 150.6°\text{C}$ with subtracted reference image.

(d) Image at $T_{\text{wall}} = 150.6°\text{C}$ with tracked and fitted boundary.

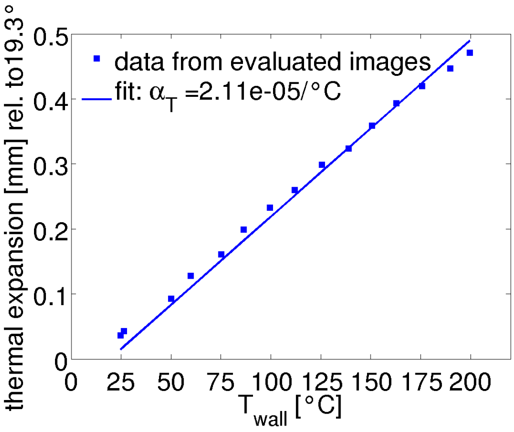

(e) Linear thermal expansion of the target assumed.

Figure B.2: Image evaluation with respect to the thermal expansion of the target.

B.3.1 Calculation of h_{film}

The local coordinates of the two-dimensional problem are chosen as shown in Figure B.3(a). The flow is assumed to be stationary and laminar with gravity as only external force. g denotes the absolute value of gravity, see Figure B.3(b). Using momentum conservation, see Equation 1.3, one obtains:

$$0 = \mu \cdot \frac{\partial^2 v(y)}{\partial y^2} + \rho \cdot g \cdot \sin\Theta \, . \tag{B.1}$$

Integration leads to a parabolic velocity profile, see Figure B.3(c):

$$v(y) = -\frac{\rho \cdot g}{2 \cdot \mu} \cdot \sin\Theta \cdot y^2 + a \cdot y + b \, . \tag{B.2}$$

The boundary conditions on the wall, $v(0) = 0$ (no-slip condition), and on the free surface, $\frac{dv}{dy}|_{y=h_{\text{film}}} = 0$ (continuity of the normal components of the shear stress tensor), give:

$$v(y) = -\frac{1}{2} \cdot \frac{\rho \cdot g}{\mu} \cdot \sin\Theta \cdot (y - 2 \cdot h_{\text{film}}) \cdot y \, . \tag{B.3}$$

Introducing the volume flux

$$\dot{Q} = 2 \cdot \pi \cdot R_0 \cdot \sin\Theta \cdot \int_0^{h_{\text{film}}} v(y)\, dy = \frac{2}{3} \cdot \pi \cdot R_0 \cdot \frac{\rho \cdot g}{\mu} \cdot (\sin\Theta)^2 \cdot h_{\text{film}}^3 \, , \tag{B.4}$$

the film thickness results:

$$h_{\text{film}} = \left(\frac{3}{2 \cdot \pi \cdot R_0 \cdot g} \cdot \frac{\mu}{\rho} \cdot \frac{\dot{Q}}{(\sin\Theta)^2} \right)^{1/3} \, . \tag{B.5}$$

Equation B.5 is only valid for $\Theta > 0$. The considerations are not applicable in the direct proximity of the target apex.

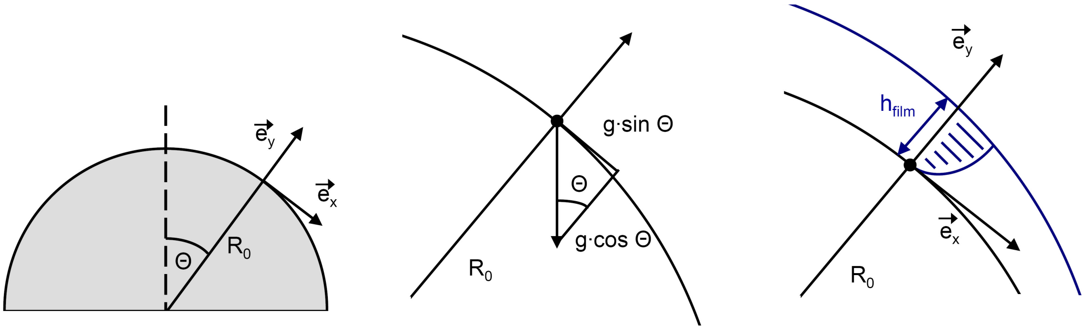

(a) Local coordinate system. (b) Gravity vector components. (c) Velocity profile.

Figure B.3: Definitions for the calculation of h_{film}.

B.3.2 Evaluation of the film thickness

There are two shortcomings in the application of Equation B.5: The film surface is probably not ideally smooth but wavy and irregular. Moreover, the volume flux of the oil fluid is not known accurately. In preliminary work it has been determined by collecting the oil flow several times for different time intervals and calculating the mean. For the considered settings of the film pump, the values $\dot{Q}_{1,\mathrm{meas}} \approx 1.85\,\mathrm{ml/min}$ and $\dot{Q}_{2,\mathrm{meas}} \approx 0.89\,\mathrm{ml/min}$ are found. Yet, these values are deemed not very reliable and too large because the available possibilities to measure the volume flux have been very limited and additional oil mass has probably been collected unwantedly at the start and the end of the measurement.

To obtain more reliable values, an image analysis is performed analogous to the evaluation of the thermal expansion. The same steps are carried out, cf. Figures B.4(a)-B.4(b), only the boundary is not fitted to a circle but to the theoretical progression $h_{\mathrm{film}} = fd_{\mathrm{image}} \cdot (\sin\Theta)^{-2/3}$ starting at $\Theta = 10°$.

Three images are taken and evaluated, i.e. three single values of fd_{image} are determined for several wall temperatures and pump settings. Figures B.5(a) and B.5(b) show that the values differ which confirms the waviness of the film surface.

Mean values $fd_{\mathrm{image},10}$ of the three single values at every setting are then determined and compared to the coefficients fd_{calc} which are calculated according to Equation B.5 with the measured values $\dot{Q}_{1,\mathrm{meas}}$ and $\dot{Q}_{2,\mathrm{meas}}$. It shows that their dependence on Θ agrees rather well. Yet, fd_{calc} seems to be systematically larger than $fd_{\mathrm{image},10}$ and, consequently, the measured values $\dot{Q}_{1,\mathrm{meas}}$ and $\dot{Q}_{2,\mathrm{meas}}$ are assumed to include a systematic error. Hence, a fit of $\frac{fd_{\mathrm{calc}}}{\dot{Q}_{\mathrm{meas}}^{1/3}} \cdot \dot{Q}_{\mathrm{fit}}^{1/3}$ to the values $fd_{\mathrm{image},10}$ is done. It results in values of $\dot{Q}_{1,\mathrm{fit}} \approx 0.92\,\mathrm{ml/min}$ and $\dot{Q}_{2,\mathrm{fit}} \approx 0.44\,\mathrm{ml/min}$, see Figures B.5(a), B.5(b), which are significantly smaller than the measured one, as expected.

Figures B.5(c)-B.5(d) show the associated film thicknesses for the expected main impact area around $\Theta = 45°$.

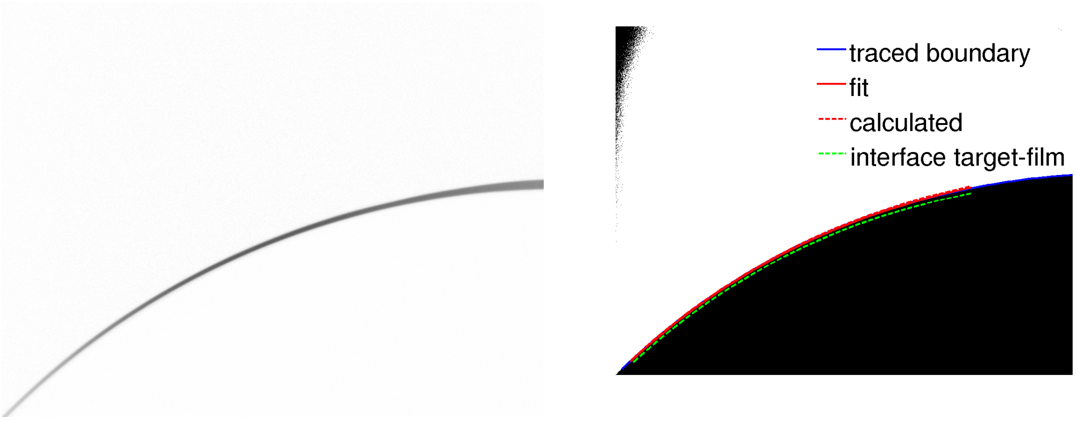

(a) Image at $T_{\mathrm{wall}} = 150.6°\mathrm{C}$ with $\dot{Q}_{1,\mathrm{meas}} \approx 1.85\,\mathrm{ml/min}$. The reference image of the dry target is subracted.

(b) Evaluated image at $T_{\mathrm{wall}} = 150.6°\mathrm{C}$ and $\dot{Q}_{1,\mathrm{meas}} \approx 1.85\,\mathrm{ml/min}$. The green dashed line marks the dry target surface.

Figure B.4: Determination of the oil film thickness using image evaluation.

B.4 Influence of an oil film on the velocity components

This appendix to Section 4.2 studies the question whether it is sufficient to consider the target surface always as dry in the setup of the coordinate system defining the

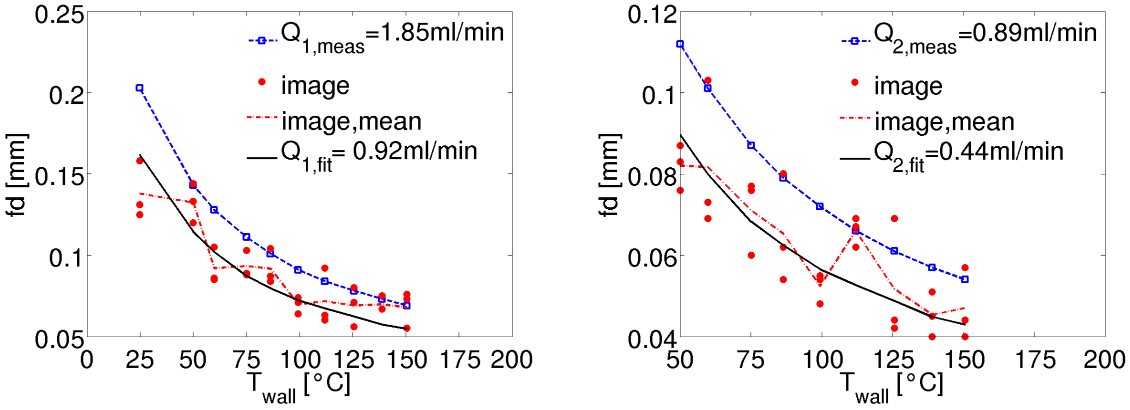

(a) fd for $\dot{Q}_{1,\mathrm{meas}} \approx 1.85\,\mathrm{ml/min}$. (b) fd for $\dot{Q}_{2,\mathrm{meas}} \approx 0.89\,\mathrm{ml/min}$.

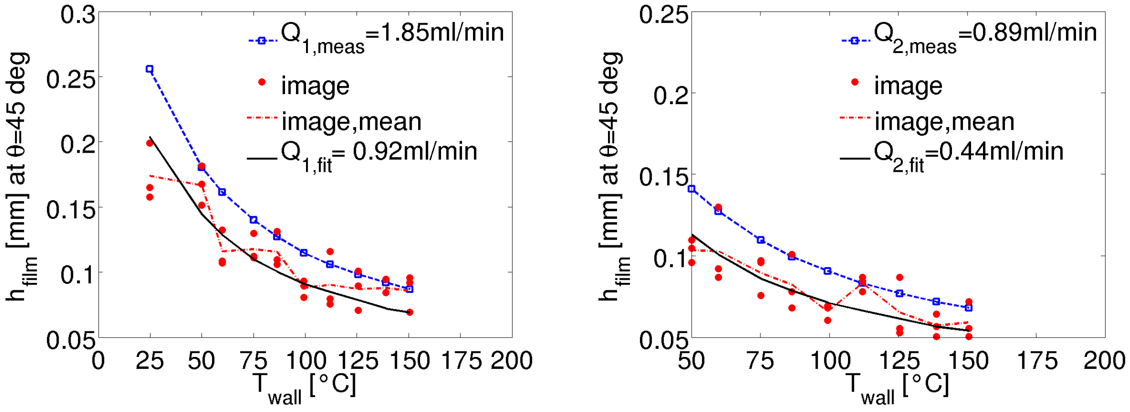

(c) h_{film} for $\dot{Q}_{1,\mathrm{meas}} \approx 1.85\,\mathrm{ml/min}$ at $\Theta = 45\mathrm{deg}$. (d) h_{film} for $\dot{Q}_{2,\mathrm{meas}} \approx 0.89\,\mathrm{ml/min}$ at $\Theta = 45\mathrm{deg}$.

Figure B.5: Values of fd and h_{film}.

wall-normal and wall-tangential velocity components $U2$ and $V2$. Or if the film surface has to be regarded in case of an oil film applied on the target.

Consider the case of an oil covered target. The film thickness is calculated as $h_{\mathrm{film}} = fd \cdot (\sin\Theta)^{-2/3}$, see Equation 3.5 and Appendix B.3. Two coordinate systems are defined normally and tangentially to the surface: coordinate system 1 referring to the dry target, coordinate system 2 to the oil covered target. They are slightly tilted by an angle $\omega(\Theta)$, see Figure B.6(a):

- gradient at arbitrary Θ of the dry surface:

$$\begin{aligned} x &= -R_0 \cdot \sin\Theta \\ y &= +R_0 \cdot \cos\Theta \\ \left(\frac{dy}{dx}\right)_1 &= \tan\Theta\,. \end{aligned}$$

- Gradient at the same Θ of the film-covered surface:

$$\begin{aligned} x &= -(R_0 + h_{\text{film}}(\Theta)) \cdot \sin\Theta \\ y &= +(R_0 + h_{\text{film}}(\Theta)) \cdot \cos\Theta \\ \left(\frac{dy}{dx}\right)_2 &= \tan\Theta \cdot \left(1 + \frac{2 \cdot h_{\text{film}}(\Theta)}{(3 \cdot R_0 + h_{\text{film}}(\Theta)) \cdot \sin^2\Theta}\right) . \end{aligned}$$

$\Rightarrow$ Tilt: $\omega(\Theta) = \arctan\left(\frac{dy}{dx}\right)_2 - \arctan\left(\frac{dy}{dx}\right)_1$.

In Figure B.6(b), $\omega(\Theta)$ is shown for the case of thickest occuring film ($fd_{1,\text{fit}} \approx 0.162\,\text{mm}$) with $T_{\text{wall}} = 25^\circ\,\text{C}$, $\dot{Q}_{1,\text{fit}} \approx 0.92\,\text{ml/min}$. The influence of the position Θ is not very large in the valid range, i.e. for not too small Θ, $\Theta > 5^\circ$. For smaller values the equation for $\omega(\Theta)$ does not hold because the equation of the film thickness is not valid.
Moreover, only the first primary drops presumably find an undisturbed film surface. For drops impacting later, no information on the state of the oil film is available. And the isooctane wall film which only forms under spray impact is not known either and has not been considered so far in this section.
Consequently, the coordinate systems to define $U2$ and $V2$ will always be set up for a dry target - no matter whether an oil film exists or not.

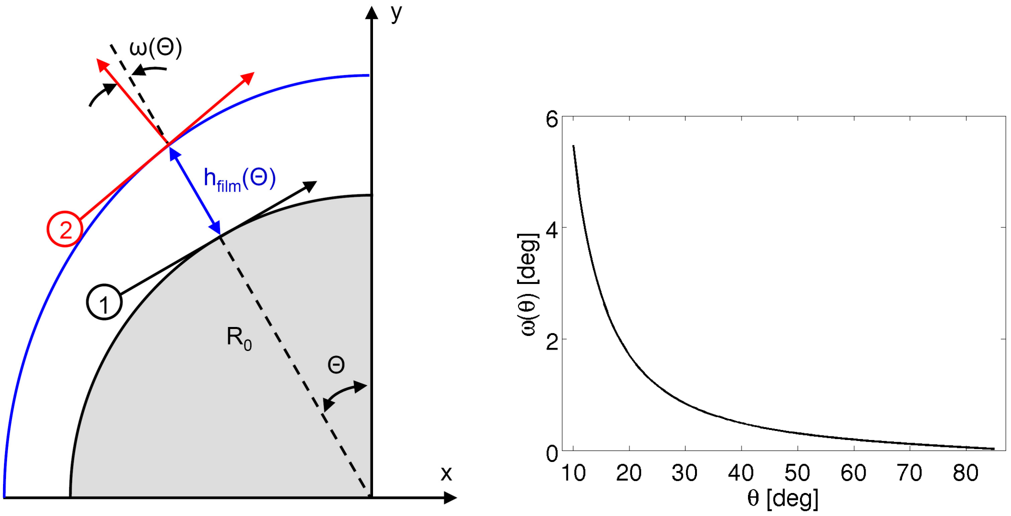

(a) Defintion of $\omega(\Theta)$.

(b) Calculated $\omega(\Theta)$ for "worst" case with $fd_{1,\text{fit}} = 0.162\,\text{mm}$.

Figure B.6: Tilt $\omega(\Theta)$ between coordinate systems set up on a film covered and a dry surface respectively.

B.5 Basic data testing

As stated in Section 4.3.1, some basic tests on the data have to be performed to estimate their reliability. The exemplary measurement, see Table 4.1, is used for illustration in this appendix where the evaluation procedure described in Section 4.2 is applied.

B.5.1 Data reproducability: test points

In order to check data reproducibility, data collection is repeated at some arbitrary measurement points with all settings adjusted anew. Dry and oil-wetted target has been considered. The results for the measurement point ($d_i = 3\,\mathrm{mm}$, $\Theta_i = 35°$) are exemplarily shown in Figure B.7. The reproducability seems sufficiently satisfied in the Θ-region where not too few samples are assigned to. The outside Θ-regions and possible outliers are less significant as hardly any samples are collected there.

Note that the curves of Figure B.7 need not resemble the figures in Section 4.2.3, because the mean values per Θ-class are calculated here with data of only a single measurement point and not with data collected from all measurement points with the same d_i.

B.5.2 Influence of the target on primary drops

Measurements without a target have been performed to demonstrate the influence of the target on primary drops. The evaluation is carried out in the same way but for a virtual target.

Figure B.8 shows the comparison for the exemplary measurement, where data from all measurement points at $d_i = 2\,\mathrm{mm}$ are included. The wrongly assigned secondary drops in the measurements without a target are most probably due to the recirculating flow. They are very few and no mean values have been calculated for them. The mean values for primary drops agree quite well, which signifies that impinging drops are only weakly disturbed by the target.

Note that the measurement grid has been much finer in cases without a target (5° between neighbouring points). Therefore, validated sample numbers are higher. The fact that the results for primary drops yet agree quite well proves also that the actual measurement grids, see Section 3.1.2, are sufficiently fine.

B.5.3 Sensitivity analysis on the width of the Θ-classes

In the evaluation procedure, see Section 4.2, drops are sorted into Θ-classes on the target. Using the new definition of the Θ-classes, see Section 4.2.5, which is adapted to the main impact region, any user-defined value of $\delta\Theta$ is in principle possible. Yet, it is important to perform a sensitivity analysis on the choice. To do so, the mean values are calculated and plotted in Figure B.9 for $\delta\Theta = 5°$ and $\delta\Theta = 15°$. In Figure 4.19 the results for $\delta\Theta = 10°$ are presented.

The validated sample numbers and the mean quantities fluctuate considerably for $\delta\Theta = 5°$ because only few drops are sorted into certain classes. For $\delta\Theta = 15°$, the distributions seem roughly resolved but resemble quite well those for $\delta\Theta = 10°$.

No “correct” value of $\delta\Theta$ exists and finally the choice is a matter of statistics. However, values of $\delta\Theta < 10°$ must be questioned because information is demanded with a better resolution on the surface than the original measurement grid provided.

Throughout the work, the value of $\delta\Theta = 10°$ is used.

B.5.4 Robustness towards measurement errors

A necessary part of every data evaluation is to test the robustness towards measurement errors. The origins of such errors depend on the specific experiment. In the considered

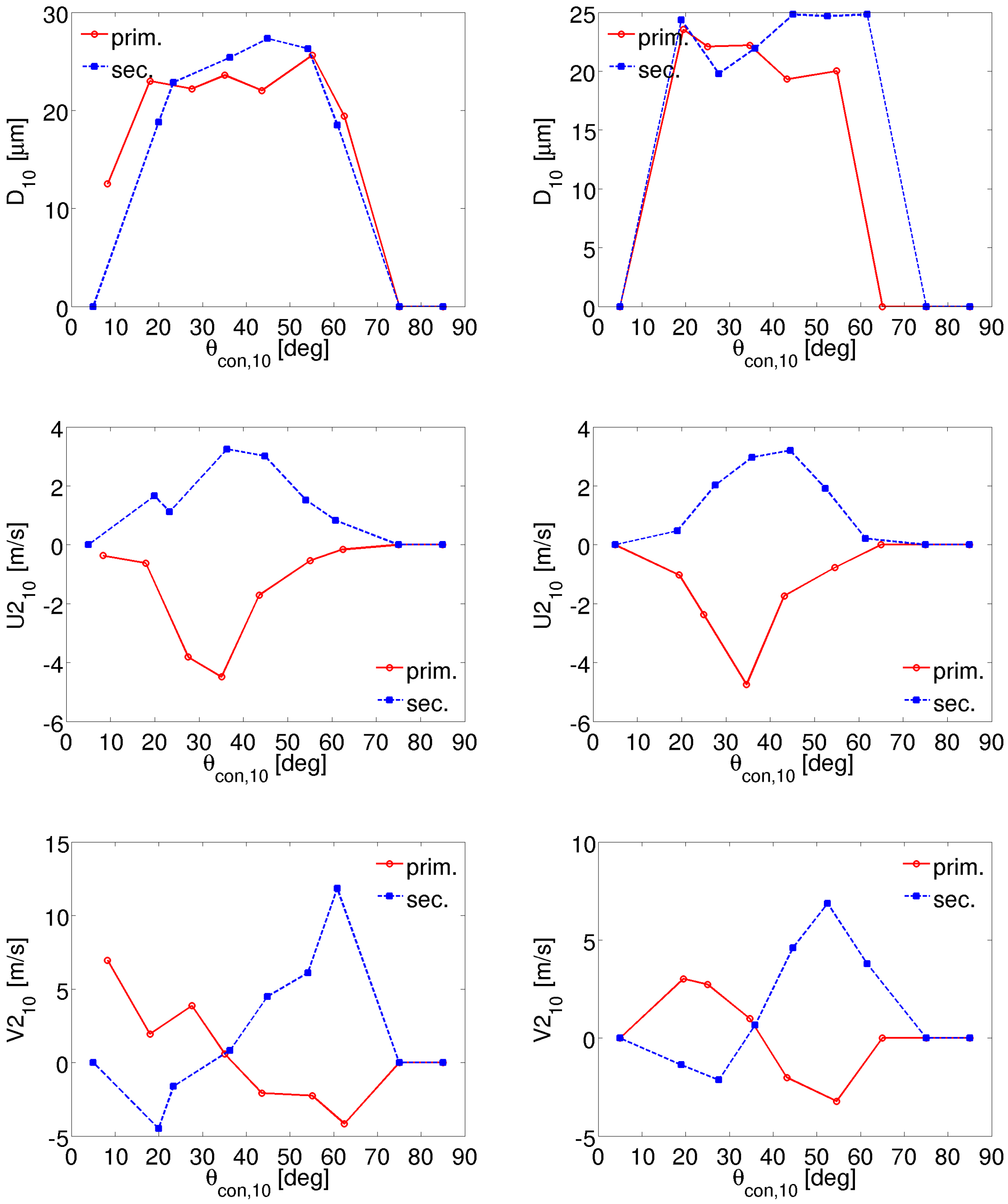

Figure B.7: D_{10}, $U2_{10}$ and $V2_{10}$ versus Θ at ($d_i = 3\,\text{mm}$, $\Theta_i = 35°$); test point (left), original measurement (right).

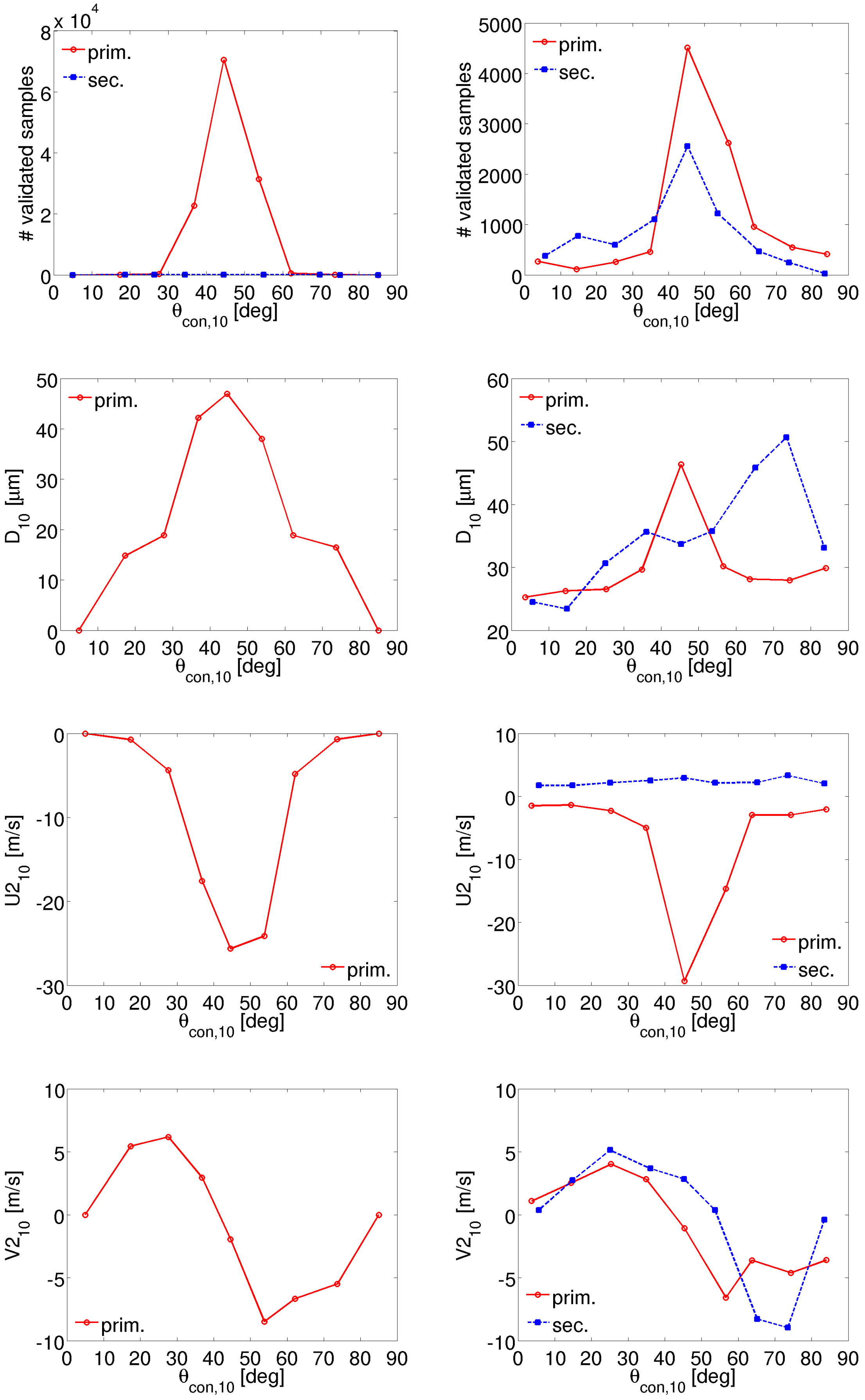

Figure B.8: Validated sample numbers, D_{10}, $U2_{10}$ and $V2_{10}$ versus Θ; without target (left), including target (right).

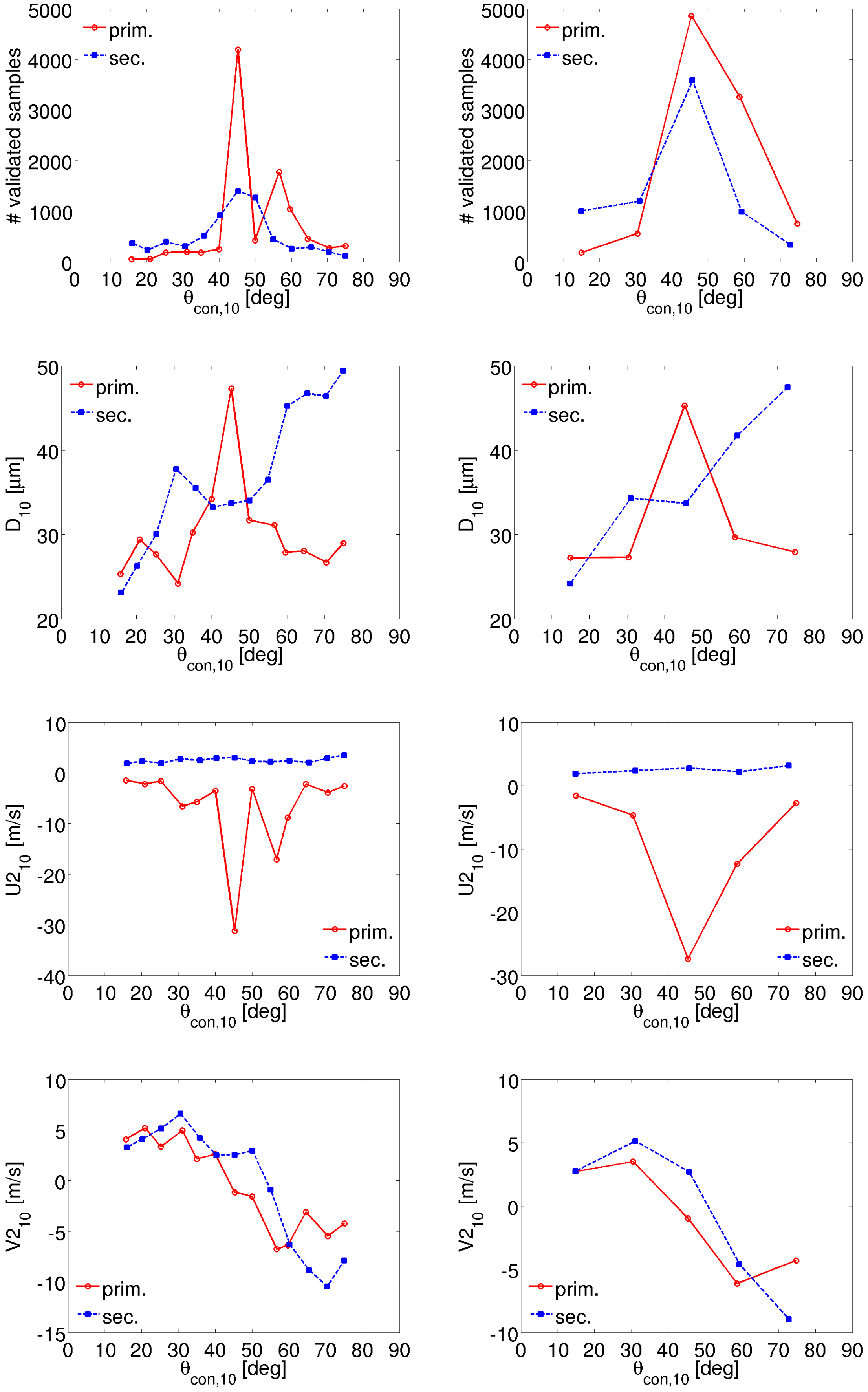

Figure B.9: Validated sample number, D_{10}, $U2_{10}$ and $V2_{10}$ versus Θ; $\delta\Theta = 5°$ (left), $\delta\Theta = 15°$ (right).

case, they are mainly found in the adjustments of injector, target and the measurement points.

To estimate their influence, the value of the target radius, $R_0 = 20\,\mathrm{mm}$, which enters the evaluation and which is important, for instance, in determining the wall contact point of each drop, is varied to $R_0 = 19\,\mathrm{mm}$ and $R_0 = 21\,\mathrm{mm}$. This is equivalent to moving the measurement positions by ±1 mm in their distance d_i to the surface. Figure B.10 together with Figure 4.19 show that the consequences are minor and that sufficient robustness of the results can be stated.

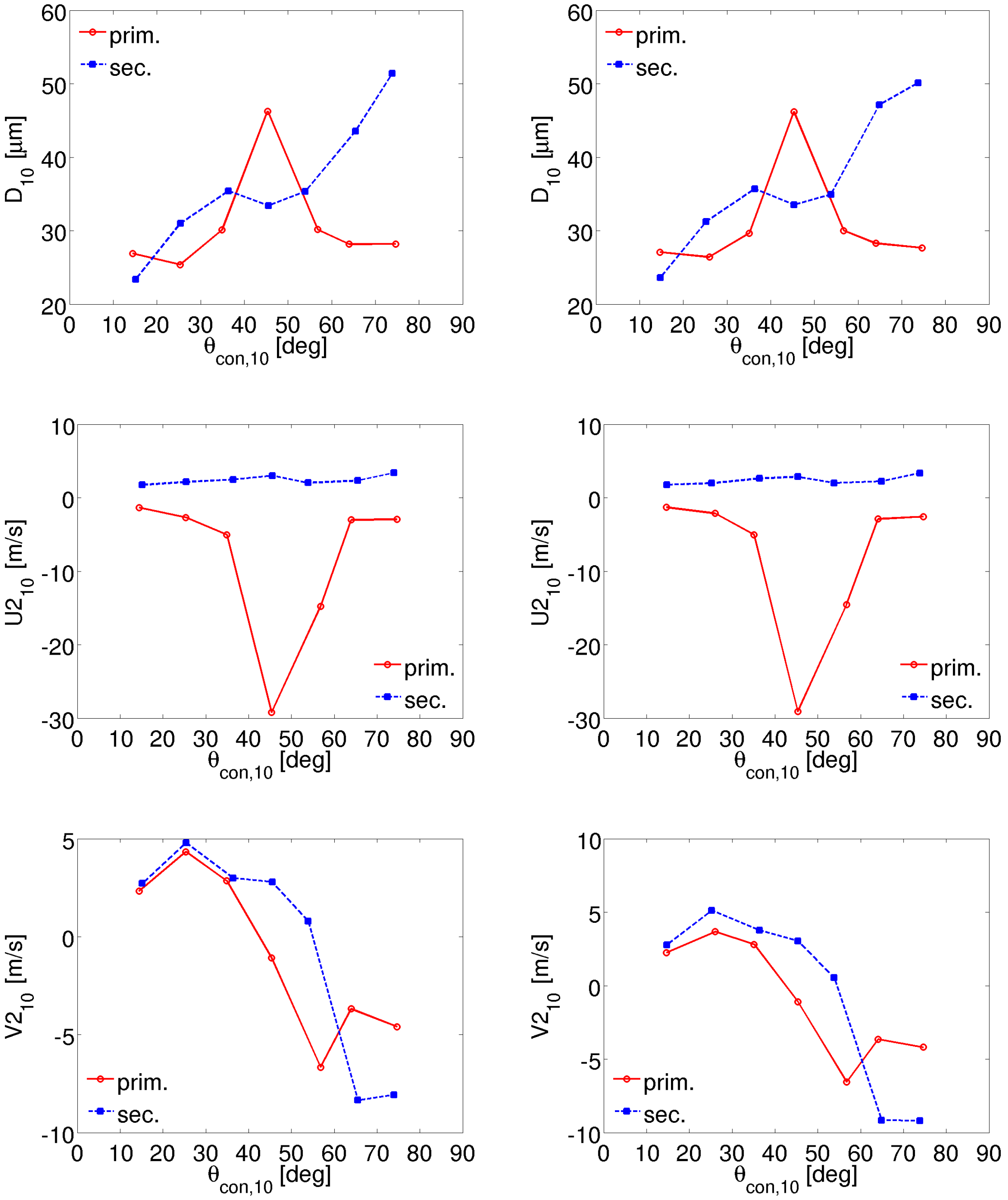

Figure B.10: D_{10}, $U2_{10}$ and $V2_{10}$ versus Θ; $R_0 = 19\,\mathrm{mm}$ (left), $R_0 = 21\,\mathrm{mm}$ (right).

B.5.5 Influence of the near-wall flow

In Section 4.2.3, it showed that the finite distance d_i between measurement points MP_i and surface must not be neglected in the evaluation. Every drop is therefore projected from its measurement position onto the surface along its velocity vector. If near-wall flow played an important role, this determination of the wall contact point could be rather erroneous because the velocity vectors could be changed significantly.
To study if this is the case, Figure B.11 shows the mean values per Θ-class for varied values of d_i. Some differences can be seen, e.g. for the diameters of secondary drops assigned to the inside of the spray cone where $\Theta > \Theta_0$. For primary drops a strange peak occurs for $d_i = 5\,\mathrm{mm}$ near $\Theta = 65°$ in the wall-normal and consequently also in the absolute velocity.
However, the overall agreement is quite good and the absolute velocities do not change much either: If the value of d_i was decisive, primary drops should have a notably larger absolute velocity for increasing d_i, whereas secondary drops should have a reduced one due to the drag force.
As the errors due to near-wall flow are certainly larger for larger d_i, data with minimal d_i of the respective measurement grid are used for final evaluation of the experiment.

B.6 Measurement and detection volume

In Section 4.4, the diameter $d_{t,i}$ of the detection volume in PDA measurements and its projection $d_{w,i}$ on the target are used to calculate data correction and weighting factors. Their definition and determination are addressed in this appendix.

B.6.1 Measurement and detection volume

Figure B.12(a) shows an exemplary measurement point of the PDA setup with both measured velocity components. The name measurement *point* is quite misleading. To be precise, three different kinds of *volumes* must be distinguished for every velocity component separately, see [2]: the illuminated volume, the measurement volume and the detection volume.

The illuminated volume is defined by the intersection of the two laser beams forming an interference pattern. The boundaries are usually set where the intensity has decreased to e^{-2} of its central maximum. The resulting ellipsoid has the half axes:

$$a_0 = \frac{r_w}{\cos(\Theta_{\mathrm{op}}/2)} \quad , \quad b_0 = r_w \quad , \quad c_0 = \frac{r_w}{\sin(\Theta_{\mathrm{op}}/2)} \, , \tag{B.6}$$

where r_w is half the beam diameter at beam waist and Θ_{op} signifies the angle enclosed by the laser beams.
Figure B.12(a) shows the intersection of the illuminated volumes of both measured directions, $U1$ (green) and $V1$ (blue), with the measurement plane. Figure B.12(b) provides a perpendicular view from above onto the target along the target axis. As the value $\Theta_{\mathrm{op}} = 5.64°$ is very small in the measurements, the approximation $a_0 \approx b_0$ can be done and the illuminated volumes can be considered as prolate spheroids. If well adjusted, the positions of both spheroids coincide. Due to the different wavelengths,

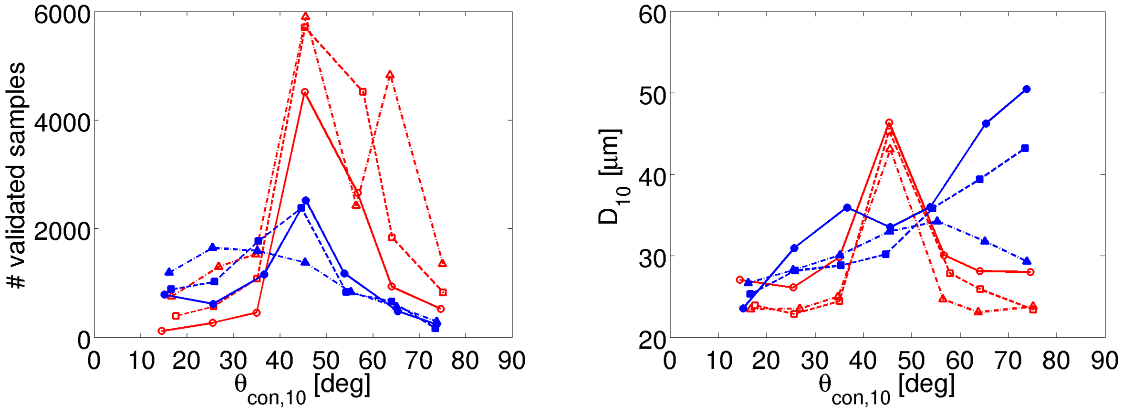

(a) Number of validated samples versus $\Theta_{\mathrm{con},10}$.

(b) $D_{10}(\Theta_{\mathrm{con},10})$.

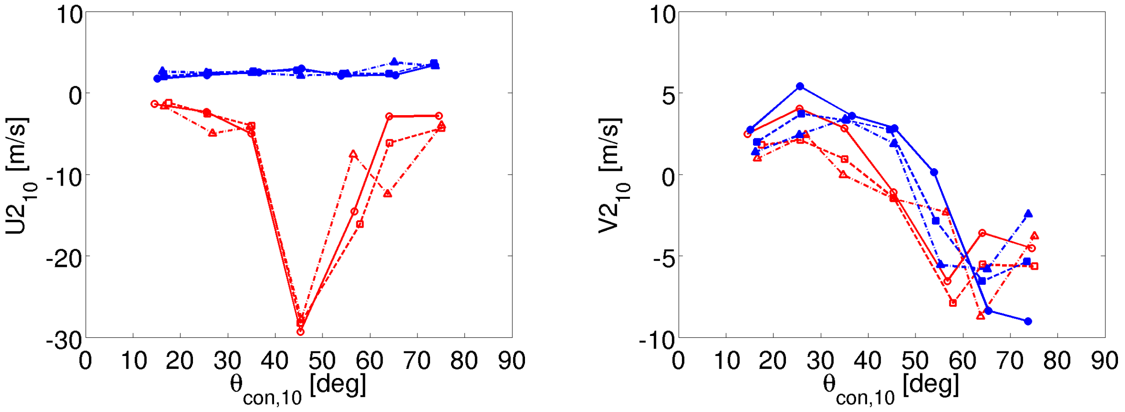

(c) $U2_{10}(\Theta_{\mathrm{con},10})$.

(d) $V2_{10}(\Theta_{\mathrm{con},10})$.

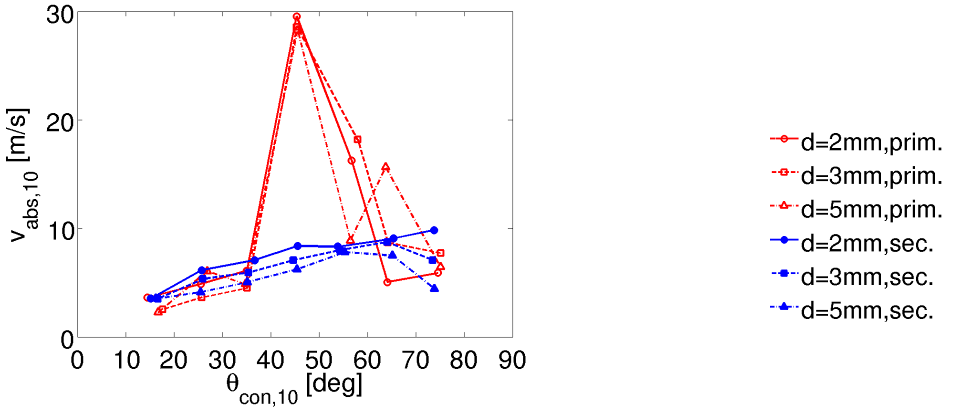

(e) $v_{\mathrm{abs},10}(\Theta_{\mathrm{con},10})$.

(f) Legend.

Figure B.11: Comparison of different distances d_i between measurement points and target.

the green spheroid is slightly larger than the blue one: $a_{0,\text{green}} \approx b_{0,\text{green}} \approx 0.291\,\text{mm}$ and $a_{0,\text{blue}} \approx b_{0,\text{blue}} \approx 0.276\,\text{mm}$.

The definitions of the measurement volume, which is the scattered image of the illuminated volume, and the detection volume, which can actually be seen by the detector, are more abstract than that of the illuminated volume:

- For small particles ($D << \lambda_b$, incident and glare points coincide approximately with the center of the particle[1]), the measurement volume is practically identical to the illuminated volume. It is independent of the detector position and also of the particle diameter although larger particles scatter higher intensities (the scattered intensity is proportional to D^2) because its dimensions are defined relative to the maximal scattered intensity.
  Due to the minimal detectable intensity I_d which is determined by the sensitivity of the photo-detectors, the detection volume is slightly different from the measurement volume. It depends on particle properties and on the position and size of the detector surface.
- For larger particles, the measurement volume is slightly shifted compared to the illuminated volume. The displacement is dependent on the particle properties relevant for scattering (diameter D, refractive index n_{refr}) as well as on the scattering order and the position of the detector. For the detection volume, I_d must be additionally considered.

As signals are registered only from the detection volume, the latter is of interest in the following.

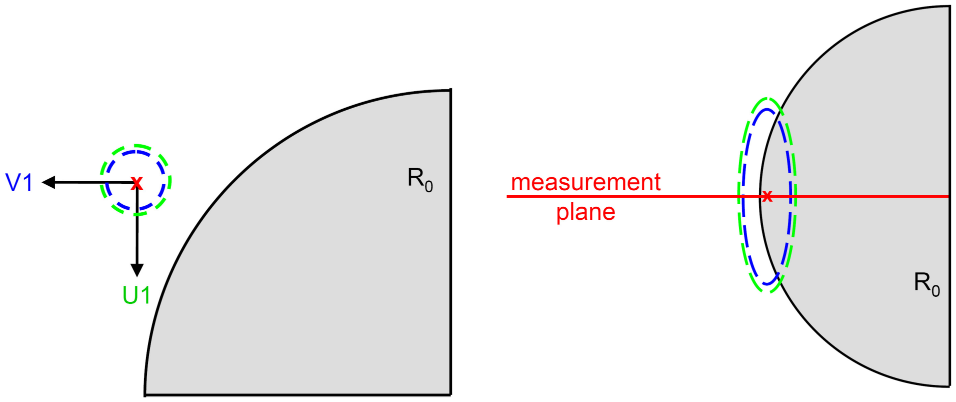

Figure B.12: Illuminated volumes.

B.6.2 Diameter of the detection volume

The derivation of $d_{t,i}$ is given in detail in [61] and [2]. The drops are sorted in size classes k and several cases must be distinguished. Slit apertures in the receiving optics are used to provide a well-defined length of the detection volume.

---

[1] Note that diameter determination is not possible in case of coinciding glare points. A phase change has to be measurable, i.e. a minimal particle size is required.

- For small drops, the detection volume may not be truncated by the slit aperture. The condition for that case can be estimated as

  $$\bar{L}_k < \frac{2 \cdot l_s}{3 \cdot \mu_l \cdot \sin \Phi_{\mathrm{op}}}\,, \tag{B.7}$$

  where $\bar{L}_k$ is the mean Doppler burst length of size class k ($L_i = \tau_i \cdot \sqrt{U1^2 + V1^2}$ with τ_i the residence/transit time). $\mu_l = c_0/a_0$ is the ratio of the long half axis to the small half axis of the illuminated volume and $\Phi_{\mathrm{op}} = 30°$ is the detection angle in the chosen PDA setup. The effective slit length (= physical width / magnification factor of the receiving optics) is $l_s = 0.32\,\mathrm{mm}$.
  If the condition of Equation B.7 is true, the diameter of the detection volume is given as

  $$d_{t,k} = \frac{3}{2} \cdot \bar{L}_k\,. \tag{B.8}$$

  The value is independent of the individual drop trajectories in this case.

- If the detection volume is cut by the slit, its diameter gets dependent on the drop trajectory as well. For the derivation (restricted to validated drops) it is assumed that the largest half axis of the detection volume lies in z-direction perpendicular to the measurement plane and that the velocity component in x-direction is to be measured. The x-direction denotes the main flow direction and might refer to $U1$ or $V1$. The slit is not bounded in the x-direction.

  - If $\sin \gamma_i = v_y / \sqrt{v_x^2 + v_y^2} = 0$ the diameter is given as follows:

    $$d^*_{t,i} = \frac{4}{\pi} \cdot L_i\,. \tag{B.9}$$

  - Else, $d^*_{t,i}$ is determined as the solution of

    $$(d^*_{t,i})^2 - \frac{3}{2} \cdot \left(L_i + \frac{l_s}{\cos \Phi_{\mathrm{op}} \cdot \sin \gamma_i} \right) \cdot d^*_{t,i} + \frac{6}{\pi} \cdot \frac{l_s \cdot L_i}{\cos \Phi_{\mathrm{op}} \cdot \sin \gamma_i} = 0\,, \tag{B.10}$$

    where the negative root must be chosen when solving the quadratic equation.

  The value $d^*_{t,i}$ is calculated for every single drop first. Then, an averaging is done for each size class which gives the values $d_{t,k}$. These values are used, not the single values $d^*_{t,i}$. The averaging is already done at an earlier step of the derivation in [61]. The values $d_{t,k}$ for a size class then result directly. However, the early averaging includes also an averaging over the droplet trajectories, i.e. over $\sin \gamma_i$. This is reasonable for free spray measurements but not for spray/wall interaction where primary and secondary directions differ strongly.

Using the formulae above, the data of every measurement point are treated separately. Figure 4.28 shows the results for the exemplary measurement point.

B.6.3 Projection of the detection volume onto the target

As explained in Section 4.4, $d_{t,i}$ is of interest for free spray considerations but not for spray/wall interaction. For the latter, it must be transferred to the target in order to

get an uncertainty area $\Delta\Theta_{\text{con},i}$ for the wall contact point $\Theta_{\text{con},i}$ of drop i.
To do so, the end points of $d_{t,i}$ are projected along the velocity vector of the drop to the positions Θ_1 and $\Theta_2 \in [0°, 90°]$ on the target surface. The procedure is completely analogous to the determination of the wall contact point itself. Figure B.13 illustrates this for both situations, $\Theta_{\text{con},i} \leq \Theta_i$ and $\Theta_{\text{con},i} > \Theta_i$ respectively.
The values $d_{w,i}$ and $\Delta\Theta_{\text{con},i}$ are then calculated where $d_{w,i} = R_0 \cdot \Delta\Theta_{\text{con},i} = R_0 \cdot (\Theta_2 - \Theta_1)$ with $\Theta_2 > \Theta_1$.
Figures B.14-B.16 show some exemplary results for $\Delta\Theta_{\text{con},i}$. The kinks for small and large values of Θ_{con} are conspicuous at first glance. Yet, these are quite plausible: For a measurement point (d_i,Θ_i), the possible values of Θ_{con} are geometrically restricted to a range $[\Theta_{\text{con,min}}, \Theta_{\text{con,max}}]$, see Figure B.17. Drops with a calculated value of $\Theta_{\text{con},i}$ outside that band are filtered out in the evaluation, see Section 4.2.3. For a given $d_i > 0$, $\Theta_i \in]0°, 90°[$, these limits can be calculated:

$$\Theta_{\text{con},i} \leq \Theta_i \quad : \quad \begin{cases} \tan\Theta_{\text{con,min}} = \frac{+R_0 \cdot \cos\Theta_{\text{con,min}} - (R_0 + d_i) \cdot \cos\Theta_i}{-R_0 \cdot \sin\Theta_{\text{con,min}} + (R_0 + d_i) \cdot \sin\Theta_i} \,, \\ \Rightarrow \Theta_{\text{con,min}} = \max[0; \Theta_i - \arccos\frac{R_0}{R_0 + d_i}]\,; \end{cases}$$

$$\Theta_{\text{con},i} > \Theta_i \quad : \quad \begin{cases} \tan\Theta_{\text{con,max}} = \frac{-R_0 \cdot \cos\Theta_{\text{con,max}} + (R_0 + d_i) \cdot \cos\Theta_i}{+R_0 \cdot \sin\Theta_{\text{con,max}} - (R_0 + d_i) \cdot \sin\Theta_i} \,, \\ \Rightarrow \Theta_{\text{con,max}} = \min[90; \Theta_i + \arccos\frac{R_0}{R_0 + d_i}]\,. \end{cases}$$

If a wall contact point $\Theta_{\text{con},i}$ lies near such a limit, the restriction of Θ_2 (Θ_1) to the range $[0°, 90°]$ yields $\Delta\Theta_{\text{con},i} = 90° - \Theta_1$ ($\Delta\Theta_{\text{con},i} = \Theta_2 - 0°$). If the value of Θ_{con} lies even nearer to the limit $\Theta_{\text{con,max}}$ ($\Theta_{\text{con,min}}$) in this case, the value of $\Delta\Theta_{\text{con},i}$ decreases again, because Θ_1 increases (Θ_2 decreases). This is reflected in the kinks in Figures B.14-B.16.

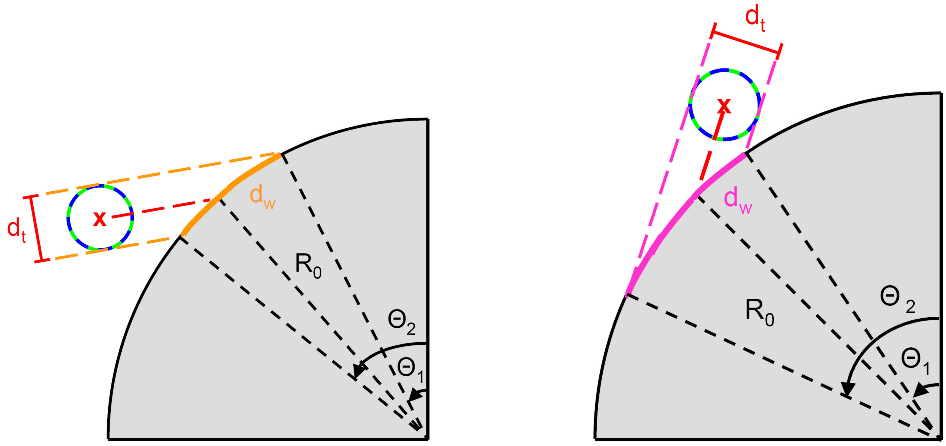

(a) $\Theta_{\text{con},i} \leq \Theta_i$ (b) $\Theta_{\text{con},i} > \Theta_i$

Figure B.13: Calculation of $d_{w,i}$ and $\Delta\Theta_{\text{con},i}$.

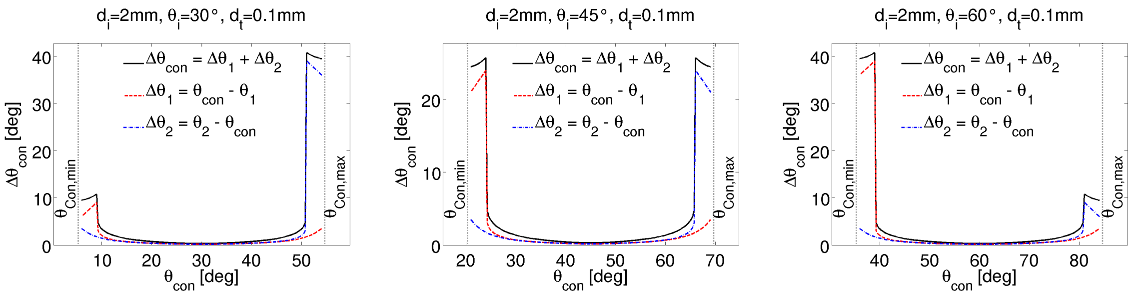

(a) $\Theta_i = 30°$. (b) $\Theta_i = 45°$. (c) $\Theta_i = 60°$.

Figure B.14: $\Delta\Theta_{\text{con}}$ versus Θ_{con} for varied Θ_i. $d_i = 2\,\text{mm}$, $d_t = 0.1\,\text{mm}$.

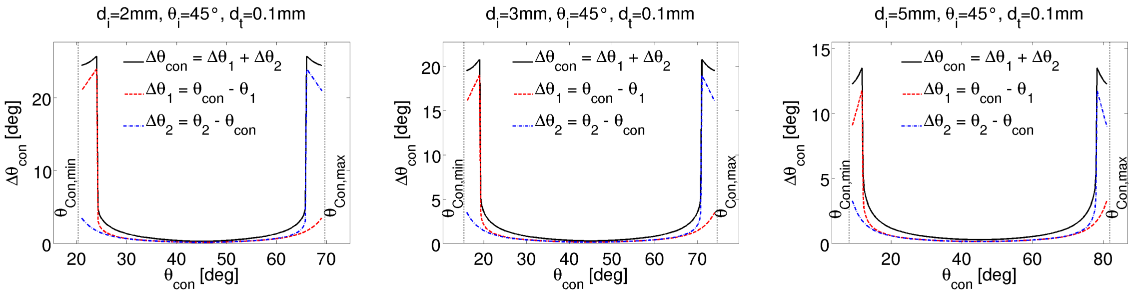

(a) $d_i = 2\,\text{mm}$ (b) $d_i = 3\,\text{mm}$ (c) $d_i = 5\,\text{mm}$

Figure B.15: $\Delta\Theta_{\text{con}}$ versus Θ_{con} for varied d_i. $\Theta_i = 45°$, $d_t = 0.1\,\text{mm}$.

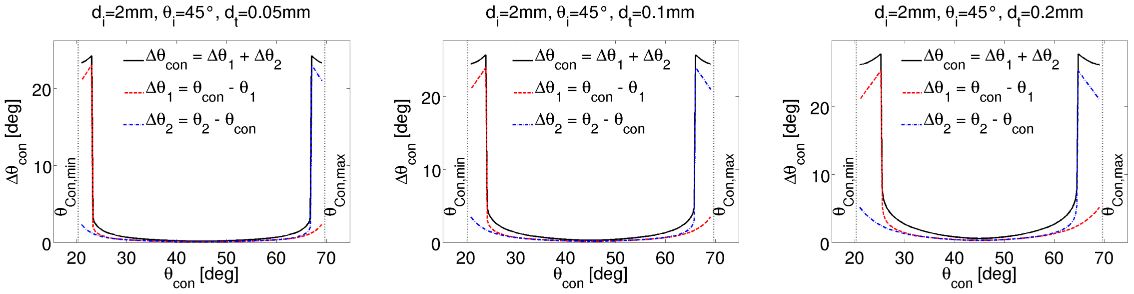

(a) $d_e = 0.05\,\text{mm}$ (b) $d_e = 0.1\,\text{mm}$ (c) $d_e = 0.2\,\text{mm}$

Figure B.16: $\Delta\Theta_{\text{con}}$ versus Θ_{con} for varied d_t. $d_i = 2\,\text{mm}$, $\Theta_i = 45°$.

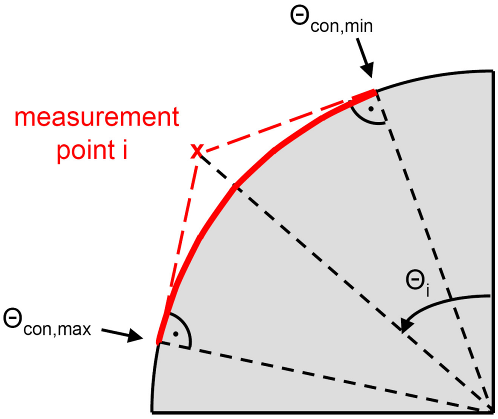

Figure B.17: Restricted area of possible $\Theta_{\text{con},i}$: For $\Theta_{\text{con,min}}$ and $\Theta_{\text{con,max}}$ respectively, the straight connection to the measurement point is tangential to the surface.

Appendix C

Model validation and comparison of chapter 6

C.1 Flow formation in simulations of the experiment

Simulating the experiment in Section 6.2, only a quasi-steady state is of interest but not the start of injection. Therefore, only parcels which attain their target-nearest position at $t \geq 5\,\mathrm{ms}$ are evaluated. This choice is justified in this appendix by considering the formation of the air flow and its influence on drop distributions. The latter are evaluated as described in Section 6.2.2. Elsässer's spray/wall interaction model is exemplarily applied with the film thickness set to zero in the calculations, i.e. $h_{\mathrm{film}} = 0$.

Considerations for the default mesh. Figures C.1 and C.2 show the air velocity as well as the parcel tracks from $t = 1.0\,\mathrm{ms}$ till $t = 8.0\,\mathrm{ms}$ in timesteps of $1.0\,\mathrm{ms}$ for the default mesh with maximal $1\,\mathrm{mm}$ edge length of the tetrahedral cells. Spray impact starts shortly before $t = 1.0\,\mathrm{ms}$. The air flow, however, takes about $5.0\,\mathrm{ms}$ to reach a quasi-steady state.
To see if the strong variations in the air flow formation, which is driven by the high-pressure spray, also influence the liquid phase in return, the distributions of the wall-normal velocity components on the target are exemplarily studied in Figure C.3. On the left-hand side, the evaluation comprises all parcels which attain their target-nearest position from $t = 0\,\mathrm{ms}$ onwards. On the right-hand side, it includes only those which do so from $t = 5.0\,\mathrm{ms}$ onwards. For the primary drops and the secondary ones assigned to the inside of the spray cone the differences are very small. As fewer drops are reflected to the outside of the spray hollow cone according to Elsässer's wall interaction model, the differences are more pronounced there. The same results are found for the distributions of diameters and wall-tangential velocity components.
In summary, it shows that the formation of the air flow only has a minor influence on the liquid phase. Nevertheless, the evaluation of the distributions in Section 6.2 and in the following is done only for parcels with target contact at $t \geq 5\,\mathrm{ms}$.

Influence of the mesh resolution. The average cell size of the computational grid presumably affects the formation of the air flow strongly. To cover this aspect, the results for the default mesh with maximal $1\,\mathrm{mm}$ edge length of the tetrahedra are compared to those for meshes with maximal $0.5\,\mathrm{mm}$ and $2\,\mathrm{mm}$ size respectively. To

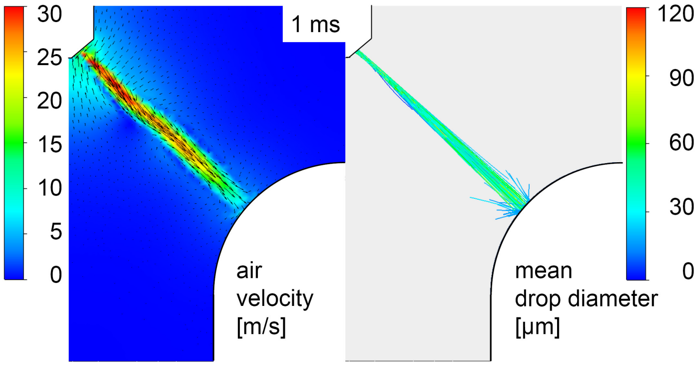

(a) $t = 1.0\,\mathrm{ms}$.

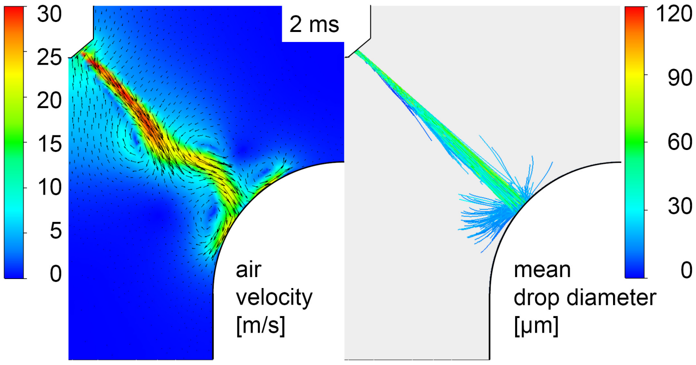

(b) $t = 2.0\,\mathrm{ms}$.

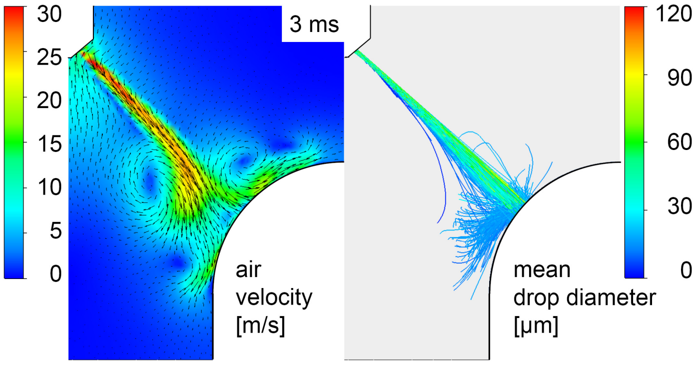

(c) $t = 3.0\,\mathrm{ms}$.

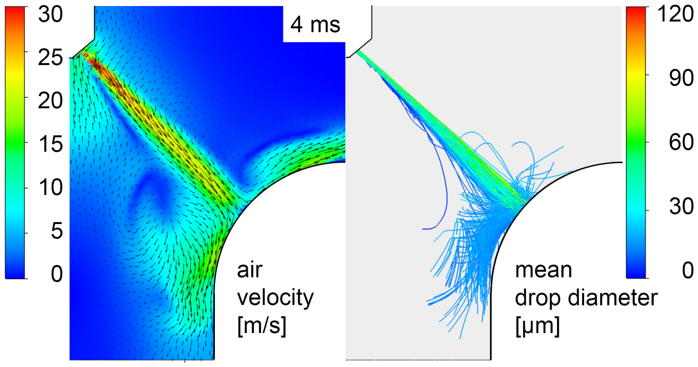

(d) $t = 4.0\,\mathrm{ms}$.

Figure C.1: Air velocity and parcel tracks for $t = 1.0\,\mathrm{ms}$ - $4.0\,\mathrm{ms}$ using the default mesh.

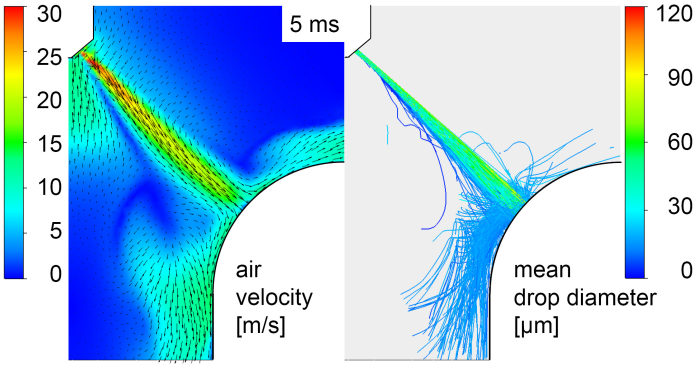

(a) $t = 5.0\,\mathrm{ms}$.

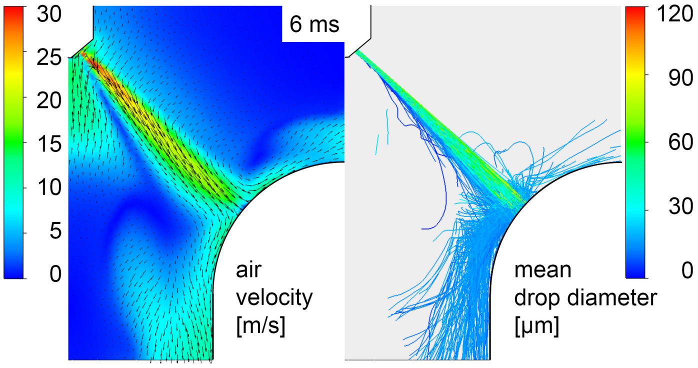

(b) $t = 6.0\,\mathrm{ms}$.

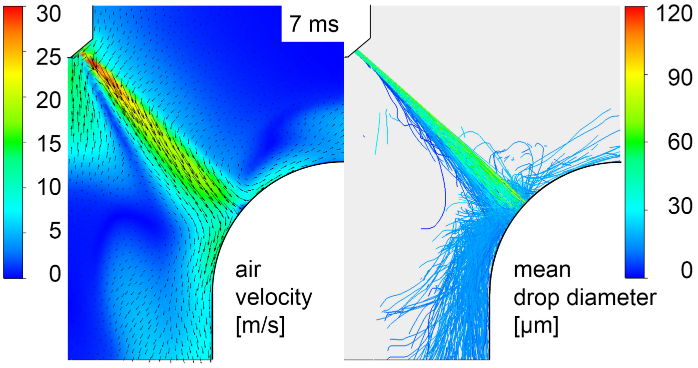

(c) $t = 7.0\,\mathrm{ms}$.

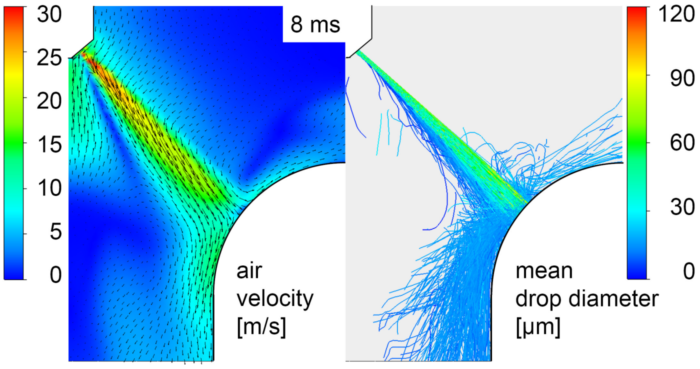

(d) $t = 8.0\,\mathrm{ms}$.

Figure C.2: Air velocity and parcel tracks for $t = 5.0\,\mathrm{ms}$ - $8.0\,\mathrm{ms}$ using the default mesh.

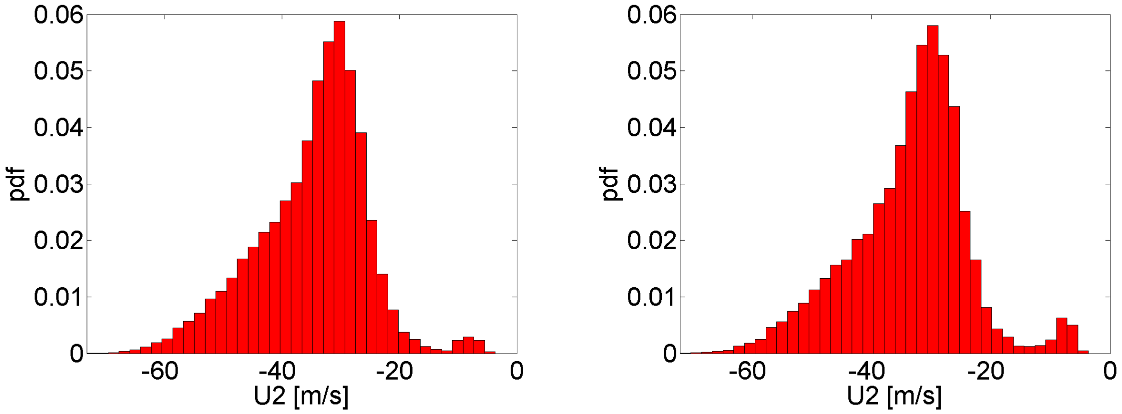

(a) Primary drops, $t \geq 0\,\mathrm{ms}$. (b) Primary drops, $t \geq 5.0\,\mathrm{ms}$.

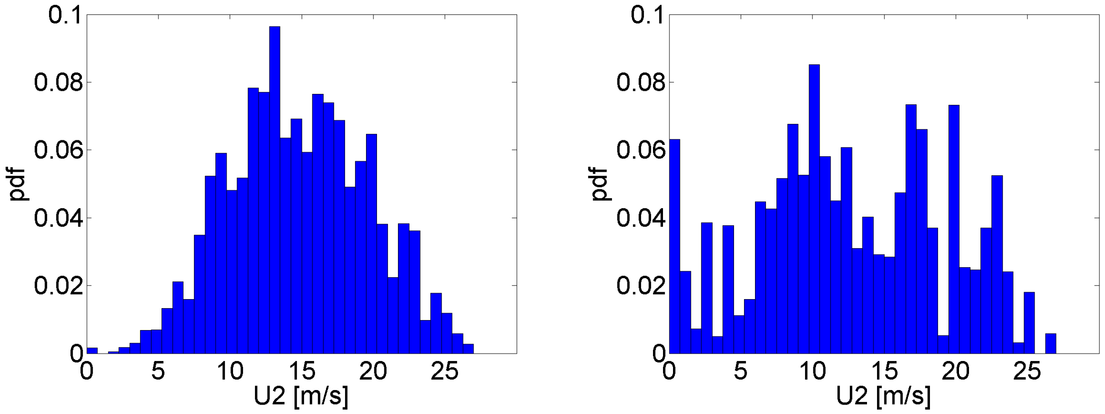

(c) Secondary drops assigned to the outside of the spray cone, $t \geq 0\,\mathrm{ms}$. (d) Secondary drops assigned to the outside of the spray cone, $t \geq 5.0\,\mathrm{ms}$.

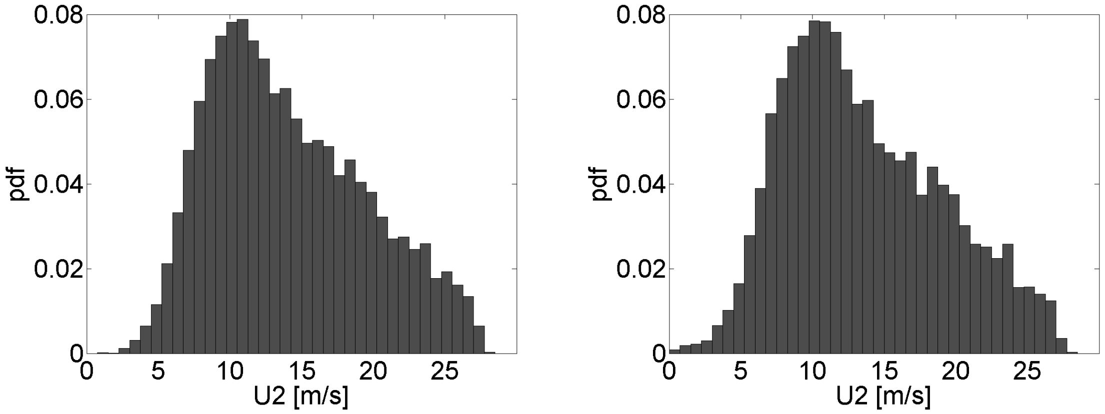

(e) Secondary drops assigned to the inside of the spray cone, $t \geq 0\,\mathrm{ms}$. (f) Secondary drops assigned to the inside of the spray cone, $t \geq 5.0\,\mathrm{ms}$.

Figure C.3: Distribution functions of the wall-normal velocity components for all drops which attain their target-nearest position from $t = 0\,\mathrm{ms}$ onwards (left) and from $t = 5\,\mathrm{ms}$ onwards (right).

reduce the computational effort for the fine mesh, the geometry is diminished with a depth of 10 mm instead of 20 mm, cf. Figure 6.2(b). The time step is reduced to $5.0 \cdot 10^{-6}$ s in this case.

Figure C.4 exemplarily shows the distributions of the wall-normal velocity components for the meshes with 0.5 mm and 2 mm size. The differences to those for the default mesh, see Figure C.3 on the right, are insignificant. This is reassuring because the results for the air flow field are by contrast remarkably affected by the mesh resolution in the considered range, cf. Figures C.5 and C.6: The air vortices, which are visible for the fine mesh and still for the default mesh with an already different appearance, are dampened by the coarse mesh from the beginning. The upward air flow inside the spray cone towards the injector is yet more pronounced for this mesh.

Due to the changes in the air flow, the trajectories of small secondary drops, which follow the flow, look also very different for the coarse grid in some distance to the impact area. It could be assumed that these deviations are due to the surface elements on the target being too coarse to model the curvature of the hemisphere sufficiently. This would lead to tilted impact angles compared to the finer meshes. Yet, this is disproved because it would also affect the distribution functions of Figure C.4 which is not the case.

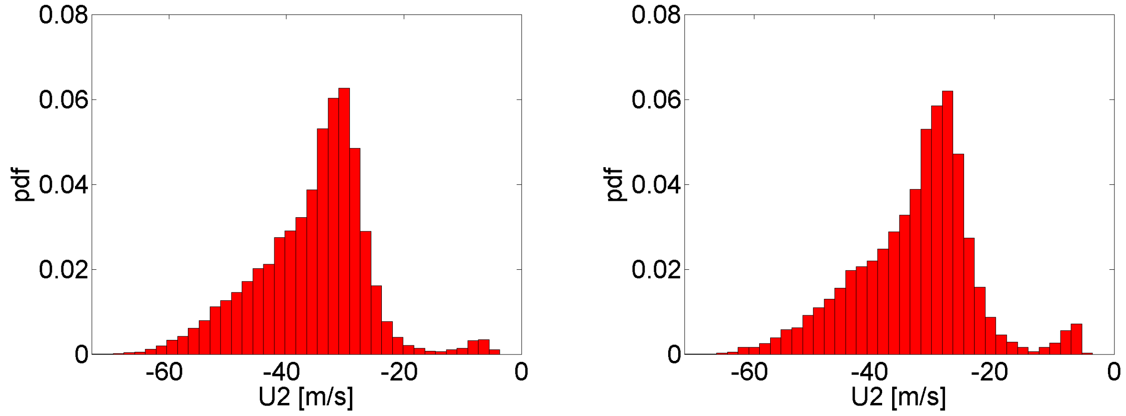

(a) Primary drops, 0.5 mm mesh. (b) Primary drops, 2 mm mesh.

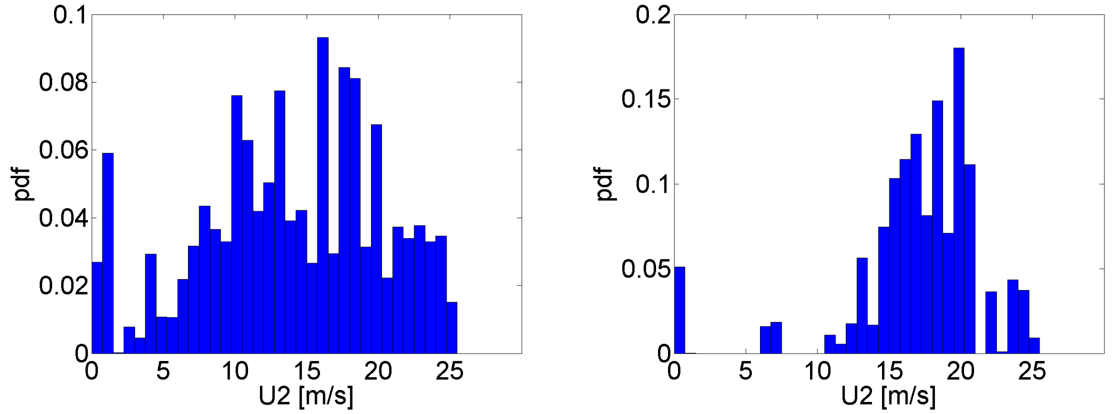

(c) Secondary drops assigned to the outside of the spray cone, 0.5 mm mesh. (d) Secondary drops assigned to the outside of the spray cone, 2 mm mesh.

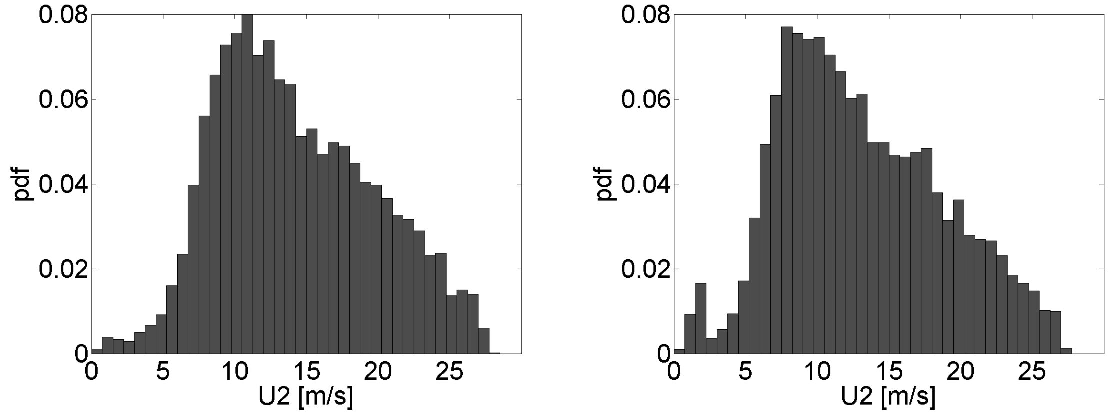

(e) Secondary drops assigned to the inside of the spray cone, 0.5 mm mesh. (f) Secondary drops assigned to the inside of the spray cone, 2 mm mesh.

Figure C.4: Distribution functions of the wall-normal velocity components for all drops which attain their target-nearest position for $t \geq 5.0\,\mathrm{ms}$ on a fine and a coarse mesh.

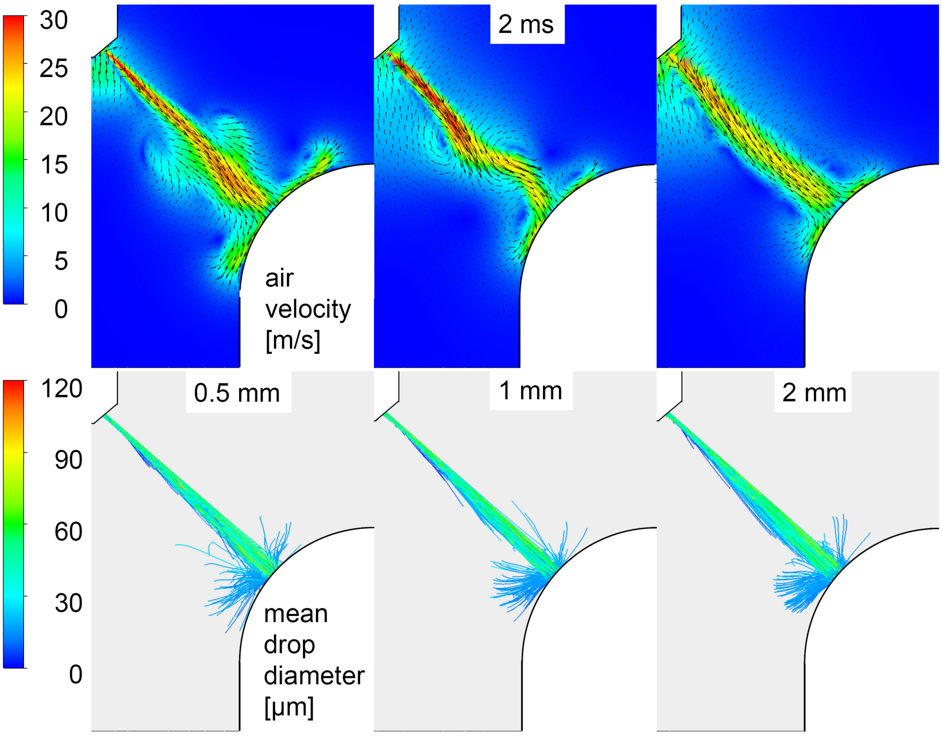

(a) $t = 2.0\,\mathrm{ms}$.

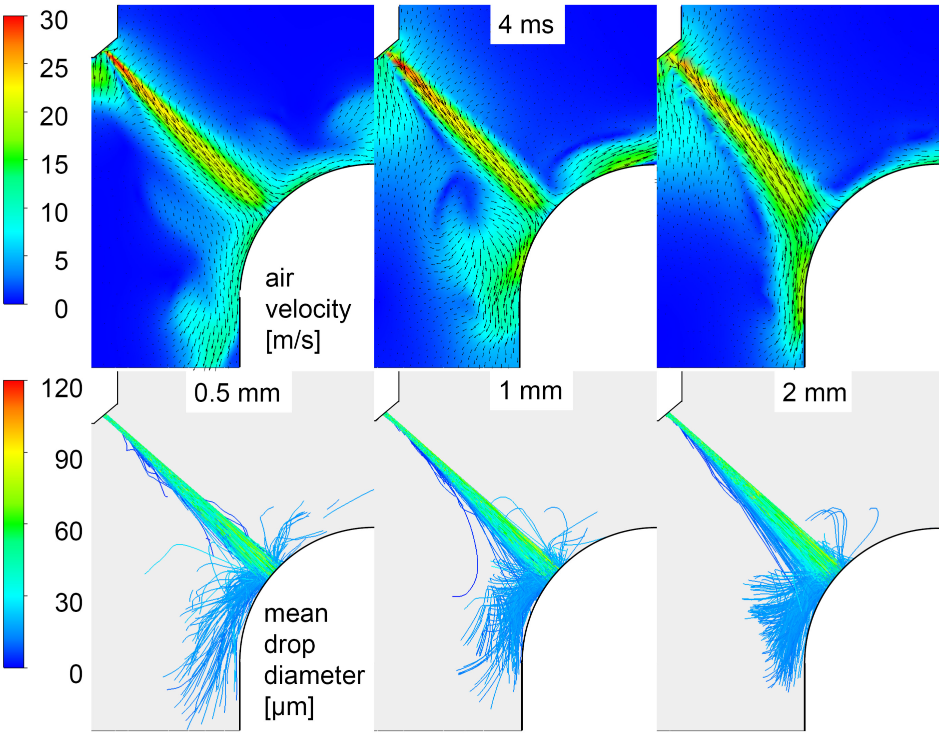

(b) $t = 4.0\,\mathrm{ms}$.

Figure C.5: Air velocity and parcel tracks at $t = 2\,\mathrm{ms}$ and $t = 4\,\mathrm{ms}$ for different mesh resolutions.

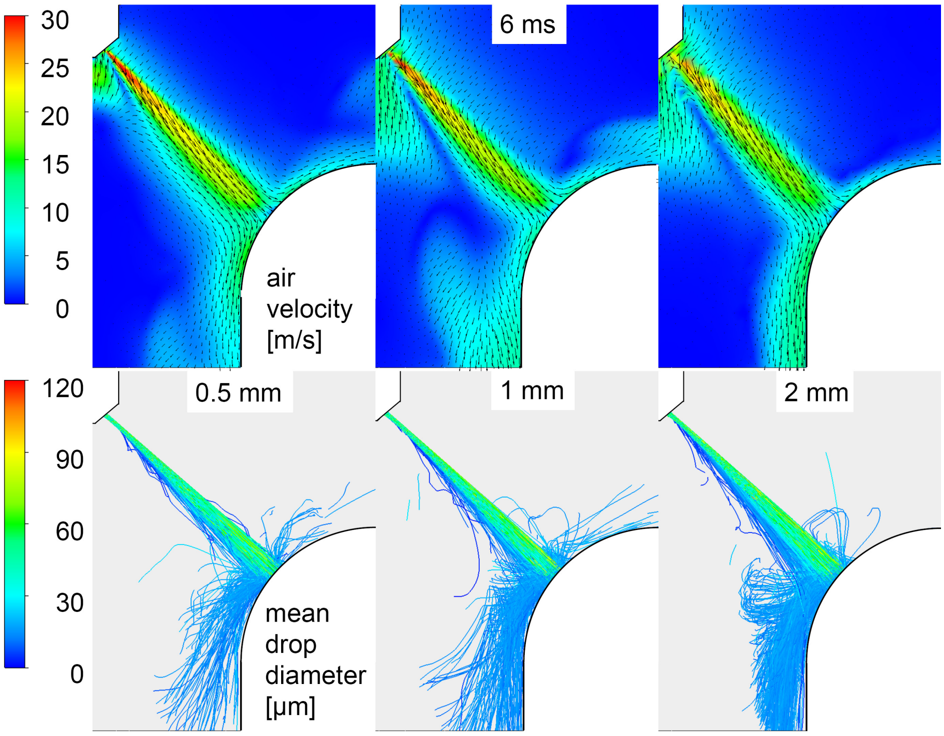

(a) $t = 6.0\,\mathrm{ms}$.

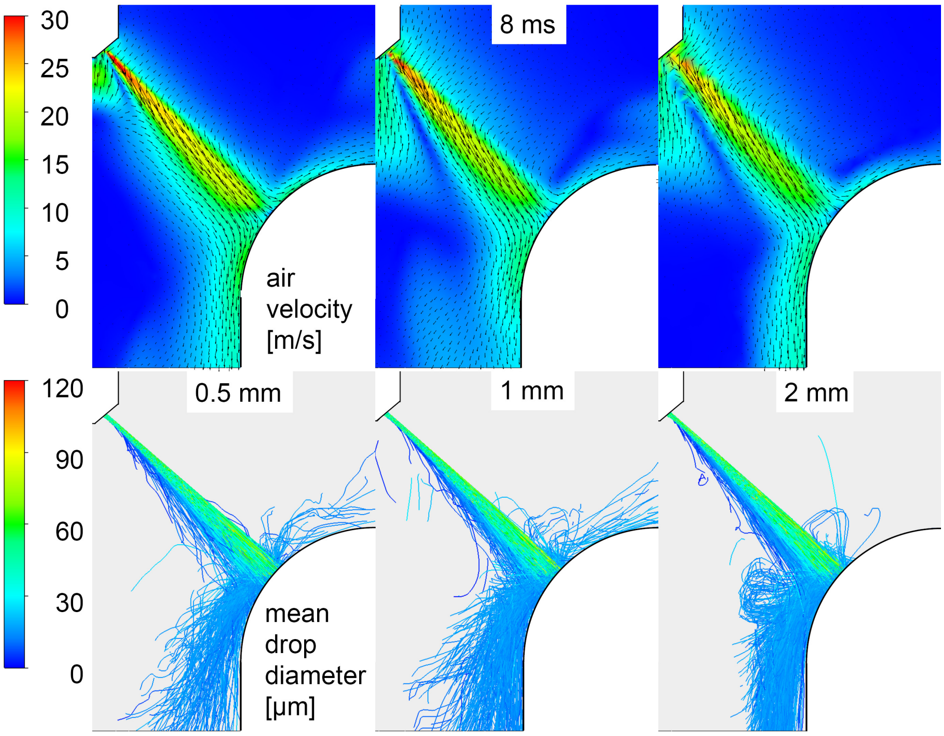

(b) $t = 8.0\,\mathrm{ms}$.

Figure C.6: Air velocity and parcel tracks at $t = 6\,\mathrm{ms}$ and $t = 8\,\mathrm{ms}$ for different mesh resolutions.

C.2 Test of the extrapolation to oblique impacts

In Section 6.3 the spray impact on an oblique plate is considered and the simulation results applying the new empirical model are compared to transmitted-light images. The case is used to validate the extrapolation to olique impacts which is based on simple assumptions, see Section 5.4.2. These are adapted to best reproduce the impact on a horizontal plate, i.e. for a mean impact angle of $\alpha_{10} = 45°$: The open parameter k_T in the proposed function $f_{\mathrm{T,forward}}(\alpha_{10}) = 0.203 + k_T \cdot \sin\alpha_{10}$ is set to $k_T = 0.28$.
In order to study if this choice of k_T also leads to the best results for the impact on the oblique plate, where impact angles from 32° to 58° occur, a variation is shown in Figure C.7. The presented values of $k_T = 0.14$, $k_T = 0.28$ and $k_T = 0.42$ correspond to $f_{\mathrm{T,forward}}(45°) = 0.3$, $f_{\mathrm{T,forward}}(45°) = 0.4$ and $f_{\mathrm{T,forward}}(45°) = 0.5$ in Figure 5.23 referring to the impact on the horizontal plate.
It turns out that $k_T = 0.28$ also yields the best results for the impingement on the oblique plate which affirms the extrapolation of the empirical correlations to oblique impact angles.

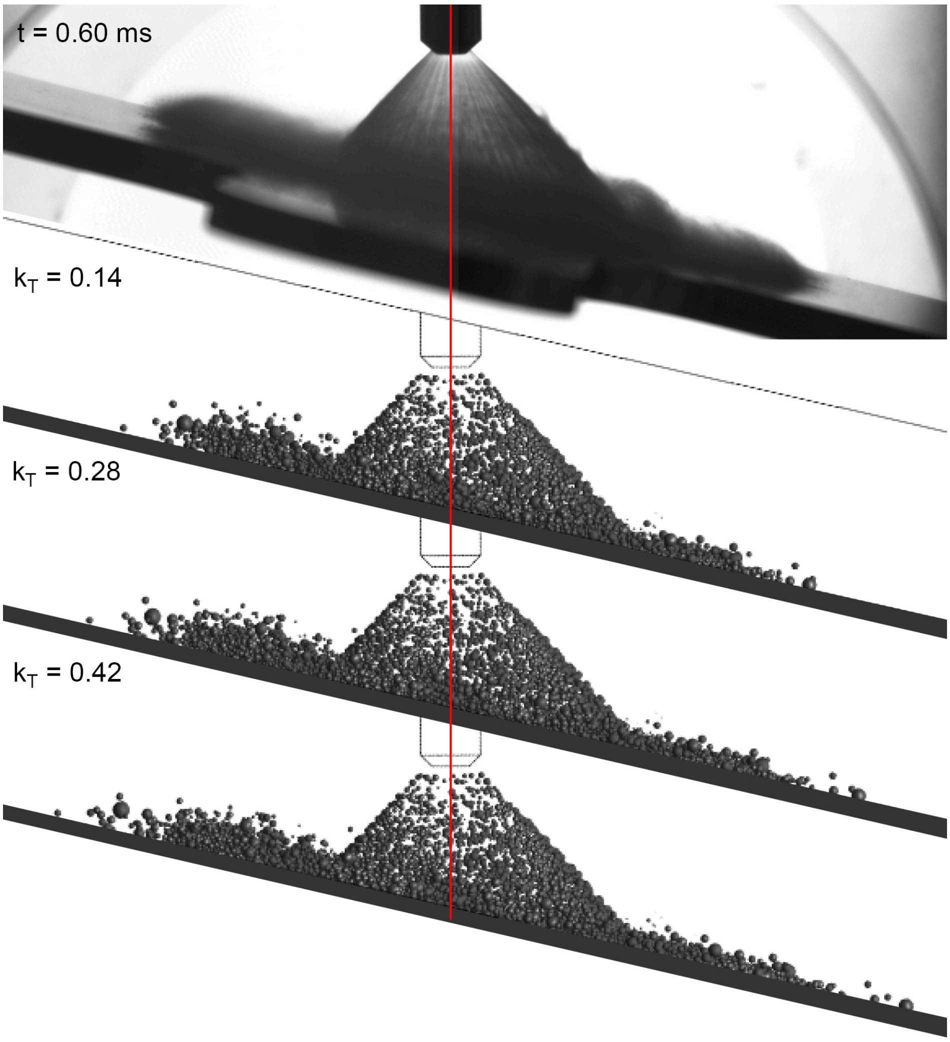

Figure C.7: Variations in k_T, i.e. in $f_{\mathrm{T,forward}}(\alpha_{10})$, at $t = 0.60\,\mathrm{ms}$.

List of Figures

List of Tables

Bibliography

[1] M. Al-Roub, P. V. Farrell, and J. Senda. Near wall interaction in spray impingement. *SAE Technical Paper Series*, 960863, 1996.

[2] H.-E. Albrecht, M. Borys, N. Damaschke, and C. Tropea. *Laser Doppler and Phase Doppler Measurement Techniques.* Springer-Verlag Berlin Heidelberg, 2003.

[3] ANSYS CFX. *Manual for CFX11*, 2006.

[4] C. C. Bai and A. D. Gosman. Development of methodology for spray impingement simulation. *SAE Technical Paper Series*, 950283, 1995.

[5] C. X. Bai, H. Rusche, and A. D. Gosman. Modeling of gasoline spray impingement. *Atomization and Sprays*, 12:1–27, 2002.

[6] K. J. Baumeister and F. F. Simon. Leidenfrost temperature - its correlation for liquid metals, cryogens, hydrocarbons and water. *Transactions of the ASME*, pages 166–173, 1973.

[7] R. B. Bird, W. E. Steward, and E. N. Lightfoot. *Transport Phenomena.* Cambridge University Press, 1960.

[8] J. Boussinesq. Theory of the vortex breakdown phenomenon. *Journal of Fluid Mechanics*, 14:593–629, 1962.

[9] S. Chandra and C. T. Avedisian. On the collision of a droplet with a solid surface. *Proc. R. Soc. London*, A(432):13–41, 1991.

[10] A. Coghe, G. Brunello, G. E. Cossali, and M. Marengo. Single drop splash on thin film: measurements of crown characteristics. *Proc. of the Conference on Liquid Atomization and Spray Systems, ILASS-Europe*, 1999. Toulouse, France.

[11] G. Cossali, M. Marengo, and M. Santini. Single drop empirical models for spray impact on solid walls: A review. *Atomization and Sprays*, 699, 2005.

[12] G. E. Cossali, A. Coghe, and M. Marengo. The impact of a single drop on a wetted solid surface. *Experiments in Fluids*, 22:463–472, 1997.

[13] G. E. Cossali, M. Marengo, and M. Santini. Multiple drop impact on heated surface. *Proc. of the Int. Conference on Liquid Atomization and Sprays Systems, ICLASS*, 2003. Sorrento, Italy.

[14] G. E. Cossali, M. Marengo, and M. Santini. Drop array impacts on heated surfaces: secondary atomization characteristics. *Proc. of the Conference on Liquid Atomization and Spray Systems, ILASS-Europe*, 2004. Nottingham, England.

[15] G. E. Cossali, M. Marengo, and M. Santini. Impact of single and multiple drop array. *Proc. of the Conference on Liquid Atomization and Spray Systems, ILASS-Europe*, 2004. Nottingham, England.

[16] G. E. Cossali, M. Marengo, and M. Santini. Splashing characteristics of multiple and single drop impacts onto a thin liquid film. *Proc. of the 6th International Conference on Multiphase Flow (ICMF)*, 2007. Leipzig, Germany.

[17] G. E. Cossali, M. Marengo, M. Santini, and J. Watanabe. Secondary droplet atomisation from single drop impact on heated surfaces. *Proc. of the Conference on Liquid Atomization and Spray Systems, ILASS-Europe*, 2002. Zaragoza, Spain.

[18] J. K. Dukowicz. A particle-fluid numerical model for liquid sprays. *Journal of Computational Physics*, 35(229), 1980.

[19] F. Durst. *Grundlagen der Strömungsmechanik.* Springer-Verlag Berlin Heidelberg, 2006.

[20] F. Durst, A. Melling, and J. H. Whitelaw. *Theorie und Praxis der Laser-Doppler-Anemometrie.* Wissenschaft und Technik, 1987.

[21] J. Eggers and E. Villermaux. Physics of liquid jets. *Reports on Progress in Physics*, 71(036601), 2008.

[22] G. Elsässer. *Numerische und experimentelle Untersuchungen zur Ausbreitung und Reflexion von Kraftstoffstrahlen.* Diplomarbeit, Universität Karlsruhe, Fakultät für Maschinenbau, 1998.

[23] G. Elsässer. *Experimentelle Untersuchung und numerische Modellierung der freien Kraftstoffstrahlausbreitung und Wandinteraktion unter motorischen Randbedingungen.* PhD thesis, Universität Karlsruhe, Fakultät für Maschinenbau, 2001.

[24] EU energy project N° NNE5-1999-20015, contract number ENK6-CT2000-00051. *Droplet-wall-interaction Phenomena Of Relevance To Direct Injection Gasoline Engines (DWDIE)*, 2003.

[25] J. H. Ferziger and M. Perić. *Computational Methods for Fluid Dynamics.* Springer-Verlag Berlin, 3 edition, 2002.

[26] T. Frank. *Parallele Algorithmen für die numerische Simulation dreidimensionaler, disperser Mehrphasenströmungen und deren Anwendung in der Verfahrenstechnik.* Habilitationsschrift, Technische Universität Chemnitz, Fakultät für Maschinenbau und Verfahrenstechnik, 2002.

[27] Z. Han, Z. Xu, and N. Trigui. Spray/wall interaction models for multidimensional engine simulation. *International Journal of Engine Research*, 1(1), 2000.

[28] K. Horvat. *Computational modelling of spray impingement accounting for the wall film formation.* PhD thesis, Technische Universität Darmstadt, Fachbereich Maschinenbau, 2006.

[29] Robert Bosch GmbH (Hrsg.). *Ottomotor-Management.* Friedr. Vieweg & Sohn Verlag Wiesbaden, 3 edition, 2005.

[30] T. Jonas. *Transiente Phänomene beim Tropfenaufprall auf temperierte Wände*. PhD thesis, Institut für Angewandte Mechanik und Strömungsphysik, Georg-August-Universität Göttingen, 1996.

[31] D. Kalantari. *Characterization of liquid spray impact onto walls and films*. PhD thesis, Technische Universität Darmstadt, Fachbereich Maschinenbau, 2006.

[32] D. Kalantari and C. Tropea. Comparison between splash of a droplet in isolation and in a spray. *Spray Workshop, Technische Universität Darmstadt, Chair of Fluid Mechanics and Aerodynamics*, May 29-30th 2006.

[33] A. M. Kubitzek. *Experimentelle Untersuchungen des Phasenübergangs beim Tropfenaufprall auf heiße Wände*. Forschungsbericht 97-21, Deutsche Forschungsanstalt für Luft- und Raumfahrt e.V., Institut für Srömungsmechanik Göttingen, 1997.

[34] D. Kuhnke. *Spray/Wall-Interaction Modelling by Dimensionless Data Analysis*. PhD thesis, Technische Universität Darmstadt, Fachbereich Mathematik, 2004.

[35] E. Kumzerova. *Validation of Spray Simulations in CFX-11*. ANSYS, 2008.

[36] B. E. Launder and D. B. Spalding. The numerical computation of turbulent flows. *Computer Methods in Applied Mechanics and Engineering*, 3(2):269–289, 1974.

[37] A. H. Lefebvre. *Atomization and Sprays*. Hemisphere Publishing Corporation, 1989.

[38] Z. Liu, T. Obokata, and R. D. Reitz. Modeling drop drag effects on fuel spray impingement in direct injection diesel engines. *SAE Technical Paper Series*, 970879, 1997.

[39] W. C. Macklin and G. J. Metaxas. Splashing of drops on liquid layers. *Journal of Applied Physics*, 47(9):3963–3969, 1976.

[40] P. Marmottant and E. Villermaux. Fragmentation of stretched liquid ligaments. *Physics of Fluids*, 16(8), 2004.

[41] F. R. Menter. Two-equation eddy-viscosity turbulence models for engineering applications. *American Institute of Aeronautics and Astronautics (AIAA)*, 32(8):1598–1605, 1994.

[42] E. Michaelides. *Particles, bubbles & drops*. World Scientific Publishing Co. Pte. Ltd., 2006.

[43] S. Mukherjee and J. Abraham. Crown evolution in drop impact on wet walls. *Proc. of 6th International Conference on Multiphase Flow (ICMF)*, 2007. Leipzig, Germany.

[44] C. Mundo. *Zur Sekundärzerstäubung newtonscher Fluide an Oberflächen*. PhD thesis, Universität Erlangen-Nürnberg, 1996.

[45] C. Mundo, M. Sommerfeld, and C. Tropea. Droplet-wall collisions: experimental studies of the deformation and breakup processes. *International Journal of Multiphase Flow*, 21:151–173, 1995.

[46] J. D. Naber and P. V. Farrell. Hydrodynamics of droplet impingement on a heated surface. *SAE Technical Paper Series*, 930919, 1993.

[47] J. D. Naber and R. D. Reitz. Modeling engine spray/wall impingement. *SAE Technical Paper Series*, 880107, 1988.

[48] N. Nagai and S. Nishio. Leidenfrost temperature on an extremely smooth surface. *Experimental Thermal and Fluid Science*, 12:373–379, 1996.

[49] M. Nagaoka, H. Kawazoe, and N. Nomura. Modelling fuel spray impingement on a hot wall for gasoline engines. *SAE Technical Paper Series*, 940525, 1994.

[50] T. Okawa, T. Shiraishi, and T. Mori. Production of secondary drops during the single water drop impact onto a plane water surface. *Experiments in Fluids*, 41:965–974, 2006.

[51] P. J. O'Rourke. *Collective Drop Effects on Vaporizing Liquid Sprays.* PhD thesis, Princeton University, 1981.

[52] K. Park and A. P. Watkins. Comparison of wall spray impaction models with experimental data on drop velocities and sizes. *International Journal of Heat and Fluid Flow*, 17:424–438, 1996.

[53] S. Pischinger. *Verbrennungsmotoren I und II.* Vorlesungsumdruck, RWTH Aachen, Lehrstuhl für Verbrennungskraftmaschinen, 23 edition, 2002.

[54] W. E. Ranz and W. R. Marshall. Evaporation from drops, part ii. *Chem. Eng. Progr.*, 48:173–180, 1952.

[55] M. Rein. Phenomena of liquid drop impact on solid and liquid surfaces. *Fluid Dynamics Research*, 12:61–93, 1993.

[56] C.-H. Rexroth. *Methoden zur effizienten Berechnung komplexer Strömungen auf unstrukturierten Gittern.* PhD thesis, Universität Karlsruhe, Fakultät für Maschinenbau, 1996.

[57] R. Rioboo, M. Marengo, and C. Tropea. Outcomes from a drop impact on solid surfaces. *Proc. of the Conference on Liquid Atomization and Spray Systems, ILASS-Europe*, 1999. Toulouse, France.

[58] I. V. Roisman, L. Araneo, M. Marengo, and C. Tropea. Evaluation of drop impingement models: experimental and numerical analysis of a spray impact. *Proc. of the Conference on Liquid Atomization and Spray Systems, ILASS-Europe*, 1999. Toulouse, France.

[59] I. V. Roisman, K. Horvat, and C. Tropea. Spray impact: Rim transverse instability initiating fingering and splash, and description of secondary spray. *Physics of Fluids*, 18(102104), 2006.

[60] I. V. Roisman, R. Rioboo, and C. Tropea. Normal impact of a liquid drop on a dry surface: Model for spreading and receding. *Proc. R. soc. London, Ser. A*, 458(1411), 2002.

[61] I. V. Roisman and C. Tropea. Flux measurements in sprays using phase doppler techniques. *Atomization and Sprays*, 11:667–699, 2001.

[62] I. V. Roisman and C. Tropea. Impact of a drop onto a wetted wall: description of crown formation and propagation. *Journal of Fluid Mechanics*, 472:373–397, 2002.

[63] I. V. Roisman and C. Tropea. Fluctuating flow in a liquid layer and secondary spray created by an impacting spray. *International Journal of Multiphase Flow*, 31:179–200, 2005.

[64] W. Samenfink. *Grundlegende Untersuchungen zur Tropfeninteraktion mit schubspannungsgetriebenen Wandfilmen.* PhD thesis, Universität Karlsruhe (TH), Fakultät für Maschinenbau, 1997.

[65] M. Santini. *Effect of surface properties on secondary atomization by impact of drops over heated surfaces.* PhD thesis, Universitã degli Studi di Parma, Facoltã di Ingegneria, 2004.

[66] M. Santini. Private communication, 2008.

[67] M. Schäfer. *Numerik im Maschinenbau.* Springer-Verlag Berlin Heidelberg, 1999.

[68] M. Schneider. *Experimentelle Untersuchungen zur Tropfen-Film-Wechselwirkung (Studienarbeit).* PhD thesis, Universität Karlsruhe (TH), 1989.

[69] R. M. Schotland. Experimental results relating to the coalescence of water drops with water surfaces. *Discussions of the Faraday Society*, 30:72–77, 1960.

[70] J. Senda, T. Kanda, M. Al-Roub, P. Farrell, T. Fukami, and H. Fujimoto. Modeling spray impingement considering fuel film formation on the wall. *SAE Technical Paper Series*, 970047, 1997.

[71] J. Senda, M. Kobayashi, S. Iwashita, and H. Fujimoto. Modeling of diesel spray impingement on a flat wall. *SAE Technical Paper Series*, 941894, 1994.

[72] W. A. Sirignano. *Fluid Dynamics and Transport of Droplets and Sprays*. Cambridge University Press, 1999.

[73] D. Sivakumar and C. Tropea. Splashing impact of a spray onto a thin liquid film. *Physics of Fluids*, 15(1), 2002.

[74] M. Sommerfeld. Validation of a stochastic lagrangian modelling approach for interparticle collisions in homogeneous isotropic turbulence. *International Journal of Multiphase Flow*, 27:1829–1858, 2001.

[75] Springer-Verlag Berlin. *VDI-Wärmeatlas*, 8 edition, 2001.

[76] J. Spurk and N. Aksel. *Strömunglehre.* Springer-Verlag Berlin Heidelberg, 7 edition, 2007.

[77] D. W. Stanton and C. J. Rutland. Modeling fuel film formation and wall interaction in diesel engines. *SAE Technical Paper Series*, 960628, 1996.

[78] D. W. Stanton and C. J. Rutland. Multi-dimensional modeling of heat and mass transfer of fuel films resulting from impinging sprays. *SAE Technical Paper Series*, 980132, 1998.

[79] C. D. Stow and R. D. Stainer. The physical products of a splashing water drop. *Journal of the Meteorological Society of Japan*, 55(5):518–531, 1977.

[80] K. Takeuchi, J. Senda, and Y. Sato. Experimental studies on the behavior of a small droplet impinging upon a hot surface. *Proc. of the Int. Conference on Liquid Atomization and Sprays Systems, ICLASS*, 1982. University of Wisconsin-Madison, USA.

[81] R. W. Temple-Pediani. Fuel drop vaporization under pressure on a hot surface. *Proc. Instn. Mech. Engrs.*, 184(38):677–696, 1970.

[82] C. Tropea and I. V. Roisman. Modelling of spray impact on solid surfaces. *Atomization and Sprays*, 10:387–408, 2000.

[83] M. F. Trujillo and C. F. Lee. Modeling crown formation due to the splashing of a droplet. *Physics of Fluids*, 13(9):2503–2516, 2001.

[84] R. van Basshuysen and F. Schäfer (Hrsg.). *Handbuch Verbrennungsmotor.* Friedr. Vieweg & Sohn Verlag Braunschweig/Wiesbaden, 2 edition, 2002.

[85] H. K. Versteeg and W. Malalasekera. *An introduction to Computational Fluid Dynamics, The Finite Volume Method.* Pearson Prentice Hall Harlow England, 1995.

[86] E. Villermaux. Fragmentation. *Annual Review of Fluid Mechanics*, 39:419–446, 2007.

[87] E. Villermaux, P. Marmottant, and J. Duplat. Ligament-mediated spray formation. *Physical Review Letters*, 92(7), 2004.

[88] L. H. J. Wachters and N. A. J. Westerling. The heat transfer from a hot wall to impinging water drops in the spheroidal state. *Chemical Engineering Science*, 21:1047–1056, 1966.

[89] A. Wang and C. Chen. Splashing impact of a single drop onto very thin liquid films. *Physics of Fluids*, 12(9), 2000.

[90] A. Wang and C. Chen. On some new aspects of splashing impact of drop-liquid surface interactions. *Drop-Surface Interactions*, 2002. Rein, Springer-Verlag.

[91] D. C. Wilcox. *Turbulence Modeling for CFD.* DCW Industries Inc., La Cañada, 1993.

[92] N. Wruck. *Transientes Sieden von Tropfen beim Wandaufprall.* PhD thesis, RWTH Aachen, 1999.

[93] T. Y. Xiong and M. C. Yuen. Evaporation of a liquid droplet on a hot plate. *International Journal of Heat and Mass Transfer*, 34(7):1881–1894, 1991.

[94] A. L. Yarin. Drop impact dynamics: splashing, spreading, receding, bouncing.... *Annual Review of Fluid Mechanics*, 38:159–192, 2006.

[95] A. L. Yarin and D. A. Weiss. Impact of drops on solid surfaces: self-similar capillary waves, and splashing as a new type of kinematic discontinuity. *Journal of Fluid Mechanics*, 283:141–173, 1995.

The author's background

Personal details:

Name:	Monika Mühlbauer
Date of birth:	26th of May, 1981
Place of birth:	92224 Amberg, Germany
Nationality:	German

Education:

09/1987–07/1991	Primary school, Kümmersbruck
09/1991–05/2000	Gregor-Mendel-Gymnasium, Amberg

University studies:

10/2000–03/2006	Studies in physics at the Technische Universität München 2004: Semester abroad within the Sokrates-Erasmus-program at the Université Pierre et Marie Curie, Paris, France Final degree: Diplom-Physikerin Univ.
05/2006–09/2009	Ph.D. at the Technische Universität Darmstadt, (Chair of Fluid Mechanics and Aerodynamics, Prof. Dr.-Ing. Dr.-Ing. habil. C. Tropea) in cooperation with the BMW AG München (Department of Thermodynamics, Team CAE Combustion, Dr.-Ing. B. Durst)